**HELLENIC REPUBLIC**
**UNIVERSITY OF IOANNINA**
**SCHOOL OF ENGINEERING**
**DEPARTMENT OF MATERIALS SCIENCE AND ENGINEERING**

# NOVEL CONCEPTS FOR OPTIMIZING THE SELF-HEALING PROCESSES IN ADVANCED AEROSPACE COMPOSITE STRUCTURES

**KOSARLI MARIA**
MATERIALS SCIENCE ENGINEER

Thesis for the degree of Doctor of Philosophy

**IOANNINA, 2022**

**ΕΛΛΗΝΙΚΗ ΔΗΜΟΚΡΑΤΙΑ**
**ΠΑΝΕΠΙΣΤΗΜΙΟ ΙΩΑΝΝΙΝΩΝ**
**ΠΟΛΥΤΕΧΝΙΚΗ ΣΧΟΛΗ**
**ΤΜΗΜΑ ΜΗΧΑΝΙΚΩΝ ΕΠΙΣΤΗΜΗΣ ΥΛΙΚΩΝ**

# ΚΑΙΝΟΤΟΜΕΣ ΤΕΧΝΟΛΟΓΙΕΣ ΓΙΑ ΤΗ ΒΕΛΤΙΣΤΟΠΟΙΗΣΗ ΤΗΣ ΑΥΤΟ-ΙΑΣΗΣ ΣΕ ΚΑΤΑΣΚΕΥΕΣ ΠΡΟΗΓΜΕΝΩΝ ΣΥΝΘΕΤΩΝ ΥΛΙΚΩΝ

**ΚΟΣΑΡΛΗ ΜΑΡΙΑ**
ΜΗΧΑΝΙΚΟΣ ΕΠΙΣΤΗΜΗΣ ΥΛΙΚΩΝ

ΔΙΔΑΚΤΟΡΙΚΗ ΔΙΑΤΡΙΒΗ

**ΙΩΑΝΝΙΝΑ, 2022**

*«Η έγκριση της διδακτορικής διατριβής από το Τμήμα Μηχανικών Επιστήμης Υλικών της Πολυτεχνικής Σχολής του Πανεπιστημίου Ιωαννίνων δεν υποδηλώνει αποδοχή των γνωμών του συγγραφέα Ν. 5343/32, άρθρο 202, παράγραφος 2».*

**Application date of Ms. Maria Kosarli:** 14-11-2017

**Appointment date for the three-membered advisory committee:** 22-11-2017

**Members of the three-membered advisory committee:**

Supervisor
**Alkiviadis S. Paipetis**, Professor at the Dept. of Materials Science and Engineering, School of Engineering, University of Ioannina

Members
**Apostolos Avgeropoulos,** Professor at the Dept. of Materials Science and Engineering, School of Engineering, University of Ioannina
**Evaggelia Kontou-Drouga**, Professor at the School of Applied Mathematical & Physical Sciences, National Technical University of Athens

**Subject appointment date:** 22-11-2017
"Novel concepts for optimizing the self-healing processes in advanced aerospace composite structures"

**APPOINTMENT DATE FOR THE SEVEN-MEMBERED ADVISORY COMMITTEE:** 24-05-2022

**Alkiviadis S. Paipetis**, Professor at the Dept. of Materials Science and Engineering, School of Engineering, University of Ioannina
**Evaggelia Kontou-Drouga,** Professor at the School of Applied Mathematical & Physical Sciences, National Technical University of Athens,
**Apostolos Avgeropoulos,** Professor at the Dept. of Materials Science and Engineering, School of Engineering, University of Ioannina,
**Nektaria-Marianthi Barkoula**, Professor at the Dept. of Materials Science and Engineering, School of Engineering, University of Ioannina
**Stamatina Vouyiouka,** Associate Professor at the Dept. of Chemical Engineering, National Technical University of Athens
**Dimitrios Gournis,** Professor at the Dept. of Materials Science and Engineering, School of Engineering, University of Ioannina,
**Leonidas Gergidis,** Associate Professor at the Dept. of Materials Science and Engineering, School of Engineering, University of Ioannina

The Ph.D. thesis was awarded with grade "EXCELLENT" at **30-05-2022**

**The Head of the Department**

**Apostolos Avgeropoulos**
**Professor**

**The Secretary of the Department**

**Maria Kontou**

**Ημερομηνία αίτησης της κ. Κοσαρλή Μαρίας:** 14-11-2017

**Ημερομηνία ορισμού Τριμελούς Συμβουλευτικής Επιτροπής:** 22-11-2017

**Μέλη Τριμελούς Συμβουλευτικής Επιτροπής:**

Επιβλέπων
**Παϊπέτης Αλκιβιάδης,** Καθηγητής του Τ.Μ.Ε.Υ. της Πολυτεχνικής Σχολής του Πανεπιστημίου Ιωαννίνων

Μέλη
**Αυγερόπουλος Απόστολος,** Καθηγητής του Τ.Μ.Ε.Υ. της Πολυτεχνικής Σχολής του Πανεπιστημίου Ιωαννίνων
**Κοντού-Δρούγκα Ευαγγελία,** Καθηγήτρια της Σ.Ε.Μ.Φ.Ε. του Ε.Μ.Π.

**Ημερομηνία ορισμού θέματος:** 22-11-2017
«Καινοτόμες τεχνολογίες για τη βελτιστοποίηση της αυτο-ίασης σε κατασκευές προηγμένων σύνθετων υλικών»

**ΔΙΟΡΙΣΜΟΣ ΕΠΤΑΜΕΛΟΥΣ ΕΞΕΤΑΣΤΙΚΗΣ ΕΠΙΤΡΟΠΗΣ:** 24-05-2022

**Αλκιβιάδης Παϊπέτης**, Καθηγητής του Τ.Μ.Ε.Υ. της Πολυτεχνικής Σχολής του Πανεπιστημίου Ιωαννίνων
**Ευαγγελία Κοντού-Δρούγκα**, Καθηγήτρια της Σ.Ε.Μ.Φ.Ε. του Ε.Μ.Π.
**Απόστολος Αυγερόπουλος,** Καθηγητής του Τ.Μ.Ε.Υ. της Πολυτεχνικής Σχολής του Πανεπιστημίου Ιωαννίνων
**Νεκταρία-Μαριάνθη Μπάρκουλα,** Καθηγήτρια του Τ.Μ.Ε.Υ. της Πολυτεχνικής Σχολής του Πανεπιστημίου Ιωαννίνων
**Σταματίνα Βουγιούκα,** Αν. Καθηγήτρια της Σχολής Χημικών Μηχανικών του Ε.Μ.Π.
**Δημήτριος Γουρνής,** Καθηγητής του Τ.Μ.Ε.Υ. της Πολυτεχνικής Σχολής του Πανεπιστημίου Ιωαννίνων
**Λεωνίδας Γεργίδης,** Αν. Καθηγητής του Τ.Μ.Ε.Υ. της Πολυτεχνικής Σχολής του Πανεπιστημίου Ιωαννίνων

Έγκριση Διδακτορικής Διατριβής με βαθμό **«ΑΡΙΣΤΑ»** στις **30-05-2022**

Ο Πρόεδρος του Τμήματος
Απόστολος Αυγερόπουλος
Καθηγητής

Η Γραμματέας του Τμήματος
Μαρία Κόντου

To my parents
Anastasios and Androniki
& my brother Ilias

Στους γονείς μου
Αναστάσιο και Ανδρονίκη
& στον αδερφό μου Ηλία

# Abstract

Fiber Reinforced Polymers (FRPs) are among the essential technological materials in the industrial and research communities due to their excellent specific properties. The low fracture toughness of the FPRs can consequence in detrimental damage phenomena that may reduce their structural integrity. The repair of damage is both time and money-consuming. Besides the traditional repair techniques, the approach of self–healing materials has attracted the attention of the research community. Inspired by the biological organisms, self-healing materials can heal (partially or fully) defects induced during service life by utilizing one or more of the existed methods. The extrinsic approaches are the capsule-based self-healing materials and the vascular. The intrinsic approach is based on the reversible dynamic bonds inside the polymer.

The current thesis is based on the manufacturing of smart, multi-functional polymer composite materials with self-healing properties. More analytically, the optimization of the self-healing materials was accomplished via the nanomodification of capsule-based composites that can restore both the mechanical and electrical properties simultaneously. This achievement can lead to a composite that has both self-healing and self-sensing properties- as well as integrating the structural health monitoring functionality. It should be noted that the object of this thesis is only the study of the optimization of self-healing properties. In the intrinsic approach, intrinsically self-healing polymeric films were manufactured for easy application in composites. The reversible cross-links were introduced using three bis-maleimide oligomers with different molecular masses.

# Περίληψη

Τα ινώδη σύνθετα υλικά πολυμερικής μήτρας αποτελούν μια από τις σημαντικότερες κατηγορίες υλικών καθότι παρουσιάζουν μια πληθώρα ιδιοτήτων οι οποίες διεγείρουν το ενδιαφέρον της επιστημονικής κοινότητας αλλά και της βιομηχανίας. Η χαμηλή τους δυσθραυστότητα οδηγεί σε σημαντικούς και «επικίνδυνους» για την δομική ακεραιότητα του συνθέτου, τύπους αστοχίας κατά την διάρκεια λειτουργίας του ενώ η επισκευή των ατελειών/βλαβών στο εσωτερικό του συνθέτου, χαρακτηρίζεται από υψηλή δυσκολία καθώς και αυξημένο κόστος. Πέραν των συμβατικών προσεγγίσεων επισκευής, η τεχνολογία της αυτο-ίασης (AI) έχει προκαλέσει μεγάλο ενδιαφέρον στην επιστημονική κοινότητα.

Εμπνευσμένα από τους βιολογικούς οργανισμούς, τα αυτο-ιάσιμα υλικά επιτρέπουν την σχεδόν αυτόνομη διάγνωση και επούλωση των ατελειών που δύναται να σχηματιστούν στο εσωτερικό των υλικών χρησιμοποιώντας μία ή και περισσότερες από τις μεθόδους αυτο-ίασης. Η πρώτη βασίζεται στην ενσωμάτωση καψουλών στο υλικό, η δεύτερη στην ενσωμάτωση αγγείων ή δικτύων και η τρίτη σε εγγενώς αυτο-ιάσιμα πολυμερή.

Σκοπός της παρούσας διατριβής είναι η παρασκευή προηγμένων έξυπνων πολυ-λειτουργικών σύνθετων υλικών πολυμερικής μήτρας με ικανότητα αυτο-ίασης της βλάβης. Συγκεκριμένα, πραγματοποιήθηκε η βελτιστοποίηση μέσω νανο-τροποποίησης της μεθόδου αυτο-ίασης με κάψουλες για την εισαγωγή τους σε σύνθετα υλικά όπου θα μπορούν να ανακτούν τις μηχανικές αλλά και τις ηλεκτρικές τους ιδιότητες ταυτόχρονα. Ο συνδυασμός της ανάκτησης των παραπάνω ιδιοτήτων μπορεί να οδηγήσει σε ένα σύνθετο το οποίο θα έχει την δυνατότητα αυτο-διάγνωσης της βλάβης και κατ' επέκταση παρακολούθησης της δομικής του ακεραιότητας μέσω ηλεκτρικών μεθόδων. Στην διατριβή αυτή περιλαμβάνεται μόνο η μελέτη της αυτο-ίασης των μηχανικών και ηλεκτρικών ιδιοτήτων ταυτόχρονα και όχι της αυτο-διάγνωσης της βλάβης. Για την μέθοδο της εγγενούς αυτο-ίασης πραγματοποιήθηκε η κατασκευή πολυμερικών φιλμ ώστε να δίνεται η δυνατότητα στον κατασκευαστή να εισάγει την τεχνολογία με εύκολο τρόπο στο σύνθετο.

# Acknowledgments

During the development of this Ph.D. research, I had the opportunity to collaborate with several remarkable people who significantly contributed to the realisation of this effort, and I would like to dedicate the following paragraphs as an acknowledgment to them.

First and foremost, I would like to express my special appreciation and thanks to my advisor, Alkiviadis Paipetis, Professor at the Dept. of Materials Science and Engineering (MSE), who kept me focused throughout my graduate career and was patient through all of my mistakes I made as a graduate student. I appreciate the scientific discussions as well as the opportunities he has opened up for me. His advice on both research as well as on my career has been priceless, and without his support, it would not be possible to conduct this research.

I want to express my gratitude to Apostolos Avgeropoulos, Professor at the Dept. of MSE, for his participation as a member of the advisory committee. I also wish to thank Evagelia Kontou, Professor at the Dept. of Theoretical and Applied Mechanics, of the National Technical University of Athens, for her participation on my advisory committee.

At this point, I want to express my sincere gratitude to Nektaria-Marianthi Barkoula, Professor at the Dept. of MSE, for her scientific advice and our many insightful discussions. Her contribution to my research career was more than precious.

Furthermore, I would like to thank for honoring me with his participation in my committee, Leonidas Gergidis Assistant Professor of the Dept. of MSE who has witnessed my progress throughout my academic years. Also, I would like to sincerely thank, Dimitrios Gournis Professor at the Dept. of MSE, for honoring me with his presence as a member of my committee. I also want to thank, Stamatina Vouyiouka Assistant Professor of the School of Chemical Engineering at the National Technical University of Athens for her participation in my committee.

I would like to express my sincere gratitude to my instigator, Dr. Dimitrios Bekas, for his precious friendship, guidance, and collaboration. Our stimulating discussions cautiously encouraged me to explore new things, and his advice was more than precious. I gratefully thank Dr. Kyriaki Tsirka for her collaboration, friendship, and precious assistance, especially regarding the Raman Spectroscopy and Scanning Electron Microscopy.

At this stage, I want to express my special thanks to my friend and “partner-in-crime” PhD candidate, Georgios Foteinidis, for his assistance from my first steps to the final stage of this thesis. His collaboration, guidance, patience, and care were more than precious, and without his support, it would not be possible to conduct this research.

Also, I would like to give my love and special thanks for their patience to my wonderful friends and Ph.D. candidates, Katerina Gkaravela and Ioanna Vareli. These girls offer me great collaboration, help, and support inside and outside the lab but most importantly, their friendship.

My sincere thanks to my colleagues at the CSML, Ph.D. candidates, Anastasia Polymerou, Christos Mytafides, Labros Koutsotolis, Eva Tzouma, Aggelos Ntaflos, Aggelos Voudouris-Itskaras, and Michaela Konstantinidou. I would also like to thank other old and new members of the CSML, first as friends and then as partners, MSc. Marilena Georgosopoulou, Dr. Mariliza Kouli, Dr. Dimitrios Baltzis and Dr. Georgios Karalis for our collaboration. I also want to thank Dr. Andreas Karydis of the Polymers Lab of the Dept. of MSE for his assistance on DSC experiments. A big thank you to Dr. Christina Gioti of the Dept. of MSE for her assistance with BMIs grinding process.

Moreover, I want to thank all the students who worked and collaborated with me during this research: Marios Bantis, Stella Chalari, Antigoni Palantza, Alexandros Karpenisiotis, Myrto Doumpou, Pantelis Nikiforidis, Vasilina Piha, Theoni Aggelopoulou, Maria Vasdeki, and Konstantinos Anagnostou.

In addition, I would like to express my gratitude to my friends Anastasia Koutsianou, Dionisios Peticaris, Athanasia Charizani, Vasileios Melios, Evgenia Tahou, Katerina Kontouli, and Katerina Vlachou for their support.

Last but not least, I want to sincerely thank some special people like my father Anastasios, my mother Androniki, and my brother Ilias for encouraging me during this journey and giving me strength, especially during my difficulties. I would not be here without their support.

The current Ph.D. thesis has been co-financed by Greece and the European Union (European Social Fund- ESF) through the Operational Programme «Human Resources Development, Education and Lifelong Learning 2014-2020» in the context of the project “Smart, multifunctional, advanced composites with EMI Shielding and Self-Healing capabilities for the recovery of mechanical and electromagnetical properties- SHIELD” (MIS: 5047645).”

And partially has received funding from the European Union's Horizon 2020 research and innovation program under grant agreement No 769274, “AIRPOXY”.

# Contents

## List of figures

# CHAPTER 1

# Introduction

## 1.1 Introduction to advanced, multifunctional polymer composites for aeronautics

The first aircraft that contained composite materials was demonstrated in 1916 during World War I. However, polymer composites have been used widely in aeronautics since 1980, while approximately 780 tons of carbon and aramid fibers were used in aerospace. A composite component was 25% lighter and 40% cheaper than the original metal structure [1]. The Airbus A350 currently consists of 53% of composite material (**Figure 1**). Their high stiffness and strength and low cost and weight have emerged as a significant and high class of structural materials for lightweight applications. Other important benefits are their fatigue behavior and corrosion resistance. Some limitations of composites are based on their low electrical conductivity and sudden failure [2].

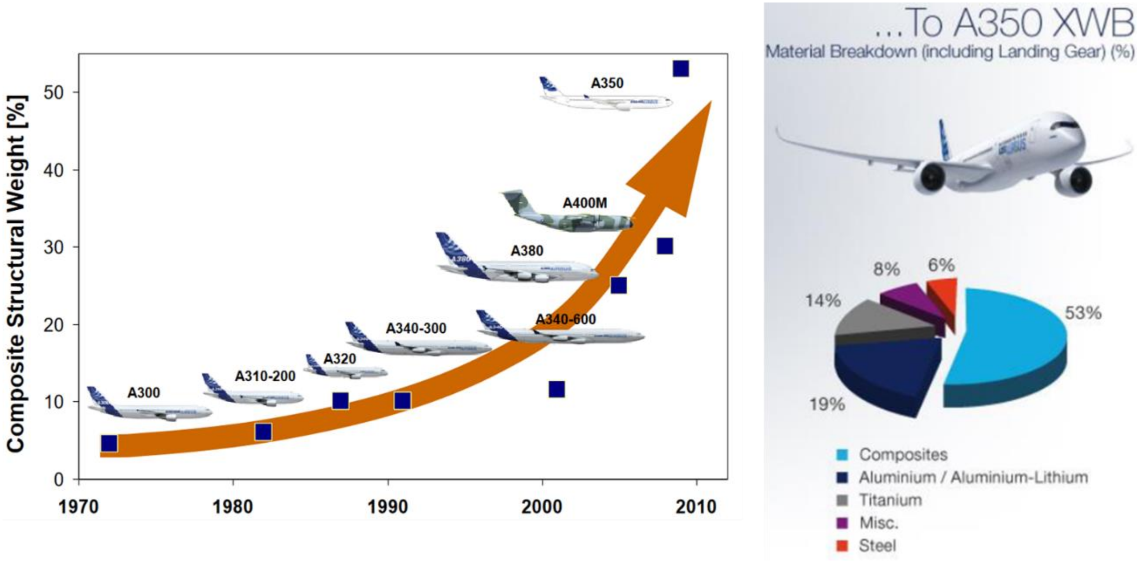

**Figure 1**. Composite materials used in Airbus aircrafts. *(Original source: AIRBUS INDUSTRY)*

With the increasing use of traditional composites in critical structures with extended service life, it was necessary to develop new and advanced, multifunctional composite systems with an inherent capacity to detect-sense any mechanical damage or chemical degradation as well as the ability to heal. By incorporating conductive fibers, such as metal wires and carbon fibers, many researchers started to develop sensing and monitoring capabilities using these fibers as interconnections [3]. Self-sensing composites may be very useful for aerospace composite parts in order to perform continuous monitoring of any strain and damage. These composites can improve the safety of such structures and reduce maintenance and repair costs by detecting the damage at an early stage [4].

## 1.2 Damage tolerance & conventional repair

The initial state of a system is typically considered as the initial condition of the material before any changes are made due to its use. Changes that affect any function and/or performance can be described as damage. Composites are susceptible to damage due to many parameters that have a severe impact on the composite load redistribution and load-carrying capability. Their complex damage mechanisms, such as delamination, matrix cracking, and fiber breakage, can interact with each other, making the prediction of the failure difficult or even impossible [5].

Damage tolerance is the ability to predict the strength or load-carrying capability of a material when it has been damaged by service loading or environment (high or low temperature, humidity, etc.) [6]. This capability can be achieved at the design stage of the material. The designer should have considered that the structure might suffer from any damage during the service life without total failure until the detection of the damage. The inspection of the structure is usually performed by Non-Destructive Evaluation (NDE) testing using techniques such as IR-Thermography or ultrasonics [7,8]. According to the results, the component must be replaced or repaired. A repair is necessary when the intended stresses can no longer be met and/or an operating permit expires.

It is a major challenge to repair a damaged composite part to its original mechanical property. Several conventional or traditional repair methods include patch repair, welding process, in-situ curing of the resin, speed tape, potted repair, room-temperature or elevated-temperature wet lay-up, and pre-preg repair. Each repair technique has its limitations and is appropriate for specific damage characteristics such as the size of the damage, the kind of the damage (interlaminar, intralaminar, etc.), the available materials, etc. The types of damage generally in composite structures and the repair methods are more complicated than in metals [9,10].

However, the repair processes are time-consuming and costly, complicated and need specialized operators. The properties of the original part will usually not be identical to those of the repaired one. Human errors and inconsistencies in repair processes can significantly influence the structural strength and durability of composite repairs [11]. All these limitations led the scientific community to develop a new and beyond the state of the art class of traditional repairing materials known as self-healing materials.

## 1.3 Self-healing polymers & composites

Besides the economic benefits of having longer-lasting materials, the limitation of the natural resources also leads to the production of self-repairing polymers. Self-healing materials are state-of-the-art technologies capable of healing and restoring internal damage or functionalities in a material [12]. Inspired by nature, these materials can repair themselves without any external intervention. The first self-healing material was manufactured in 1993, and it was a white cement-based specimen that contained liquid methyl methacrylate (healing agent) into hollow porous polypropylene fibers. In case of damage, the crack propagates breaking the hollow fibers, causing the release of the healing agent and its delivery into the pores of the damage. The wax coating of the fibers melts with the application of low heating, and the agent polymerizes in order to heal the damage [12].

Due to their excellent properties, polymers are often considered a substitute for metals. However, they are not as durable as metals; they have a low heat durability and lower stiffness, leading to limited mechanical use [13]. Self-healing properties are the key to the continuous development of polymers and their derivatives. The concept of self-healing polymers and composites can be classified as intrinsic or extrinsic (**Figure 2**) according to the mechanism the healing agent is sequestered into the material [14].

The intrinsic self-healing principle is based on the idea that polymers can restore their initial properties through chemical or physical processes such as ionomeric bonding, thermally reversible reactions, or molecular diffusion [15]. They exploit latent functionalities triggered by induced damage or an external incentive. There is no healing agent isolated in this case, but the matrix is inherently self-healing. With this approach, problems with compatibility, integration, or reactivity of the agent with the matrix can be avoided. Since this method is based on reversible reactions, the healing cycles could be multiple [16].

Extrinsic self-healing is a process that involves the delivery of healing components to a targeted site in a material. This method is straightforward to apply in commercially available polymers since there is no need to modify the polymer. The first extrinsic approach is based on the incorporation of vascular or hollow fibers inside the material mimicking the biological systems such as the human blood network at one (1-D), two (2-D), or three (3-D) dimensions [17]. The healing agent resides on the network or the hollow fibers or is introduced from an external reservoir. The second extrinsic method focuses on encapsulating the healing agent into discrete capsules at micro or nano dimensions and their integration into the material. The healing process starts with the rupture of the polymeric capsule shell-wall or the vascule, followed by delivery of the agent into the crack and polymerization [18–20]. In the case of the capsule-based method, there is only one local healing cycle since, after damage, the healing agent is consumed (locally). However, in vascular self-healing materials, the network can be refilled by an interconnected channel or externally; thus, the healing cycles can be more than one.

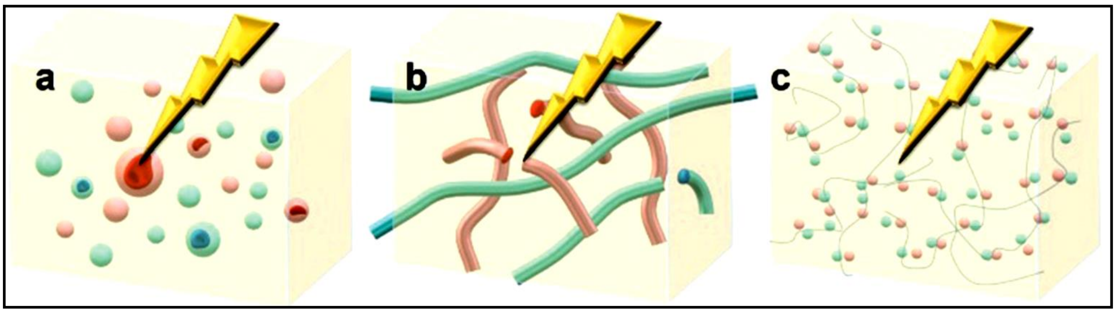

**Figure 2.** Schematic representation of the three self-healing approaches, a) capsule-based, b) vascular, and c) intrinsic approach.

## 1.4 Structural Health Monitoring (SHM) & self-sensing

Structural health monitoring (SHM) is another functionality of composite materials that can provide useful information about the structural integrity of the material. The techniques used for SHM are based on non-destructive inspection or evaluation (NDE). With this functionality, the periodic inspections of a component can be replaced. It could also reduce the contribution of humans to the inspection process and decrease the possibility of human errors. The user or the inspector can be informed immediately in case of any damage (on-line structural health monitoring) from the sensors incorporated inside the material or attached externally. The off-line SHM can offer data for the health of the material periodically, i.e., when the user activates the inspection system [21].

Usually, the sensors have to be cost-effective, lightweight, and must not affect the initial structural strength of the material. Some of them are the conventional resistance strain gauges, fiber optic sensors, piezoelectric wafer active sensors, and electrical properties sensors. Each type of sensor exploits different physical principles of the material in order to monitor its health [22]. Bekas et al. [23] developed a planar interdigital capacitive sensor that was attached (by printing) to the surface of a composite joint in order to monitor the curing process of the adhesive and the progress of developed damage (**Figure 3**). The composite's structural integrity assessment was performed by monitoring its dielectric profile via impedance spectroscopy measurements. The curing process was successfully monitored, while the sensor was also able to locate the presence of manufacturing defects. SHM results indicated that the sensor was susceptible to damage progress which was also confirmed by infrared thermography. It should be noted that the sensor did not affect the quality of the bonded area, and its weight was negligible.

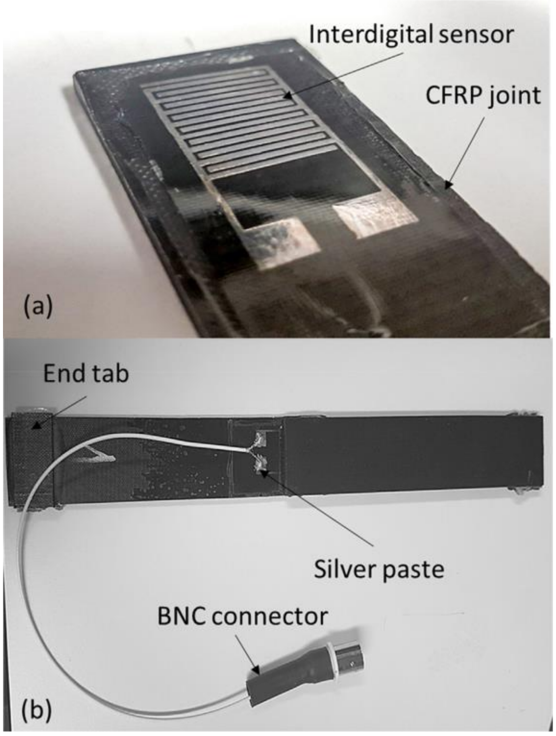

**Figure 3.** (a) The printed interdigital sensor and (b) the sensor attached to the composite joint. ("Used with permission of Composite Structures, from Quality assessment and damage detection in nanomodified adhesively-bonded composite joints using inkjet-printed *interdigital sensors, D.G. Bekas, Z. Sharif-Khodaei, D. Baltzis, M.H. Ferri Aliabadi, and A.S. Paipets, 211:557-563, permission conveyed through Copyright Clearance Center, Inc.")*

However, the use of external sensors either on top or inside the composite can degrade the structural performance since the sensors may act as damage initiation sites or internal defects. In this case, many researchers have been focused on the development of self-sensing smart materials. The sensing capability is based on the inherent ability of a composite structure to sense its damage or strain using its functions and without the need for external or embedded sensors [24]. Typically, this can be achieved through electrical methods such as electrical resistance or impedance [25]. As the polymer matrix is an insulator, carbon fibers, as referred above, are an excellent candidate for the sensing capability [26]. In the case of the glass fiber composites, conductive nanofillers are usually dispersed into the matrix, such as carbon nanofibers, carbon nanotubes, graphene, and carbon black. Foteinidis and Paipetis developed a smart, self-sensing, novel composite material with 2D and 3D damage mapping topography via impedance measurements without using external sensors [27]. The sensing elements were formed at the through-thickness junction points of the embedded carbon fiber strips into the material (**Figure 4**). The nanomodified glass fiber composite was tested under a ballistic impact. In impacted areas of the composite, the magnitude of the impedance increased due to entrapped air induced by damage. By combining these two functions/techniques, it is possible to develop a smart structure that can both sense and repair damage and degradation.

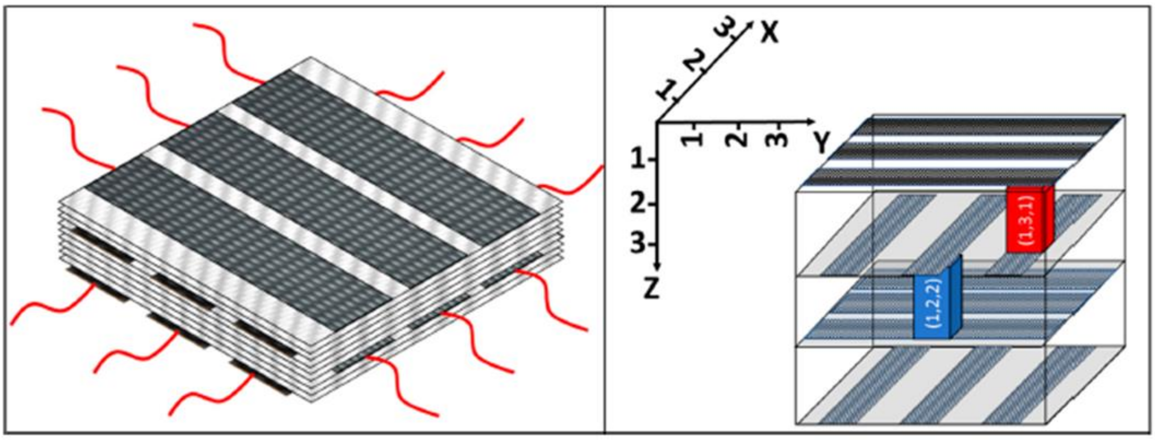

**Figure 4.** The layout of the smart composite material with the 3D mapping topography function and the formatted sensing elements. (*Original source: G. Foteinidis and A. S. Paipetis, A Novel Composite with Structural Health Monitoring Functionality via 2D and 3D Impedance Mapping Topography, Applied Sciences, 11, 1647, 2021)*

## 1.5 Motivation

The motivation for this research was the continuing progress of composite materials into advanced, multifunctional structures. Apart from the conventional repair methods or damage tolerant design concepts, self-healing composites have already attracted great interest in the scientific community. With self-healing functionality, composites can heal their damage and restore fully or not their initial performance. Until now, studies have focused on developing self-healing methods and the triggering mechanisms. Part of them was also the evaluation of the mechanical healing efficiency using the three self-healing approaches. This research can move further towards advanced composite systems and their functionalities. The main scope was the recovery/healing of more than one of the properties of a composite.

The electrical properties of a polymer composite can act as a very sensitive indicator for evaluating its structural integrity. Changes in their electrical resistance can be related to the evolution of internal damage into the composite [25,27]. The strain or damage sensing functionality is based on this phenomenon. The main target of this research is the manufacturing of a multi-functional composite that can sense in situ and heal the damage simultaneously. A percolated system can act as a nerve network or a sensor and, in case of damage, can inform the user. Therefore, the recovery of electrical properties can be an important factor for the confirmation of the restoration of the mechanical properties, too.

## 1.6 Thesis outline

The aim of this thesis is the development of novel multi-functional self-healing composites. The research includes the development, characterization and incorporation of the self-healing processes to the composite materials. The self-healing assessment was evaluated using several testing protocols and configurations.

In terms of capsule-based systems, the main purpose was the concurrent restoration of both mechanical and electrical properties of the composite. By this achievement, the self-healing composites can lead also to a self-sensing system based on electrical methods. This was accomplished by the nano-modification, with carbon filles, of the healing agent or/and the shell-wall of capsules.

In detail, chapter two includes the investigation of the dispersion parameters of the fillers in the Diglycidyl Ether of bisphenol-A (DGEBA) epoxy resin. The DGEBA resin was used as the matrix phase and/or as the healing agent. The studied dispersion factors were the hours of the process and the filler type (carbon nanotubes or/and carbon black), and weight. The study included the investigation of the electrical and mechanical properties of the modified matrix.

In chapter three, microcapsules containing nanomodified healing agent were developed. This part included two case studies; the first focuses on the evaluation of mechanical healing efficiency by changing different parameters, such as capsule, catalyst, or solvent percentage and healing process parameters. The second case study included the capsule characterization in terms of their morphology and thermal stability using various techniques. The capsules were then incorporated into the nanomodified polymer matrix, and the healing efficiency was evaluated in terms of both mechanical and electrical properties.

The fourth chapter consists of the synthesis of microcapsules with nanomodified shell wall. Three different percentages were chosen for the modification of the capsules shell wall, and their thermal stability properties were studied. The effect of the addition of capsules in a semi-conductive polymer matrix on the electrical properties was also investigated. In this case, only the mechanical healing efficiency was evaluated since the shell wall was destroyed after the breakage of microcapsules.

Chapter five includes the investigation of the effect of the addition of different types and sizes of capsules into a modified polymer matrix on the percolation threshold as well as the electrical properties of the matrix. Four different sets of microcapsules were produced and incorporated into two nanomodified matrices, the first one was conductive and the second was semi-conductive. The sets of the capsules were: i) neat capsules, ii) capsules with a nanomodified healing agent, iii) capsules with nanomodified shell wall, and iv) capsules with nanomodified both core and shell wall.

The final, sixth, chapter of capsule-based self-healing materials reports the manufacturing and characterization of the multi-functional, self-healing composites that can restore both the mechanical and electrical properties. Capsules were introduced into composites and were mechanically tested at mode-II fracture toughness and low velocity impact tests. The low velocity impact tests included also the investigation of the addition and the healing performance of a capsule-based system into self-sensing composties. Furthermore, capsules were introduced and used as adhesive at lap strap specimens. This geometry can simulate the mechanical behaviour of a stiffened panel (model structure level).

Chapter seven is concerned with synthesizing and characterizing three intrinsically self-healing polymers. The reversible cross-links that were introduced were realized using three bis-maleimide oligomers with different molecular masses. The BMI-modified polymers were shaped into films and used as interleaves into composites. The healing performance of the three systems was assessed via the mode-II testing configuration after three healing cycles. The changes in the molecular structure of the BMI polymers after the manufacturing and the three healing cycles were investigated via Raman spectroscopy.

Chapter eight refers to the conclusions and the publications that resulted from this work and suggestions for future work. Chapter nine includes the references used in this research.

# CHAPTER 2

# Dispersion protocol of the DGEBA resin

## 2.1 Introduction

Polymer matrices, especially thermosetting epoxy resins, are currently being used in many applications. Precisely, at protective coatings to matrices for composite materials that are used for marine applications [6], wind turbine blades [28] or aeronautics, including highly complex structural parts of airplanes [29]. They have valuable properties such as high adhesion strength, good processability, high modulus, failure strength, and high chemical and creep resistance [30]. However, the high cross-link density decreases the fracture toughness of the epoxies due to internal stresses that are induced during the curing process of the resins [31]. Moreover, their inherent insulating nature and low thermal conductivity are still limitations [32]. The electrical insulation can have a detrimental effect on lightning strikes, as in the case of the wind turbine structures or the wings of an aircraft (**Figure 5**), where the electrical flow dissipation is limited or impossible [33].

**Figure 5**. Damage occurred from a lightning strike at aircraft.

These weaknesses can now be easily overwhelmed by modifying the epoxy resins with the integration of various conductive nanofillers for advanced composite applications [34]. The development of nanocomposites has attracted significant interest from the scientific committees since improved mechanical and electrical properties of such materials can be achieved by using highly potential carbon fillers. The addition of carbon nanofillers into the epoxy resins has been proven that can sufficiently increase the fracture toughness of thermosetting polymers [35]. In addition, the increment of the thermal conductivity can be useful in extreme weather exposure for the de-icing of exposed surfaces [36]. Furthermore, high electrical conductivities can lead to multi-functionality, usually using electrical-based non-destructive evaluation methods via strain sensing and damage monitoring [37].

Optimum performance of the nanocomposite can be achieved by the proper dispersion of the nanofillers in the epoxy. The most common nanomaterials used are the Single, Double, or Multi-Walled Carbon Nano Tubes (SWCNTs, DWCNTs, MWCNTs, respectively) due to their excellent properties, such as their high aspect ratio [38]. Graphene [39], carbon nanofibers, or milled carbon black (CB) [40] are some of the nano-scaled fillers (**Figure 6**).

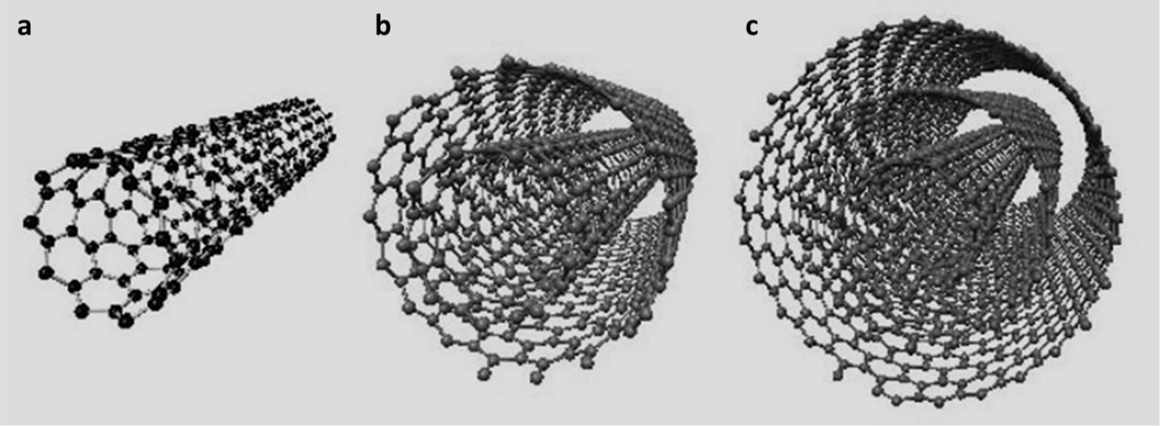

**Figure 6.** Single (a), Double (b), and Multi-Walled (c) Carbon Nano Tubes.

Carbon nanotubes are large cylindrical molecules that consist of the hexagonal arrangement of hybridized carbon atoms. They may be formed by rolling up sheet(s) of graphene and were first reported by Sumio Ijima [41]. CNTs are classified by the number of graphene layers in their sidewalls as single, double, and multi-walled, as referred above. Their high mechanical properties are based on the $sp^2$ carbon-carbon bonds than are more substantial than the $sp^3$ bonds in diamonds [42]. Their Young’s modulus is about 1.2 TPa, and their tensile strength reaches 50 to 200 GPa [43]. The supply of CNTs into entangled bundles with their poor interfacial interaction between the polymer matrix results in difficulties in their dispersion. Jamal-Omidi and ShayanMehr proposed a multi-stage dispersion method by functionalizing SWCNTs and their mechanical dispersion, followed by an ultra-sonication process [44]. Bending tests revealed an improvement in the mechanical properties of the nanocomposites by 10%. CNTs do not only improve the mechanical properties of a polymer matrix but their electrical properties, too. SWCNTs and graphene dispersion into a polymer result in more conductive composites even at shallow weight contents, while in the case of MWCNTs and CB is required a higher weight percentage has identical electrical conductivity values. Jakubinek et al. demonstrated the development of a structural and conductive adhesive incorporating SWCNTs at low loadings [45]. At 1 wt% SWCNT into the adhesive, conductivity was as high as $10^{-1}$ S/m, and a 30% increase of peel strength at lap shear tests was achieved. However, SWCNTs are cost-effective, which is an important disadvantage, especially in industrial processes. To overdraw this problem, the inclusion of more than one filler is now proposed. A multi-scaled carbon reinforcement into a polymer matrix was presented by Baltzis et al. exploiting the synergistic effects between CNTs and CB [46]. The effect of different dispersion duration on the mechanical and electrical properties was investigated. The systems that contained the two fillers exhibited improved fracture toughness even after only one hour of dispersion since the formation of a hybrid 3D micro/nano-scaled hybrid network was very effective at hindering crack propagation (**Figure 7**).

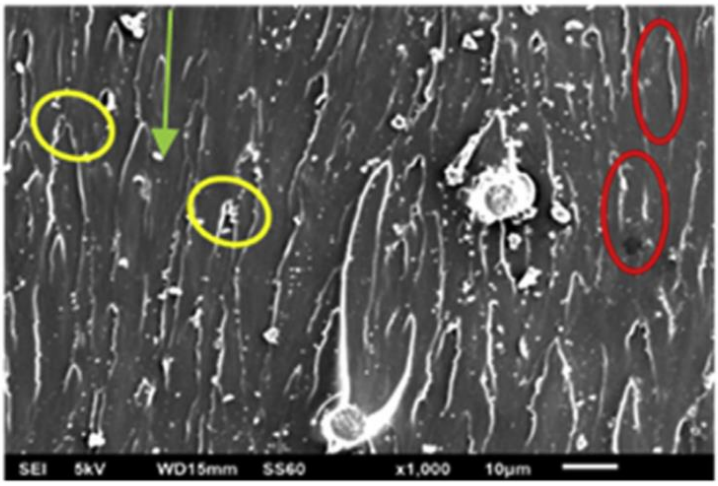

**Figure 7.** SEM image of the CNTs/CB system that proved the crack deviations.

The network created due to the dispersion of the fillers had also improved the electrical properties of the matrix. A rapid formation of a conductive path consisting of the CNTs/CB fillers led to an enhanced conductive system after one hour of dispersion.

The dispersion conditions of the fillers are directly correlated to the final properties of the matrix. The dispersion duration, intensity, and method are some important factors [47]. Due to their electrostatic interaction and the van den Waals force, the dispersion of the nanotubes is complicated. The dispersion method may separate the CNTs from the agglomerates without reducing their properties or degrading the matrix phase. Some of the most common dispersion techniques are ball milling, calendaring, high shear force mixing, extrusion, or ultra-sonication [49], and their advantages and disadvantages are depicted in **Figure 8**. The ball milling procedure was used by Krause et al. for the dispersion of CNTs into polycarbonate [48]. After the process, the size of the agglomerates was reduced from 675 μm to 50 μm. However, the length of the nanotubes was also decreased by 54% and 35% after a 5-hour and 10-hour process, respectively. Montazeri and Chitsazzadeh [49] used the ultra-sonication process in order to disperse MWCNTs into an epoxy resin. The influence of the power output and the time process on the tensile strength were investigated. Results indicated that the most valuable tensile properties were achieved at intermediate levels of power and duration. As at the ball milling process, higher power and dispersion duration resulted in a sufficient dispersion, but a reduction of the CNTs' length was observed.

Before the main experimental campaign, a preliminary study on the dispersion of different percentages of fillers (CNTs & CB) at different dispersion hours in the Epikote 828 DGEBA epoxy resin was performed. The study included the investigation of electrical and mechanical properties. The dispersion process was selected to be the high shear force mixing.

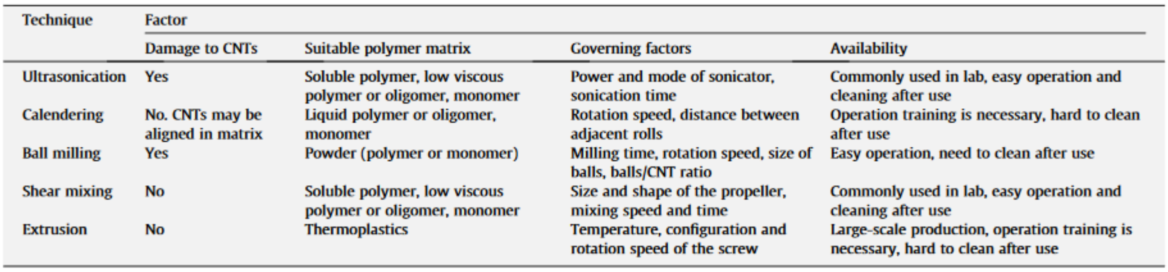

| Technique | Factor | | | |
|---|---|---|---|---|
| | Damage to CNTs | Suitable polymer matrix | Governing factors | Availability |
| Ultrasonication | Yes | Soluble polymer, low viscous polymer or oligomer, monomer | Power and mode of sonicator, sonication time | Commonly used in lab, easy operation and cleaning after use |
| Calendering | No. CNTs may be aligned in matrix | Liquid polymer or oligomer, monomer | Rotation speed, distance between adjacent rolls | Operation training is necessary, hard to clean after use |
| Ball milling | Yes | Powder (polymer or monomer) | Milling time, rotation speed, size of balls, balls/CNT ratio | Easy operation, need to clean after use |
| Shear mixing | No | Soluble polymer, low viscous polymer or oligomer, monomer | Size and shape of the propeller, mixing speed and time | Commonly used in lab, easy operation and cleaning after use |
| Extrusion | No | Thermoplastics | Temperature, configuration and rotation speed of the screw | Large-scale production, operation training is necessary, hard to clean after use |

**Figure 8.** Advantages and disadvantages of each dispersion method. ("Used with permission of Composites Part A: Applied Science and Manufacturing, from Dispersion and functionalization of carbon nanotubes for polymer-based nanocomposites: A review, P. Ma, N. Siddiqui, G. Marom and J. Kim, 41:1345-1367, (2010), permission conveyed through Copyright Clearance Center, Inc.")

## 2.2 Experimental

### 2.2.1 Materials

Graphistrength C-100 MWCNTs from ARKEMA, France, were used for the dispersions. The length and diameter of the CNTs ranged from 1 to 10 μm and 10 to 15 nm, respectively. The second material used as reinforcement was the milled carbon black (CB) supplied by R & G composites GmbH with an agglomeration size from 5 to 50 μm in diameter. As the matrix phase, the two-part Diglycidyl Ether of bisphenol-A epoxy system (DGEBA, Epikote 828 epoxy resin, and Epikure 541 hardener) was selected, purchased by Dichem Polymers, Greece.

### 2.2.2 Dispersion process

The dispersions were performed using a Dispermat high shear dissolver by VMA-GETZMANN, Germany. The container was double-walled and coupled with a thermostatic bath by GRANT to keep stable temperature control during the dispersion within ±1°C. For the application of medium shear forces capable of reducing the agglomerate size, a 45mm diameter toothed impeller disk was chosen. Each dispersion was performed at 25°C, with an agitation rate of 3000 rounds per minute (rpm).

### 2.2.3 Filler type and weight/ Dispersion protocols

Different filler weight contents and dispersion duration were selected in order to investigate the mechanical and electrical properties of the modified matrix. The first type of system manufactured was the binary system that consisted of two ingredients, the resin, and the CNTs or CB. The second type was the ternary systems containing epoxy, CNTs, and CB (three components). In the case of the ternary systems, they were investigated to evaluate the synergistic effects that CNTs and CB could provide after their dispersion. The selected parametersre summarized in **Table 1** and were chosen from previous research [50].

**Table 1.** Dispersion percentages and parameters that were used.

| Name | Dispersion duration (hours) | CNT’s (% wt.) | CB (% wt.) |
|---|---|---|---|
| 0.1 CNT's-I | 1 | 0.1 | |
| 0.1 CNT’s-II | 2 | 0.1 | |
| 0.1 CNT’s-III | 3 | 0.1 | |
| 0.1 CNT’s-IV | 4 | 0.1 | |
| 0.3 CNT's-I | 1 | 0.3 | |
| 0.3 CNT’s-II | 2 | 0.3 | |
| 0.3 CNT’s-III | 3 | 0.3 | |
| 0.3 CNT’s-IV | 4 | 0.3 | |
| 0.5 CNT’s-I | 1 | 0.5 | |
| 0.5 CNT’s-II | 2 | 0.5 | |
| 0.5 CNT’s-III | 3 | 0.5 | |
| 0.5 CNT’s-IV | 4 | 0.5 | |
| 0.5 CB-I | 1 | | 0.5 |
| 0.5 CB-II | 2 | | 0.5 |
| 0.5 CB-III | 3 | | 0.5 |
| 0.5 CB-IV | 4 | | 0.5 |
| 1 CB-I | 1 | | 1 |
| 1 CB-II | 2 | | 1 |
| 1 CB-III | 3 | | 1 |
| 1 CB-IV | 4 | | 1 |
| 2 CB-I | 1 | | 2 |
| 2 CB-II | 2 | | 2 |
| 2 CB-III | 3 | | 2 |
| 2 CB-IV | 4 | | 2 |
| 0.5 CNT’s & 1 CB-I | 1 | 0.5 | 1 |
| 0.5 CNT’s & 1 CB-II | 2 | 0.5 | 1 |
| 0.5 CNT’s & 1 CB-III | 3 | 0.5 | 1 |
| 0.5 CNT’s & 1 CB-IV | 4 | 0.5 | 1 |
| 0.5 CNT’s & 2 CB-I | 1 | 0.5 | 2 |
| 0.5 CNT’s & 2 CB-II | 2 | 0.5 | 2 |
| 0.5 CNT’s & 2 CB-III | 3 | 0.5 | 2 |
| 0.5 CNT’s & 2 CB-IV | 4 | 0.5 | 2 |

### 2.2.4 Manufacturing of SENB specimens

Mechanical properties were investigated via the single-edge notched beam (SENB) geometry. Specimens were manufactured with dimensions 52×12×4mm after each dispersion process. The epoxy resin, Epikote 828, was mixed with a ratio of 100:50 with the Epikure 541 hardener. The mixture was placed in a laboratory vacuum oven, left for degassing three times for 1 minute, and cast into silicon rubber molds. The curing process was performed at room temperature for 24 hours. Specimens were ground in order to have the desired dimensions and eliminate any surface defects. Six specimens were produced for the mechanical characterization, while three were evaluated for their electrical conductivity before testing. After conductivity measurements, the specimens were pre-cracked using a metal saw and a fresh razor blade.

## 2.3 Characterization techniques

### 2.3.1 Evaluation of the conductivity properties

The Impedance technique was used to evaluate the conductivity values of the produced nanocomposites. Measurements were performed using the Advanced Dielectric Thermal Analysis System (DETA-SCOPE) supplied by ADVICE, Greece. Specimens were placed between two parallel copper plates. **Figure 9** illustrates the experimental setup for the conductivity measurements. Scans were performed at the frequency value of 0.01 Hz. All measurements were performed under a stable temperature of 25°C.

**Figure 9.** Experimental configuration of IS measurements of SENB specimens.

### 2.3.2 Fracture toughness tests

The fracture toughness was assessed through three-point bending on single edge notched beam (SENB) specimens according to ASTM D5045 [51]. Mechanical testing took place at a mini tensile testing frame manufactured by Fullam Inc. USA, with a displacement rate of 1 mm/min (**Figure 10**). The critical stress intensity factor, $K_{ic}$, and the energy per unit area of the crack surface or critical strain energy release rate, $G_{ic}$, were calculated according to Equations (1) and (2).

$$K_{IC} = \frac{P_{max}}{B \times W^{\frac{1}{2}}} f(x) \tag{1}$$

$$G_{IC} = \frac{U}{B \times W_{\varphi}} \tag{2}$$

Where $P_{max}$ is the maximum load, B is the specimen thickness, W is the specimen width, U is the corrected energy under the load vs. displacement curve, and f(x) and φ are calibration factors dependent on the a/W ratio, where a is the measured crack length.

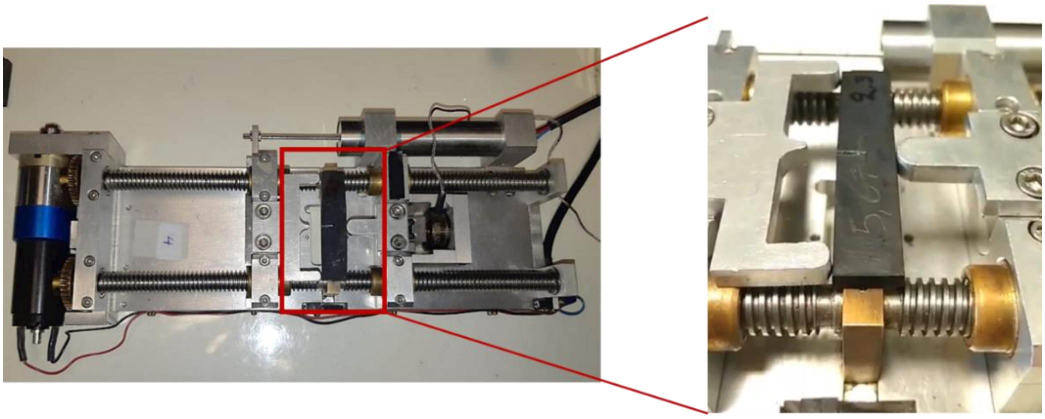

**Figure 10.** Experimental configuration of mechanical testing of SENB specimens.

## 2.4 Results

### 2.4.1 Fracture toughness

**Figure 11** depicts the $K_{ic}$ and $G_{ic}$ values of specimens containing CNTs. As can be observed, the fracture toughness ($K_{ic}$) was generally increased for all the percentages. Specifically, systems with 0.1 wt. % CNTs increased their fracture toughness by approximately 40% at the third hour of dispersion compared with the reference system. However, after four hours of dispersion, the values decreased by 15%. This can be attributed to a threshold at the dispersion duration that may be achieved, and no improvement of the fracture toughness can be seen. After four hours of dispersion, all the CNT modified specimens led to a decrease in the Gic values compared to the neat specimens. Similarly, specimens containing 0.3 wt.% of CNTs increased their toughness properties by 53% after three hours of dispersion compared to the reference system. The agglomerates, in this case, were reduced to such an extent that their size could not stop the crack propagation. However, at the 0.5 wt.% of CNTs specimens, the first hour of dispersion was enough to improve Kic by 34% while further hours of dispersion led to lower values. In terms of Gic, all systems had similar behavior as the Kic values except of the 0.1 CNTs-I specimens that exhibited an increase of 142% after one hour of dispersion. This increment can be attributed to the large size of the CNT agglomerates that increased the energy required until the fracture of the specimens.

| **Name** | **$K_{IC}$ (MPa*m$^{1/2}$)** | **$G_{IC}$ (kJ/m$^2$)** |
|---|---|---|
| Reference | 1.08 ± 0.04 | 0.42 ± 0.06 |
| 0.1 CNT's-I | 1.53 ± 0.13 | 1.02 ± 0.12 |
| 0.1 CNT’s-II | 1.54 ± 0.06 | 0.76 ± 0.06 |
| 0.1 CNT’s-III | 1.56 ± 0.11 | 0.81 ± 0.08 |
| 0.1 CNT’s-IV | 1.36 ± 0.05 | 0.58 ± 0.05 |
| 0.3 CNT's-I | 1.09 ± 0.08 | 0.48 ± 0.04 |
| 0.3 CNT’s-II | 1.20 ± 0.18 | 0.51 ± 0.06 |
| 0.3 CNT’s-III | 1.66 ± 0.16 | 0.84 ± 0.13 |
| 0.3 CNT’s-IV | 1.06 ± 0.07 | 0.39 ± 0.04 |
| 0.5 CNT’s-I | 1.46 ± 0.04 | 0.42 ± 0.07 |
| 0.5 CNT’s-II | 1.36 ± 0.09 | 0.38 ± 0.07 |
| 0.5 CNT’s-III | 1.33 ± 0.20 | 0.45 ± 0.12 |
| 0.5 CNT’s-IV | 1.07 ± 0.08 | 0.34 ± 0.06 |

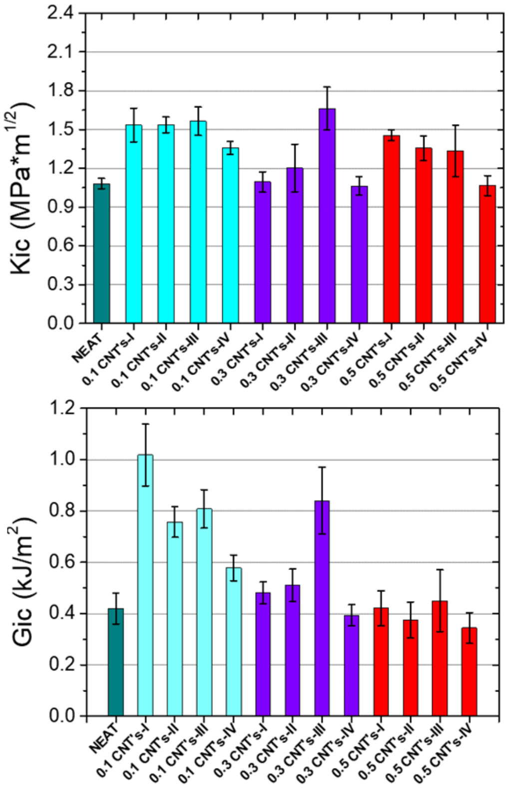

**Figure 11.** $K_{ic}$ & $G_{ic}$ values of specimens containing CNTs.

As in the case of CNTs, systems with CB exhibited a general increase of the $K_{ic}$ values, increasing the filler percentage and the dispersion hours (**Figure 12**). However, the values were slightly different with the reference system due to the different characteristics of the CB compared with the CNTs. Additionally, there was no correlation between the dispersion hours and the $K_{ic}$ contrarywise with specimens with CNTs. In terms of $G_{ic}$, the values remained unaltered within the experimental error. The addition of 0.5 wt. % of CB led to a degradation of the properties, while at 1 or 2 wt. % the mean values were insignificantly increased compared to the reference system.

| **Name** | **$K_{IC}$ (MPa*m$^{1/2}$)** | **$G_{IC}$ (kJ/m$^2$)** |
|---|---|---|
| Reference | 1.08 ± 0.04 | 0.42 ± 0.06 |
| 0.5 CB-I | 1.18 ± 0.07 | 0.41 ± 0.07 |
| 0.5 CB-II | 1.15 ± 0.15 | 0.39 ± 0.07 |
| 0.5 CB-III | 1.06 ± 0.20 | 0.34 ± 0.04 |
| 0.5 CB-IV | 1.08 ± 0.11 | 0.33 ± 0.08 |
| 1 CB-I | 1.29 ± 0.12 | 0.48 ± 0.06 |
| 1 CB-II | 1.15 ± 0.05 | 0.41 ± 0.12 |
| 1 CB-III | 1.26 ± 0.13 | 0.47 ± 0.08 |
| 1 CB-IV | 1.42 ± 0.06 | 0.43 ± 0.07 |
| 2 CB-I | 1.39 ± 0.06 | 0.48 ± 0.03 |
| 2 CB-II | 1.43 ± 0.15 | 0.47 ± 0.04 |
| 2 CB-III | 1.37 ± 0.13 | 0.46 ± 0.04 |
| 2 CB-IV | 1.46 ± 0.08 | 0.40 ± 0.06 |

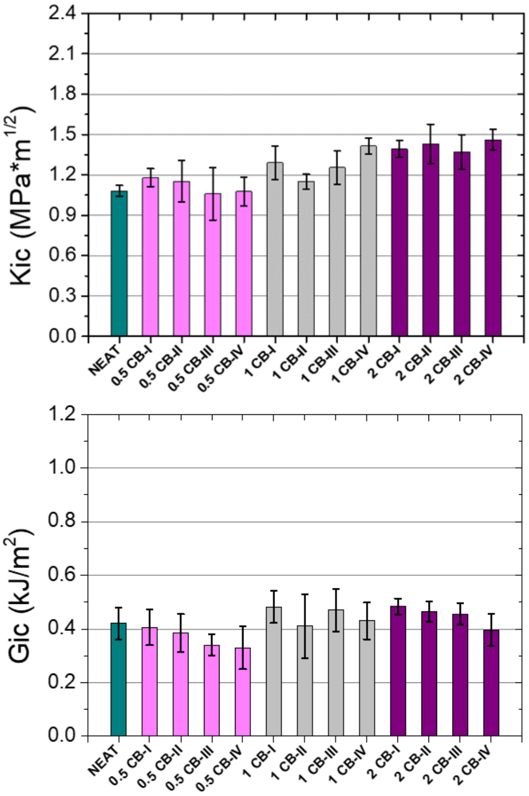

**Figure 12.** $K_{ic}$ & $G_{ic}$ values of specimens containing CB.

Sufficient results of the $K_{ic}$ and $G_{ic}$ values were exhibited from specimens containing both CNTs and CB (**Figure 13**). All systems revealed increased fracture toughness ($K_{ic}$) concerning the reference values. An increase of 40% of the $K_{ic}$ after the fourth hour of dispersion was observed at specimens containing 0.5 wt. % CNTs and 1 wt. % CB.

Increasing the CB filler to the 2 wt. %, the values were increased by 81% compared to the reference system. The very significant increased values resulted from combining the two fillers that have nano and micro dimensions and created a synergetic effect capable of impeding crack propagation and producing crack bifurcation events. In addition, the $G_{ic}$ values remained unaltered at 0.5 CNTs & 1 CB specimens, while an increase of 65% was exhibited in the case of the 0.5 CNTs & 2 CB-III and the 0.5 CNTs & 2 CB-IV systems when compared to the reference specimens.

| **Name** | **$K_{IC}$ ($MPa*m^{1/2}$)** | **$G_{IC}$ ($kJ/m^2$)** |
|---|---|---|
| Reference | 1.08 ± 0.04 | 0.42 ± 0.06 |
| 0.5 CNT's & 1 CB-I | 1.32 ± 0.07 | 0.48 ± 0.05 |
| 0.5 CNT's & 1 CB-II | 1.43 ± 0.15 | 0.43 ± 0.05 |
| 0.5 CNT's & 1 CB-III | 1.46 ± 0.17 | 0.49 ± 0.12 |
| 0.5 CNT's & 1 CB-IV | 1.51 ± 0.14 | 0.43 ± 0.02 |
| 0.5 CNT's & 2 CB-I | 1.46 ± 0.20 | 0.44 ± 0.14 |
| 0.5 CNT's & 2 CB-II | 1.53 ± 0.20 | 0.49 ± 0.08 |
| 0.5 CNT's & 2 CB-III | 1.66 ± 0.16 | 0.72 ± 0.08 |
| 0.5 CNT's & 2 CB-IV | 1.96 ± 0.20 | 0.75 ± 0.06 |

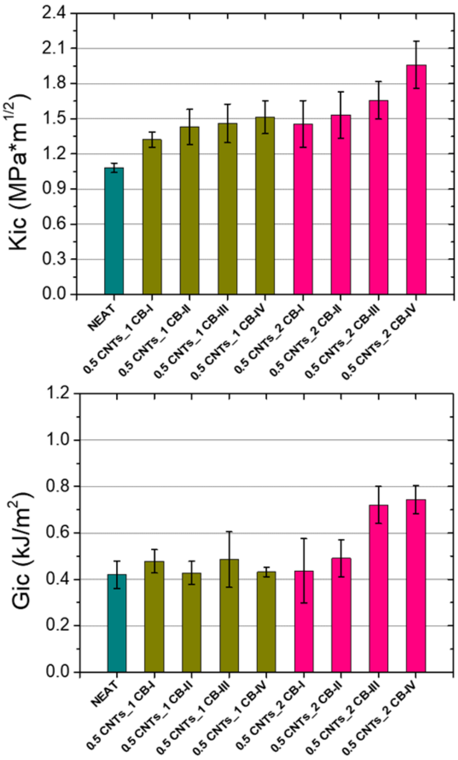

**Figure 13.** $K_{ic}$ & $G_{ic}$ values of specimens containing CNTs & CB.

## 2.4.2 Electrical properties of the polymer matrix

The electrical properties of the nanomodified polymer matrix were studied simultaneously with the mechanical properties. The addition of the carbon nanofillers into the insulating polymer matrix can lead to the formation of a conductive network inside the material. The necessary concentration of the nanofillers must exceed a critical value, the percolation threshold. Above this percentage, the material is conductive.

**Figure 14** depicts the conductivity measurements of specimens containing only CNTs. The first percentage that was studied was the 0.1 wt. % of CNTs. After four hours of dispersion, conductivity was not affected by the inclusion of nanotubes since all values remained at the order of 10-10 S/m, proving that the matrix remained an insulator. It should be noted that the reference (neat) matrix exhibited a conductivity value of 2.03× $10^{-10}$ S/m by increasing the percentage at 0.3 wt. % of CNTs, the conductivity increased by 3-4 orders of magnitude compared to the reference. Specifically, after the first hour of dispersion, the conductivity reached 3.61 × $10^{-7}$ S/m. The second hour exhibited values of 1.08× $10^{-6}$ S/m, the third hour 7.08× $10^{-7}$ S/m, and the fourth hour a conductivity of 4.34× $10^{-6}$ S/m. In this case, the conductivity was higher than the reference but not completely sufficient. It can be said that in the case of 0.3 wt. % of CNTs, a partially or semi-formatted conductive network was achieved.

Additionally, the conductive network was formatted fully in the case of 0.5 wt. % of CNTs dispersion. After one hour of dispersion, the conductivity was increased to 5.34 × 10-5 S/m. At the second dispersion hour, the values reached 1.09 × $10^{-4}$ S/m, while they exhibited a higher value of 1.42 × $10^{-4}$ S/m after three dispersion hours. However, after the fourth hour of dispersion, the conductivity decreased to 6.06 × $10^{-5}$ S/m. This phenomenon can be attributed to the structural degradation of the CNTs due to the extensive dispersion process.

| Name | σ (S/m) |
|---|---|
| Reference | 2.03E-10 |
| 0.1 CNT's-I | 2.50E-10 |
| 0.1 CNT’s-II | 2.79E-10 |
| 0.1 CNT’s-III | 1.24E-10 |
| 0.1 CNT’s-IV | 1.28E-11 |
| 0.3 CNT's-I | 3.61E-7 |
| 0.3 CNT’s-II | 1.08E-6 |
| 0.3 CNT’s-III | 7.08E-7 |
| 0.3 CNT’s-IV | 4.34E-6 |
| 0.5 CNT’s-I | 5.34E-5 |
| 0.5 CNT’s-II | 1.09E-4 |
| 0.5 CNT’s-III | 1.42E-4 |
| 0.5 CNT’s-IV | 6.06E-5 |

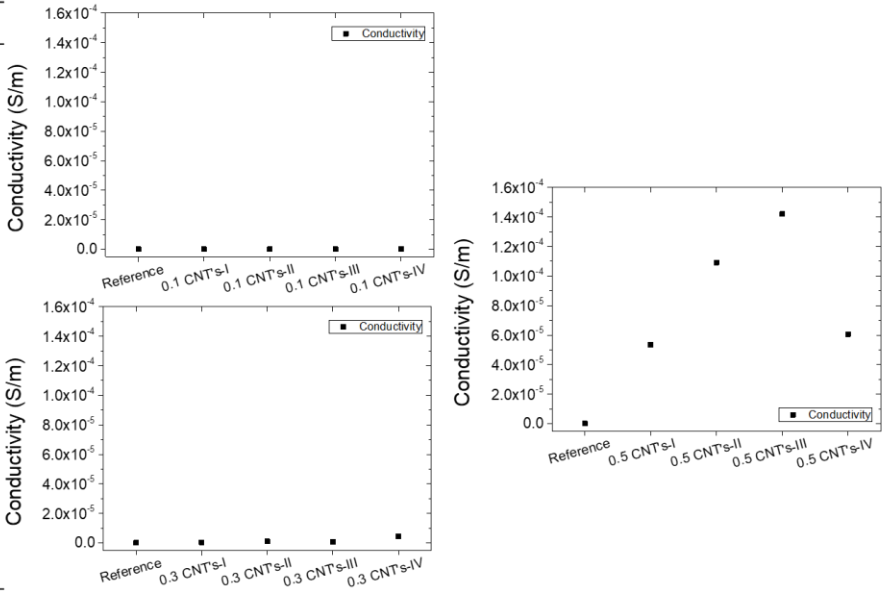

**Figure 14.** Conductivity values from specimens containing CNTs.

The second system that was studied was the dispersion of carbon black. The conductivity values of the selected CB percentages regarding the dispersion duration are depicted in **Figure 15**. In this case, the values did not change and remained very low since the conductive network was not achieved either at 2 wt. % of CB. Specifically, at 0.5 wt. % of CB, the conductivity remained at the order of $10^{11}$ S/m. The same trend was also observed at 1 wt. % and 2 wt. % CB. Many research confirmed these results since the formation of a conductive network in CB systems was not achieved even at 9 wt. % [52].

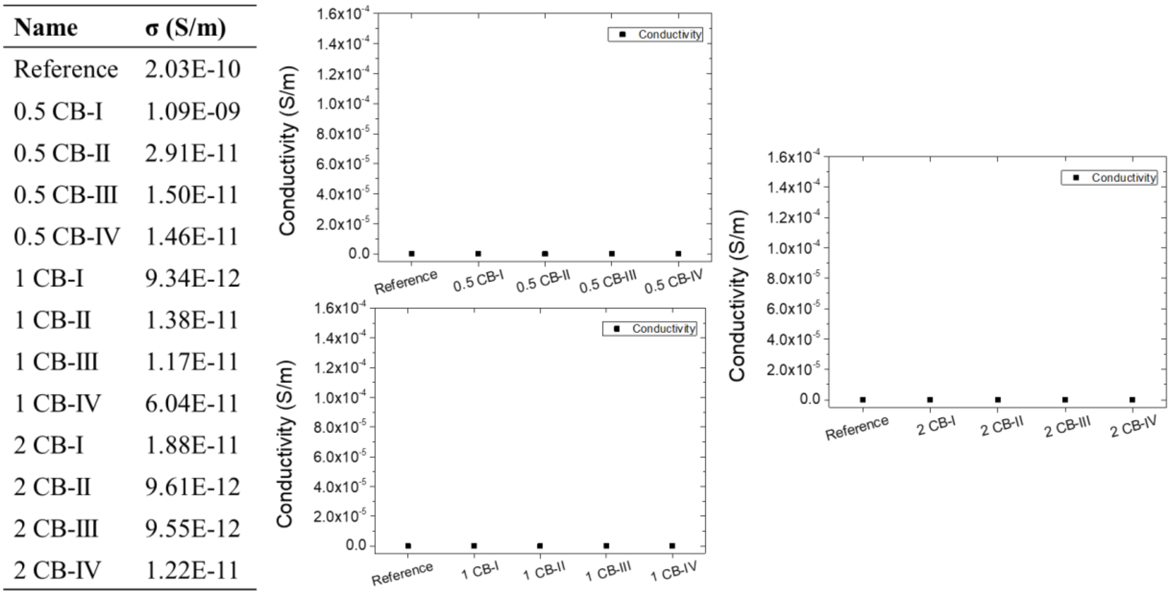

| Name | σ (S/m) |
|---|---|
| Reference | 2.03E-10 |
| 0.5 CB-I | 1.09E-09 |
| 0.5 CB-II | 2.91E-11 |
| 0.5 CB-III | 1.50E-11 |
| 0.5 CB-IV | 1.46E-11 |
| 1 CB-I | 9.34E-12 |
| 1 CB-II | 1.38E-11 |
| 1 CB-III | 1.17E-11 |
| 1 CB-IV | 6.04E-11 |
| 2 CB-I | 1.88E-11 |
| 2 CB-II | 9.61E-12 |
| 2 CB-III | 9.55E-12 |
| 2 CB-IV | 1.22E-11 |

**Figure 15.** Conductivity values from specimens containing CB.

The most optimal and acceptable conductivity results were reached in systems containing both CB and CNTs. At 0.5 wt. % CNTs and 1 wt. % CB after one hour of dispersion, the conductivity was at $7.23 \times 10^{-5}$ S/m. After the second hour, the values increased at $2.06\times 10^{-4}$ S/m, i.e., by one order of magnitude. At the third and fourth hours, the values were insignificantly increased at $2.98 \times 10^{-4}$ S/m and $2.71\times 10^{-4}$ S/m, respectively. The system with 0.5 wt. % CNTs and 2 wt. % CB after one hour of dispersion exhibited a conductivity value of $1.14 \times 10^{-4}$ S/m. In the second hour, the conductivity was slightly increased to $1.23 \times 10^{-4}$ S/m as well as after the third hour reached $1.72\times 10^{-4}$ S/m. However, after four hours, due to the extensive dispersion process (as previously in CNTs), the structural degradation of the CNTs led to a decreased conductivity value of 3.83 × $10^{-5}$ S/m. As a result, the synergy effects of the CNTs and the CB offered improved conductivity and electrical properties compared with the one-component systems.

| Name | σ (S/m) |
|---|---|
| Reference | 2.03E-10 |
| 0.5 CNT’s & 1 CB-I | 7.23E-05 |
| 0.5 CNT’s & 1 CB-II | 2.06E-04 |
| 0.5 CNT’s & 1 CB-III | 2.98E-04 |
| 0.5 CNT’s & 1 CB-IV | 2.71E-04 |
| 0.5 CNT’s & 2 CB-I | 1.14E-04 |
| 0.5 CNT’s & 2 CB-II | 1.23E-04 |
| 0.5 CNT’s & 2 CB-III | 1.72E-04 |
| 0.5 CNT’s & 2 CB-IV | 3.83E-05 |

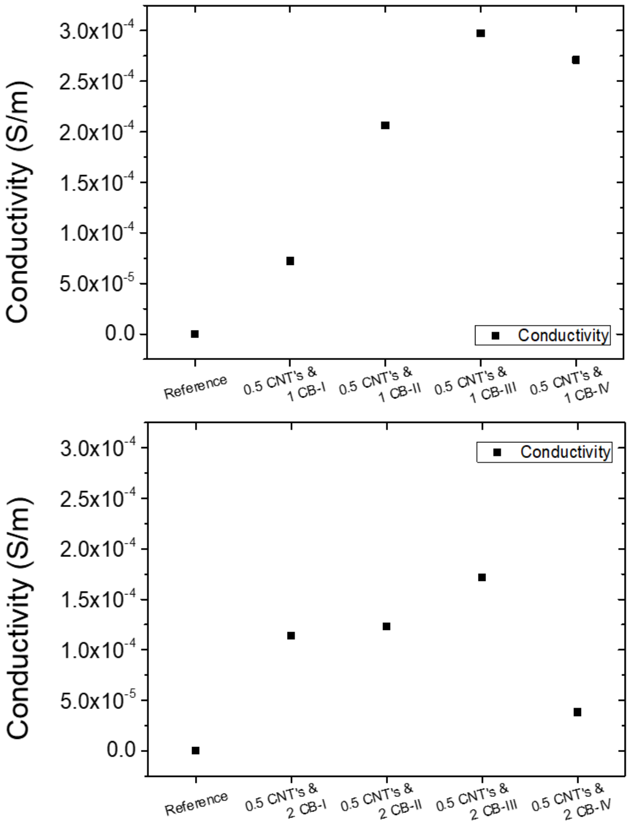

**Figure 16.** Conductivity values from specimens containing CNTs & CB.

## 2.5 Conclusions

This chapter assessed the effect of CNTs and CB dispersion in Diglycidyl Ether of bisphenol-A (DGEBA) epoxy resin on the electrical and mechanical properties. The electrical properties of the modified matrix were investigated by applying the Impedance Spectroscopy. Mechanical properties were evaluated using the single edge notch bending (SENB) geometry according to the ASTM D 5045.

A parametric study was performed to examine the effect of the addition of filler content/type and dispersion duration into the polymer matrix. The modification of the epoxy resin generally increased its fracture toughness. In most cases, all systems containing CNTs presented enhanced mean values of $K_{ic}$ and $G_{ic}$ after three hours of dispersion. Systems with CB exhibited insignificantly improved values of $K_{ic}$, and no correlation between their dispersion duration was observed. However, the Gic values decreased or remained stable. Systems with CNTs and CB showed increased fracture toughness as filler percentage and dispersion time increased. Substantial improvement of the $G_{ic}$ was found for 0.5 CNTs & 2 CB-III and the 0.5 CNTs & 2 CB-IV systems.

$K_{ic}$ values were improved in all systems, with the sufficient protocol being the 0.5 CNTs & 2 CB-IV system due to the synergistic effects that CNTs and CB create. The maximum energy required to fracture ($G_{ic}$) was significantly increased in the case of CNTs in all percentages exploiting the excellent properties of CNTs as their high aspect ratio (length-to-diameter ratio).

In terms of electrical properties, conductivity measurements revealed that systems containing MWCNTs indicated the formation of a conductive network for concentrations over 0.3 wt. % MWCNTs. The optimal electrical properties were found at 0.5 wt% CNTs after three hours of dispersion. After the fourth hour, a conductivity decrease was probably caused by CNTs structural degradation. Regarding the CB dispersion, none of the systems present a sufficient conductivity at all hours of the dispersion duration. In the case of the two-system nanofillers with CNTs and CB, all hours of dispersion revealed improved electrical properties compared to the CNTs systems. This behavior was attributed to the synergistic effects of the CNTs/CB network. The conductivity and mechanical measurements showed a direct correlation between the electrical and mechanical properties of the nanomodified epoxy resin.

# CHAPTER 3

# Capsule-based self-healing polymers with nanomodified healing agent

## 3.1 Introduction

Capsule-based self-healing materials attracted the attention of the scientific community due to their easy application in polymers and composites or coatings [53,54]. The healing agent is embedded in the capsules that break when a propagating crack reaches them, releasing the healing agent at the fractured area. Afterwards, the cracked area is repaired through chemical and/or physical interactions between the healing components. The design cycle of capsule-based self-healing materials consists of (i) the development of capsules (encapsulation), (ii) integration of capsules/catalyst into the material, (iii) evaluation of the mechanical properties, (iv) triggering/releasement of the healing agent and (v) evaluation of the healing efficiency (**Figure 17**).

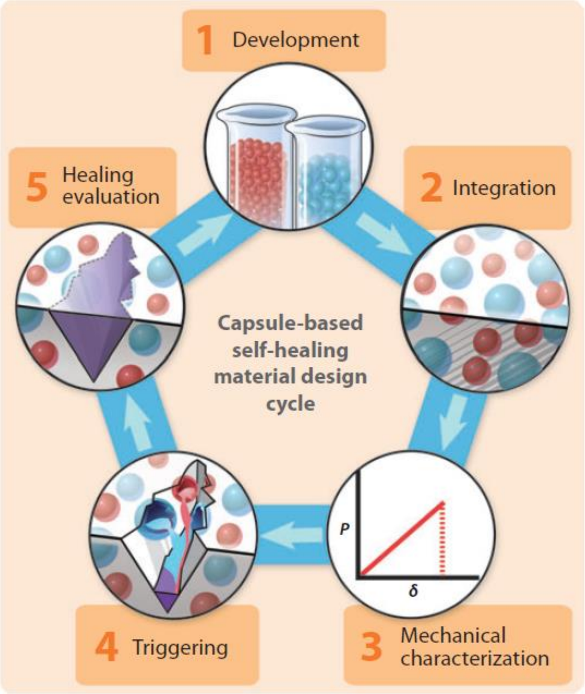

**Figure 17.** Design cycle of capsule-based self-healing materials. ("Used with permission of Annual Reviews, Inc., from Self-healing polymers and composites, B.J. Blaiszik, S.L.B. Kramer, S.C. Olugebefola, J.S. Moore, N.R. Sottos and S.R.White, 40:179-211, permission conveyed through Copyright Clearance Center, Inc.")

There are five categories of encapsulated healing agent systems that have already been proven efficient, as shown in **Figure 18** [20]. The first one is the single-capsule system with at least one healing agent encapsulated, a monomer, a solvent, or a low-melting point metal. Secondly, the capsule/dispersed catalyst self-healing system is related to the encapsulation of a self-healing agent within the capsules and the dispersion of a catalyst within the matrix. Capsules release the monomer, and when it encounters the catalyst, the polymerization occurs. Rodriguez et al. investigated the optimized position of the catalyst scandium triflate ($Sc(OTf)_3$) on the healing efficiency in terms of fracture toughness [55]. Polymethylmethacrylate (PMMA) microcapsules and PMMA capsules with the catalyst incorporated in the shell wall (PMMA/$Sc(OTf)_3$-walled microcapsules) containing an epoxy resin as a healing agent were synthesized. Results indicated that in the use of PMMA/Sc(OTf)3-walled capsules, the healing efficiency was increased by 11% and 24% when the healing process took place at 80 and 120 °C, respectively. In the third approach of the phase-separated droplet/capsule system, at least one of the healing components undergoes phase separation while the other element is encapsulated.

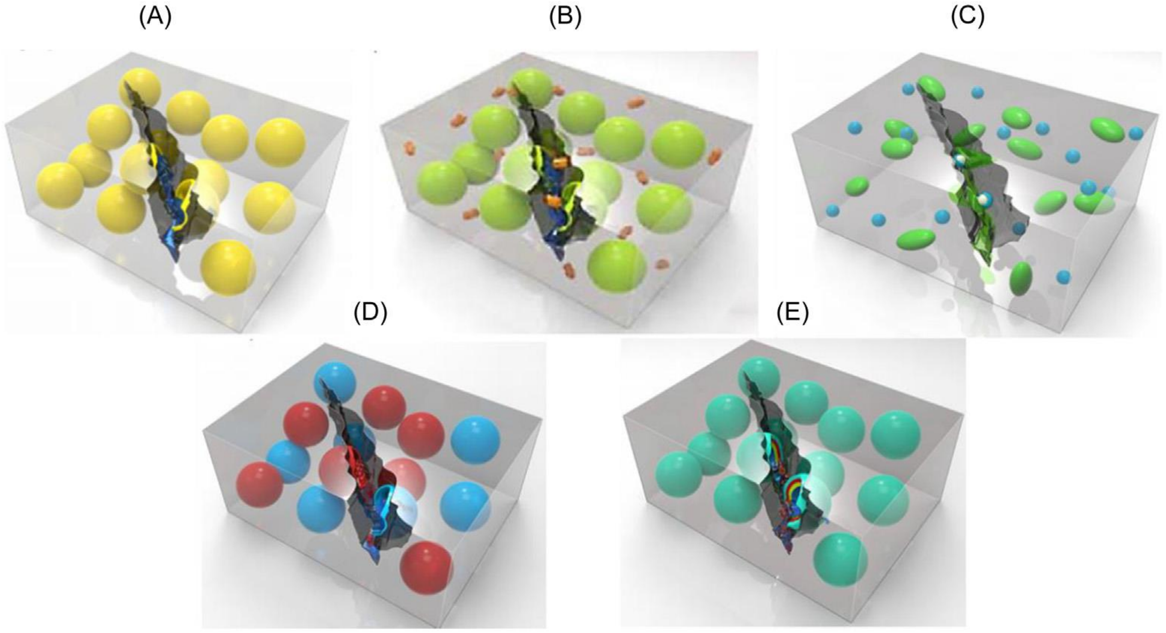

**Figure 18.** Capsule-based self-healing systems, (A) single capsules, (B) capsule/dispersed catalyst, (C) phase-separated droplet/capsules, (D) double-capsule, and (E) all-in-one microcapsules. (*"Reprinted from Progress in Polymer Science, Vol. 49-50, D.Y. Zhu, M.Z. Rong, M.Q. Zhang, Self-healing polymeric materials based on microencapsulated healing agents: From design to preparation, 175-220, (2015), with permission from Elsevier."*)

The fourth system includes the double-capsule system (**Figure 18**D). This method is based on encapsulating one or more healing agents into different capsules. In order to improve the healing efficiency of an epoxy matrix, Qi Li et al. demonstrated a dual-capsule system of DGEBA and polyether amine (hardener) microcapsules using the water-in-oil-in-water emulsion solvent evaporation technique with polymethyl methacrylate (PMMA) as the wall material [56]. Results indicated that the content and the ratio of the capsules affected the healing efficiency of the epoxy system. The healing process took place successfully at room temperature, but, as was expected, an increase in the temperature during the process led to higher healing efficiency values.

In the final approach, the monomer and the catalyst are either integrated into the core or/and the shell wall of the same multilayer capsule, isolated by layers or encapsulated in separate smaller spheres deposited into a larger capsule, creating a capsule-in-capsule system. Upon breakage, the healing agent fills the crack area, and when it comes in contact, the catalyst repairs the damage. Tian and his coworkers demonstrated the synthesis of double-walled capsules that contained both the healing agent and the amine-based curing agent into melamine-formaldehyde shell-walls [57]. Although microcapsules broke earlier than the resin matrix, the mechanical performance of the cured double-layer capsules was similar to that of the cured resin matrix, indicating that they were capable of successfully healing the cracks. Recently, Da Costa et al. [58] investigated the self-healing capsule-based triggering mechanism using the non-destructive technique of the X-ray micro-computed tomography (μCT) combined with the scanning electron microscopy (SEM). Capsules filled with amino-functional polysiloxane (PDMS-a) were introduced into a DGEBA epoxy resin matrix. After the microcapsule eruption, the PDMS-a was released and was able to fill the crack plain sufficiently, as observed after the healing process.

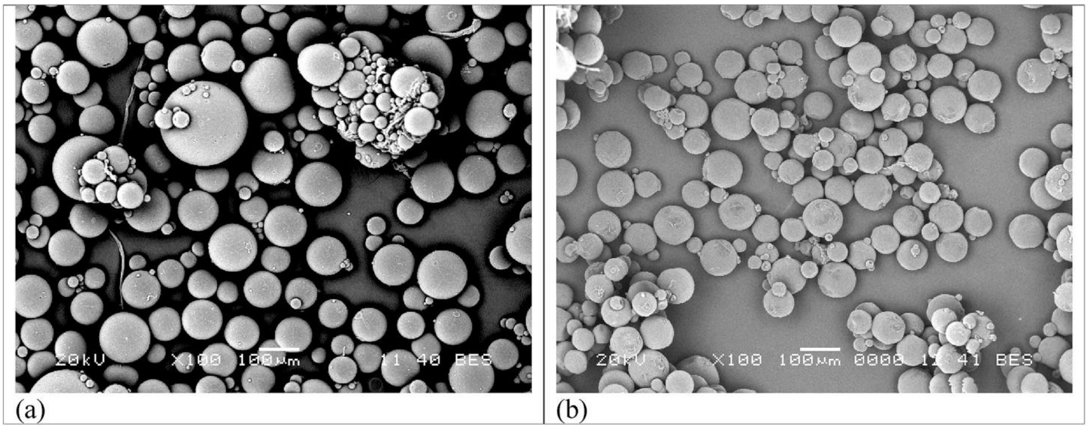

**Figure 19.** SEM images of (a) PMMA-walled microcapsules and (b) PMMA/Sc(OTf)$_3$-walled microcapsules. (Original source: R. Rodriguez, D. G. Bekas, S. Florez, M. Kosarli, A. S. Paipetis, Development of self-contained microcapsules for optimised catalyst *position in self-healing materials, Polymer, 187, 122084, 2019)*

Capsules are produced at micro- or nano- dimensions and generally are spherical in shape. However, in a numerical study, Mookhoek et al. studied the effect of elongated capsules on the healing efficiency and the comparison with the spherical capsules [59]. The models predicted the amount of healing agent released regarding the capsule size, volume fraction aspect ratio, and capsule orientation for the elongated capsules. Results indicated that healing efficiency improved in the case of the elongated capsules, with the most significant factor being the capsule orientation. In another study, Lv et al. developed analytical models for the effect of capsule shape on the amount of the healing agent released based on the probability of the crack intersection with capsules [60]. The models exhibited very promising results in the development of elongated capsules.

A very important parameter for a successful capsule-based system is the encapsulation techniques that should always be selected according to the healing agent properties. The most common and easily scalable encapsulation method is the in-situ polymerization since the stirring rate can directly affect the capsule size and exhibits mass production. By increasing the stirring rate, the mean capsule diameter is decreased [61]. Healing efficiency and change of the initial mechanical properties after the self-healing system incorporation regarding capsule size were studied using five different mean sizes of UF microcapsules [62]. The capsules were introduced into a polymer matrix using the TDCB geometry and tested under Mode I tensile mode. Results confirmed that the effect of capsule size is inversely proportional to the reduction of the mechanical properties as well as had a proportional relationship to healing efficiency, clearly proving that there is an optimal capsule size (about 180μm) to achieve both properties (**Figure 20**). The first self-healing capsule-based system was developed by White et al. [63] in 2001 and included the addition of DCPD-filled microcapsules and Grubbs' catalyst in an epoxy matrix. After that, the TDCB geometry was used in many research performed in the context of self-healing capsule-based systems to evaluate the healing performance in terms of fracture toughness [64–67]. Blaiszik and his team tried to perform the healing ability in nano dimensions [58]. They are produced via the in situ emulsification polymerization UF nano-capsules containing dicyclopentadiene (DCPD). The small size of capsules was achieved via the simultaneous use of sonication and mixing, and the mean diameter was estimated at 220 nm, while a shell wall thickness of 77 nm was achieved. The incorporation of nano-capsules in the epoxy matrix increased significantly (by 59%) the mode-I fracture toughness with a small capsule volume fraction of $\Phi_f$=0.015.

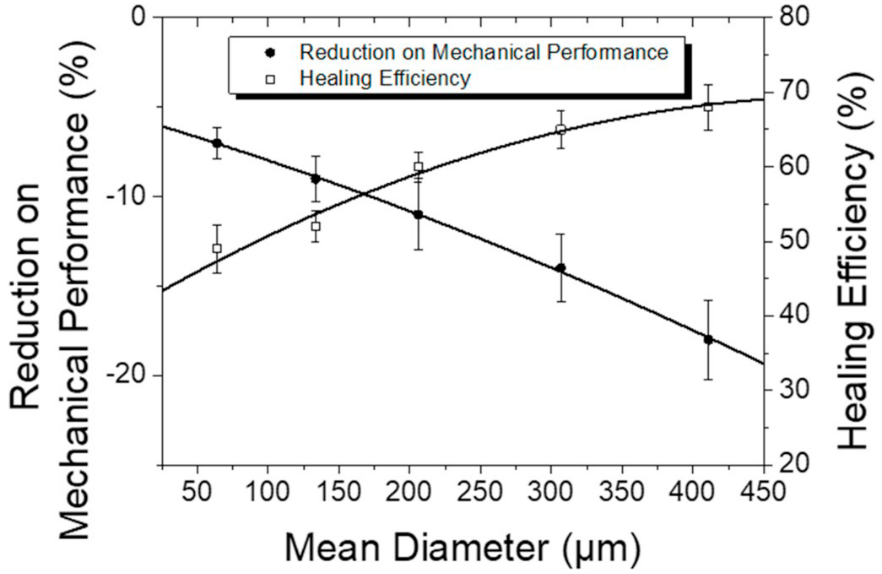

**Figure 20.** Healing efficiency is proportional to capsule size, and the reduction of the mechanical properties has an inversely proportional relationship. (*Original source: M. Kosarli, D. G. Bekas, K. Tsirka, D. Baltzis, D. T. Vaimakis-Tsogkas, S. Orfanidis, G. Papavassiliou, A. S. Paipetis, Microcapsule-based self-healing materials: Healing efficiency and toughness reduction vs. capsule size, Composites Part B: Engineering, 78-86, 2019)*

A novel approach for the implementation of a Lewis acid-catalyzed self-healing system into an epoxy matrix was proposed by Coope et al. [68]. In this research, the self-healing performance was evaluated using the TDCB geometry, and the effect of several parameters such as the capsule content, healing temperature, and time was also examined. The Lewis acid- catalyzed self-healing epoxy resin demonstrated good compatibility and interlocking between capsules and the host matrix. At the same time, a recovery value of greater than 80% of fracture strength was reported. Another very interesting research from Zhang and his coworkers included the development of a skin-inspired, fully autonomous, self-warning, and self-healing polymeric material [69]. They reported a dual microcapsule system containing an epoxy monomer dyed with a pH indicator and a polyamine embedded into the matrix. After impact damage, the material was able to inform the user by changing its color to red. Increasing the concentration of microcapsules from 5 to 10 wt.%, the recovery of mechanical properties, i.e., the healing efficiency, improved by 25% (from 70% to 95%).

Microcapsules are not only used for the restoration of mechanical properties. Caruso et al. described the encapsulation of single-walled carbon nanotubes (SWCNTs) suspended in chlorobenzene and ethyl phenylacetate (EPA) via the in-situ emulsification polymerization [70]. Electrical measurements showed that by increasing the percentage of the SWCNTs, the average conductivity of the system was also increased, creating a bridge between the probe tips. In a similar study, Odom et al. [71] used polymer-stabilized carbon nanotube and graphene UF microcapsules for the autonomic restoration of the electrical conductivity in damaged gold lines. After the fracture, the SWCNTs and the graphene flakes were released from the polymeric microcapsules. At the same time, the concurrent application of an electric field of ca. 5V caused the nanotubes to be transferred to the damaged location. Zamal et al. reported the manufacturing of PMUF microcapsules containing a suspension of CNTs/52EN (5-ethylidene-2-nobornone) as a healing agent [72]. These capsules were used to recover mechanical properties after their introduction into a polymer matrix or restore electrical properties at conductive epoxy adhesives up to 80% in both cases. In another study, Bailey et al. demonstrated electrically conductive semi-cured epoxy coatings to restore both mechanical and electrical properties [73]. Microcapsules containing nano-enhanced epoxy resin with CNTs or neat epoxy resin with ethyl phenylacetate (EPA) were incorporated into the epoxy. The electrochemical impedance spectroscopy was utilized to evaluate the potential of the nano-modified or not encapsulated systems to restore the electrical properties. After an in situ electro-tensile test under a microscope, mechanical properties were recovered by 81% while electrical properties by 64%.

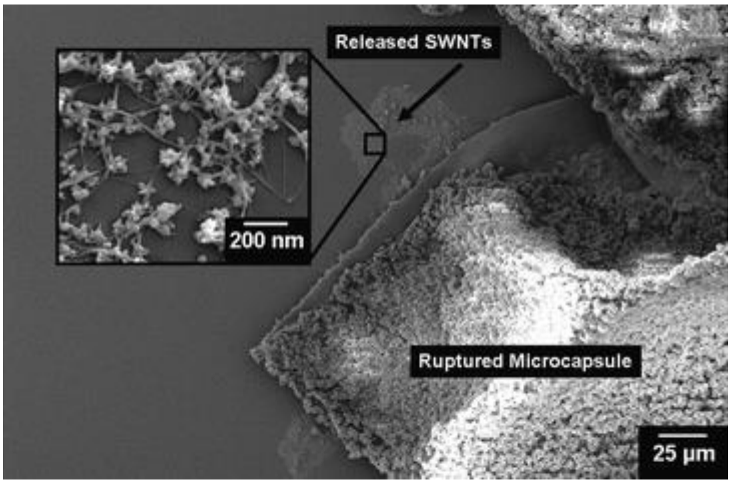

**Figure 21.** SEM image of the suspension of the SWNTs in chlorobenzene and EPA that were released from a ruptured microcapsule. (*"Used with permission of Royal Society of Chemistry, from Microcapsules containing suspensions of carbon nanotubes, Caruso Mary M., Schelkopf Stuart R., Jackson Aaron C., Landry Alexandra M., Braun Paul V., Moore Jeffrey S., 19, 34, 2009; permission conveyed through Copyright Clearance Center, Inc."*)

## 3.2 Scope

The scope of this chapter is the evaluation of healing efficiency in terms of mechanical and electrical properties at the polymer matrix level. The most sufficient results from this experimental campaign were transferred in Chapter 6 to manufacture and identify the smart & multifunctional composites. **Figure 22** depicts the workflow of this chapter.

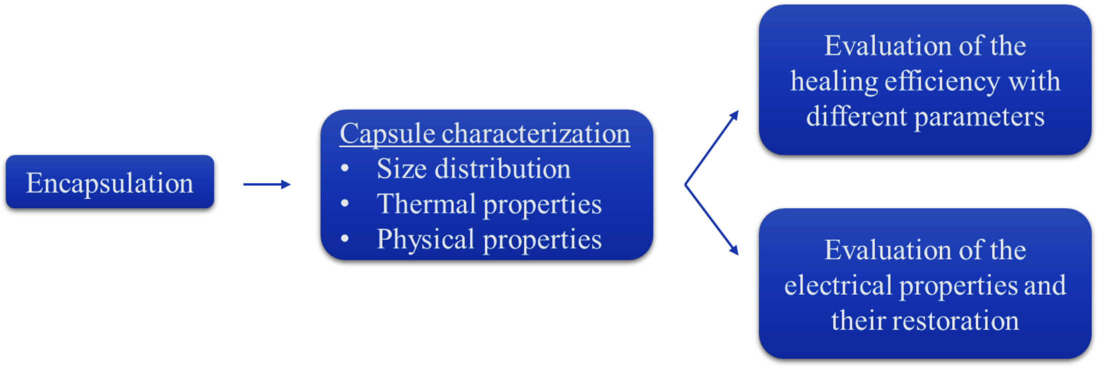

**Figure 22.** Schematic of the workflow followed at capsule-based self-healing polymers with a nanomodified healing agent.

This chapter is separated into two main case studies. Case study one focuses on evaluating the healing efficiency in terms of mechanical properties. For this scope, ternary nanomodified capsules were incorporated into a neat polymer matrix, changing different parameters. The parameters are illustrated in **Figure 23**. The healing agent was nanomodified with nano- and micro- fillers, MWCNTs, and CB, exploiting the results from chapter 2. Capsules' mean size was evaluated before the mechanical characterization. In case study two, a nanomodified healing agent with low CNTs percentage was encapsulated into UF capsules. Capsules were characterized at a material level, and their healing efficiency was evaluated in terms of electrical & mechanical properties after their incorporation into the nanomodified polymer matrix. In all cases, conventional (neat) microcapsules were manufactured as reference capsules for comparison.

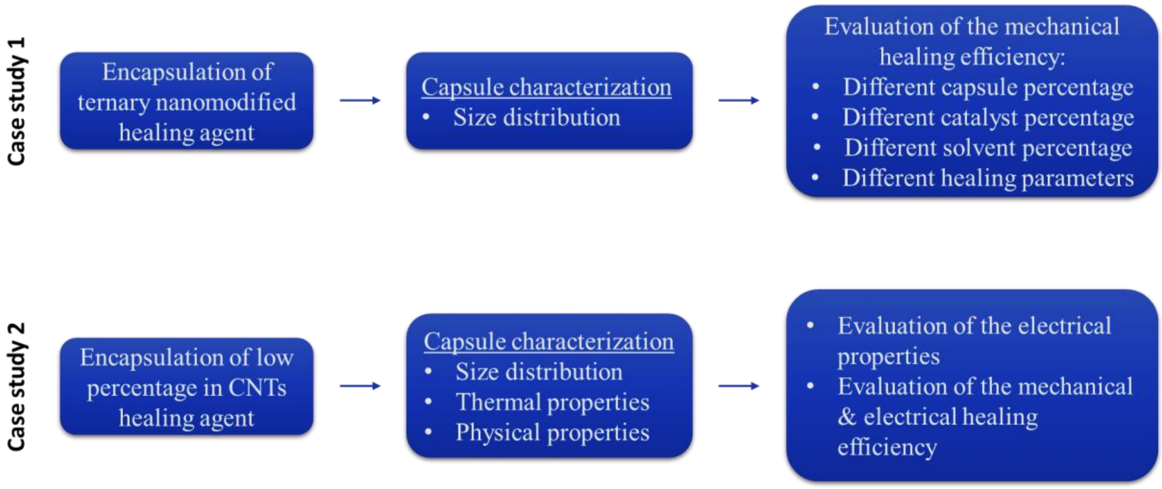

**Figure 23.** Schematic of the workflow followed at the two case studies.

## 3.3 Experimental

### 3.3.1 Materials

The two main materials of the shell wall were urea ($NH_2CONH_2$) and formalin (37 wt. % formaldehyde in water). As surfactant, the poly(ethylene-maleic-anhydride) (EMA, $M_w$ = 100,000–500,000 g/mol) copolymer powder was used. Ammonium chloride ($NH_4Cl$) and resorcinol ($C_6H_4$-1,3-$(OH)_2$) were used as stabilizers for the formation of the shell wall. All the materials above were supplied by Sigma-Aldrich company. The core of the capsules that was the healing agent was the diglycidyl ether of bisphenol-A (DGEBA, Epikote 828 lvel) epoxy resin. The same epoxy resin (Epikote 828) with the Epikure 541 hardener at a ratio of 100:50 % wt., supplied from Dichem Polymers, Greece, was selected as the matrix phase. The nanomodification of the epoxy was performed using the Graphistrength C-100 MWCNTs from ARKEMA, France. The length and the diameter of the CNTs ranged from 1 to 10 μm and 10 to 15 nm, respectively. As secondary reinforcement, the milled carbon black (CB), provided by R&G composites GmbH, with an average agglomerate size ranging from 50 mm to 5 mm in diameter, was selected. The viscosity of the healing agent was tuned using the non-toxic solvent ethyl phenylacetate (EPA) from Sigma-Aldrich. The catalyst for the healing process was the Aluminium (III) triflate ($Al(OTf)_3$) supplied from Sigma-Aldrich, too.

### 3.3.2 Nanomodification of the healing agent

In case study one, 0.5 wt. % MWCNTs and 2 wt. % CB were dispersed within the healing agent (epoxy resin) using a high shear mixer (Dispermat AE, VMA-GETZMANN DMBH, Germany), as shown in Chapter 2. The dispersion protocol involved continuous agitation at 25 $^oC$ under vacuum. According to the protocol, the agitation rate was set at 3000 rpm, and the duration was 4 hours [74]. For the second case study, 0.1 wt. % CNTs were dispersed within the DGEBA epoxy resin for 3 hours under the same parameters.

### 3.3.3 Encapsulation process

The selected method for the encapsulation of the healing agent was the in situ emulsification polymerization [20,75]. Initially, 25 mL of 2.5 % w/v surfactant solution were added to the high shear mixer with 100 mL of deionized water under continuous stirring. The stirring rate was set at 500 rpm for the first case study and 200 rpm for the second. The agitation rate that affects the capsules' size was chosen according to our previous research [76]. Then, 2.5 g urea, 0.25 g resorcinol, and 0.25 g ammonium chloride were placed in the beaker. When the solution became clear, the pH of the mixture was adjusted at 3.5 using sodium hydroxide (NaOH), and 60 g of diluted resin at the desired ratio was added. In the first case study that included the evaluation of healing efficiency using different solvent percentages, three percentages were chosen for the nanomodified capsules, at 25, 30, and 35 wt. %. and a 10 wt. % dilution for the neat capsules. The percentages mentioned above for the nanomodified capsules were selected after viscosity measurements in order to attain the values of the neat resin that were achieved in the case of 30%. A 15 wt.% dilution was selected for both modified and unmodified capsules for the second case study. After 15 min, 6.33 g formalin was placed in the mixer, the temperature increased to 55 °C with a rate of 10 °C/min, and the reaction was left to proceed for 4 hours. After the encapsulation process, the mixture was left to cool down at room temperature, and the suspended microcapsules were rinsed with ethanol using a Buchner filter. The final UF microcapsules were left to dry in an oven at 30 $^{o}$C.

## 3.4 Characterisation techniques & equipment

### 3.4.1 Scanning Electron Microscopy (SEM)

The morphological characterization and size distribution evaluation of the produced capsules was performed using a JEOL JSM 6510LV, Oxford Instruments, scanning electron microscope. The produced microcapsules were initially gold-platinum sputter-coated, and the operating voltage was set at 5 keV to avoid their decomposition due to high voltage. The evaluation of the mean diameter of the capsules was performed by taking measurements from approximately 100 different individual capsules.

### 3.4.2 Thermogravimetric Analysis (TGA)

The thermal stability of the microcapsules was examined via thermogravimetric analysis (TGA). TGA scans were achieved using the PerkinElmer Pyris Diamond TG/DTA instrument. Measurements were performed between 27 and 600 $^{o}$C with a 10 $^{o}$C/min heating rate under a nitrogen atmosphere.

### 3.4.3 Raman spectroscopy

Raman spectroscopy was employed to confirm the successful encapsulation of the nano-reinforced epoxy within the UF microcapsules. Raman spectra of the neat epoxy resin, the CNTs, the nano-reinforced resin, and the developed microcapsules were recorded with the Labram HR–Horiba confocal Raman microscope. The 514.5 nm line of an argon-ion laser operating at 1.5 mW at the focal plane was employed for the Raman excitation. An optical microscope served as the collector of the Raman scattering equipped with a 100×objective. Raman spectra were acquired in the spectral range of 100–3500 cm$^{-1}$. Additionally, the Raman spectra of the shell material (Urea-Formaldehyde) were recorded with a longer wavelength diode laser line of 784 nm operating at 1 mW at the focal plane in order to overcome the fluorescence. Spectral processing included a baseline subtraction using a third-order polynomial and a normalization for easing the comparison process among different spectra. The normalization was performed with respect to the peak with the maximum intensity; this band was the D vibrational mode for the CNT spectrum at 1346 cm$^{-1}$ and a vibrational mode at 3069 cm$^{-1}$ for both the DGEBA and the DGEBA+CNTs spectra.

### 3.4.4 Manufacturing of the self-healing specimens (TDCB geometry)

The initial evaluation of the healing performance of the capsules in terms of toughness was performed using the modified Tapered Double Cantilever Beam (TDCB) [64,77]. The TDCB specimens consist of a rectangular central grooved section that includes the capsule-modified polymer embedded in a plain epoxy coupon (self-healing section). For the first case study, the main body of the TDCB specimen (central groove) was the neat epoxy DGEBA resin. The second case study included the nanomodification of the polymer matrix at 0.5 wt. % of CNTs. This percentage of MWCNTs exceeded the percolation threshold over which the employed polymers were considered electrically conductive [74]. The dispersion of the CNTs within the polymeric matrix was performed for 3h at 3000rpm using a high shear mixer.

The central groove consisted of dispersed microcapsules and $Al(OTf)_3$ particles [64,78] as a catalyst. For case study one, three different percentages at 15, 20, and 25 wt. % of capsules were incorporated into the self-healing section. In case study two, 20 wt. % of microcapsules were added. Two different catalyst percentages were chosen at 2 and 3 wt. % for the first case study and 3 wt. % for the second. Using a high shear mixer, microcapsules and catalyst particles were dispersed within the polymeric matrix. The hardener (Epikure 541) was placed into the mixture at the end of this process. The mixture was then degassed for 2 min using a laboratory oven, cast into silicon molds, and left for curing at 25 $^{o}$C for 24 hours. To evaluate the mechanical performance reduction after incorporating the self-healing system in the epoxy matrix, 5 specimens without capsules were manufactured and tested. Hereafter, TDCB specimens without capsules are noted as “reference,” specimens after the incorporation of the self-healing system are noted as “virgin” and specimens after the mechanical characterization and healing process are noted as “healed”. All TDCB specimens were pre-cracked with a fresh razor blade at 10 mm and tested using a mini tensile testing frame manufactured by Fullam Inc. USA at a displacement rate of 1 mm/min (**Figure 24**).

Two healing processes took place in a laboratory oven for the first case study at 80 $^{o}$C for 24 and 48 hours. The healing process was performed at 80 $^{o}$C for 48 hours for the second case study. After the healing procedure, the specimens were left to cool to room temperature and were subsequently retested under the same conditions. All the different parameters for the first case study are summarized in (**Figure 25**). The change of the initial properties after the self-healing system incorporation or the knockdown effect was evaluated using equation (1). The healing efficiency was calculated as the ratio of the peak load of the virgin specimen to the peak load of the healed specimen (equation (2)).

$$k\% = 1 - \frac{\mathrm{P_c^{Virgin}}}{\mathrm{P_c}^{Reference}} * 100\% \qquad (1)$$

$$n\% = \frac{\mathrm{P_c^{Healed}}}{\mathrm{P_c}^{Virgin}} * 100\% \qquad (2)$$

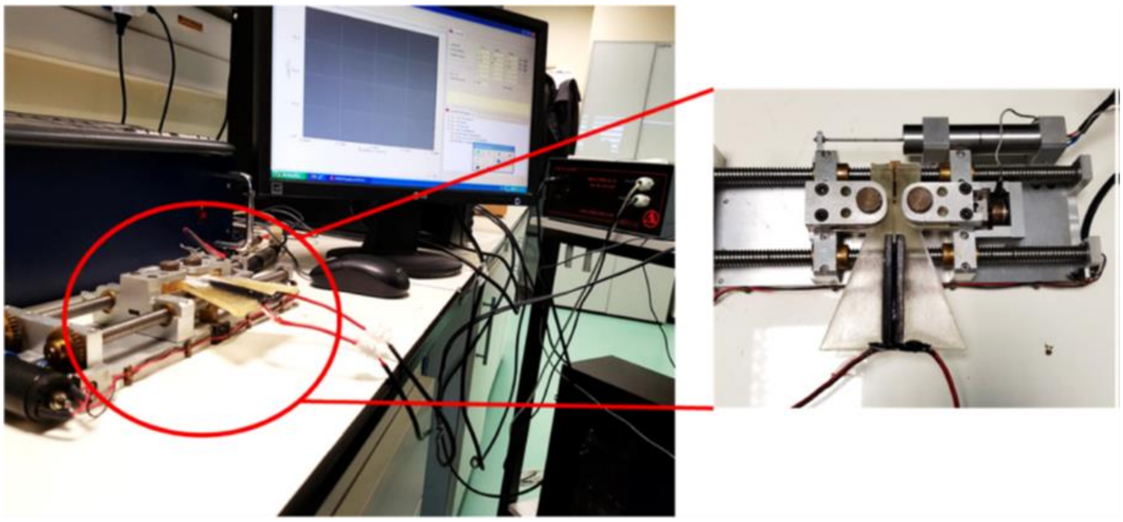

**Figure 24.** Mechanical testing of TDCB specimens with the simultaneous use of Impedance Spectroscopy.

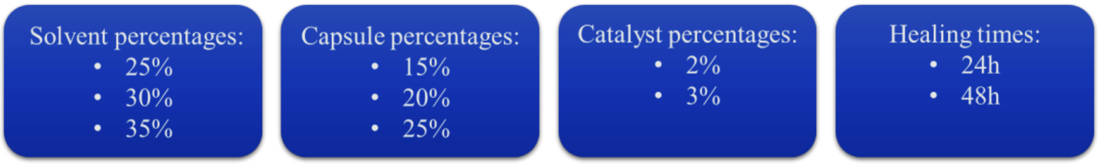

**Figure 25.** The different parameters that examined in case study one.

### 3.4.5 Manufacturing of SENB specimens

The Single Edge Notch Beam (SENB) geometry was chosen to evaluate electrical properties for the second case study. The specimens were also tested under three-point bending loading in order to evaluate the recovery of both mechanical and electrical properties in case of a total failure of a polymer matrix. As the matrix phase, the same nanomodified DGEBA resin was used with 20 wt. % capsules and 3 wt. % catalyst particles under the same manufacturing process as at TDCB geometry. Testing conditions and the healing process were the same as previous.

### 3.4.6 Restoration of electrical properties

The Impedance technique was used in order to evaluate the electrical properties of the polymer matrix and the efficiency of the healing system to regain its initial electrical properties. Measurements were performed using the Advanced Dielectric Thermal Analysis

System (DETA-SCOPE) supplied by ADVICE, Greece. SENB specimens were placed between two parallel copper plates with dimensions of 52×12 mm or, in case of TDCB geometry, two copper cables were incorporated in the central groove (self-healing section). Scans were performed at the frequency value of 1 Hz. All measurements were performed under a stable temperature of 25 °C.

The assessment of the electrical properties was performed in an off-line way by the following steps: (i) conductivity measurements of the virgin specimens before mechanical loading, (ii) implementation of the mechanical characterization and the healing process, and (iii) conductivity measurements after the healing process. The electrical properties of the polymer matrix and their restoration was evaluated from the ratio of the DC conductivity values of the healed specimens to the DC conductivity values of the virgin specimens through equation (3).

$$e\% = \frac{\sigma^{\mathrm{Healed}}}{\sigma^{Virgin}} * 100\% \tag{3}$$

## 3.5. Results & Discussion- Case study one

### 3.5.1 Size distribution/ morphology

All microcapsules were spherical in shape and had a rough exterior wall that was an important parameter for better interlocking between the matrix and the capsules (**Figure 26**). Capsules containing ternary nanomodified healing agents diluted at 25 % with solvent will be called “ternary 25%”, etc. The mean size was calculated from 100 individual measurements of capsules diameter. Neat capsules had a mean size of approximately 114 μm; ternary 25% had an average size of 54.6 μm, ternary 30% at 54.6 μm, and ternary 35% had a mean diameter of 39.5 μm. As it can be observed increasing the dilution percentage, the mean size was decreased. This can be attributed to the monomer droplets that became unstable, increasing the percentage of the solvent, especially in higher temperatures in which the polymerization takes place (55 °C). The stability of the droplets and subsequently the emulsion depends largely on the surface tension of the core liquid that, in this case, decreased as the viscosity decreased [79].

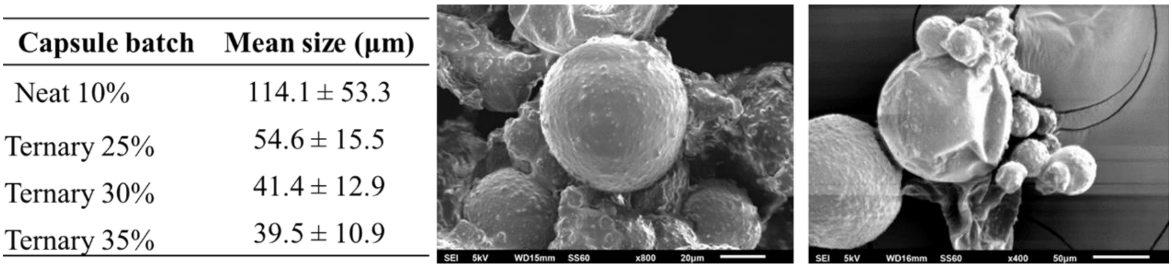

| Capsule batch | Mean size (μm) |
|---|---|
| Neat 10% | 114.1 ± 53.3 |
| Ternary 25% | 54.6 ± 15.5 |
| Ternary 30% | 41.4 ± 12.9 |
| Ternary 35% | 39.5 ± 10.9 |

**Figure 26.** Mean size of the different capsule batches that produced (left) and SEM images from discrete capsules (right).

## 3.5.2 Investigation of the recovery of fracture toughness with different parameters

### *3.5.2.1 Different solvent percentage*

Due to the high viscosity of the nanomodified DGEBA resin used as a healing agent, the effect of the dilution percentage on the healing efficiency was investigated. The neat capsules were diluted at 10 wt. % while for nanomodified capsules, the same viscosity was achieved after 30 wt. % dilution of EPA solvent. All specimens were manufactured with the same parameters, i.e., same catalyst percentage (2 wt. %), capsule concentration (20 wt. %), and healing process (24 hours at 80 °C). Results indicated that specimens containing neat capsules exhibited a healing efficiency of 26 %, while at ternary 30% systems, the values increased by 5 % (**Figure 27**). Although the size of the nanomodified ternary 30% capsules was half compared with the neat category, the healing efficiency increased due to the CNTs inclusion. As it is known, CNTs, as well as ternary nanomodified systems (CNTs and CB), can provide enhanced both mechanical and electrical properties after their dispersion at epoxies [50,74]. At higher viscosities of the healing agent (TDCB-ternary 25%), the healing efficiency was decreased compared to the TDCB-neat 10% systems proving that the delivery of the agent was not sufficient. However, at a higher dilution percentage (ternary 35%), with the viscosity of the nanomodified healing agent being lower than this of the neat resin, the healing efficiency increased by about 8%. This can be attributed to the more sufficient delivery of the agent into the cracked areas. The change of the initial properties of the polymer matrix after the incorporation of the self-healing system (capsules and catalyst), i.e., the knockdown effect, was also evaluated. Specimens containing neat 10% capsules reduced the properties by about -4 % in contrast to all nanomodified systems (TDCB-ternary 25%, 30%, and 35%) that not only eliminated the knockdown effect but also improved their mechanical properties by 5-7 %. This phenomenon was associated with the remaining droplets of the nanomodified agent attached to the exterior shell-wall and allowed a better interlocking between the matrix and the introduced capsules [80].

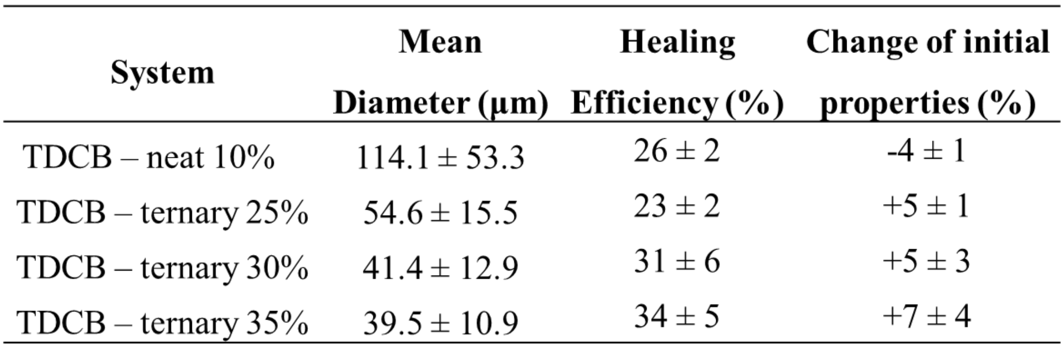

| System | Mean Diameter (μm) | Healing Efficiency (%) | Change of initial properties (%) |
|---|---|---|---|
| TDCB – neat 10% | 114.1 ± 53.3 | 26 ± 2 | -4 ± 1 |
| TDCB – ternary 25% | 54.6 ± 15.5 | 23 ± 2 | +5 ± 1 |
| TDCB – ternary 30% | 41.4 ± 12.9 | 31 ± 6 | +5 ± 3 |
| TDCB – ternary 35% | 39.5 ± 10.9 | 34 ± 5 | +7 ± 4 |

**Figure 27.** Healing efficiency and change of initial properties of the self-healing TDCB specimens containing capsules with different solvent percentages.

### *3.5.2.2 Different capsule percentage*

In self-healing capsule-based polymers, the embedded capsules were incorporated from low percentages such as 5% [81] to higher percentages of 20% [64]. In this case, the effect of capsule percentage on self-healing efficiency was investigated. Specimens containing capsules at 15, 20, and 25 wt. % were manufactured using ternary nanomodified and neat capsules. The neat capsules that were used were diluted at 10 wt. % while for the nanomodified, the ternary 35% capsules were chosen according to the previous results. The specimens were produced with a catalyst percentage of 2 wt. % while the healing process took place for 24 hours at 80 °C. **Figure 28** depicts the obtained results of the healing efficiency and the knockdown effect for the different categories. Specimens containing 15 wt.% neat capsules exhibited recovery of their properties of about 23%, while after the core modification, the efficiency increased by 6%. Increasing capsules percentage by 5%, the efficiency was improved by 3% in the case of neat capsules and by 5% in the case of ternary capsules. As was expected, in the case of 25 wt. % the healing efficiency was increased more, i.e., by 8% at specimens with neat capsules and by 13% with ternary capsules. In terms of the knockdown effect, the initial mechanical properties from specimens containing neat capsules were not affected in the case of 15% and 25%. In comparison, at 20%, a negligible knockdown effect was observed. However, in specimens with ternary capsules, the initial mechanical properties improved by 37%, 23% and 18% at 15%, 20%, and 25%, respectively. As explained previously, the improved properties can be attributed to the remaining droplets at the exterior shell wall. Conclusively, the healing efficiency was enhanced by increasing the capsule percentage. At the same time, the initial mechanical properties were not affected in the case of the addition of neat capsules and improved in the case of the modified capsules.

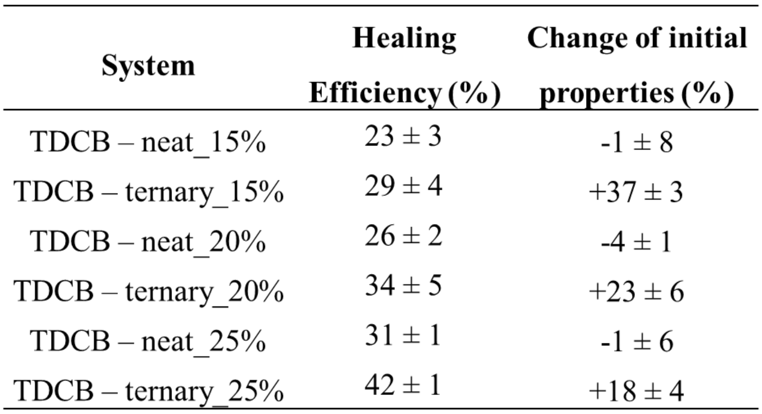

| System | Healing Efficiency (%) | Change of initial properties (%) |
|---|---|---|
| TDCB – neat_15% | 23 ± 3 | -1 ± 8 |
| TDCB – ternary_15% | 29 ± 4 | +37 ± 3 |
| TDCB – neat_20% | 26 ± 2 | -4 ± 1 |
| TDCB – ternary_20% | 34 ± 5 | +23 ± 6 |
| TDCB – neat_25% | 31 ± 1 | -1 ± 6 |
| TDCB – ternary_25% | 42 ± 1 | +18 ± 4 |

**Figure 28.** Healing efficiency and change of initial properties of the self-healing TDCB specimens containing different capsule percentages.

### *3.5.2.3 Different catalyst percentage*

In capsule-based self-healing polymers, the healing process starts when the healing agent comes in contact with the catalyst particles dispersed into the host matrix. The two selected percentages were 2 & 3 wt.% of $Al(OTf)_3$ particles. Different systems with all ternary capsules (with different solvent percentages) were examined. Specimens contained 20 wt.% of capsules, and the healing process was at 80 °C for 24 hours. Healing efficiency increased by 11% at both neat and ternary 35% systems when the catalyst increased from 2 wt. % to 3 wt. %. At ternary 25% and 30% systems, the mechanical properties were restored by 6 and 9%, respectively. Results proved that the viscosity of the healing agent significantly affected the healing efficiency in that case. As the viscosity decreased, the healing agent was not sufficiently delivered into the crack plane resulting in lower efficiencies although the increased catalyst percentage. Initial properties were reduced by about 4-5% in the case of systems with neat capsules, contrary to systems with nanomodified capsules that increased their properties by about 5-10%. Adding 1% more catalyst did not significantly affect the initial properties.

| System | Healing Efficiency with 2% catalyst (%) | Healing Efficiency with 3% catalyst (%) | Change of initial properties with 2% catalyst (%) | Change of initial properties with 3% catalyst (%) |
|---|---|---|---|---|
| TDCB – neat 10% | 26 ± 2 | 37 ± 5 | -4 ± 1 | -5 ± 4 |
| TDCB – ternary 25% | 23 ± 2 | 29 ± 3 | +5 ± 1 | +5 ± 2 |
| TDCB – ternary 30% | 31 ± 6 | 40 ± 2 | +5 ± 3 | +10 ± 6 |
| TDCB – ternary 35% | 34 ± 5 | 45 ± 3 | +7 ± 4 | +5 ± 4 |

**Figure 29.** Healing efficiency and change of initial properties of the self-healing TDCB specimens containing different catalyst percentages.

### *3.5.2.4 Different healing times*

A very important parameter that affects the healing efficiency is the healing process. Usually, healing processes occur at high temperatures for 24 or 48 hours [64,78]. Specimens contained 20 wt.% of capsules and 2 wt.% of catalyst were manufactured for this investigation. Healing efficiency was improved by 21% in the case of neat capsules and about 6% in the case of nano-modified capsules (ternary 35%). The increment in the nanomodified system was lower than that of the neat system due to the nanomodification of the core with MWCNTs. The inclusion of CNTs into the resin improved the thermal conductivity properties, and the polymerization (healing process) was accomplished prior to the 24 as well as the 48 hours.

| System | Healing Efficiency 24h 80°C (%) | Healing Efficiency 48h 80°C (%) |
|---|---|---|
| TDCB – neat 10% | 26 ± 2 | 47 ± 10 |
| TDCB – ternary 35% | 34 ± 5 | 40 ± 4 |

**Figure 30.** Healing efficiency of the self-healing TDCB specimens after different healing times.

## 3.6 Results & Discussion- Case study two

### 3.6.1 Size distribution/ morphology

The successful nanomodification of the healing agent can be easily observed. **Figure 31**a depicts an optical microscopy image from nanomodified microcapsules. As in the first case study, capsules had a rough exterior, too (**Figure 31**b). However, the mean diameter was not affected since the nanomodified capsules presented mean diameter values of 409.07 μm ± 77.30 μm (Fig. 2d). At the same time, the reference (unmodified) microcapsules had a mean diameter of 410.90 μm ± 21.91 μm. In this case, the dilution percentage that affected the capsule size was the same in neat and nanomodified capsules; thus, the average diameter was the same.

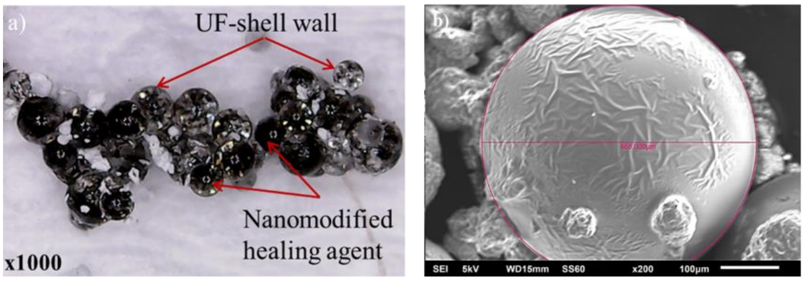

| Capsule batch | Mean size (μm) |
|---|---|
| Neat capsules | 410.9 ± 21.9 |
| Nano-modified capsules | 409.1 ± 77.3 |

**Figure 31.** a) optical microscopy image and b) SEM image from nanomodified capsules & capsule mean size.

### 3.6.2 Thermal stability

Both unmodified and nanomodified capsules manufactured in case study two were examined for thermal stability via thermogravimetric analysis.

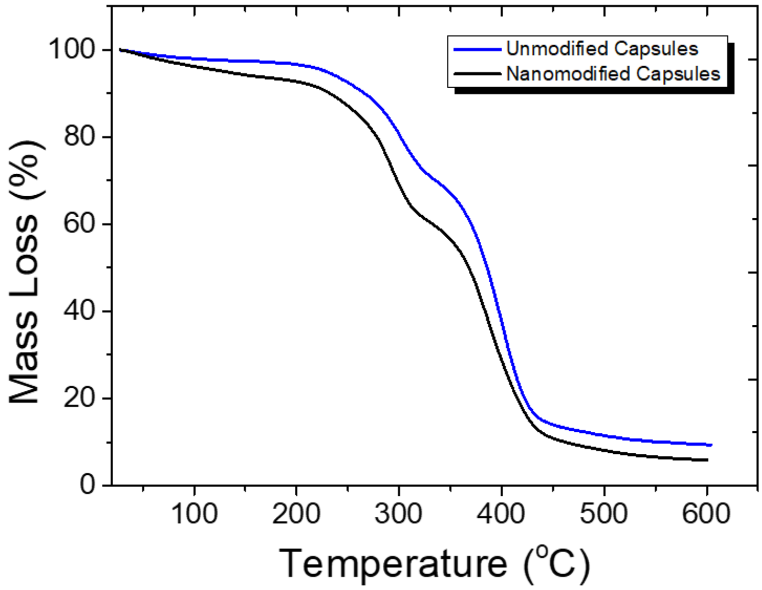

**Figure 32**. Comparison of TGA measurements of the neat capsules with the capsules containing nanomodified healing agent.

As observed (**Figure 32**), the mass loss occurred in two distinct steps. Initially, a small drop on capsules with CNTs was observed due to the evaporation of excess water. The first significant drop can be attributed to the decomposition of the urea-formaldehyde shell wall and the beginning of the evaporation of the solvent [82]. Practically, the temperature where the shell decomposition began ($T_{onset}$) was also the maximum operating temperature of the capsules, 227.3 °C for the reference capsules and 222.2 °C for the capsules containing MWCNTs. The second drop was observed from 360 °C to approximately 440 °C in both cases and was attributed to the homopolymerization of the encapsulated epoxy resin [75]. This mass loss was correlated with the percentage of the encapsulated healing agent (epoxy resin since the solvent has already evaporated). The core content of the neat and the nanomodified capsules was estimated at approximately 53.6 wt. % and 55.1 wt. %, respectively.

### 3.6.3 Confirmation of encapsulation via Raman spectroscopy

The Raman spectra of the epoxy resin, the CNTs, and the CNT modified epoxy resin are depicted in **Figure 33**. These reference spectra were upshifted by 100 a.u. in order to ease the comparison. The spectral window of interest is 1200 -1700 cm$^{-1}$, whereby the most prominent vibrational modes of the CNTs occur. The D or disorder-induced vibrational mode and the G or graphitic band are found in the spectrum of the CNTs at 1345 cm$^{-1}$ and 1575 cm$^{-1}$, respectively [83]. Additionally, the 2D vibrational mode, which is connected with the existence of long-range order in the material, is located at 2687 cm$^{-1}$ [84]. The DGEBA resin did not present any Raman activity in the close vicinity of the D peak, and only a vibrational mode at 1610 cm$^{-1}$, attributed to the C=C symmetric stretching, was observed [85]. Following the dispersion of the CNTs into the epoxy resin, the spectrum of the nanomodified polymer presents contributions from both starting materials. In more detail, most of the vibrational modes in that composite spectrum are due to the epoxy resin, as they were also encountered in the reference spectrum of the DGEBA resin. The CNTs contributed to this composite spectrum by their D and G vibrational modes. These Raman active modes were still visible, even though the CNTs were dispersed only at a small content into the resin. However, the frequency of these modes was slightly blueshifted at 1348 cm$^{-1}$ and 1581 cm$^{-1}$, respectively, compared to the CNT spectrum, as indicated by the black arrows in the spectrum of the nanomodified polymer (DGEBA+CNTs). Other researchers have also reported that the dispersion of MWCNTs in a polymeric matrix results in an upshifting (blueshift) of their vibrational frequencies, indicating less intertube interaction and better dispersion of the MWCNTs in the epoxy medium [86].

On the other hand, the 2D vibrational mode is not clearly distinguished in the spectrum of the nanomodified resin, and this might suggest alterations in the long-range order of the CNTs due to the dispersion process or chemical bonding of the CNTs with the resin, which might also have caused the shift in the D and G vibrational modes. Additionally, concerning the 2687 cm$^{-1}$ Raman vibrational mode that is not visible in the nanomodified resin spectrum, one has to consider that this was the less prominent feature in the CNTs spectrum depicted in Figure 5 (red curve), presenting less than half of the intensity of the other CNTs peaks. The examination of the spectrum of the composite (DGEBA+CNTs) reveals that the D and G vibrational modes, which have a considerable intensity in the CNTs spectrum, are seen as low-intensity bands in that composite spectrum. Therefore, the absence of a clear vibrational mode in the composite spectrum (DGEBA+CNTs) is reasonable.

Subsequently, the spectrum of the nanomodified resin was compared with the spectra of the encapsulated nanomodified resin. For this reason, Raman spectra were acquired both from the microcapsule shell with the laser beam focused on the outer surface and form the core of the same capsule, with the laser beam focused 60 μm away from the outer shell and towards the core (**Figure 33**). As can be seen, there was no noticeable difference between the spectra acquired from the outer surface and the nano-modified resin-filled core of the microcapsules. This result indicated that the Raman activity of the thin transparent capsule shell is negligible compared to the spectral signature of the core.

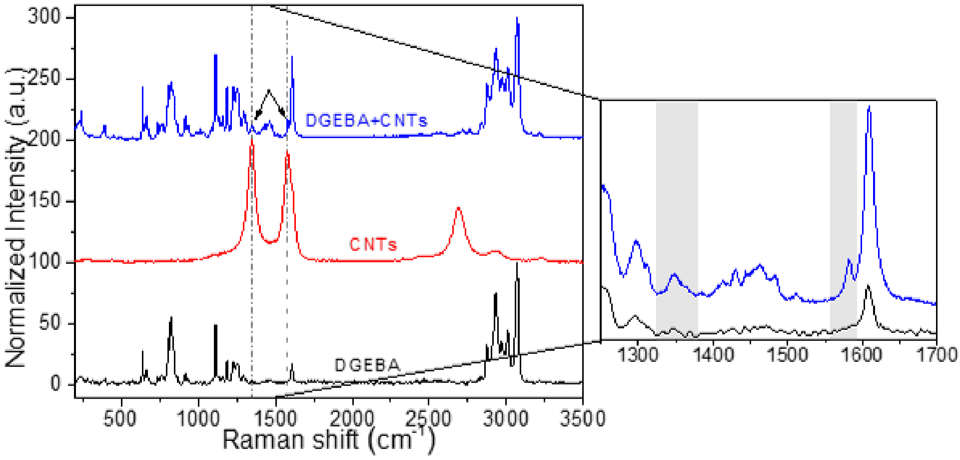

**Figure 33.** Raman spectra of the CNTs and the resin before and after the addition of CNTs (left). The dash-dot vertical lines guide the eye to the vibrational modes of interest, and the black arrows point at the resulting modes in the spectrum of the nano-modified resin. (right) Higher magnification plots focus on D and G vibrational modes in DGEBA (black curve) and DGEBA+CNTs (blue curve).

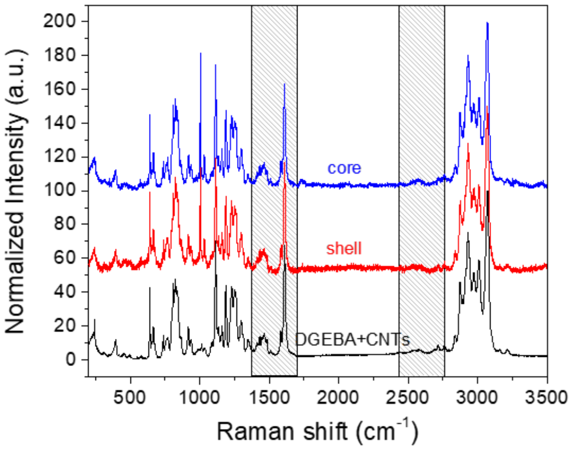

**Figure 34.** Raman spectra collected from the shell (red line) and the core (blue line) of the microcapsules in comparison to the spectrum of the nano-modified epoxy resin (black line). The shaded regions indicate the spectral window of interest for this study.

### 3.6.4 Recovery of the mechanical properties (TDCB geometry)

The fracture toughness of the specimens containing unmodified (neat) capsules was recovered by 70% after the healing process. In comparison, the fracture toughness of the specimens reinforced with the nanomodified microcapsules presented a healing efficiency of 82% (**Figure 35**). As is well known, the fracture toughness of epoxy is inversely proportional to the polymer cross-link density [87]. Therefore, this increase can be attributed to the effect of CNTs on the curing process of epoxy [88]. In addition, the reduction of the initial properties (knockdown effect) was not only eliminated, but the integration of the self-healing system further improved the performance by 22% (**Figure 36**). This behaviour can be associated with the remaining droplets of the nanomodified healing agent attached to the capsules shell wall [80] and enabled a better interlocking between the matrix and the embedded microcapsules.

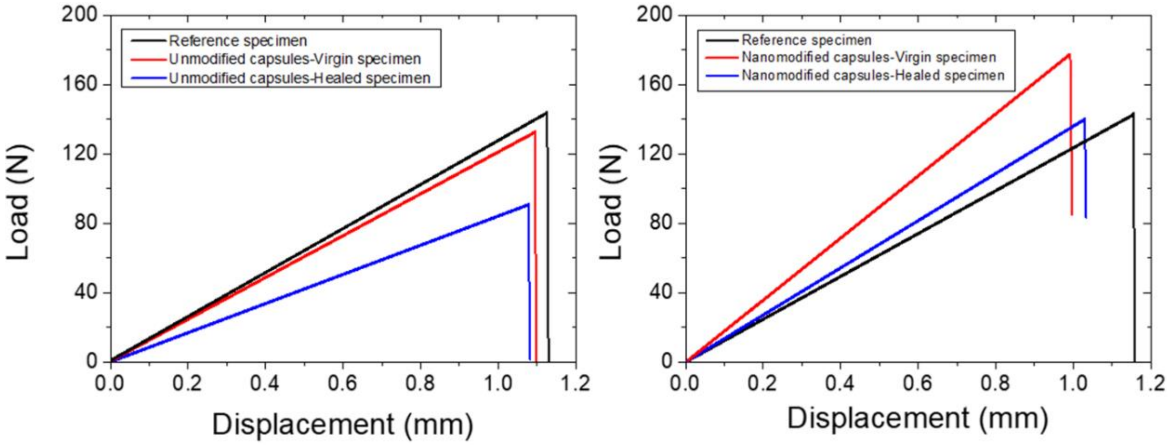

**Figure 35.** Representative load-displacement plots from reference (black line), virgin (red line), and healed (blue line) TDCB specimens with unmodified (left) and nanomodified (right) microcapsules.

| System | Mean Diameter (μm) | Max stress Virgin (MPa) | Max stress Healed (MPa) | Healing Efficiency (%) | Change of initial properties (%) |
|---|---|---|---|---|---|
| Reference | | 232.91 ± 7.33 | | | |
| Unmodified capsules | 205.8 ± 26.3 | 228.08 ± 17.24 | 207.33 ± 39.53 | 90.67 | -2.07 |
| Nanomodified capsules | 167.2 ± 10.2 | 233.68 ± 18.25 | 240.07 ± 32.21 | 107.36 | +0.03 |

**Figure 36.** Healing efficiency and change of initial properties of the self-healing TDCB specimens.

### 3.6.5 Recovery of the electrical properties (TDCB geometry)

IS was utilized to evaluate the restoration of the electrical properties of the TDCB specimens. An initial measurement at virgin specimens was employed before the disruption of the conductive network of the CNTs (mechanical loading), and a second scan at healed specimens was performed after the healing process. Both the first scan on virgin specimens and the second scan on the healed specimens with nanomodified capsules revealed the same electrical behavior. The initial conductivity values slightly changed from $2.48 \times 10^{-5}$ S/m to $2.37 \times 10^{-5}$ S/m, indicating an almost complete restoration of the electrical properties after the healing process. On the contrary, specimens with the unmodified capsules exhibited conductivity values from $2.48 \times 10^{-5}$ S/m to $1.99 \times 10^{-5}$ S/m, indicating a less efficient recovery. Capsules with the nanomodified healing agent led to the restoration of the conductivity by more than 95% in comparison to the neat capsules, which led to a restoration of the conductivity at 83% (**Figure 37**).

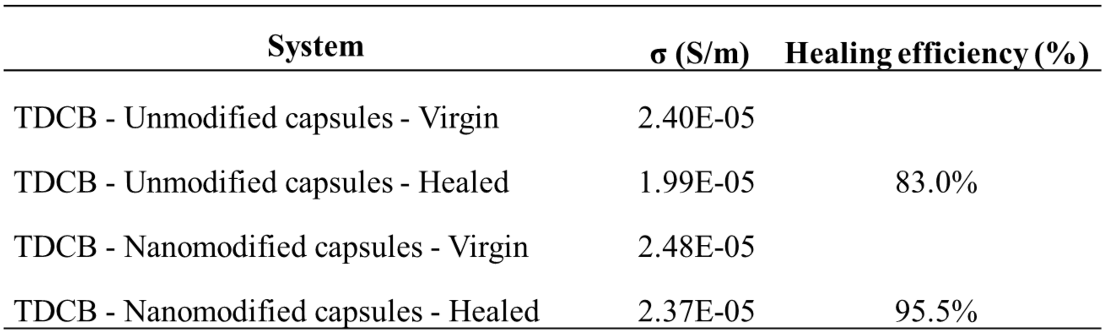

| System | σ (S/m) | Healing efficiency (%) |
|---|---|---|
| TDCB - Unmodified capsules - Virgin | 2.40E-05 | |
| TDCB - Unmodified capsules - Healed | 1.99E-05 | 83.0% |
| TDCB - Nanomodified capsules - Virgin | 2.48E-05 | |
| TDCB - Nanomodified capsules - Healed | 2.37E-05 | 95.5% |

**Figure 37.** Healing efficiency of the TDCB specimens in terms of electrical properties.

### 3.6.6 Recovery of the mechanical properties (SENB geometry)

SENB nanomodified specimens were also mechanically characterized in order to examine the concurrent electrical and mechanical restoration after a total failure of a polymer matrix. **Figure 38** presents representative plots of SENB specimens containing neat and nanomodified capsules. The healing efficiency was evaluated at 46 % in the case of neat capsules. However, as observed (**Figure 39**), specimens with nanomodified capsules exhibited a healing efficiency of 57 % with an increase of 11% compared to the system that contained neat capsules.

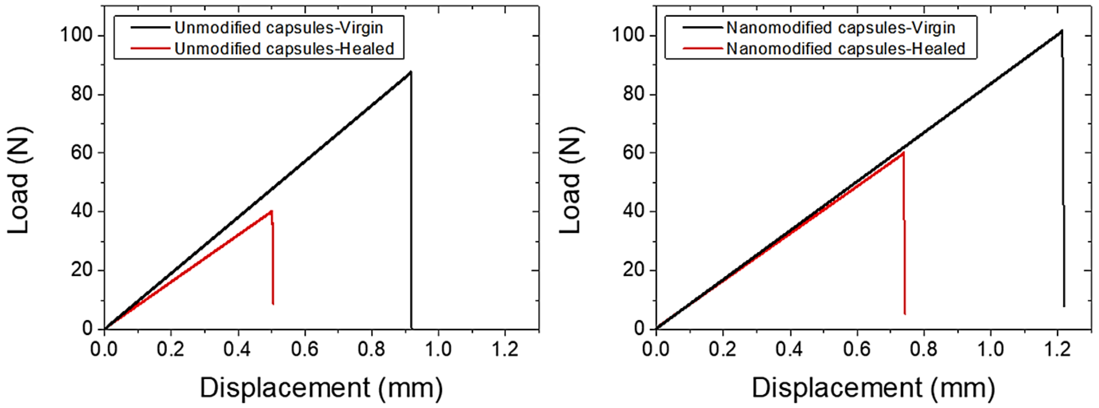

**Figure 38.** Representative load-displacement plots from virgin (black line) & healed (red line) SENB specimens with unmodified (left) and nanomodified (right) microcapsules.

| System | Mean Diameter (μm) | Max Load Virgin (N) | Max Load Healed (N) | Healing Efficiency (%) |
|---|---|---|---|---|
| Unmodified capsules | 410.90 ± 21.91 | 90 | 42 | 46 ± 6 |
| Nanomodified capsules | 409.07 ± 77.30 | 105 | 60 | 57 ± 7 |

**Figure 39.** Healing efficiency and toughness reduction of the SENB specimens.

### 3.6.7 Recovery of the electrical properties (SENB geometry)

As on the TDCB geometry, IS was utilized in order to evaluate the restoration of the electrical properties. In this case, the initial conductivity values at specimens containing conventional capsules significantly decreased after the healing process from 1.98 × 10-5 S/m to 2.06 × 10-6 S/m, indicating no restoration of the electrical properties (**Figure 40**). However, specimens with the nanomodified capsules recovered their conductivity values from 4.99 × $10^{-5}$ S/m to 3.98 × $10^{-5}$ S/m, demonstrating an electrical healing efficiency of almost 80%. Capsules with the nanomodified healing agent on SENB geometry led to the restoration of the conductivity in comparison to the neat capsules that provided no restoration.

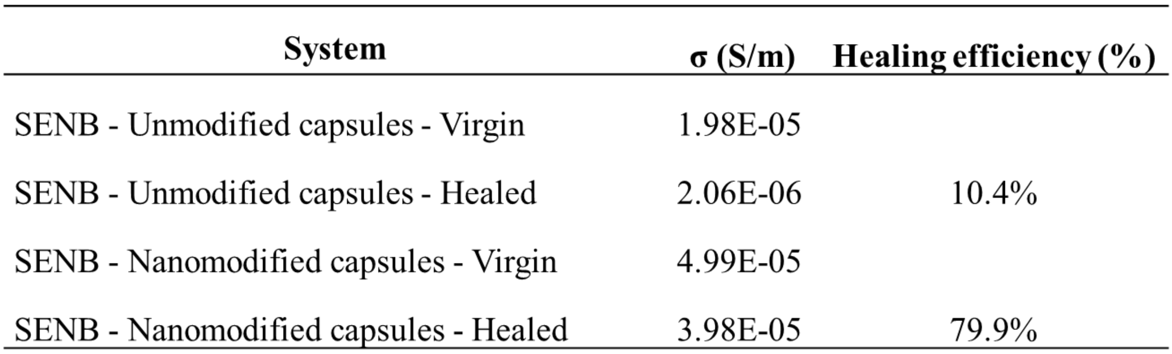

| System | σ (S/m) | Healing efficiency (%) |
|---|---|---|
| SENB - Unmodified capsules - Virgin | 1.98E-05 | |
| SENB - Unmodified capsules - Healed | 2.06E-06 | 10.4% |
| SENB - Nanomodified capsules - Virgin | 4.99E-05 | |
| SENB - Nanomodified capsules - Healed | 3.98E-05 | 79.9% |

**Figure 40.** Healing efficiency of the SENB specimens in terms of electrical properties.

### 3.6.8 Fractography

The fractured surfaces of healed TDCB specimens containing unmodified (**Figure 41**) and nanomodified capsules (**Figure 42**) were examined via SEM fractography. Almost every microcapsule was ruptured by the propagating crack indicating a sufficient interlocking between the host matrix and the capsules' wall. As can be observed, capsules acted as crack deflections or defects inside the material. In the case of the system containing neat capsules, they acted more as defects since there were few crack deviations. However, in the case of the incorporation of nano-modified capsules, there were a significant number of deflections, thus explaining the increased initial mechanical properties of the polymer matrix. As mentioned before, this observation can be related to the remaining droplets of the nanomodified healing agent, which were attached to the capsules shell wall [32] and enabled a better interlocking between the matrix and the microcapsules. Moreover, it is observed that at several locations of the fractured area, the crack path significantly deviates in and out of the fracture plane and branches out of the plane, especially at sites with increased CNT-particle agglomeration.

SEM fractography also confirmed the brittle UF shell wall at both neat and nanomodified capsules (**Figure 41**c & **Figure 42**c). As can be seen from fractured capsules in both cases, the shell wall was brittle, and distinct wall pieces can be observed.

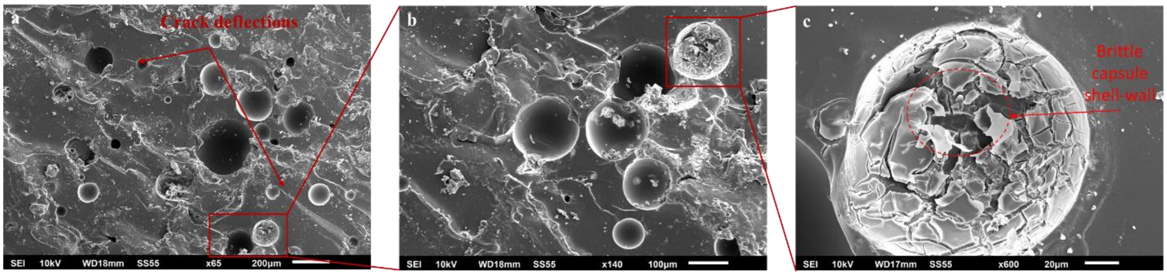

**Figure 41.** Fractured surfaces of a TDCB specimen with embedded unmodified (neat) capsules at three different magnifications, a) x65, b) x140, and c) x600.

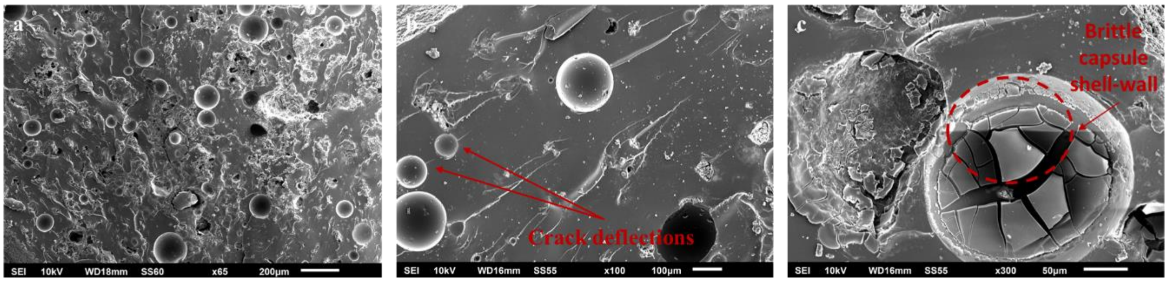

**Figure 42.** Fractured surfaces of a TDCB specimen with embedded nanomodified capsules at three different magnifications, a) x65, b) x100, and c) x300.

## 3.7 Conclusions

### 3.7.1 Case study one

This case study examined the different parameters that affect the self-healing system performance. Healing efficiency was evaluated after the nanomodification of the healing agent using MWCNTs and CB. Poly(urea-formaldehyde) microcapsules filled with the modified healing agent were prepared via in situ microencapsulation oil-in-water emulsion polymerization. The produced capsules were incorporated into the DGEBA polymer matrix in order to assess the healing efficiency of the system at matrix level using TDCB geometry. The specimens were manufactured, changing critical parameters that affect the healing efficiency, such as capsule, solvent, catalyst percentage, and healing time. Obtained results indicated that as the percentage of the solvent increased, healing efficiency was also improved since the healing agent was more sufficiently delivered to the crack area. In the case of capsule percentage, the same trend was observed, i.e., as the capsule percentage increased by 10 wt.

%, the healing efficiency was enhanced by about 13%. The percentage of the incorporated catalyst was also a significant parameter for a successful healing process. By increasing the percentage of the catalyst from 2 wt. % to 3 wt. %, the healing efficiency improved by 11%. Regarding the different healing times studied, results indicated that the healing efficiency of the neat system was improved by 21%. In comparison, the nanomodified systems increased by 6% when the healing process duration expanded by 24 hours.

### 3.7.2 Case study two

In this case study, the conventional self-healing system was transformed into a multi-functional system providing the concurrent restoration of both the mechanical and the electrical properties with in-situ damage and healing process monitoring at polymer matrix level. Microcapsules containing nanomodified healing agent were successfully produced. The stirring rate that affects microcapsule size was 200 rpm, leading to a mean diameter of 409.07 ± 77.30μm. SEM images from microcapsules and SEM fractography from healed and fractured specimens revealed a rough external wall that was successfully formed in order to improve the interlocking between the capsules and the host matrix. Capsules exhibited excellent thermal stability up to 222.2 $^{o}$C, while the amount of the healing agent was indirectly assessed by the TGA measurements to approximately 55.1%. The successful encapsulation of the nanomodified healing agent inside the capsules was confirmed via Raman Spectroscopy. It was generally proved that the nanomodification of the healing agent did not affect the capsule properties, i.e., mean diameter, thermal properties, or even the shell wall.

The self-healing efficiency was evaluated in terms of restoring the mechanical and electrical properties by fracture toughness tests and electrical impedance measurements. TDCB specimens exhibited the concurrent restoration of their mechanical and electrical properties. The healing efficiency for the specimens with unmodified capsules in terms of restoration of the mechanical properties was estimated at 70%, with a reduction of the initial properties by -9% after the self-healing system incorporation. The electrical properties, in this case, were restored by 83%. Conversely, the specimens with nanomodified capsules presented an increase in the initial mechanical properties by about 22% after the self-healing system integration and recovery of fracture toughness by about 82%. In this scenario, the electrical properties were recovered by 95.5%.

SENB geometry was also tested to investigate the mechanical and electrical properties recovery. In terms of mechanical properties, the healing efficiency was evaluated at 46% in the case of neat capsules. In comparison, specimens with nanomodified capsules revealed an increase of 11% the efficiency compared to the neat system. The electrical properties of the polymer matrix

### 3.7.3 Results transferred to chapter six

The most promising results from the experimental campaign of this chapter that was performed in the context of case studies one and two were evaluated and transferred at chapter six to scale up this research to composite level. In detail, from case study one, the capsule & catalyst percentage, the dilution percentage, and the healing time were evaluated. The selected capsule percentage for composites was higher than that studied at 25 wt. % since in order to scale up the technologies at composite level, a sufficient quantity of healing agent will be necessary. The increase of the capsule percentage from 15 to 25 wt. % exhibited an increase of 13% in self-healing efficiency. The percentage of the incorporated catalyst was also a significant parameter for a successful healing process. By increasing the percentage of the catalyst from 2 wt. % to 3 wt. %, the healing efficiency improved by 11%. However, considering the cost of the catalyst ($Al(OTf)_3$ particles), the percentage selected to be used at composite level was 2.5 wt. %. Regarding the different healing times studied, results indicated that the healing efficiency of the neat system was improved by 21%, while the nanomodified systems increased by 6% when the healing process duration expanded by 24 hours. The healing duration chosen for the self-healing composites was 48 hours.

In case study two, the incorporation of a low percentage of CNTs (0.1 wt.%) led to the successful simultaneous recovery of both mechanical and electrical properties. The healing efficiency was increased by 12% when the healing agent was nanomodified. Moreover, the electrical properties were recovered by 95.5%. Observing the above results of both case studies one and two, the CNT's percentage can remain stable at 0.5 wt.%, and since the viscosity was too high and the results with 0.1 wt.% CNTs were sufficient; the CB will be excluded from the nanomodification of the healing agent for the capsules that will be used at the composite and model structure level.

# CHAPTER 4

# Capsule-based self-healing polymers with nanomodified shell-wall

## 4.1 Introduction

One of the most significant characteristics that capsules should have is a shell wall that is strong enough to withstand the incorporation process in the matrix but, at the same time, thin and brittle enough to break in case of a propagating crack for a successful healing process. Several encapsulation methods include centrifugal extrusion, pan coating, spray drying, and emulsion-based methods [14]. The most common synthesis techniques for self-healing applications are the emulsion-based methods, where the shell wall forms at the aqueous/organic interface of the droplets of the chosen healing agent. In this category, emulsification polymerization is the most used method. Another technique that is used commonly is interfacial polymerization in emulsions. Other methods are the layer-by-layer assembly, the coacervation, and the internal phase separation, as illustrated in **Figure 43** [89].

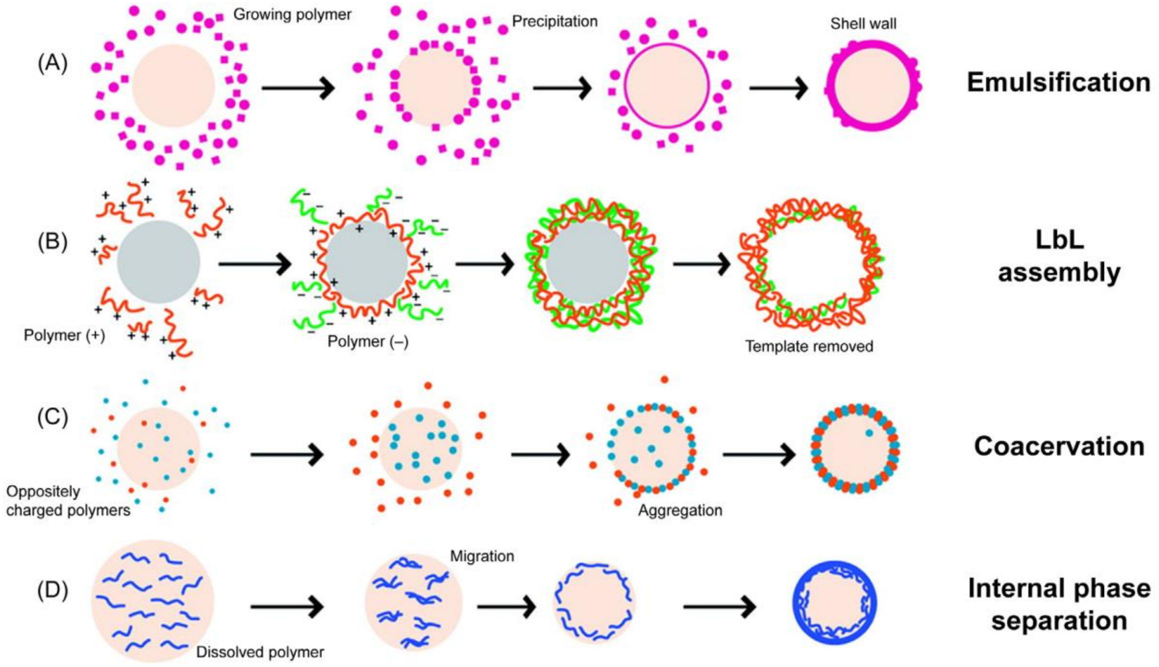

**Figure 43.** Emulsion-based encapsulation methods: (A) in situ emulsification polymerization, (B) layer-by-layer assembly (LbL), (C) coacervation, and (D) internal phase separation. *(Reprinted with permission from A.P. Esser-Kahn, S. A. Odom, N.R. Sottos, S.R. White, J.S. Moore, Triggered release from polymer capsules, Macromolecules 44 (2011) 5539-5553, DOI:10.1021/ma201014n, Copyright (2019), American Chemical Society.)*

One of the most significant criteria in order to choose the encapsulation method is the compatibility and the reactivity of the shell wall with the core materials. The encapsulation of polyamine hardeners was demonstrated by Zhang et al. in order to develop a self-healing epoxy material based on epoxy-amine chemistry [90,91]. A novel synthesis method based on non-equilibrium droplets for the inclusion of polyamine hardeners was presented. They combined the microfluidic T-junction and interfacial polymerization that promptly formed a polymer membrane on the droplet surface by rapid interfacial polymerization. In the final stage, the thickens of the shell wall was increased to achieve high-quality microcapsules. However, this technique was not able to encapsulate high viscosity liquids, and mass capsule production was not achieved. In a step forward, the same authors presented a new method based on the interfacial polymerization combined with electrospraying for the inclusion of the high viscosity F10B, bisphenol F diglycidyl ether (BFDGE) epoxy resin [92]. Capsules characterization exhibited a high impurity, controllable and tunable size, excellent thermal stability and tightness, and a highly effective core fraction (**Figure 45**). Xu et al. produced polyvinyl alcohol/polyurethane/polyurea (PVA/PU/PUA) microcapsules filled with isophorone diisocyanate (IPDI) by interfacial polymerization in an oil-in-water emulsion using different PVA as an emulsifier for self-healing coatings [93]. Capsule size was reduced while the thermal stability increased as the polymerization and alcoholysis degree of PVA increased. The highly crosslinked capsule shell wall offered excellent storage stability and compatibility with the paint of the coating.

Mookhoek et al. demonstrated binary microcapsules containing two distinct liquids manufactured with two different encapsulation techniques to create an autonomous system [94]. UF microcapsules filled with dibutylphthalate (DBP) with an average size of 1.4 μm and a shell wall thickness of 75 nm synthesized by in situ polymerization were used as stabilizers in Pickering emulsions. New, larger capsules were synthesized with a mean diameter of 140 μm and shell wall thickness of 3-9 μm filled with dicyclopentadiene (DCPD) via an isocyanate-alcohol interfacial polymerization. The small capsules (DBP) produced a layer around the core (DCPD) and were polymerized into the shell wall (**Figure 44**). The confirmation of the presence of both capsules was performed via DSC scans with the predicted volume fraction of small capsules of 8.8% to be in agreement with the theoretical calculations.

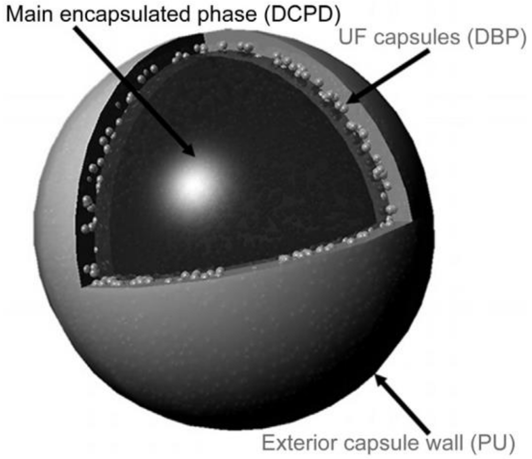

**Figure 44.** The peripherally decorated PU- DCPD capsule with UF-DBP in the shell wall. (Reprinted with permission from S.D. Mookhoek, B.J. Blaiszik, H.R. Fischer, N.R. Sottos, S.R. White, S. Van Der Zwaag, Peripherally decorated binary microcapsules containing two liquids, J. Mater. Chem. 18 (2008) 5390-5394, DOI:10.1039/b810542a, Copyright (2019), Royal Society of Chemistry)

In the emulsification polymerization process, the shell wall is formed at the aqueous/organic interface of the healing agent droplets (oily phase) in an oil-in-water emulsion [79]. The wall must be brittle but thin in order to ensure the capsule fracture in the presence of a propagating crack front. Of primary importance is that the exterior part of the wall is rough to provide better interlocking with the matrix. In this way, a strong capsule–matrix interface allows the crack to propagate through the capsule, thus delivering the healing agent to the damaged area. Some of the wall materials that have been reported are urea-formaldehyde [95], melamine-formaldehyde [96], melamine-urea-formaldehyde [97], polyurethane [98,99] or PMMA [100]. However, double-walled capsules can be produced [72,93,101]. As expected, the mechanical properties of the capsule wall are strongly dependent on its material. Sun and Zhang [102] investigated the mechanical properties of capsules made of three different shell wall materials, melamine-formaldehyde, urea-formaldehyde, and gelatin-gum arabic coacervate. Single microcapsules were tested by a micro-manipulation technique in which they were compressed between two surfaces. MF and UF capsules indicated a viscoelastic behavior with plastic deformation of 19% and 17% and deformation at breakage at 68% and 35%, respectively, while gelatin capsules exhibited an elastic behavior. They did not fail under compression.

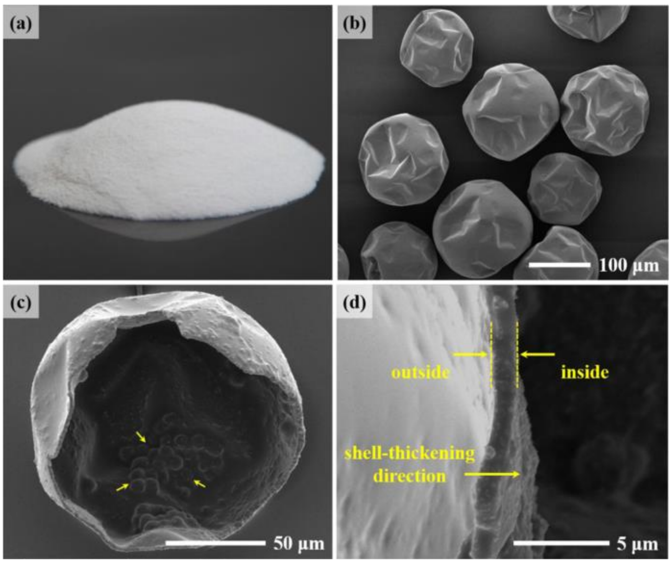

**Figure 45.** (a) Shell wall material, (b-d) SEM images of the fabricated capsules. ("Used with permission of Journal of Material Science & Technology, from Epoxy microcapsules for high-performance self-healing materials using a novel method via integrating electrospraying and interfacial polymerization, H. Zhang, K. Xiao, Z. Lin, and S. Shi, 112, 59-67, (2022); permission conveyed through Copyright Clearance Center, Inc.")

A material that has been shown to satisfy most of the desirable criteria is UF. A UF capsule shell wall provides desirable mechanical properties and easy mass-production via emulsification polymerization. Yuan Li and his team presented different UF microcapsules by changing several parameters during encapsulation, including the surfactant type and concentration, heating rate, and pH value [103]. An improvement in the surface roughness was observed when the surfactant concentration increased. This was also noticed when the pH adjusting time was reduced and the heating rate increased. Capsule size was reduced in the first case, while there was no significant influence in the second case. Among different surfactants, the optimum type was sodium dodecylbenzene sulfonate (SDBS), which also provided excellent solvent resistance, good storage stability, and sufficient mechanical strength. In another interesting study, Katoueizadeh et al. investigated the effect of urea/formaldehyde molar ratio, reaction time, temperature, and pH on the formation of UF microcapsules DDD. The most appropriate properties (formation and morphology of the capsules & thermal stability) were observed at microcapsules produced at a pH value of 3, the temperature at 85 $^{o}$C, a U/F ratio of 2.81, and a reaction time of 4 hours.

In order to improve the capsule shell wall properties or give other functionalities to capsules, modification or coating of the wall can be performed. Fereidoon [104] n and his co-workers investigated the effect of the addition of nanoparticles (single-walled carbon nanotubes or nano-alumina) to a UF shell-wall on the morphology and the thermal properties of the microcapsules. Furthermore, Ghorbanzadeh Ahangari et al. [105] estimated the effect on the micromechanical and surface properties. The results indicated that the nanoparticles imparted thermal stability, water resistance, a small contact angle, and, most significantly, improved stiffness and hardness of the shell wall. In contrast, the surface was smoother, the average size was reduced, and the core content was not affected. Moreover, Jackson et al. developed poly(urea-formaldehyde)-shell microcapsules with a silica coating on the shell wall in order to functionalize and protect submicron and micron size DCPD monomer-filled capsules and the Grubb’s catalyst particles [106]. This coating increased the dispersion efficiency of the capsules and catalyst particles inside the epoxy matrix.

In a recent study, Roche et al. proposed the synthesis of fluorescent core-shell PU/PUF microcapsules by the in-situ polymerization for the development of self-sensing materials [107]. Capsules were introduced in a black epoxy resin and using a conventional 254 nm ultraviolet (UV) lamp, it was possible to identify and detect the microcracks induced. As was expected, capsules had an improved compression load as their size decreased and a rough exterior surface. Also, Matsuda et al. [108] produced microcapsules that are sensitive to pH changes. Cerium nitrate-containing pH-MC (Ce-MC) for corrosion inhibition and aluminum nitrate-containing pH-MC (Al-MC) microcapsules were produced by water-in-oil emulsion polymerization. These capsules were coated with metal substrates and placed in corrosive (acidic or alkaline) environments. Al-MCs were found sensitive to acidic and basic environments while were inactive in neutral environments. The Ce-MC capsules were proved to inhibit corrosion through open circuit potential measurements.

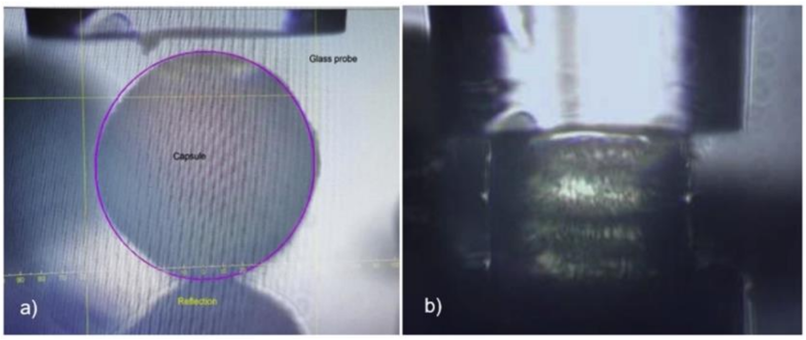

**Figure 46.** (a) Single PU/PUF capsule before compression testing and (b) Capsule during compression. (Original source: S. Roche, G. Ibarz, C. Crespo, A. Chiminelli, A. Araujo, R. Santos, Z. Zhang, X. Li, and H. Dong, Self-sensing polymeric materials based on fluorescent microcapsules for the detection of microcracks, Journal of Materials Research and Technology, 16, 505-515, 2022)

## 4.2 Scope

This chapter includes the encapsulation of a healing agent into a nanomodified UF polymeric shell wall with different percentages of MWCNTs for the first time. Three different percentages (0.3% w/v, 0.5% w/v, and 1.0% w/v) of MWCTNs were dispersed into the EMA solution that exists in the interior shell wall. The effect of the nanomodification was investigated in terms of capsule properties (mean size and thermal properties) and healing efficiency (fracture toughness tests- TDCB geometry). The electrical properties were evaluated after incorporating the modified microcapsules into an epoxy matrix. Since after the breakage of microcapsules, the shell wall is destroyed, the restoration of the electrical properties was not studied. As in chapter three, the most sufficient results from this experimental campaign were transferred in Chapter 6 to manufacture and identify the smart & multifunctional composites.

## 4.3 Experimental

### 4.3.1 Materials

The two main materials of the shell wall were urea ($NH_2CONH_2$) and formalin (37 wt. % formaldehyde in water). As surfactant, the poly(ethylene-maleic-anhydride) (EMA, $M_w$ = 100,000–500,000 g/mol) copolymer powder was used. Ammonium chloride ($NH_4Cl$) and resorcinol ($C_6H_4$-1,3-$(OH)_2$) were used as stabilizers supplied by Sigma-Aldrich company. The diglycidyl ether of bisphenol-A (DGEBA, Epikote 828 lvel) epoxy resin was chosen as a healing agent. The same epoxy resin (Epikote 828) with the Epikure 541 hardener at a ratio of 100:50 % wt., supplied from Dichem Polymers, Greece, was selected as the matrix phase. The nanomodification of the epoxy was performed using the Graphistrength C-100 MWCNTs from ARKEMA, France, as in previous chapters. The viscosity of the healing agent was tuned using the non-toxic solvent ethyl phenylacetate (EPA) from Sigma-Aldrich. The catalyst for the healing process was the Aluminium (III) triflate ($Al(OTf)_3$) supplied from Sigma-Aldrich, too.

### 4.3.2 Nanomodification of the shell-wall

The UF shell-wall was modified to improve the electrical properties of the wall compared to the conventional microcapsules and the electrical properties of the polymer matrix. The nanomodification was performed at the surfactant solution (EMA). The EMA polymer creates a thin polymeric “membrane” at the aqueous/organic interface of the resin droplet and creates the shell wall [79]. A 2.5% w/v aqueous solution was prepared by adding 2.5 g EMA powder with 100 ml of deionized water in a beaker and mixed overnight in a warm bath. MWCNTs were dispersed at the surfactant at 3 different percentages (0.3% w/v, 0.5% w/v, and 1% w/v) by sonication using a UP400S by Hielscher SA, Germany. The amplitude was at 0.3 and the pulse at 0.5. The sonication duration was 90 min, while every 30 minutes, the process was paused, and the mixture was magnetically stirred for 5 minutes. At the end of the process, the solution was filtrated to remove the agglomerations of CNTs that were not distributed to the surfactant.

### 4.3.3 Encapsulation Process

The encapsulation process that followed was the same as previous, differentiating that the EMA solution was nanomodified and the core was neat epoxy DGEBA resin diluted at 5 wt. %. The reaction was left to proceed for 2 hours. After the encapsulation process, the mixture was cooled down to room temperature, the suspended microcapsules were rinsed with ethanol using a Buchner filter and finally were left to dry. Hereafter, the produced capsules will be referred to as “neat capsules” for the unmodified (neat) capsules and “0.3% capsules”, “0.5% capsules”, and “1% capsules” for the capsules with a nanomodified wall containing 0.3% w/v, 0.5% w/v, and 1% w/v CNTs, respectively.

### 4.3.4 Manufacturing of the Self-Healing Specimens

Healing efficiency was evaluated in fracture toughness at polymer matrix level using modified tapered double cantilever beam geometry as in chapter 3. The two-part nanomodified with 0.3 wt. % MWCNT epoxy system (Epikote 828-Epikure 541) was used as a matrix phase at a 100:50 ratio. The microcapsules and the catalyst were dispersed at 20 wt. % and 1.5 wt. % in the matrix, respectively. At the end of this process, the mixture was placed in a vacuum laboratory oven for degassing for 2 min and cast in silicone molds. The curing process took place at room temperature for 24 h. In order to estimate the effect of the incorporation of the self-healing system on the initial mechanical properties, specimens without capsules and catalyst were manufactured as “reference” samples. Hereafter, TDCB specimens with neat capsules will be referred to as “neat system,” and specimens with 0.3%, 0.5%, and 1% capsules will be called “0.3% system”, “0.5% system”, and “1% system”, respectively. All specimens were pre-cracked using a fresh razor blade and tested (virgin specimens) using the mini tensile testing frame manufactured by Fullam Inc. USA, with a 1 mm/min displacement rate. The healing process took place at 60 $^{o}$C for 24 hours in a laboratory oven. The specimens were retested after healing using the same experimental conditions (healed specimens). The change of the initial mechanical properties after the self-healing system incorporation and the healing efficiency were evaluated using the same equations (1 and 2) as previously in Chapter 3.

### 4.3.5 Manufacturing of the specimens for electrical conductivity measurements

Impedance spectroscopy was employed to investigate the effect of the introduction of the microcapsules in the nano-enhanced matrix. The 0.3 wt. % MWCNTs were dispersed in the DGEBA epoxy resin. The percolation threshold was reached at 0.5 wt. % MWCNTs. In this study, a 0.3 wt. % CNT loading was selected to investigate the effect of introducing different capsules on the electrical properties. This percentage was chosen as it is close to the aforementioned percolation threshold. The dispersion process lasted 3 hours in the dissolver at 3000 rpm and at room temperature. Microcapsules were introduced into the nanomodified resin, and the system was mixed with Epikure 541 hardener in a 100:50 ratio. The mixture was cast in silicon rubber molds. The specimens for electrical characterization had dimensions of 52 × 12 × 3 $mm^3$.

## 4.4 Characterisation techniques & equipment

### 4.4.1 Scanning Electron Microscopy (SEM)

The mean diameter of 100 individual capsules was evaluated via SEM images. The morphological characterization was performed using the same electron microscope as previously. The microcapsules were also gold/platinum sputter coated to avoid decomposition due to the high applied voltage.

### 4.4.2 Thermogravimetric Analysis (TGA)

The thermal stability of the microcapsules was examined via thermogravimetric analysis (TGA). The scans were performed between 25 $^oC$ and 700 $^oC$, with a heating rate of 10 $^oC$/min, under an Ar atmosphere. The mass of each sample was 3.8 mg, and the gas flow at 60 mL/min. The measurements were performed using a PerkinElmer Pyris Diamond TG/DTA instrument.

### 4.4.3 Electrical properties of the polymer matrix

The advanced dielectric thermal analysis system (DETA-SCOPE), supplied by ADVISE Greece, was performed for the conductivity measurements as previously. The specimens were placed inside a capacitor consisting of two copper plates with dimensions of 52 × 12 $mm^2$. All measurements were performed under a stable temperature of 25 $^oC$. The electrical properties of the polymer matrix were evaluated from the DC conductivity values of the specimens at 0.01 Hz.

## 4.5 Results

### 4.5.1 Size Distribution/SEM Images

**Figure 47** illustrates the SEM images from the neat capsules and the modified CNTs. As observed, the shell wall in the case of the unmodified capsules was smooth. This is due to the lower duration of the encapsulation process since the desired roughness of the wall is observed after the second hour of the polymerization time [109]. The shell wall was rough and thicker for modified capsules due to the incorporation of CNTs. Results indicated that the mean size decreased after the addition of the CNTs in the shell wall (**Figure 48**). As observed in the literature [110,111], smaller microcapsules were produced after the incorporation of nanoparticles due to the reduced number of collisions between the smaller droplets.

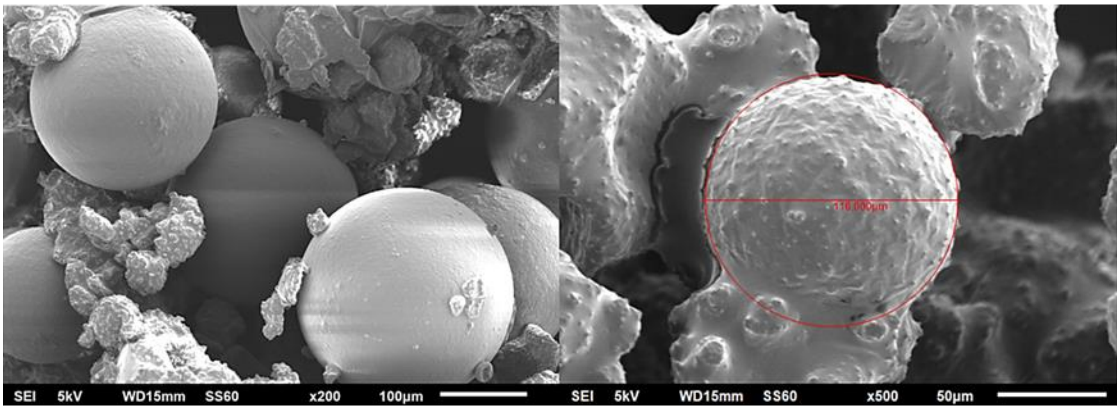

**Figure 47.** SEM images from a) unmodified (neat) capsules and b) capsules with nanomodified shell-wall at 0.5 % w/v.

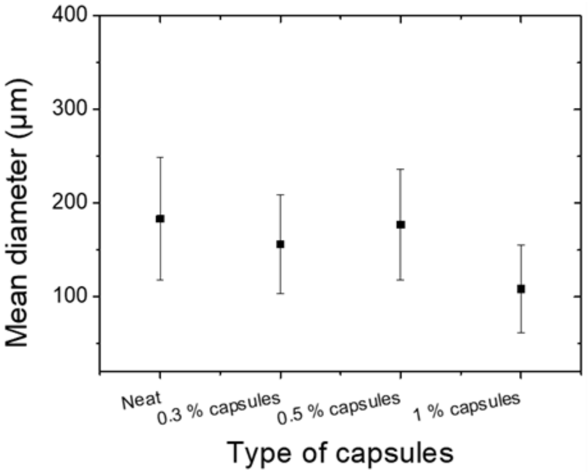

| Type of capsules | Mean diameter (μm) |
|---|---|
| Neat | 182.95 ± 65.57 |
| 0.3 % capsules | 155.79 ± 52.54 |
| 0.5 % capsules | 146.86 ± 59.08 |
| 1 % capsules | 108.27 ± 47.12 |

**Figure 48.** Mean diameter of the different capsule types that were produced.

## 4.5.2 Thermal properties of the microcapsules

The thermal stability of the microcapsules was investigated via thermogravimetric analysis upon heating from 25 ºC to 700 ºC. Capsules were allowed to dry at 60ºC for 2 hours before the scans to remove any residual water. The mass loss was exhibited in two main steps for all capsule batches. More specifically, the first step of the mass loss was observed at a temperature range from ca. 250 ºC to 360 ºC for the neat capsules, while for 0.3 %, 0.5 %, and 1 % capsules, at 264 ºC to 330 ºC, 240 ºC to 340 ºC, 240 ºC to 330 ºC, respectively. This first mass loss was related to the thermal decomposition of the poly(UF) shell wall material and the starting point of the evaporation of the EPA solvent. The above-measured values of minimum temperature for each range define the maximum temperatures at that capsules can be used ($T_{onset}$). The second step was observed at a temperature range from ca. 360 ºC to 440 ºC for the neat capsules and from ca. 340 ºC to 440 ºC, 370 ºC to 440 ºC, 350 ºC to 420 ºC for the 0.3 %, 0.5 %, and 1 % capsules, respectively. The second mass loss step was assigned to the homopolymerization of the encapsulated resin. The obtained results revealed that the capsules remained thermally stable at high temperatures (approximately up to 230 ºC), and the addition of the CNTs did not affect their thermal properties.

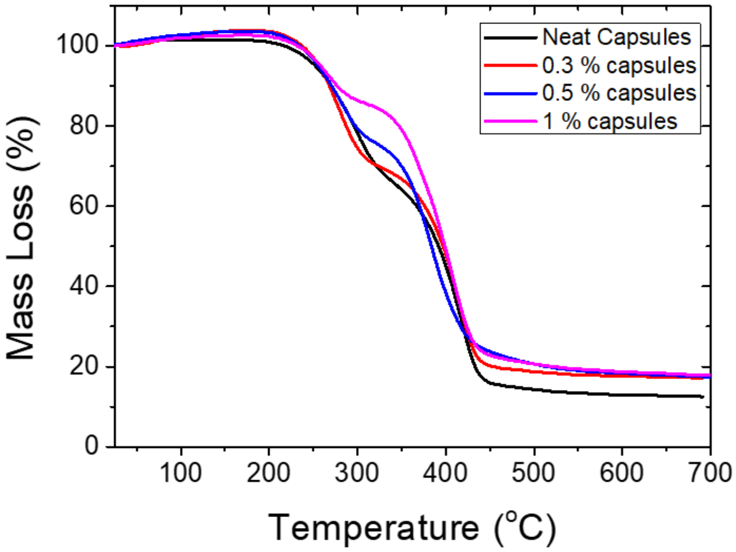

**Figure 49.** TGA measurements of neat capsules (black line), 0.3 % capsules (red line), 0.5 % capsules (blue line) and 1 % capsules (purple line).

### 4.5.3 Recovery of the fracture toughness

The healing efficiency was evaluated in terms of fracture toughness. TDCB specimens with neat microcapsules (neat system) exhibited a healing efficiency of about 48%, while 0.3 % system and 0.5% system provided the same values (47%). However, in the 1 % system, the healing efficiency was significantly reduced and revealed values of about 27%. This can be attributed to the increased strength of the UF shell wall due to the incorporation of a greater quantity of CNTs. As is well-known, the incorporation of CNTs enhances both the mechanical and electrical properties in polymeric materials [50,74,112–114] making the rupture of the shell wall more difficult.

The effect on the initial mechanical properties of the epoxy matrix after the introduction of the self-healing system was also evaluated. A substantial decrease of ca. -25% in the peak load was observed at neat systems. Capsules were easily detached from the matrix due to their smooth external surface, which led to the fracture toughness deterioration and this significant decrease. This was not observed in the case when 0.3 % CNTs were introduced in the capsules shell wall, where the reduction in strength was ca. -13 %. This was attributed to the fact that the incorporation of CNTs into the polymer shell wall improved the interlocking with matrix due to the increased roughness of the exterior wall, as shown in **Figure 47**. Additionally, for the 0.5% system, the mechanical properties increased after the incorporation of the self-healing agent by ca. +26%. As the percentage of the CNTs increased, the mechanical strength of the shell wall also increased, which subsequently led to increased properties. This was also observed in the case of the 1 % system. However, since the healing efficiency was decreased in this case, this system was not identical. The most optimal choice seems to be the 0.5 % system since it has increased initial mechanical properties and similar healing efficiency to the neat system.

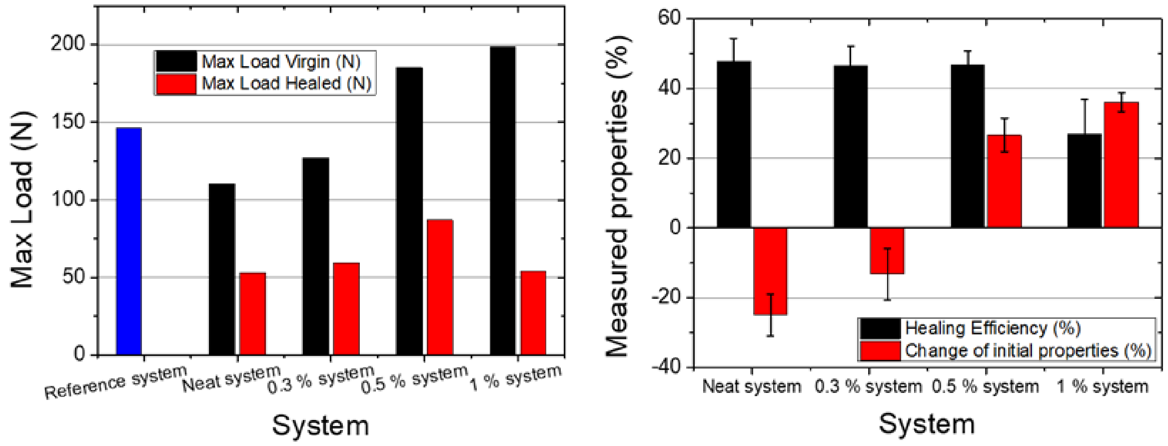

**Figure 50.** Bar charts of maximum load of virgin & healed specimens (left), healing efficiency and change of initial properties (right) of all capsule systems.

| System | Mean Diameter (μm) | Healing Efficiency (%) | Change of initial properties (%) |
|---|---|---|---|
| Neat system | 182.95 ± 65.57 | 48 ± 6 | -25 ± 6 |
| 0.3 % system | 155.79 ± 52.54 | 47 ± 5 | -13 ± 7 |
| 0.5 % system | 146.86 ± 59.08 | 47 ± 4 | +27 ± 5 |
| 1 % system | 108.27 ± 47.12 | 27 ± 9 | +36 ± 3 |

**Figure 51.** Healing efficiency and change of initial mechanical properties of all capsule systems.

### 4.5.4 Effect of the addition of the capsules to the electrical properties of the polymer matrix

The effect of the incorporation of neat and nanomodified microcapsules in the nano-enhanced polymer matrix was evaluated via conductivity measurements. The types of specimens that were measured were: (i) reference specimens (without microcapsules) and specimens with incorporated (ii) neat capsules, (iii) 0.3 % capsules, (iv) 0.5 % capsules, and (v) 1 % capsules.

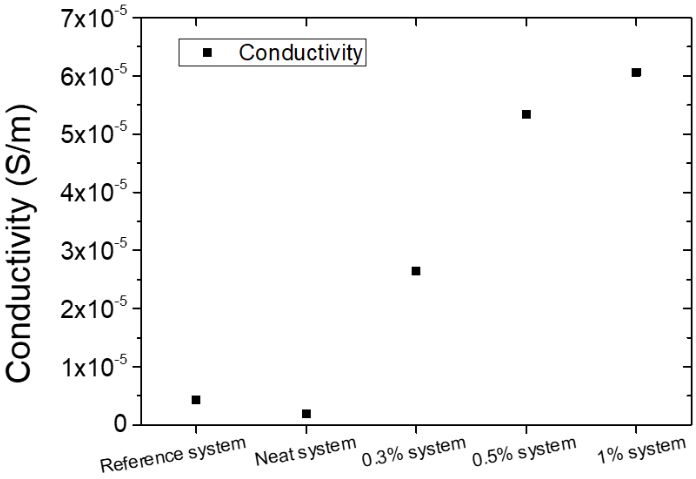

| System | σ (S/m) |
|---|---|
| Reference matrix | 4.34E-06 |
| Neat system | 1.88E-06 |
| 0.3% system | 2.65E-05 |
| 0.5% system | 5.34E-05 |
| 1% system | 6.06E-05 |

**Figure 52.** Conductivity measurements of the reference, neat, 0.3%, 0.5% and 1% system.

Reference specimens (without capsules) revealed a conductivity of 4.34 × $10^{-6}$ S/m. A decrease of the conductivity to 1.88 × 10-6 S/m was observed when incorporating neat capsules. This indicated that the inclusion of neat microcapsules reduced the electrical conductivity of the matrix by interfering with the semi-conductive CNTs network. More specifically, the conductivity decreased due to the reduction of the conductive paths in the CNT network, as the non-conductive microcapsules acted as current barriers inside the nanocomposite. However, the nanomodification of the shell wall improved the electrical properties by one order of magnitude. Specifically, capsules with 0.3 % w/v CNTs at their shell wall increased the electrical conductivity to 2.65 × $10^{-5}$ S/m after incorporation into the matrix. Further increase of the CNTs loading in the shell wall led to even more conductive systems. The inclusion of 0.5 % capsules exhibited a more conductive behaviour, while the most conductive system was observed when 1.0 % capsules were introduced. The values obtained were 5.34 × $10^{-5}$ S/m and 6.06 × $10^{-5}$ S/m for 0.5 % system and 1 % system, respectively. The conductivity values of these specimens reached the values of the percolated system (at 0.5 wt. % CNTs) as measured in chapter one.

## 4.6 Conclusions

In this chapter, electrically conductive microcapsules were produced via the incorporation of MWCTNs into the polymeric urea-formaldehyde shell-wall. The effect of the nanomodification of the capsule shell on both healing efficiency and electrical properties of the polymer matrix was evaluated. Neat (commercial) capsules and capsules with three different percentages (0.3 % w/v, 0.5 % w/v & 1 % w/v) of carbon nanotubes at their wall were manufactured. The mean diameter of the capsules was found to decrease as the nanofillers percentage increased. However, the roughness of the exterior wall was substantially improved, resulting in better interlocking between capsules and matrix and elimination of the knockdown effect. The modification did not alter the thermal stability of the polymeric shell.

Microcapsules were incorporated into a nanomodified DGEBA polymer matrix to evaluate the effect of the modification of the wall on the healing efficiency and the knockdown effect. TDCB fracture toughness tests of nano-modified resin with capsules of increasing the percentage of CNTs also exhibited an improvement in the initial mechanical properties. In detail, the incorporation of neat capsules into the matrix showed a reduction of the mechanical properties by about -25% compared to the neat matrix. In contrast, the incorporation of 1 % capsules led to an increase of 36% in fracture toughness. The healing efficiency was measured at ca. 47% and did not change with the introduction of 0.3 % and 0.5 % capsules. However, in the case of 1 % capsules, it decreased ca. 20%. This can be attributed to the limited capsule breakage as the addition of CNTs into the capsule wall significantly increased the mechanical strength of the wall, and capsules did not break.

The effect of the modification of capsules shell wall after their incorporation into a modified polymer matrix was measured in terms of electrical conductivity properties. The polymer matrix was modified with 0.3 wt. % MWCNTs. As aforementioned, this CNT loading is below the percolation threshold. However, the addition of modified capsules resulted in an increase in the conductivity values indicating that the percolation was achieved via the combined CNT and microcapsule loading.

# CHAPTER 5

# Electrical properties of the polymer matrix after the incorporation of different capsule types

## 5.1 Introduction

Incorporating capsules into polymer matrices is the first step in assessing the healing efficiency of capsule-based self-healing materials. Thermoset matrices like epoxy [115], polyurethane [116], cyanate ester [117], or even thermoplastic matrices [118] were chosen for the integration of the capsule-based healing systems depending on the final application. The inclusion of capsules into the polymer matrices is mainly achieved through dispersion processes where the capsule shell shall be strong enough to sustain the stirring forces. Then these capsule-modified polymers can be further used as coatings [119] or as a matrix in composites [120]. However, the incorporation of capsules into the matrix may affect the electrical properties.

Wang et al. studied the effect of capsule doping on the electrical properties of polyethylene insulating matrix [121]. UF/DCPD microcapsules were synthesized by a two-step in situ polymerization process. They evaluated the volumetric resistivity and the dielectric properties by changing the impurity and the interface of the microcapsule. When introducing microcapsules into the matrix, all values were increased; thus, the electrical performance of the polyethylene was also improved. Recently, in a similar study, Khan et al. investigated the effect of the addition of various microcapsule loadings on the dielectric performance of self-healing epoxies [122]. Different concentrations of 0, 5, 10, and 15 wt. % of UF capsules containing DCPD were incorporated into a DGEBA epoxy matrix. The dielectric permittivity, dielectric loss, volume, and surface resistivity were measured five times in order to accurate the results. Results proved that the dielectric permittivity and loss increased with increasing capsule loading due to the increased number of interfaces and the weak interaction zone between capsules and matrix. The DC volume/surface resistivity results indicated that the values were altered after the incorporation of capsules. Although, at a high percentage remained stable since the interaction zones were overlapped and formed a channel encouraging charge migrations.

As mentioned above, polymers are insulators, although, after the dispersion of conductive fillers, they can be conductive. The conductive network created in the matrix can enable the sensing ability via electrical methods. In order to move forward and manufacture a multifunctional composite with self-sensing and self-healing properties, the incorporation of microcapsules inside the material must not affect the conductivity of the matrix. One solution is the nanomodification of microcapsules with conductive fillers such are the CNTs.

The encapsulation of nano-modified epoxy resin could also slightly influence the exterior wall. Poly(methyl methacrylate) (PMMA) capsules were manufactured by Icduygu et al. containing epoxy resin modified with 2 wt.% MWCNTs [121]. As revealed by SEM images, microcapsules with nanomodified core exhibited a rougher surface. The presence of nanotubes at the surface and a more brittle shell wall were depicted. To better understand the morphology of these capsules, the same authors performed a three-dimensional nanomorphology investigation of PMMA capsules containing nano-modified epoxy resin [123]. The novel laser scanning confocal microscopy (LSCM) was utilized as a nondestructive evaluation technique for the 3D capsule imaging and revealed information about their morphology (**Figure 53**). TGA results proved that the amount of encapsulated agent was not influenced. At the same time, the stirring rate and the content of the CNTs affected the capsules surface, which was smooth with a variety of core-shell morphologies. With increasing mixing rate and CNT content, the surface roughness was improved due to the CNTs clustering at the exterior of the shell wall.

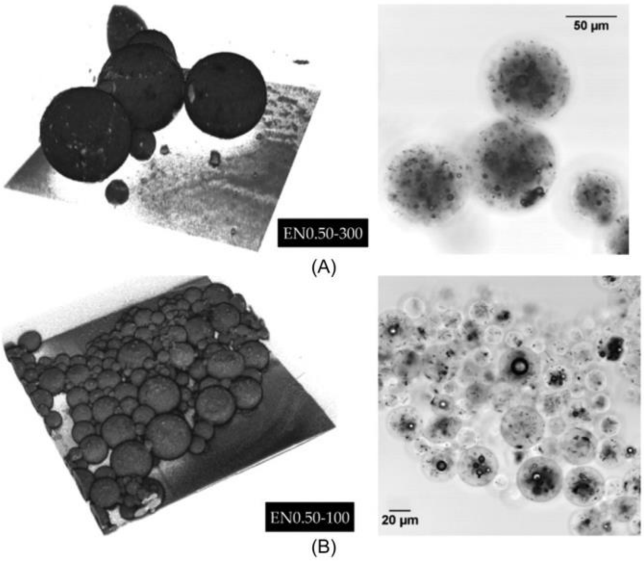

**Figure 53.** (A) 3D LSCM imaging of microcapsules containing the nanomodified healing agent (A) Capsules produced at 300 rpm, (B) Capsules produced at 1000 rpm. *(Reprinted from M.G. Icduygu, M. Asilturk, M.A. Yalcinkaya, Y.K. Hamidi, M.C. Altan, Three-dimensional nano-morphology of carbon nanotube/epoxy filled poly(methyl methacrylate) microcapsules, Materials (Basel), 12 (2019) 26, DOI:10.3390/ma12091387, under a Creative Commons license, Copyright (2019), Materials.)*

In another study, Yashchenok et al. presented the addition of SWCNTs modified by anionic polyelectrolyte molecules into the shell of polyelectrolyte multilayer microcapsules manufactured by layer-by-layer technique [124]. The shell wall was mechanically enhanced as well as the electrical properties improved. The CNTs possess broad absorption in the IR and visible range. This capability is used for the remote activation and opening of the shell by lasers working at 473 nm and 830 nm.

In a novel approach, Lanzara et al. proposed the use of CNTs as a nano reservoir for automated self-healing materials [125]. This approach reduced the voids that can be induced with the incorporation of capsules as well as can enhance the matrix toughness and conductivity. They analyzed the molecular dynamics of a fluid that simulates an organic healing agent that can flow out of a damaged SWCNT. Results indicated that the organic molecules could escape out of the CNT, but the number of molecules depended on the size of the damage to the CNT wall. This study proved that CNTs could be potentially used in the next generation of self-healing materials.

## 5.2 Scope

The scope of this chapter was to investigate the effect of the addition of different types and sizes of capsules into a nanomodified polymer matrix on the percolation threshold as well as the conductivity of the matrix. As it is well-known, epoxy matrices are insulators as all polymeric materials. An approach for improving the conductivity of an epoxy matrix is the dispersion of MWCNTs using high shear force mixing, as in chapter two. The dispersion protocol of the second chapter was used for this purpose. The selected systems were the 0.3 wt. % and 0.5 wt. % of MWCNTs. The first percentage exhibited conductivity values under but near the percolation threshold that reached at the second percentage (0.5 wt. %).

Four different sets of microcapsules were produced and incorporated into the two nanomodified matrices. Capsules were produced at five different sizes according to previous research [76]. The first set included neat (conventional) urea-formaldehyde microcapsules containing the DGEBA epoxy resin as a healing agent. For the second set, capsules with a nanomodified healing agent with 0.5 wt. % MWCNTs dispersed were manufactured, as shown the most valuable results from chapter two. The third set included nanomodified shell-walled microcapsules with 0.5 % w/v MWCNTs that exhibited the most sufficient resulted percentage from chapter three. The final set consisted of capsules with both a nano-modified shell-wall and a nanomodified healing agent. This type of capsule was synthesized for the first time.

## 5.3 Experimental

### 5.3.1 Materials

The two main materials of the shell wall were urea ($NH_2CONH_2$) and formalin (37 wt. % formaldehyde in water), as previously. As surfactant, the poly(ethylene-maleic-anhydride) (EMA, $M_w$ = 100,000–500,000 g/mol) copolymer powder was used. Ammonium chloride ($NH_4Cl$) and resorcinol ($C_6H_4$-1,3-$(OH)_2$) were used as stabilizers supplied by Sigma-Aldrich company. The diglycidyl ether of bisphenol-A (DGEBA, Epikote 828 lvel) epoxy resin was chosen as a healing agent. The same epoxy resin (Epikote 828) with the Epikure 541 hardener at a ratio of 100:50 % wt., supplied from Dichem Polymers, Greece, was selected as the matrix phase. The nanomodification of the epoxy was performed using the Graphistrength C-100 MWCNTs from ARKEMA, France, as in previous chapters. The viscosity of the healing agent was tuned using the non-toxic solvent ethyl phenylacetate (EPA) from Sigma-Aldrich. The catalyst for the healing process was the Aluminium (III) triflate ($Al(OTf)_3$) supplied from Sigma-Aldrich, too.

### 5.3.2 Nanomodification of the shell-wall or/and core

The UF shell-wall was performed at the surfactant solution (EMA) as previously. A 2.5% w/v aqueous solution was prepared by adding 2.5 g EMA powder with 100 ml of deionized water in a beaker and mixed overnight in a warm bath. MWCNTs were dispersed at the surfactant at 0.5% w/v by sonication using a UP400S by Hielscher SA, Germany. The selected percentage has resulted from chapter 4 as the most sufficient. The amplitude was at 0.3 and the pulse at 0.5. The sonication duration was 90 min, while every 30 minutes, the process was paused, and the mixture was magnetically stirred for 5 minutes. At the end of the process, the solution was filtrated to remove the agglomerations of the CNTs that were not distributed to the surfactant.

As resulted from chapter 3, 0.5 wt. % MWCNTs were dispersed within the healing agent (epoxy resin- DGEBA Epikote 828) using a high shear mixer (Dispermat AE, VMA-GETZMANN DMBH, Germany). The dispersion protocol involved continuous agitation at 25 $^{o}$C under vacuum. According to the protocol, the agitation rate was set at 3000 rpm, and the duration was 3 hours[74].

### 5.3.3 Encapsulation Process

The encapsulation process followed was the same as in previous chapters 3 & 4. The dilution percentage was 10 %, while the reaction was left to proceed for 4 hours. After the encapsulation process, the mixture was cooled down to room temperature, and the suspended microcapsules were rinsed with ethanol using a Buchner filter. Capsules were left to dry in a laboratory oven under ambient conditions.

Hereafter, the produced capsules will be referred to as “neat” for the unmodified (neat) capsules, “nano-core” for capsules containing nanomodified healing agent, “nano-wall” for capsules with nanomodified shell-wall, and “nano-all” containing both nanomodified healing agent and nanomodified shell-wall.

### 5.3.4 Manufacturing of the specimens for electrical conductivity measurements

Two CNTs loadings were employed to modify the epoxy matrix to evaluate the conductivity after the incorporation of the capsules inside the material. The 0.3 wt. % MWCNTs were dispersed in the DGEBA epoxy resin, based on a previous study [3]. In this study, a 0.3 wt. % CNT loading was selected to investigate the effect of introducing different types of capsules on the electrical properties. This percentage was chosen as it is close to the percolation threshold. The second percentage was 0.5 wt. % MWCNTs since the percolation threshold reached at this value.

The dispersion process lasted 3 hours in the dissolver at 3000 rpm at room temperature. Microcapsules were introduced into the nanomodified resin, and the system was mixed with Epikure 541 hardener in a 100:50 ratio. The mixture was cast in silicon rubber molds. The specimens for electrical characterization had dimensions of 52 × 12 × 3 mm$^3$.

## 5.4 Characterisation techniques (equipment)

### 5.4.1 Scanning Electron Microscopy (SEM)

The mean diameter of each capsule batch was estimated by 50 individual capsule measurements via SEM images. All images were extracted using the same electron microscope as previously. The microcapsules were also gold/platinum sputter coated to avoid their decomposition due to the high applied voltage.

### 5.4.2 Evaluation of the electrical properties of the polymer matrices with different capsules

As previously, the advanced dielectric thermal analysis system (DETA-SCOPE), supplied by ADVISE Greece, was utilized for the conductivity measurements. The specimens were placed inside a capacitor consisting of two copper plates with dimensions of 52 × 12 $mm^2$. All measurements were performed at room temperature. The electrical properties of the polymer matrix were evaluated from the DC conductivity values of the specimens at the frequency of 0.01Hz.

## 5.5 Results

### 5.51 SEM images/ Size distribution

SEM images revealed that microcapsules were spherical in shape and had a rough exterior wall preferred for better interlocking within the matrix (**Figure 54**). Specifically, at nanomodified shell-wall and nanomodified both core and shell-wall capsules, a more roughly exterior wall was observed due to the CNTs incorporation. Capsules mean diameter was evaluated for all sets, from 50 measurements from each category from SEM images. The size of microcapsules was decreased while increasing the stirring rate (**Figure 55**) at all sets as it was expected [76].

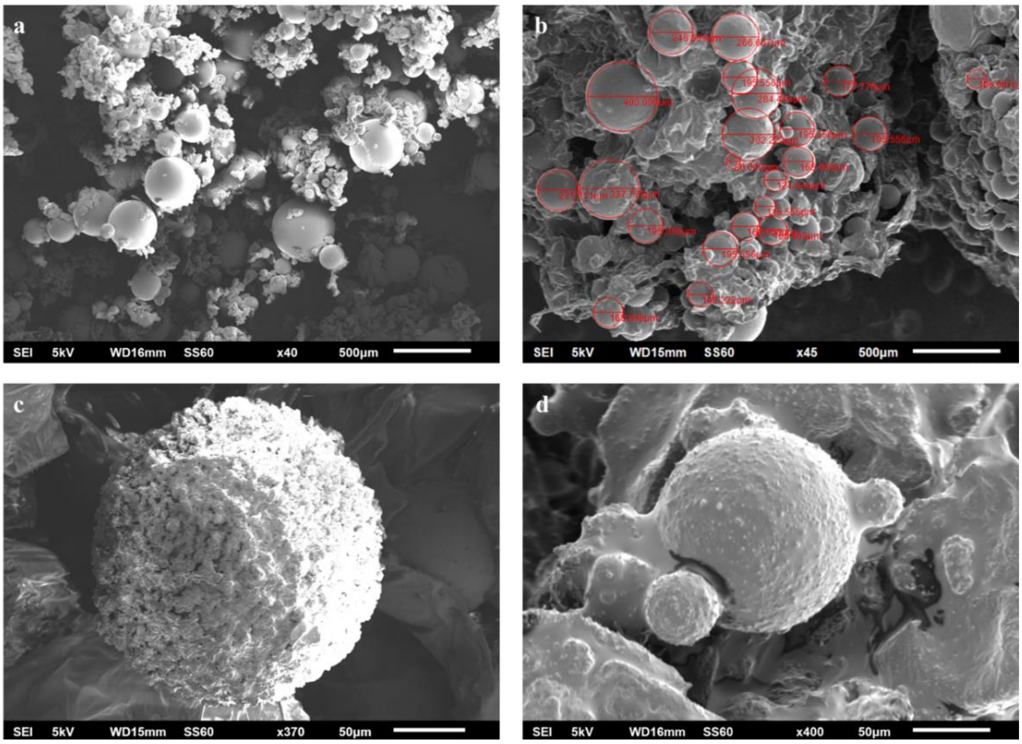

**Figure 54.** SEM images from a) neat, b) nano-core, c) nano-wall, and d) nano-all capsules.

Figure 56 depicts in detail the mean size of each capsule set. The neat capsules with five different mean sizes were manufactured for previous research [126]. The second set included microcapsules containing a nano-modified healing agent. The mean size of each capsule batch was evaluated at 353.6 ± 32.5 μm, 253.6 ± 23.1 μm, 167.2 ± 10.2 μm, 71.7 ± 16.3 μm, and 55.6 ± 19.2 μm for encapsulation processes that took place at 200 rpm, 300 rpm, 400 rpm, 600 rpm, and 800 rpm, respectively. At the third set with the nanomodified shell wall capsules, the mean size was estimated at 340.3 ± 12.3 μm, 232.7 ± 23.6 μm, 140.9 ± 3.2 μm, 107.5 ± 12.6 μm, and 57.5 ± 23.5 μm for encapsulations at 200 rpm, 300 rpm, 400 rpm, 600 rpm, and 800 rpm, respectively. The same trend was observed in the final set comprised of capsules with both nanomodified core and shell wall. Specifically, the mean diameter was calculated at 380.7 ± 42.3 μm, 245.6 ± 23.5 μm, 137.1 ± 24.6 μm, 89.6 ± 32.4 μm, and 72.8 ± 36.4 μm for the processes that were performed at 200 rpm, 300 rpm, 400 rpm, 600 rpm, and 800 rpm, respectively.

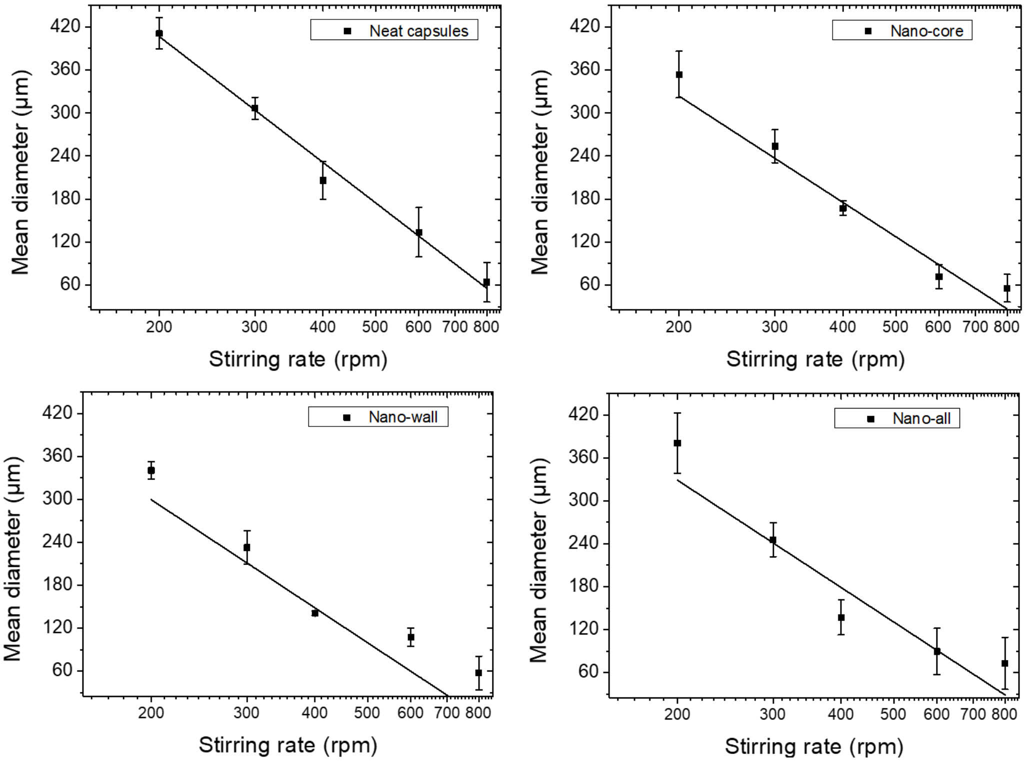

**Figure 55.** Capsule size vs. stirring rate from the different capsule batches.

| Capsule batch | Mean Diameter (μm) | Capsule batch | Mean Diameter (μm) |
|---|---|---|---|
| Neat-200 | 410.9 ± 21.9 | Nano-wall-200 | 340.3 ± 12.3 |
| Neat-300 | 306.7 ± 15.3 | Nano-wall-300 | 232.7 ± 23.6 |
| Neat-400 | 205.8 ± 26.3 | Nano-wall-400 | 140.9 ± 3.2 |
| Neat-600 | 133.5 ± 34.5 | Nano-wall-600 | 107.5 ± 12.6 |
| Neat-800 | 64.0 ± 27.6 | Nano-wall-800 | 57.5 ± 23.5 |
| Nano-core-200 | 353.6 ± 32.5 | Nano-all-200 | 380.7 ± 42.3 |
| Nano-core-300 | 253.6 ± 23.1 | Nano-all-300 | 245.6 ± 23.5 |
| Nano-core-400 | 167.2 ± 10.2 | Nano-all-400 | 137.1 ± 24.6 |
| Nano-core-600 | 71.7 ± 16.3 | Nano-all-600 | 89.6 ± 32.4 |
| Nano-core-800 | 55.6 ± 19.2 | Nano-all-800 | 72.8 ± 36.4 |

Figure 56. Mean size of each capsule batch.

### 5.5.2 Electrical properties of the 0.3 wt.% MWCNTs polymer matrix with capsules

Impedance spectroscopy was employed to investigate the effect of the introduction of the microcapsules in the nano-enhanced matrix. In the case of the 0.3 wt. % CNTs, the matrix had a semi-formatted conductive network with a conductivity value of $3.61\times10^{-7}$ S/m. The conductive network was formatted when 0.5 wt. % CNTs were dispersed and had a conductivity of $3.86\times10^{-6}$ S/m [127]. The incorporation of neat capsules inside the material offered insignificant and incoherent changes in the conductivity values that did not reach the percolation threshold (**Figure 57**). In detail, with the introduction of capsules with mean sizes of 410.9 μm and 306.7 μm, the values were slightly increased. However, the conductivity decreased when capsules with a mean diameter of 205.8 μm and 133.5 μm were enclosed inside the matrix. In the case of the smaller capsules (64.0 μm), the values were increased as observed at the biggest sizes.

The second set (nano-core) included capsules with a nano-modified healing agent with 0.5 wt. % CNTs. In that case, all conductivity values were increased, and when the capsule size decreased, the conductivity was even higher. This can be attributed to the healing agent that was more conductive than the host matrix. Specifically, the integration of the biggest capsules (353.6 μm) exhibited a conductivity of $9.02\times10^{-7}$ S/m, while the smaller capsules provided values of $1.89\times10^{-6}$ S/m. This phenomenon was related to the capsules shell wall thickness. Bigger capsules had a thicker wall since the shell wall thinning takes place with decreasing capsule diameter [128]. The thicker wall of the big capsules acted as a defect in the semi-formatted conductive network; thus, the conductivity increased when introduced smaller capsules. Nevertheless, the percolation threshold values were not reached but were close in the case of the incorporation of small capsules.

| Capsule set | Capsule size (μm) | σ (S/m) | Capsule set | Capsule size (μm) | σ (S/m) |
|---|---|---|---|---|---|
| Neat | 410.9 ± 21.9 | 5.00E-07 | Nano-wall | 340.3 ± 12.3 | 2.05E-06 |
| | 306.7 ± 15.3 | 4.54E-07 | | 232.7 ± 23.6 | 1.99E-06 |
| | 205.8 ± 26.3 | 1.81E-07 | | 140.9 ± 3.2 | 1.78E-06 |
| | 133.5 ± 34.5 | 2.96E-07 | | 107.5 ± 12.6 | 1.29E-06 |
| | 64.0 ± 27.6 | 5.64E-07 | | 57.5 ± 23.5 | 8.00E-07 |
| Nano-core | 353.6 ± 32.5 | 9.02E-07 | Nano-all | 380.7 ± 42.3 | 9.38E-07 |
| | 253.6 ± 23.1 | 8.84E-07 | | 245.6 ± 23.5 | 1.03E-06 |
| | 167.2 ± 10.2 | 1.18E-06 | | 137.1 ± 24.6 | 1.68E-06 |
| | 71.7 ± 16.3 | 1.39E-06 | | 89.6 ± 32.4 | 3.03E-06 |
| | 55.6 ± 19.2 | 1.89E-06 | | 72.8 ± 36.4 | 4.11E-06 |

**Figure 57.** Conductivity values from specimens with 0.3 wt. % CNTs containing the different capsule batches.

At the nano-wall set (third set), the capsules had a neat (conventional healing agent) but a nanomodified with 0.5 w/v% CNTs shell wall. In opposite to the previous second set, capsule size had a proportional relationship with the conductivity of the matrix. As far as larger was the capsule size, the conductivity values were higher. For example, the incorporation of capsules with a mean diameter of 340.3 μm has substantially increased the conductivity of the matrix to $2.05\times10^{-7}$ S/m. In comparison, at smaller capsules (57.5 μm), the conductivity was slightly improved to $8.00\times10^{-7}$ S/m. This was also attributed to the capsule shell wall that, in this case, was conductive and the healing agent not. When the wall was thick, in big capsules, the conductivity increased, opposing to the small capsules that had a thin shell wall and did not significantly improve the conductivity. The percolation threshold values were not reached but were close when introducing big capsules.

In the last set that included capsules with both nano-modified shell wall and core material, the conductivity values of a percolated system were achieved. At high capsule sizes (380.7 μm), the conductivity was increased at the value of $9.38\times10^{-7}$ S/m. When the capsule size was reduced to 89.6 μm, the values increased near the percolation threshold, i.e., at $3.03\times10^{-6}$ S/m. In the case of integration of smaller capsules produced, the conductivity exceeded the values of a percolated system and reached the $4.11\times10^{-}6$ S/m. A summary of all the results, as mentioned earlier, is better illustrated in the plot in **Figure 58**.

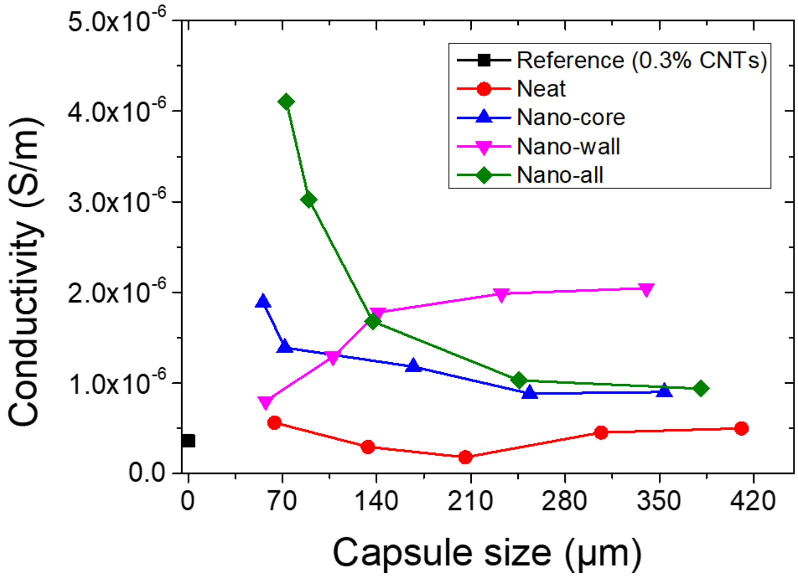

**Figure 58.** Evolution of conductivity regarding capsule size and capsule set at 0.3 wt. % CNTs matrix.

### 5.5.3 Electrical properties of the 0.5 wt. % MWCNTs polymer matrix with capsules

The effect of the incorporation of different capsule types on the electrical properties of a percolated system was also investigated. The incorporation of neat capsules did not affect the electrical properties of the polymer matrix (Figure 59). The polymer matrix was nano-modified with 0.5 wt. % CNTs exhibited a conductivity value of 3.86×10-6 S/m. In detail, at large sizes such as the 410.9 μm, the conductivity marginally decreased at $2.00\times10^{-6}$ S/m. Reducing the capsule size, the conductivity was slightly increased and reached the initial values of the matrix when introducing capsules with a size smaller than 133.5 μm. In this case, the microcapsules acted as defects in the already formatted conductive network, and reducing their size, the defects were reduced.

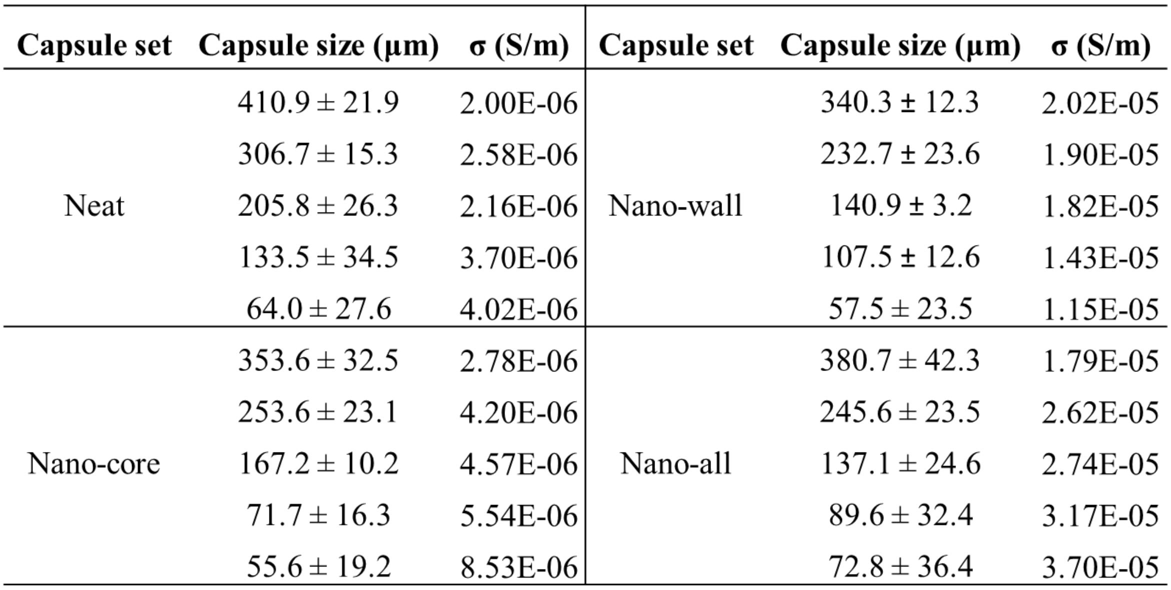

| Capsule set | Capsule size (μm) | σ (S/m) | Capsule set | Capsule size (μm) | σ (S/m) |
|---|---|---|---|---|---|
| Neat | 410.9 ± 21.9 | 2.00E-06 | Nano-wall | 340.3 ± 12.3 | 2.02E-05 |
| | 306.7 ± 15.3 | 2.58E-06 | | 232.7 ± 23.6 | 1.90E-05 |
| | 205.8 ± 26.3 | 2.16E-06 | | 140.9 ± 3.2 | 1.82E-05 |
| | 133.5 ± 34.5 | 3.70E-06 | | 107.5 ± 12.6 | 1.43E-05 |
| | 64.0 ± 27.6 | 4.02E-06 | | 57.5 ± 23.5 | 1.15E-05 |
| Nano-core | 353.6 ± 32.5 | 2.78E-06 | Nano-all | 380.7 ± 42.3 | 1.79E-05 |
| | 253.6 ± 23.1 | 4.20E-06 | | 245.6 ± 23.5 | 2.62E-05 |
| | 167.2 ± 10.2 | 4.57E-06 | | 137.1 ± 24.6 | 2.74E-05 |
| | 71.7 ± 16.3 | 5.54E-06 | | 89.6 ± 32.4 | 3.17E-05 |
| | 55.6 ± 19.2 | 8.53E-06 | | 72.8 ± 36.4 | 3.70E-05 |

**Figure 59.** Conductivity values from specimens with 0.5% CNTs containing the different capsule batches.

In the second set, the nanomodified core material that was also encapsulated did not affect the conductivity of the matrix. Specifically, the incorporation of capsules with a mean size of 353.6 μm at the matrix provided a conductivity of $2.78\times10^{-6}$ S/m. The decrement of capsule mean diameter caused a proportional increment of the conductivity that exceeded the initial conductivity value of the matrix. This was related to the reduced shell wall thickness when the capsule size was also decreased, as explained in the previous sector. Smaller capsule integration into the matrix led to conductivity values of $8.53\times10^{-6}$ S/m.

In the case of introducing microcapsules with nanomodified shell-wall, the conductivity values had a significant increment by one order. Moreover, the conductivity increased by increasing the capsule size due to the larger shell-wall thickness of big capsules. In this case, the wall was nano-modified and positively affected the electrical properties at all sizes. The electrical measurements of the polymer matrix after the incorporation of large capsules (340.3 μm) exhibited a conductivity of $2.02\times10^{-5}$ S/m as well as at small capsules (57.5 μm), the values achieved the $1.15\times10^{-5}$ S/m.

In the last set of capsules with both nanomodified shell wall and core, the electrical conductivity improved as the capsule size decreased. However, the values obtained were close as the mean diameter varied. In detail, at a mean capsule size of 380.7 μm, the conductivity reached the 1.79×10$^{-5}$ S/m, while at small capsules of 72.8 μm, it was at 3.70×10$^{-5}$ S/m. A summary of all the previous results regarding the effect of capsule type and size on the electrical properties of a percolated system is better illustrated in the plot in **Figure 60**.

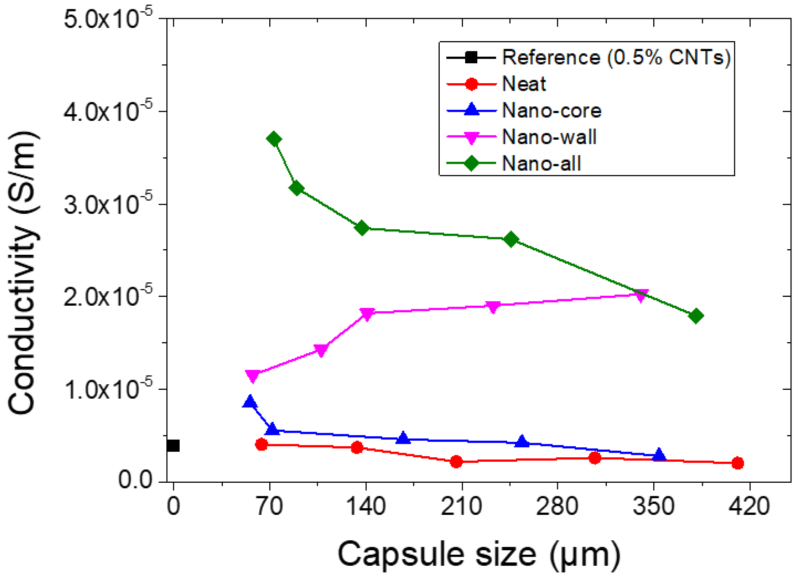

**Figure 60.** Evolution of conductivity regarding capsule size and capsule set at 0.5% CNTs matrix.

## 5.6 Conclusions

In this chapter, the effect of the incorporation of different types and sizes of UF microcapsules on the electrical properties of a conductive and semi-conductive polymer matrix was investigated. Initially, four different capsule batches (sets) were manufactured with different characteristics at five different mean sizes by changing the stirring rate of the emulsion. The agitation rates were set at 200, 300, 400, 600, and 800 rpm. The first set included neat-conventional microcapsules. For the second set, microcapsules with a nanomodified healing agent with 0.5 wt.% MWCNTs were synthesized. Microcapsules with nanomodified shell walls with 0.5 % w/v CNTs, were manufactured for the third set. At the final fourth set, microcapsules with nanomodified both healing agent and shell wall were manufactured for the first time. The mean diameter of each capsule batch was reduced by increasing the stirring rate, as was expected. The nanomodification of the healing agent or/and capsule shell wall did not affect the trend of the mean size.

The microcapsules were introduced at two nanomodified matrices that contained 0.3 wt. % and 0.5 wt. % MWCNTs. The dispersion of 0.3 wt. % MWCNTs into the epoxy matrix resulted in conductivity values below but near the percolation threshold that was found to be at 0.5 wt. % CNTs. The first case was studied to investigate if the integration of different capsules led to the formation or not of a conductive network and improved the conductivity. In the second case, the effect of capsules' incorporation into an existed conductive network was assessed.

At the incorporation of capsules in 0.3 wt. % CNTs matrix results indicated that the conductive network was successfully formatted in case of introducing capsules smaller than 90μm with both nanomodified healing agent and shell-wall. After the inclusion of neat capsules, conductivity was not significantly changed. The electrical conductivity values were improved in the case of nano-core capsules as their size increased. However, in the case of nano-wall capsules, the conductivity increased with reducing capsule size.

The conductive network was formatted after the dispersion of 0.5 wt. % CNTs into the matrix were not significantly affected after incorporating neat capsules and nano-core capsules at all sizes. Nevertheless, the nano-wall capsules integration into the matrix exhibited higher conductivity values as their mean diameter increased. Sufficiently improved electrical properties were achieved after the incorporation of nano-all capsules into the matrix, with the conductivity to be improved when reducing capsule size.

# CHAPTER 6

# Multi-functional capsule-based self-healing composites

## 6.1 Introduction

The development of self-healing composites is more difficult than polymers. The resin micro-cracks are easy to be healed similarly. Nevertheless, the fiber reinforcement inside the material increases the number of damage modes and the intricacy of the self-healing process. The self-healing functionality can be introduced to a composite material by incorporating capsules within the polymeric matrix. The capsules are ruptured in case of a damage event, and the self-healing mechanism is triggered upon the release of the encapsulated healing agent. When the healing agent reacts with the embedded catalyst upon contact, it restores the required functionality. Capsule-based self-healing composites have attracted extensive efforts by researchers towards evaluating their mechanical properties.

In the initial studies for the healing assessment in composites, Kessler and White [129] investigated the triggering and healing ability of the DCPD healing agent with Grubbs' catalyst. This curing process is based on ring-opening metathesis polymerization (ROMP). This research investigated the recovery of interlaminar fracture toughness at double cantilever beam (DCB) testing. Two healing efficiency studies were performed; the first included a manual injection of a catalyzed DCPD healing agent, while the second involved a self-activated healing. In the second case study, the catalyst was dispersed into the matrix, and an injection of the healing agent was performed after damage. The results proved that the DCPD was a very promising healing agent, although the dispersion of the catalyst was not sufficient. After this study, the same authors used the DCPD as an encapsulated healing agent in a composite material [130]. The double cantilever beam geometry was also used as previous, and 20 wt. % of capsules and 5 wt. % of catalyst were dispersed directly in the matrix. The healing efficiency of capsule-based composites exhibited a 45% recovery at room temperature, while at 80$^{o}$C the recovery was over 80%.

The micro-computed tomography (micro-CT) non-destructive evaluation method has been used on carbon fiber composites that contained DCPD microcapsules for the three-dimensional observation of the crack propagation in order to provide qualitative and quantitative structural information about the composite [131]. The micro-CT results revealed that microcapsules tended to change their shape to oval when introduced to the composite, but this was regarded on their size. The bigger capsules had a larger deformation, but the vacuum bagging techniques proved an effective manufacturing technique (**Figure 61**). Also, an evaluation of the dispersion of both capsules and Grubbs catalyst was performed as well as successful polymerization/healing was observed. The Mode-I tests exhibited a recovery about 50% in terms of healing efficiency.

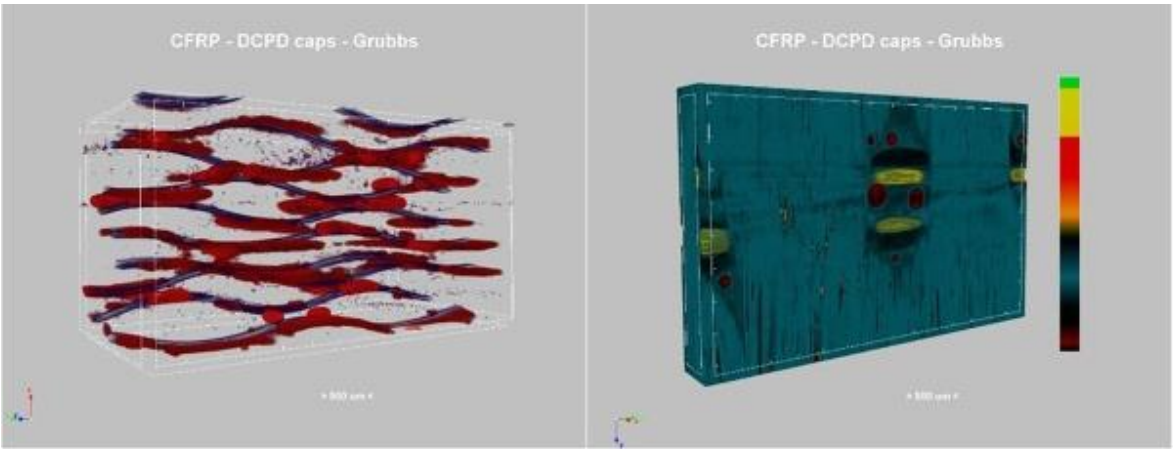

**Figure 61.** 3D micro-CT images of the composite with DCPD microcapsules and Grubbs catalyst. (Original source: Kontiza A, Semitekolos D, Milickovic TK, Pappas P, Koutroumanis N, Galiotis C, et al. Double cantilever beam test and micro-computed tomography as evaluation tools for self-healing of CFRPs loaded with DCPD microcapsules. Composite Structures 2022;279. https://doi.org/10.1016/j.compstruct.2021.114780.)

Tsilimigra et al. reported a low content capsule-based self-healing carbon reinforced composite manufactured by the wet layup method [132]. The UF microcapsules loading was only at 10 wt. % while Scandium (III) Triflate ($Sc(OTf)_3$) was used as a catalyst. Composites were subjected to three-point-bending and Mode-II fracture toughness tests, while reference specimens were manufactured to evaluate the knockdown effect. Results indicated a minor decrease of 14% in interlaminar fracture toughness ($G_{IIc}$) and a 12% and 4% reduction in the flexural strength and modulus, respectively. A significant recovery of 84% in fracture toughness was reported in terms of healing efficiency. The flexural strength was regained by 14% and the modulus by 23%.

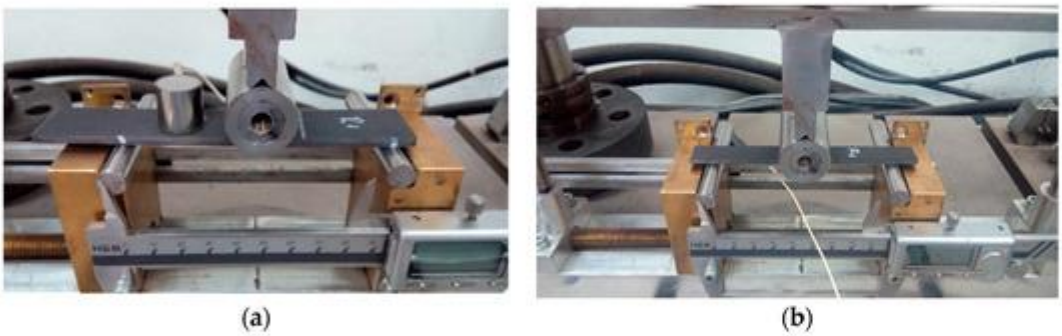

**Figure 62.** (a) Mode-II and (b) three-point-bending tests. ("Original source: Mechanical Properties Assessment of Low-Content Capsule-Based Self-Healing Structural Composites, X. Tsilimigkra, D Bekas, M Kosarli, S. Tsantzalis, A. Paipetis and V. Kostopoulos, Applied Sciences,10, 5739, (2020).

Very critical damage that may be caused at composite structures is the impact damage. Especially a low-velocity impact usually creates delamination inside the material that is difficult or even impossible to detect and repair (Barely Visible Impact Damage-BVID) [133]. Vintila et al. [134] investigated the optimal dispersion process of PUF and MUF microcapsules containing dicyclopentadiene (DCPD) and 5-ethylidene-2-norbornene (ENB) into a glass-fiber reinforced polymer composite material, respectively. Two different dispersion techniques were evaluated, with magnetic stirring being the most valuable method that presented a better homogeneity. At low-velocity impact tests, results indicated that the addition of higher percentages of PUF-DCPD microcapsules did not affect the impact strength even after suffering a thermal cycle (-20 $^oC$ to +100 $^oC$). In the case of MUF-ENB capsules, the impact response decreased while increasing the capsule percentage. However, the strength was increased with microcapsule addition after the thermal cycle except for the addition of 15 wt. % microcapsules that reduced the impact properties for both systems. Self-healing glass fabric/epoxy composites with incorporated epoxy and mercaptan-filled microcapsules were tested under low-velocity impact damage by Yuan et al. [135]. They used a dual microcapsule system while the healing process started without external intervention at room temperature. The most substantial factor for a successful healing process was the impact energy since at small energies, the damage was healed faster. Another parameter was the capsule size, with bigger capsules leading to an improved rate of damage area reduction. Patel et al. studied the residual compressive strength of capsule-based self-healing composites using DCPD-filled UF microcapsules and Grubbs' catalyst particles. Different impact energies were used while compression after impact results indicated that the self-healing improved the threshold impact energy and showed a sufficient recovery in average stress at maximum tangent stiffness and strength (**Figure 63**).

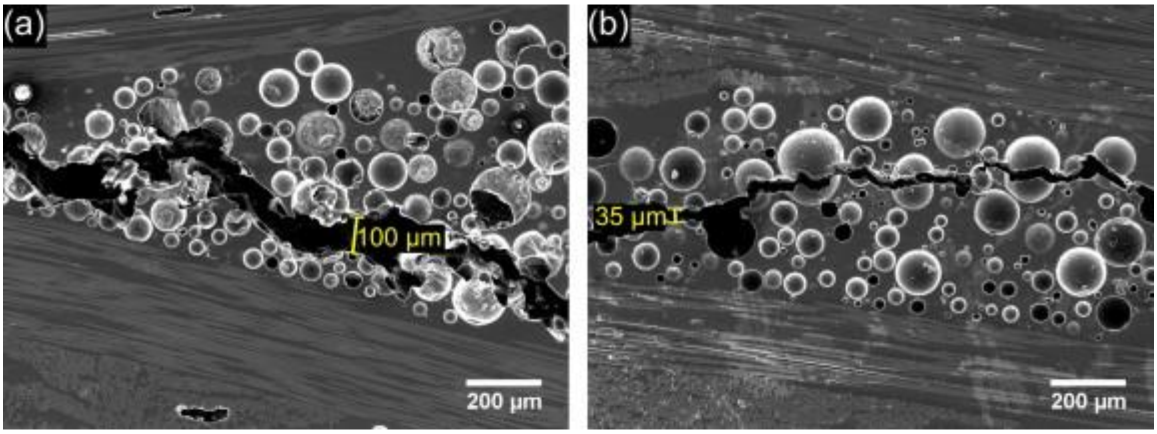

**Figure 63.** Delamination was induced after a (a) 45.1 Joule impact and (b) 17.8 Joule impact. ("Used with permission of Composites Part A: Applied Science and Manufacturing, from Autonomic healing of low-velocity impact damage in fiber-reinforced composites, A. Patel, N. R. Sottos, E. D. Wetzel and S. R. White, 41, 360-368, (2010); permission conveyed through Copyright Clearance Center, Inc.")

Fiber-reinforced polymer composites are also very vulnerable to fatigue damage. The type of damage induced in transverse plies due to fatigue loading is typically matrix cracks and fiber/matrix debonding, thus reducing the tensile modulus [136]. Kim et al. [137] estimated the self-healing efficiency of fatigue damage in cross-ply glass fiber reinforced epoxy composites. Polyurethane/poly(urea-formaldehyde) (PU/PUF) microcapsules with a 2.5 μm diameter containing an Epon 862/EPA as a healing agent were incorporated into prepregs. Control ore reference specimens without capsules were also manufactured for comparison. The specimens were tested in tension-tension fatigue loading for 15,000 cycles at 30% of their maximum strength (**Figure 64**). The healing process took place at room temperature for 24 hours, and the results exhibited a 52.4% recovery of Young's modulus.

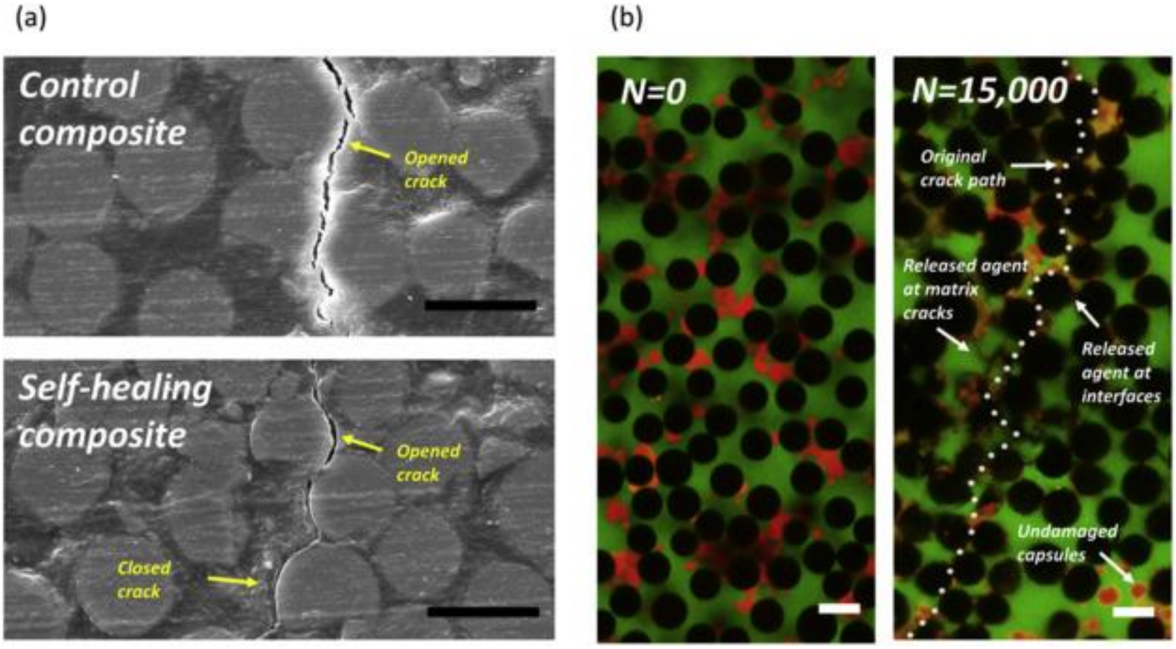

**Figure 64.** (a) SEM images of control and self-healing composites and (b) confocal fluorescent images of the self-healing composites before and after fatigue loading (with red are the microcapsules). (*"Used with permission of Composites Science & Technology, from Self-healing of fatigue damage in cross-ply glass/epoxy laminates, S. Y. Kim, N. R. Sottos, and S. R. White, 175, 122-127, (2019); permission conveyed through Copyright Clearance Center, Inc."*)

The skin-stiffened or “stringer run-outs” structures are used mostly in aerospace but are very susceptible to local damage. Usually, the stringer tends to debond from the skin, and then the delamination may further propagate in the skin [138]. The mechanical characterization of these specimens is both time-consuming and material intensive.

Luterbacher et al. proposed a simplified joint configuration via the lap strap geometry in order to characterize delamination at the tip of the flange and evaluate the self-healing efficiency using the vascular approach [139]. The results of this work showed that the simplified lap-strap specimens showed the same damage mechanisms as the stringer run-out. Firstly, the lap debonds from the strap, and then the delamination may further propagate into the strap. It should be mentioned that failure in the lap strap geometry is manifested in a mixed mode. At the early stages of the tensile test, the adhesive layer between lap and strap fails in mode II, followed by mode I failure at higher stress levels. The systems completely recovered their strength after the healing process.

## 6.2 Scope

The final chapter of capsule-based self-healing materials reports the manufacturing and characterization of the multi-functional, self-healing, and self-sensing composites. The self-healing composites were tested at two different mechanical tests, mode-II fracture toughness and low-velocity impact. All tests included the evaluation of the concurrent restoration of both mechanical and electrical properties, too.

In the case of the mode-II fracture toughness tests, two different capsule types were incorporated into the composites with a neat and nanomodified healing agent. The mechanical and electrical healing efficiency was investigated as in polymer matrix level (chapter three). The same campaign was followed in the case of the lap strap geometry analyzed in the introduction section and can simulate the mechanical behaviour of a stiffened panel (model structure level).

Two different cases were tested at low-velocity impact tests to evaluate their mechanical and electrical healing efficiency. In the first case, reference and self-healing systems were manufactured and compared. In order to enable the damage sensing capability, two different approaches were followed (second case). Following our previous research [140], the first approach included the incorporation of carbon fabric strips or tows inside the material for the formation of embedded electrodes or sensing elements in the junction points, thus eliminating the use of “external” sensors. The second approach included the spray coating of a conductive SWCNTs ink in lines inside the material that replaced the carbon tows. The formed sensing elements were used for the evaluation of the restoration of the electrical properties of each geometry. Note that part of the current research only evaluates the restoration of both the mechanical and electrical properties and the influence of the incorporation of the self-healing system on them and not the damage sensing functionality. These properties were measured and evaluated, but there is part of another research.

## 6.3 Experimental

### 6.3.1 Materials

Capsules were manufactured using the same materials as in previous chapters. As healing agent, the nanomodified diglycidyl ether of bisphenol-A (DGEBA, Epikote 828 lvel) epoxy resin was chosen. The incorporated catalyst was also the Aluminium (III) triflate ($Al(OTf)_3$) by Sigma-Aldrich, as previously mentioned. As primary reinforcement, unidirectional (UD) glass fabric with an areal density of 320 g/m$^2$ was used by Fibermax S.A. The biaxial (BI) glass fabric at ±45$^o$ with an areal density of 240 g/m$^2$ by Fibermax S.A was also used. Carbon tows T700 supplied from Torray S.A. were used as patches for the Impedance measurements at the low-velocity impact specimens. Due to the high viscosity of the nanomodified DGEBA resin, the two-part low viscosity epoxy resin Araldite LY5052 and hardener Aradur CH 5052, both provided by Huntsman Advanced Materials, Switzerland, at a mix ratio of 100:38, was used as matrix phase. The epoxy matrix was nanomodified and performed using the Graphistrength C-100 MWCNTs from ARKEMA, France, as previously, and Ketjenblack carbon black from Nanocyl S.A with a mean agglomeration size of 5-10μm. For the manufacturing of the conductive CNTs ink, the sodium-dodecylbenzenesulfonate (SDBS) polymer was used as a high-content ionic surfactant supplied by Sigma-Aldrich. The Tuball Single-Walled Carbon Nanotubes (SWCNTs) provided by OCSiAL, with an average diameter of 1.8 ± 0.4 nm, length>5 μm, carbon content: >85 wt.%, and metal impurities <15 wt. % were dispersed into the surfactant solution.

### 6.3.2 Nanomodification of the epoxy matrix

The nanomodification of the LY5052 epoxy matrix was performed through the dispersion of the nanofillers using high shear mixing using the Dispermat AE, VMA-GETZMANN GMBH, Germany, equipped with a double-walled dispersion container. The dispersion was performed according to the protocol [50] at 3000rpm for 3 hours under vacuum. The matrix was nanomodified with 0.5 wt. % MWCNTs and 1 wt. % of Carbon Black by Nanocyl S.A. The selected CB replaced the previous from the R&G company but exhibited the same conductivity values (that exceeded the percolation threshold) with the 0.5 wt. % MWCNTs and 2 wt. % CB system from our previous research [50]. A cooling bath by Grant, UK, was connected with the container in order to keep the temperature at 25 $^o$C during the dispersion process.

### 6.3.3 Nanomodification of the core

As in previous chapters, 0.5 wt. % MWCNTs were dispersed within the healing agent using the high shear mixing process. The healing agent was the DGEBA Epikote 828 lvel epoxy resin. The dispersion protocol involved continuous agitation at 25 ºC under vacuum. According to the protocol, the agitation rate was set at 3000 rpm, and the duration was 3 hours [25].

### 6.3.4 Encapsulation process

The encapsulation process that followed was the same as in previous chapters. The stirring rate for capsules manufactured for the mode-II and lap strap tests was chosen to 500rpm. For the low-velocity impact tests, to heal more extensive damage (e.g., delaminations), the stirring rate was reduced to 300rpm to manufacture larger capsules [76]. A dilution percentage of 15 wt. % was used, and the reaction was left to proceed for 4 hours. When the encapsulation process was ended, the mixture was left to cool down at room temperature, and the suspended microcapsules were rinsed with ethanol using a Buchner filter. Capsules were left to dry in a laboratory oven under ambient conditions.

Hereafter, the produced capsules will be referred to as “neat” for capsules containing the unmodified (neat) healing agent and “nanomodified” for capsules containing the nano-modified healing agent (with 0.5 wt. % MWCTNs).

### 6.3.5 Manufacturing of composite materials for Mode-II tests

Three composite laminates were manufactured for each scenario (reference, neat and nanomodified systems) using 16 plies of the UD glass fabric. The lamina thickness was approximately 0.26 mm. The manufacturing process was the hand lay-up technique with an applied pressure of 3 MPa, while curing took place at 25 ºC for 24 hours. Spacers were used in order to ensure a uniform laminate thickness of 4.2 mm. The self-healing system (neat or nanomodified) was placed at the midplane of the laminate. The nanomodified Araldite LY 5052/ Aradur CH 5052 epoxy system was chosen as the matrix phase. The healing system contained 25 wt. % capsules and 2.5 wt % Aluminium (III) triflate ($Al(OTf)_3$). Capsules and catalyst were dispersed into epoxy (at a different beaker) and then applied in the middle of the composite. A thin high-temperature release film was also placed in the mid-thickness plane to act as an initial pre-crack. After curing, specimens were cut at the desired dimensions according to AITM-1.0006 [141]. At each specimen, carbon fabric squares with dimensions of 2 ×2 mm were attached using the matrix material on both sides of the specimen to form sensing elements (electrodes). In addition, at each carbon patch, one cable was also attached using conductive silver paste (**Figure 65**). The patches were applied using a vacuum bagging process and left for curing for 24 hours at room temperature. Hereafter, the produced specimens will be referred to as "reference" for unmodified specimens (no self-healing system), as "neat system" for specimens containing neat capsules, and "nanomodified system" for specimens containing nanomodified capsules.

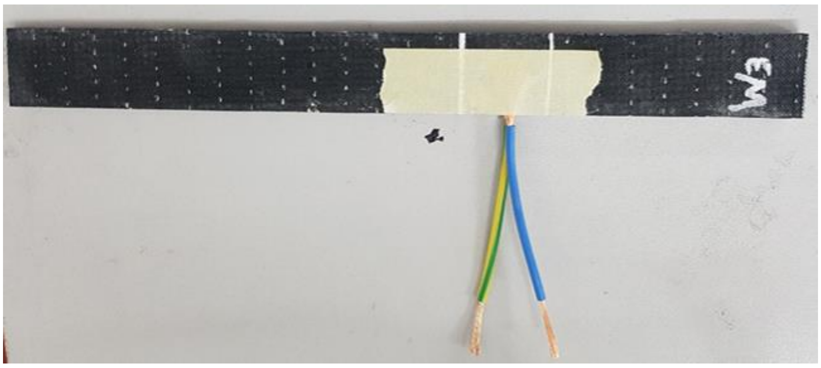

**Figure 65.** Mode-II specimen with the attached carbon patches and cables.

### 6.3.6 Manufacturing of composite materials for low-velocity impact tests

Low-velocity impact specimens were manufactured according to the ASTM D 7136 [142]. The lamination sequence was chosen to be $[0/90/\pm45]_{3S}$ using the UD and the BI glass fabrics. The manufacturing process was the hand lay-up technique with an applied pressure of 3 MPa, and curing took place at 25 $^{o}$C for 24 hours. Spacers were used in order to ensure a uniform laminate thickness of 4.7 mm. The nanomodified Araldite LY 5052/ Aradur CH 5052 epoxy system was chosen as the matrix phase. Prior to manufacturing, the self-healing system was incorporated into the matrix. 25 wt. % of microcapsules and 2.5 wt. % of the catalyst, Aluminium (III) triflate ($Al(OTf)_3$), were dispersed at the matrix. Each specimen has dimensions of 100×150 mm.

Four categories of impact specimens were manufactured. In order to evaluate the restoration of the mechanical properties and activate the 3D damage topography mapping, the third (III) and the fourth (IV) category carbon tows and spray lines were employed (see Appendix A).

### 6.3.7 Manufacturing of composite modeled structures for lap strap tests

As discussed above, lap strap geometry can simulate the stiffening of a composite panel. The lap, the strap, and the endtab were extracted from the same composite laminate. The lamination sequence was chosen to be [±45/0/90]s using the UD and the BI glass fabrics. As the matrix phase, the nanomodified LY 5052 epoxy resin was used as previously. The hand layup method was used with applied pressure in a heated hydraulic press under 3 MPa. Curing took place at 25 $^{o}$C for 24 hours. For the modification of the adhesive, 25 wt. % of capsules and 2.5 wt. % of the catalyst was dispersed into the matrix phase. When specimens were cut in the desired dimensions (**Figure 66**, up), the bonding process took place under vacuum bagging. The self-healing system was incorporated only in the measured bonding area between the lap and the strap (**Figure 66**, down). Following the Mode-II protocol, at each specimen, carbon fabric squares with dimensions of 1.5 × 1.5 mm were attached using the matrix material at both sides of the specimen for the formation of electrodes. The carbon fabric patches were applied using a vacuum bagging process and left for curing for 24 hours at room temperature. Hereafter, the produced specimens will be referred to as “reference” for unmodified specimens (no self-healing system), as “neat system” for specimens containing neat capsules, and “nanomodified system” for specimens containing nanomodified capsules.

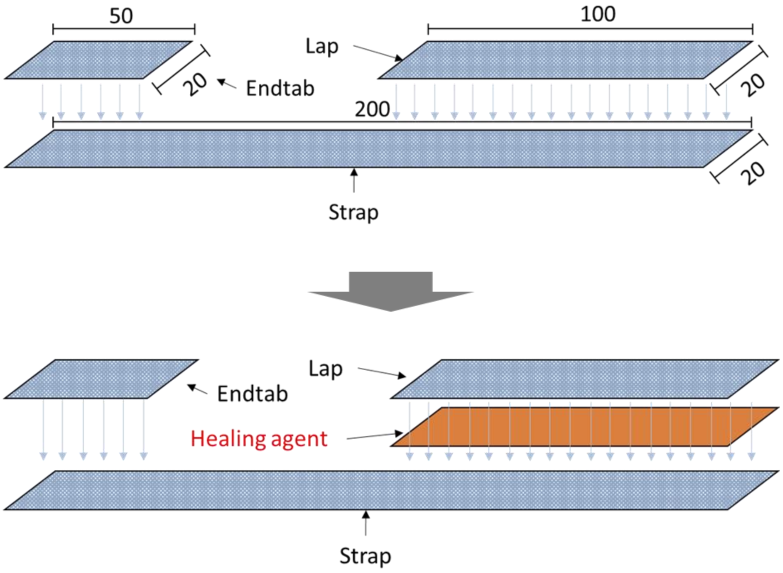

**Figure 66.** Lap strap geometry (up) & measured self-healing section (down).

## 6.4 Characterization Techniques & Equipment

### 6.4.1 Scanning Electron Microscopy (SEM)

The mean diameter of each capsule batch was estimated from 100 separate capsule measurements via SEM images. All images were extracted using the Phenom Pharos desktop SEM by Thermoscientific S.A. Microcapsules were gold/platinum sputter coated to prevent their decomposition due to the high voltage set at 5 keV.

### 6.4.2 Mode II interlaminar fracture toughness

Mode II tests were performed using a WDW-100 Jinan universal testing machine under three-point bending equipped with a 100 kN loadcell (**Figure 67**). The fracture of the interface occurring during this test is an in-plane shear fracture. The displacement rate was set at 1 mm/min while load, point displacement, and crack length were recorded. According to [143] the critical mode-II strain energy release rate, $G_{IIC}$, was calculated using the equation (4):

$$G_{IIC} = \frac{9 \times P \times a^2 \times d \times 1000}{2 \times w(\frac{1}{4}L^3 + 3a^3)} \quad (4)$$

Where $G_{IIc}$ (J/mm$^2$) is the mode -II fracture toughness energy, P is the critical load, d is the displacement at the onset of the delamination, a is the initial crack length, w is the width of the specimen, and L is the span length. The mechanical testing was stopped when the delamination at the mid-plane of the specimen occurred.

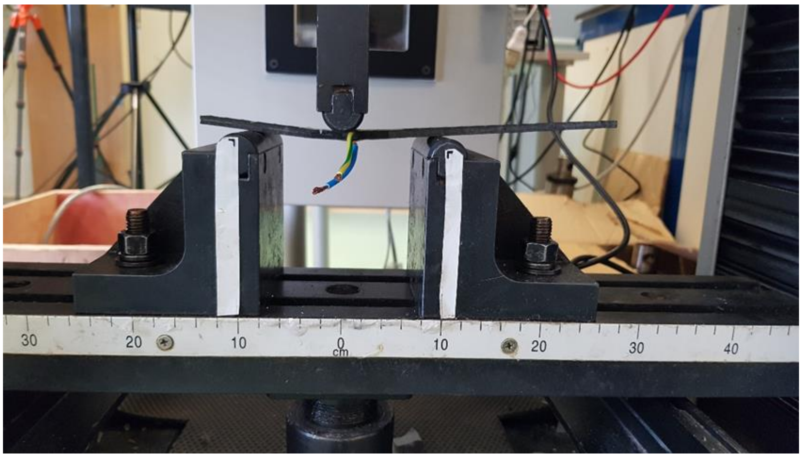

**Figure 67.** Mechanical testing of Mode-II specimen.

### 6.4.3 Low-velocity impact testing

Low-velocity impact specimens were performed according to ASTM D7136. Mechanical testing was performed at an Instron Ceast 9340 Drop Tower equipped with a 45 kN load cell and a 16mm hemispherical impactor. The impact energy was 25 J with an additional mass of 0.5 kg and a velocity of 3.71 ms$^{-1}$. The machine was also equipped with an anti-rebound system in order to ensure unique impact damage (**Figure 68**). The absorbed energy was calculated from the area under the load-displacement curve.

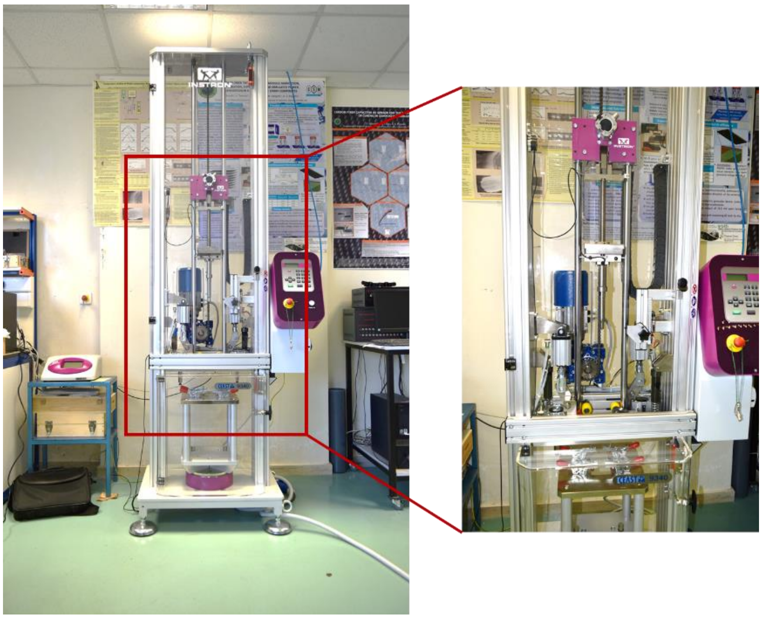

**Figure 68.** Instron Ceast impact drop-tower testing machine (left) with zoom to the impact damage area (right)

### 6.4.4 Lap strap specimen testing protocol – modeled structure composites

Lap strap tests were performed under tensile mode at a WDW-100 Jinan universal testing machine equipped with a 100 kN load cell (**Figure 69**). The displacement rate was selected at 1 mm/min. The specimens were gripped 50 mm at either end, leaving an initial grip-to-grip separation of 100 mm. All tests were stopped upon delamination of the strap from the lap. Stress was calculated as the ratio of the load to the cross-section area (thickness × width) and strain as the ratio of the extension to the grip-to-grip distance.

**Figure 69.** Mechanical testing process of lap strap specimens with online impedance measurements (left) and lap strap specimens (right).

### 6.4.5 Compression after impact (CAI) testing

CAI was performed using the Universal Testing Machine WDW-100 by Jinan S.A. equipped with a 100kN loadcell according to ASTM D7137. The displacement rate was set at 1.25 mm/min. The dimensions of each specimen were recorded. In case of carbon and spray specimens, the external copper strips were cut before the testing. Each specimen was clamped in an in-house CAI fixture that did not allow the sample to slide or move (**Figure 70**). The tests were performed after the second impact after the healing process. The maximum CAI strength (MPa) was estimated from equation (5):

$$\text{Strength}_{\text{CAI}} = \frac{P_{max}}{w \times h} \qquad (5)$$

Where P is the maximum load (N), w is the width of the specimen (mm), and h is the thickness of the specimen (mm).

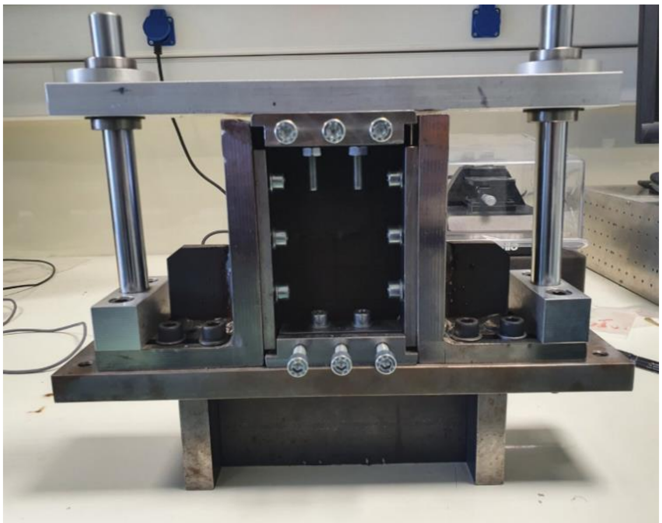

**Figure 70.** CAI fixture with the specimen inside.

### 6.4.6 Healing process/ Healing efficiency of Mode II tests

In case of the Mode-II specimens, the healing process was achieved in a laboratory oven at 80 °C for 48 hours with applied weight on the specimens (**Figure 71**). At the end of the healing process, the specimens were left to cool down at room temperature and retested under the same conditions. Healing efficiency was evaluated in terms of peak load ($P_c$) and mode-II interlaminar fracture toughness energy ($G_{IIc}$) recovery from equations (6) and (7), respectively:

$$n_p = \frac{P_c^h}{P_c^v} \tag{6}$$

$$n_G = \frac{G_{IIc}^h}{G_{IIc}^v} \tag{7}$$

where $P_c^h$ and $P_c^v$ are the peak load of the healed and the virgin specimens and the $G_{IIc}^h$ and $G_{IIc}^v$ represent the mode-II interlaminar fracture toughness energies of the healed and virgin specimens. The change of the initial properties after the self-healing system incorporation or the knockdown effect was evaluated using equation (1).

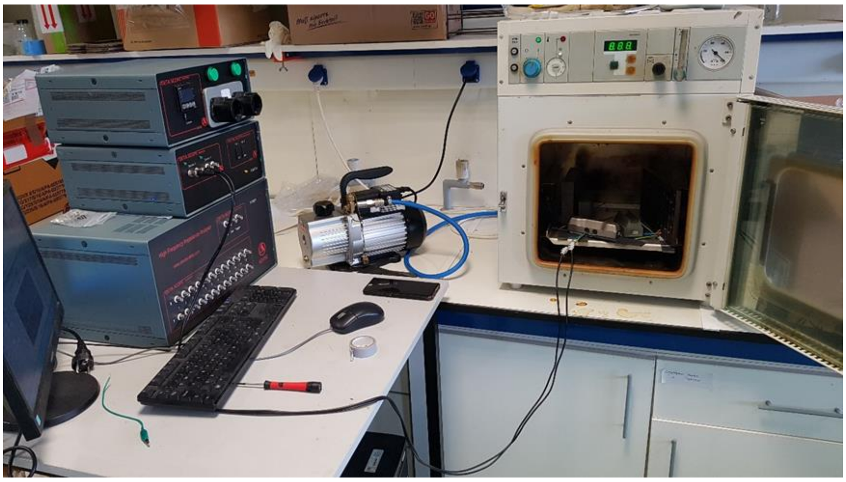

**Figure 71.** Online monitoring of the healing process of the Mode-II specimens at the oven via conductivity measurements.

### 6.4.7 Healing process/ Healing efficiency at Low-velocity impact specimens

In the case of low-velocity impact specimens, the healing process took place at a hot press with no applied pressure to ensure that the thickness remained stable after the process. The temperature was set at 80 °C for 48 hours. At the end of the healing process, the specimens were left to cool down before retesting under the same conditions. Healing efficiency was estimated in terms of the absorbed energy $n_E$ and the maximum load $n_P$, according to equations (8) and (9), respectively.

$$n_E = \frac{E^h}{E^v} \tag{8}$$

$$n_p = \frac{P^h}{P^v} \tag{9}$$

where $E^h$ and $E^v$ were the absorbed energy of the healed and the virgin specimens, while $P^h$ and $P^v$ were the maximum load of the healed and the virgin specimens, respectively. The change of the initial properties after the self-healing system incorporation or the knockdown effect was evaluated using equation (1).

### 6.4.8 Change of Compression After Impact properties

The change of the CAI properties after the incorporation of the self-healing systems and/or damage sensing systems was evaluated in terms of maximum strength according to equation (10):

$$n_S = \frac{S^m}{S^r} \tag{10}$$

where $S^r$ and $S^m$ correspond to the maximum strength of the reference and the modified specimens, respectively.

### 6.4.9 Healing process/ Healing efficiency at Lap strap specimens

The healing protocol that was followed to restore the mechanical and electrical properties of the lap strap specimens was the one described in the previous section (Mode-II specimens). Healing efficiency was related to the efficiency in the recovery of the initial strength $n_\sigma$ and according to equation (11):

$$n_\sigma = \frac{\sigma^h}{\sigma^v} \tag{11}$$

where $\sigma^v$ and $\sigma^h$ correspond to maximum stress at which the delamination initiated at the tip of the strap of virgin and healed specimens, respectively. The change of the initial properties after the self-healing system incorporation or the knockdown effect was evaluated using equation (1).

### 6.4.10 Restoration of the electrical properties

The Impedance technique was used as in previous chapters for the evaluation of the electrical properties of the composites at virgin specimens and the efficiency of the system to regain its initial electrical conductivity (at healed specimens). The process was followed at all specimen geometries (Mode-II, impact, and lap strap). Conductivity measurements were performed using the Advanced Dielectric Thermal Analysis System (DETA-SCOPE) supplied by ADVICE, Greece. The system was connected to the cables or the copper strips of each specimen for the measurements. All measurements were performed under a stable temperature of 25 °C.

The assessment of the restoration of the electrical properties in terms of electrical conductivity values was performed by: (i) IS measurements of the virgin specimens before mechanical loading, (ii) implementation of the mechanical characterization and the healing process, and (iii) IS measurements after the healing process. The electrical properties of the composites and their restoration were evaluated from the ratio of the DC conductivity values of the healed specimens to the DC conductivity values of the virgin specimens through equation (3).

### 6.4.11 IR Thermography

For the evaluation of the restoration of the impact damage, a FLIR A6750 MWIR camera was utilized, with a resolution of 640 x 512 pixels and a 125Hz frame rate. Two 1000W IR lamps were used as the heating source, triggered by a Tektronix AFG3052C signal generator, for the pulsed thermography method. The ramp pulse had a duration of 7s, and the peak-to-peak voltage was 7V. The distance between the specimen and the lamp was 1 m, and the distance between the specimen and the camera. A schematic of the experimental setup is presented in **Figure 72**.

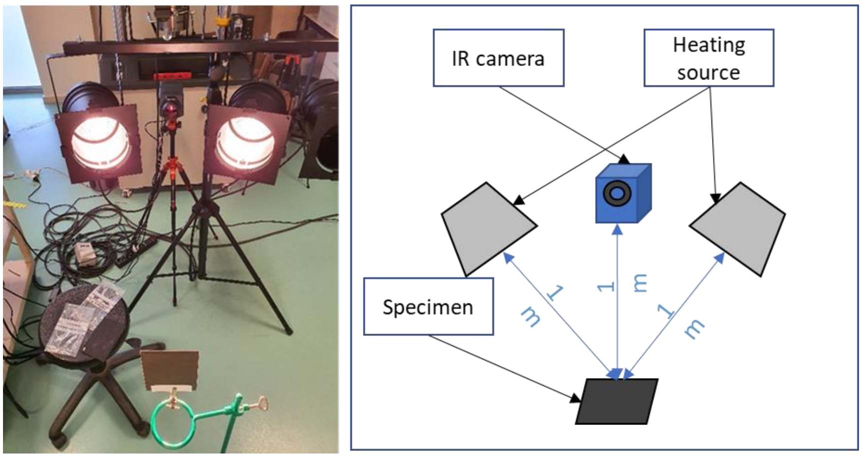

**Figure 72.** Experimental setup of the IR thermography measurements.

## 6.5 Results

### 6.5.1 SEM images

**Figure 73** shows two SEM images of the produced nanomodified microcapsules that incorporated at all composites obtained at two magnifications (i.e., x330 and x1000). SEM images revealed that the capsules were spherical in shape and had a rough exterior shell wall. The rough, porous morphology of the outer surface can be easily observed at a higher magnification image. This is an important characteristic of the interlocking between the capsules and the matrix. The neat capsules used at Mode-II and lap strap specimens had a mean size of 205.8 ± 26.3 μm. The mean diameter of the nanomodified capsules was evaluated at 167.2 ± 10.2 μm from data sets of 100 measurements. Since the damage occurring due to impact damage is larger than in the other geometries, larger capsules with a mean diameter of 424.67 ± 68.98 μm were used at impact specimens.

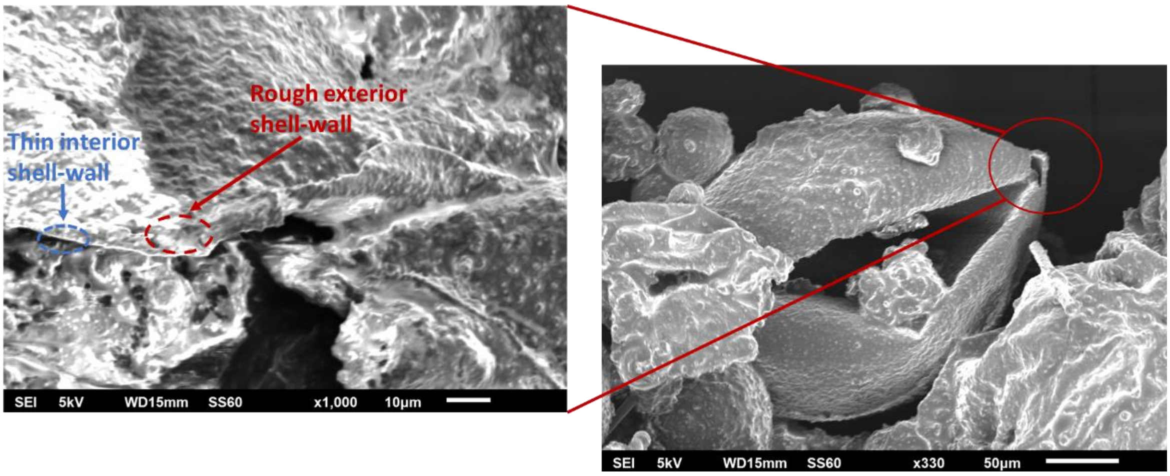

**Figure 73.** SEM images from capsules confirm the rough exterior and thin interior shell wall.

### 6.5.2 Recovery of the mode-II fracture toughness energy

**Figure 74** depicts representative plots of reference, neat system, and nanomodified system of mode-II specimens. It is observed that the load curves revealed a linear increase followed by a change in the slop from this linearity. When the crack propagated inside the specimen, a load drop was observed. This was a typical behavior observed in brittle epoxy composites [144]. Moreover, this trend was also observed in virgin and healed specimens (**Figure 75**).

After incorporating neat capsules, $G_{IIc}$ values were increased by 27.98 %, while in the case of nanomodified capsules, the values increased by 29.17 %. However, the max load was decreased with the addition of neat capsules by -6.80 % and -2.83 % at the nano-modified capsule system. This can be attributed to the embedded capsules and catalyst that may induce the toughness through two mechanisms according to [145]. The first one corresponds to the thicker resin-rich regions that led to higher plastic deformation. In contrast, the second one is based on the microcapsules ability to restrain the hackle formation [146].

**Figure 76** depicts the calculated healing efficiency values in terms of max load and $G_{IIc}$. At neat capsule systems, the mode II fracture toughness energy was recovered by 180.93 %, while the max load was regained by 109.42 %. In the case of nanomodified capsule systems, the $G_{IIc}$ was restored by 191.24 % and the load by 117.28 %. The nanomodified system recovered its properties ca. 10 % more than the neat system due to the modification of the healing agent and the excellent properties of the CNTs, as mentioned in previous chapters.

It should be mentioned that the values obtained after the healing process at neat and nanomodified systems in terms of mode II fracture toughness energy and in maximum load exceeded the initial ones, resulting in high healing efficiencies above 100 %. This phenomenon can be explained by the fact that the healing process is a thermal process similar to the post-curing process. Post-curing usually induces the toughness of the matrix and leads to higher mode-II fracture toughness properties [146]. In addition, voids that may be induced inside the material during the manufacturing process were eliminated with the healing process.

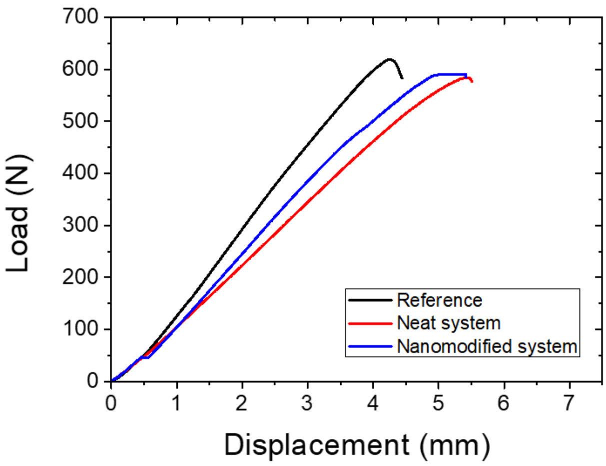

**Figure 74.** Representative plots of reference (black), neat (red line) and nanomodified (blue line) systems of Mode-II specimens.

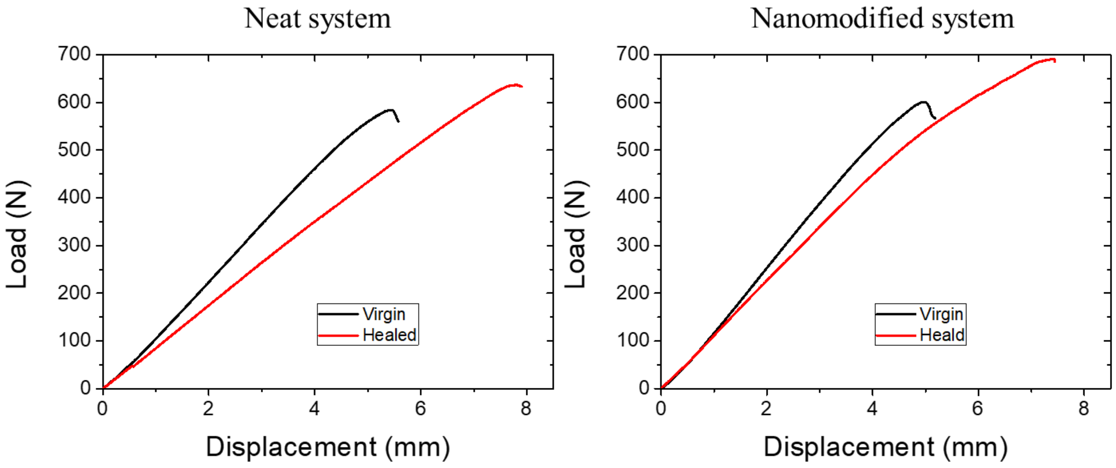

**Figure 75.** Representative plots of virgin (black line) and healed (red line) Mode-II specimens containing neat and nanomodified capsules.

| System | Mean Diameter (μm) | Gii$_c$ (kJ/m$^2$) Virgin | Gii$_c$ (kJ/m$^2$) Healed | Healing Efficiency (%) | Change of initial properties (%) |
|---|---|---|---|---|---|
| Reference | | 1.68 ± 0.11 | | | |
| Neat capsules | 205.8 ± 26.3 | 2.15 ± 0.32 | 3.89 ± 0.69 | 180.93 | +27.98 |
| Nanomodified capsules | 167.2 ± 10.2 | 2.17 ± 0.35 | 4.15 ± 0.73 | 191.24 | +29.17 |

| System | Mean Diameter (μm) | Max Load (N) Virgin | Max Load (N) Healed | Healing Efficiency (%) | Change of initial properties (%) |
|---|---|---|---|---|---|
| Reference | | 616.00 ± 33.61 | | | |
| Neat capsules | 205.8 ± 26.3 | 574.14 ± 27.25 | 628.27 ± 28.41 | 109.42 | -6.80 |
| Nanomodified capsules | 167.2 ± 10.2 | 598.57 ± 25.08 | 702.00 ± 42.29 | 117.28 | -2.83 |

**Figure 76.** Healing efficiency and change of initial mechanical properties of Mode-II specimens containing neat and nanomodified capsules in terms of $G_{IIc}$ (up) and maximum load (down).

### 6.5.3 Recovery of electrical properties at Mode-II geometry

The electrical healing efficiency was estimated from electrical conductivity measurements at virgin specimens before damage and healed specimens (**Figure 77**). In neat systems, the conductivity was evaluated at 1.32 × $10^{-5}$ S/m at virgin specimens. After the healing process, the values were regained by 60.2%, at 7.90 × $10^{-5}$ S/m. The recovery of the electrical properties was increased by 17 % when introducing capsules with a nano-modified healing agent. This increment was attributed to the inclusion of MWCNTs in the healing agent that restored the conductive network inside the material.

| System | σ (S/m) | Recovery of electrical properties (%) |
|---|---|---|
| Mode II – Neat System- Virgin | 1.32E-05 | |
| Mode II – Neat System- Healed | 7.90E-06 | 60.2 ± 6.5 |
| Mode II – Nanomodified System- Virgin | 8.62E-06 | |
| Mode II – Nanomodified System- Healed | 6.65E-06 | 77.3 ± 4.4 |

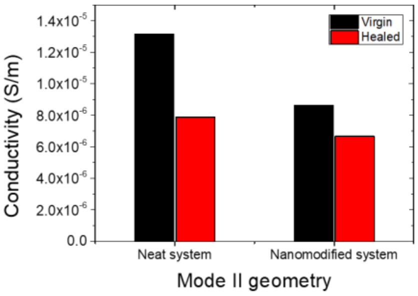

**Figure 77.** Healing efficiency of the Mode II specimens in terms of electrical properties.

### 6.5.4 Recovery of the low-velocity impact properties

The recovery of low-velocity impact properties was evaluated in terms of maximum load and absorbed energy. **Figure 78** depicts representative load-time and load-displacement curves from reference, virgin, and healed specimens (without any sensing mechanism, first case). Initially, a change in the slope of the load-time curves was observed after introducing the self-healing system, indicating that the bending stiffness and the impact modulus of the material were increased. In addition, the fluctuations after the maximum load at the reference specimens represented a progressive failure, with the main damage mode to be extensive delamination and fiber fracture. In opposite, the self-healing specimens (virgin) had smoother fluctuations which implied a progressive failure with only delamination damage mode or minor fiber breakage [135]. In terms of maximum load, the initial mechanical properties were increased by +16%, while the absorbed energy was reduced by -13% after the incorporation of the self-healing system. This was attributed to the increased stiffness of virgin specimens and the decrease of the toughness that happened with the introduction of catalyst particles for the healing process [147]. This phenomenon also indicated an insufficient catalyst dispersion [147]. As it is known, the stiffening of a polymer composite leads to higher maximum loads but lower absorbed energy [148,149].

Moreover, since the maximum load of an impact indicates the internal delamination and fiber/matrix failure, it is evident that the incorporation of the self-healing system offered an obstruction to the propagation of the internal damage [135]. A sufficient healing efficiency was calculated at 102% in maximum load and 101% for the absorbed energy [150]. A full recovery of the two measured properties was observed, with the two percentages being slightly above 100%, which can be related to eliminating any manufacturing voids that may exist.

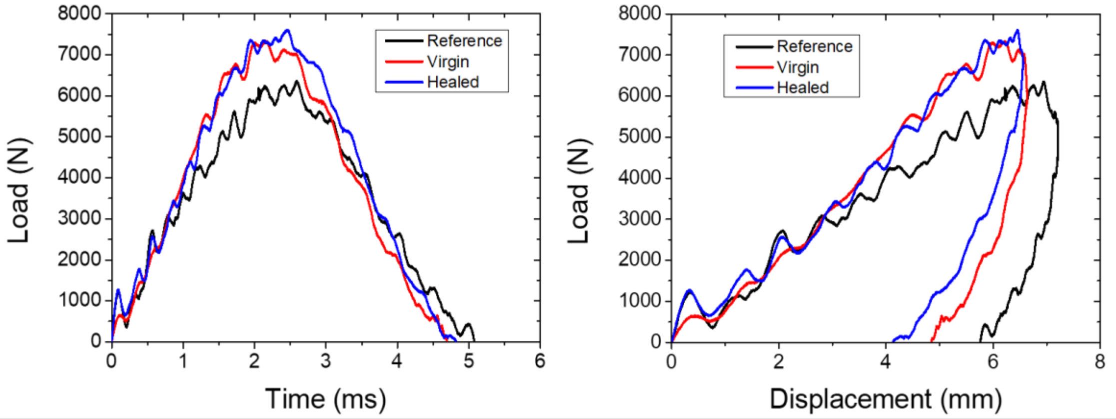

| System | Max Load (kN) | Absorbed Energy (J) | Change of initial properties (Load, %) | Change of initial properties (Energy, %) | Healing Efficiency (Load, %) | Healing Efficiency (Energy, %) |
|---|---|---|---|---|---|---|
| Reference | 6.30 ± 0.17 | 22.59 ± 0.58 | | | | |
| Virgin | 7.32 ± 0.41 | 19.60 ± 1.72 | +16.19 | -13.24 | | |
| Healed | 7.49 ± 0.49 | 19.79 ± 2.35 | | | 102.33 | 100.97 |

**Figure 78.** Healing efficiency and change of initial mechanical properties of reference (black line), virgin (red line), and healed (blue line) impact specimens.

**Figure 79** depicts representative plots of virgin specimens (that contained the self-healing system), virgin specimens with carbon tows, and virgin specimens with spray-coated lines for the damage sensing capability (first and second case). Interpreting the load-time and load-displacement curves, both carbon virgin and spray virgin specimens exhibited a decrease in the bending stiffness due to the introduction of the carbon tows and the spray lines that acted as defects. The self-healing specimens (virgin) had smooth fluctuations, as previously, resulting in a progressive failure. Carbon capsules specimens decreased their properties in terms of maximum load by -11%, while the spray capsules specimens by -16%. However, the carbon specimens exhibited an increase of the absorbed energy by +12% due to the carbon tows incorporation that acted as a “second reinforcement” and improved the initial mechanical properties. In the case of spray-coated specimens, the interlaminar fracture (delamination) toughness energy or the absorbed energy increased ca. +18% after the spray coating of the SWCNTs ink due to the bridging effects; thus, the energy absorption was higher [151].

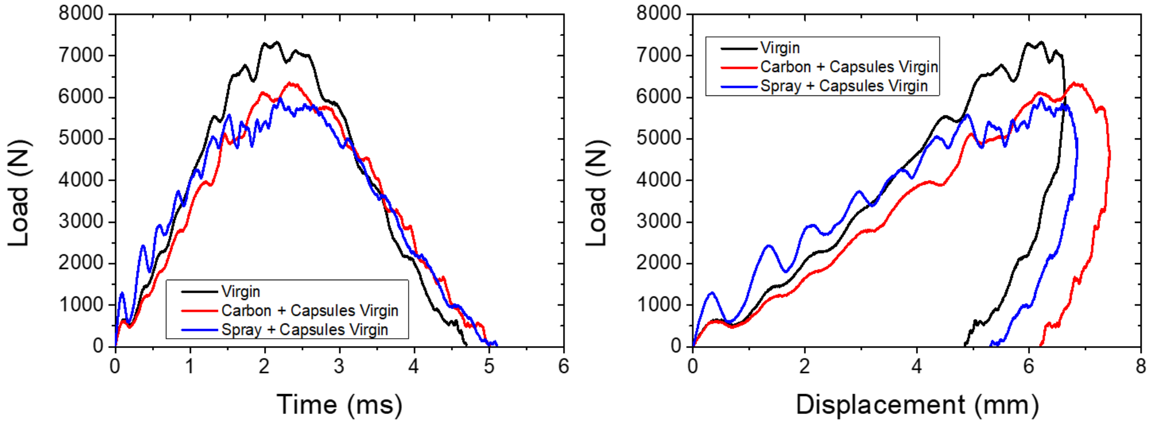

| System | Max Load (kN) | Absorbed Energy (J) | Change of initial properties (Load, %) | Change of initial properties (Energy, %) |
|---|---|---|---|---|
| Virgin | 7.32 ± 0.41 | 19.60 ± 1.72 | | |
| Carbon + Capsules Virgin | 6.51 ± 0.45 | 21.93 ± 1.32 | -11.06 | +11.89 |
| Spray + Capsules Virgin | 6.09 ± 0.39 | 23.10 ± 0.64 | -16.80 | +17.86 |

**Figure 79.** Change of the initial mechanical properties of impact specimens with capsules (black line) after the introduction of carbon tows (red) and spray lines (blue line) for the damage sensing capability.

The knockdown effect after the incorporation of the self-healing system and the healing efficiency was also evaluated in both self-sensing systems (second case). In the case of carbon tows incorporation, the addition of the self-healing system at a simple self-sensing structure improved the stiffness of the material with an increment of the maximum load by +10% and decreased the absorbed energy by -7%. This was also confirmed by observing the slops of the load-time curves from carbon reference and carbon virgin systems in **Figure 80**. This behaviour is similar to the previous case of the composites without the self-sensing methods (**Figure 78**). As previously mentioned, significant healing efficiency values were evaluated at 99.4% in terms of the max load and 101.1% in terms of the absorbed energy.

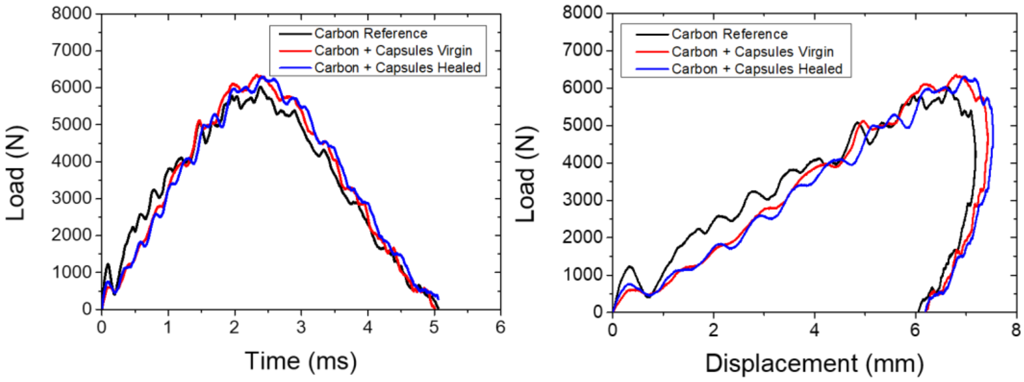

| System | Max Load (kN) | Absorbed Energy (J) | Change of initial properties (Load, %) | Change of initial properties (Energy, %) | Healing Efficiency (Load, %) | Healing Efficiency (Energy, %) |
|---|---|---|---|---|---|---|
| Carbon Reference | 5.90 ± 0.35 | 23.63 ± 0.37 | | | | |
| Carbon Virgin | 6.51 ± 0.45 | 21.93 ± 1.32 | +10.39 | -7.19 | | |
| Carbon Healed | 6.48 ± 0.48 | 22.15 ± 1.24 | | | 99.4 | 101.1 |

**Figure 80.** Healing efficiency and change of initial mechanical properties of reference (black line), virgin (red line), and healed (blue line) impact carbon specimens.

In spray-coated systems, the incorporation of the self-healing system improved the stiffness. Still, it did not affect the toughness of the material, with the maximum load to be increased by +4% and the absorbed energy to be insignificantly increased by +1% (**Figure 81**). The healing efficiency in terms of the max load values was evaluated at 102.6%, similar to the previous systems. The absorbed energy was recovered by 99.6% which was slightly lower than in the carbon specimens, indicating that the bridging effects due to the coating of the CNTs ink were affected and reduced from the transportation of the healing agent into the crack plane. The sharp fluctuations were evidence that, in this case, a progressive failure with the main damage mode to be extensive delamination and fiber fracture occurred opposing to the simple and carbon specimens.

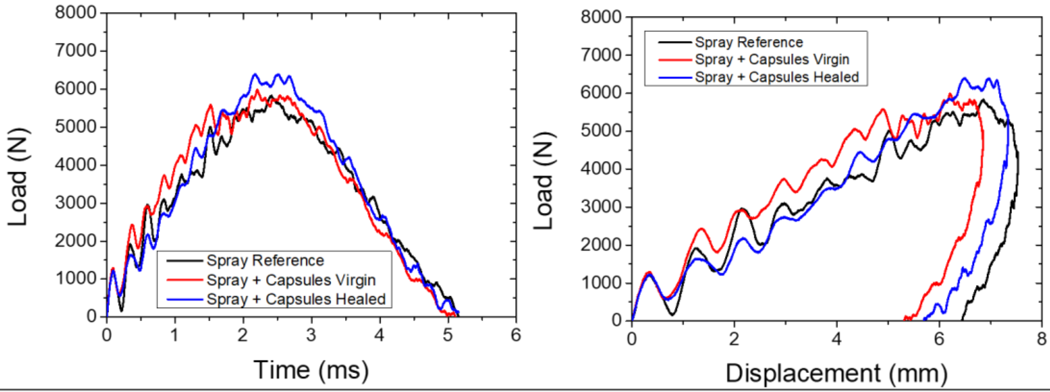

| System | Max Load (kN) | Absorbed Energy (J) | Change of initial properties (Load, %) | Change of initial properties (Energy, %) | Healing Efficiency (Load, %) | Healing Efficiency (Energy, %) |
|---|---|---|---|---|---|---|
| Spray Reference | 5.82 ± 0.18 | 23.41 ± 0.25 | | | | |
| Spray Virgin | 6.09 ± 0.39 | 23.10 ± 0.64 | +4.58 | +1.32 | | |
| Spray Healed | 6.25 ± 0.24 | 23.03 ± 0.76 | | | 102.6 | 99.6 |

**Figure 81.** Healing efficiency and change of initial mechanical properties of reference (black line), virgin (red line), and healed (blue line) impact spray specimens.

## 6.5.5 Recovery of electrical properties at low-velocity impact geometry

The recovery of the electrical properties was estimated from electrical conductivity measurements at virgin specimens before damage and healed specimens in the three categories (**Figure 82**). In the simple capsule system (no-sensing), the conductivity was evaluated at $4.7 \times 10^{-8}$ S/m at virgin specimens. After the healing process, the values were regained by 83.99 %, at $3.67 \times 10^{-8}$ S/m. In the carbon- capsules category, specimens revealed a conductivity of $7.84 \times 10^{-4}$ S/m at virgin specimens, while the healed specimens exhibited values of $7.85 \times 10^{-4}$ S/m. The electrical healing efficiency was calculated at 100 %, i.e., a full restoration was achieved. In the case of the spray- capsules system, virgin specimens exhibited conductivity values of $4.21 \times 10^{-4}$ S/m at virgin specimens. The healed specimens' conductivity was found at $4.11 \times 10^{-4}$ S/m, indicating a recovery of 97.6 %.

| System | σ (S/m) | Recovery of electrical properties (%) |
|---|---|---|
| Low velocity impact- Virgin | 4.37E-08 | |
| Low velocity impact- Healed | 3.67E-08 | 84.0 ± 4.2 |
| Low velocity impact- Carbon- Virgin | 7.84E-04 | |
| Low velocity impact- Carbon- Healed | 7.85E-04 | 100.1 ± 1.1 |
| Low velocity impact- Spray- Virgin | 4.21E-04 | |
| Low velocity impact- Spray- Healed | 4.11E-04 | 97.6 ± 3.2 |

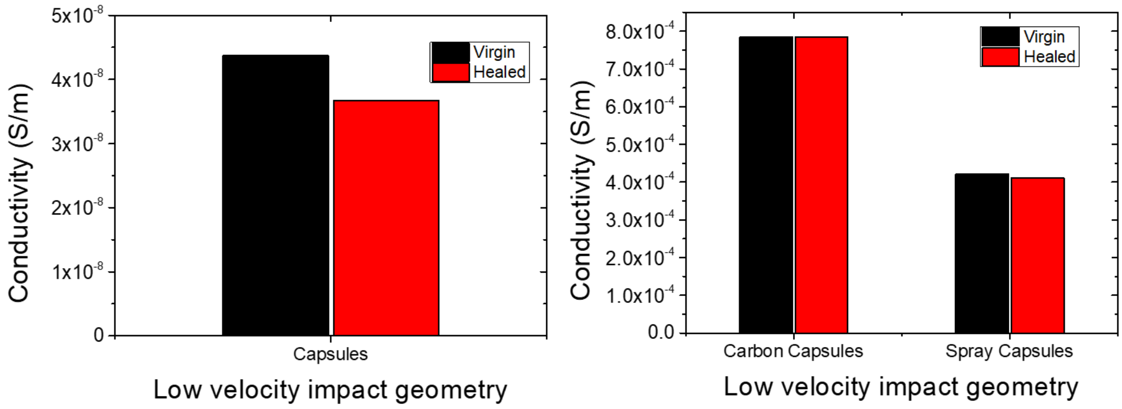

**Figure 82.** Healing efficiency of the low-velocity impact specimens in terms of electrical properties.

### 6.5.6 Non-destructive evaluation of the damage and the successful healing

As the type of damage introduced after impact is blind (BVID), the pulsed IR thermography was employed to assess i) any differences between the reference specimens and self-healing (capsule-virgin) specimens, ii) the successful damage after impact, and iii) evaluate the repair process. **Figure 83** illustrates the reference and the virgin capsule specimens IR images. As it can be observed, the thermal profile was the same in both cases, proving that the incorporation of the healing system did not affect the specimen.

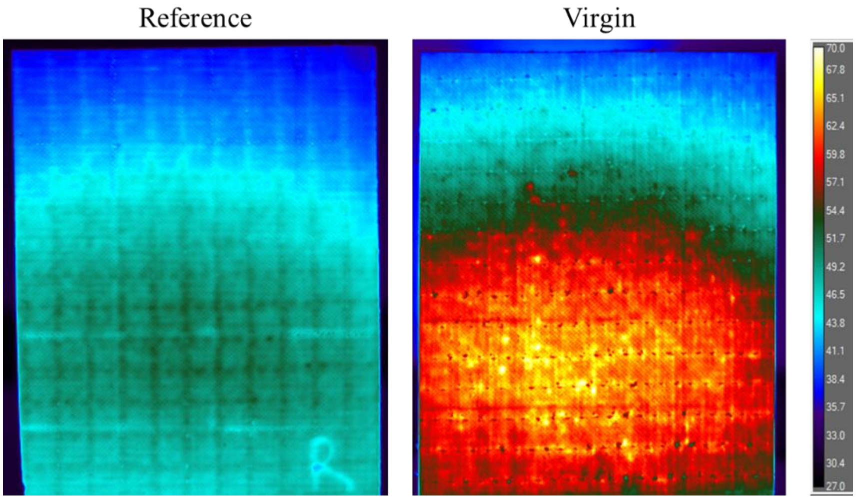

**Figure 83.** IR thermography images from reference and virgin specimens.

**Figure 84** depicts IR images from virgin, damaged, healed, and healed & damaged low-velocity impact specimens with capsules. The IR image from the virgin specimen can reveal that there were no defects inside the material. In the second image, the impact damage can be clearly seen. The substantial quantity of dissipation of the energy simultaneously with the local temperature increase revealed the delamination inside [152]. The successful healing process can be confirmed via the third image from the healed specimen that shows the elimination of the delaminations. The same damage imprint can be observed from the final image taken after the impact test after the healing process. The same observations and "pattern" can be seen in the case of the introduction of carbon tows (first damage sensing system) (**Figure 85**) as well as in the second damage-sensing system (spray lines) in **Figure 86**.

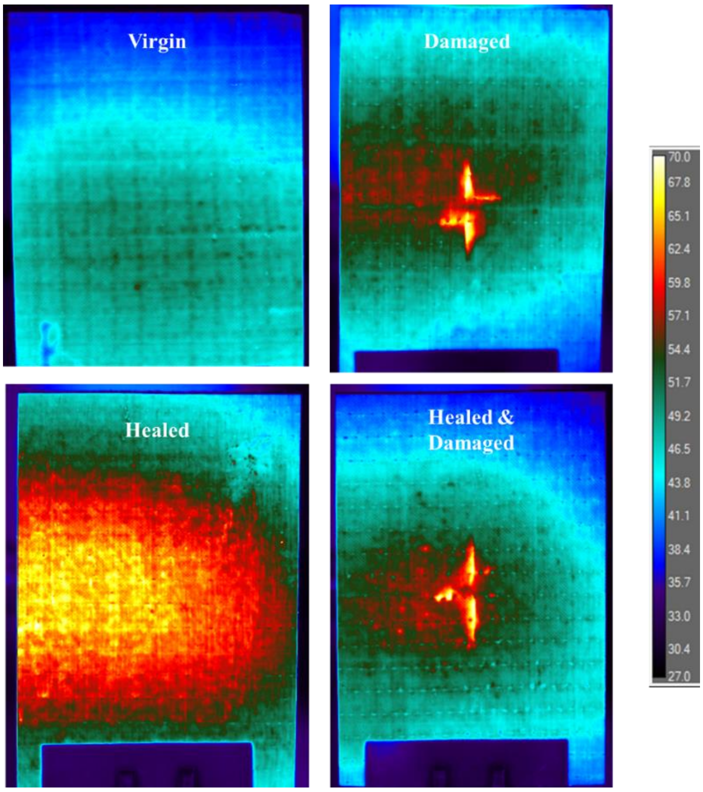

**Figure 84.** IR thermography images from virgin, damaged, healed, and healed & damaged low-velocity impact specimens.

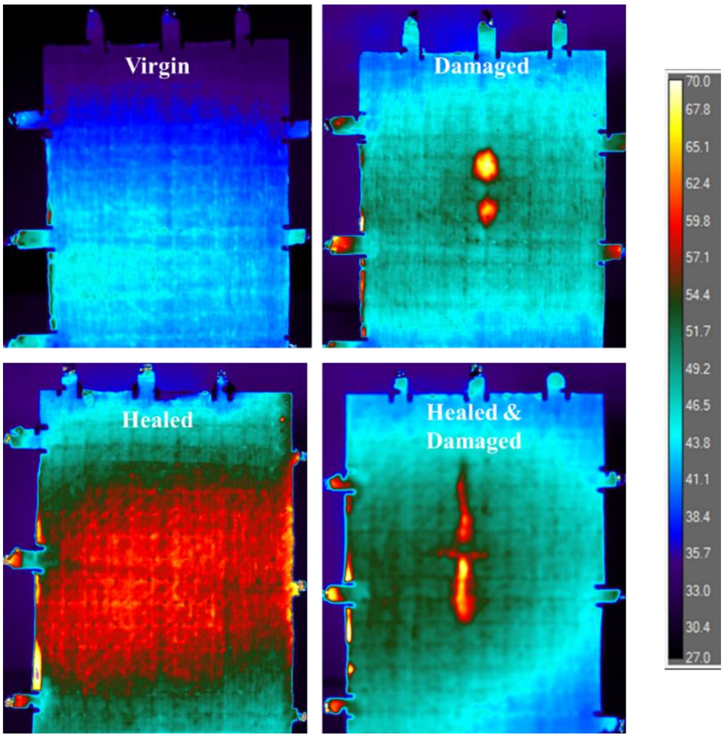

**Figure 85.** IR thermography images from virgin, damaged, healed and healed & damaged specimens with carbon tows.

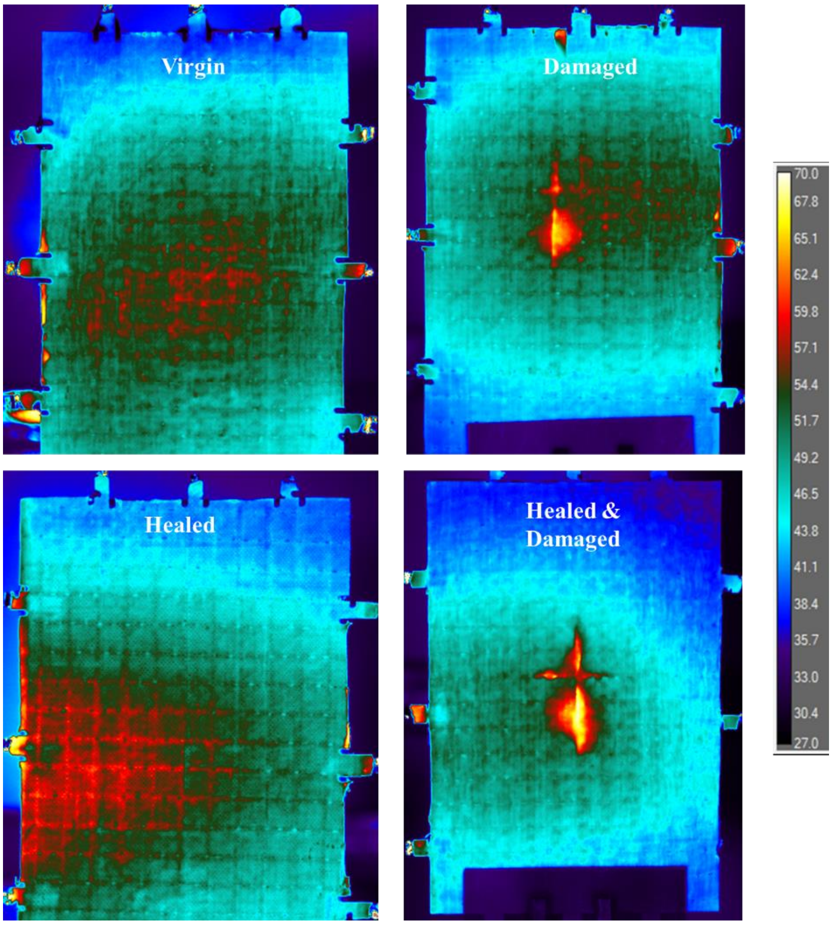

**Figure 86**. IR thermography images from virgin, damaged, healed, and healed & damaged specimens with spray lines.

### 6.5.7 Compression after impact (CAI)

CAI tests were performed after the second impact after the healing process. In the case of reference specimens, the CAI tests were performed after their first impact. **Figure 87** depicts the bar charts of the maximum CAI strength ($F_{CAI}$) and load obtained from the reference, the capsules, the carbon capsules, and the spray capsules specimens. Representative load-displacement curves and the aforementioned values are also depicted in **Figure 87**. Note that the simple-virgin specimens with capsules were compared with the reference, and both carbon capsules and spray capsules specimens were compared with the virgin capsules specimens. Results indicated that in terms of $F_{CAI}$, simple specimens with capsules reduced their properties by -22.7% in relation to the reference values. This can be attributed to the already reduced toughness of capsule specimens against the reference that had already been observed from the impact results. The two main mechanisms that usually occur at a compression after impact failure are i) crack or delamination propagation of the impact damage and ii) the buckling of the impact damage zone [153]. The buckling effect as well as the CAI strength are affected and can be enhanced from the resin-rich regions [154]. After the healing process, the repaired areas were more affluent with resin pockets; thus, the crack propagation/buckling effect was more intense.

The carbon capsules system exhibited an increase of +13.6% from the systems without the damage sensing capability. In this case, the increase can be occurred due to the addition of the carbon tows inside the material. The incorporation of carbon fabrics into a glass fiber composite (i.e., hybrid composites) can improve the compressive properties [155]. However, the spray capsules system revealed a decrease of –6.4% in relation to the virgin capsules systems due to CNTs coating that decreased the compressive strength [156].

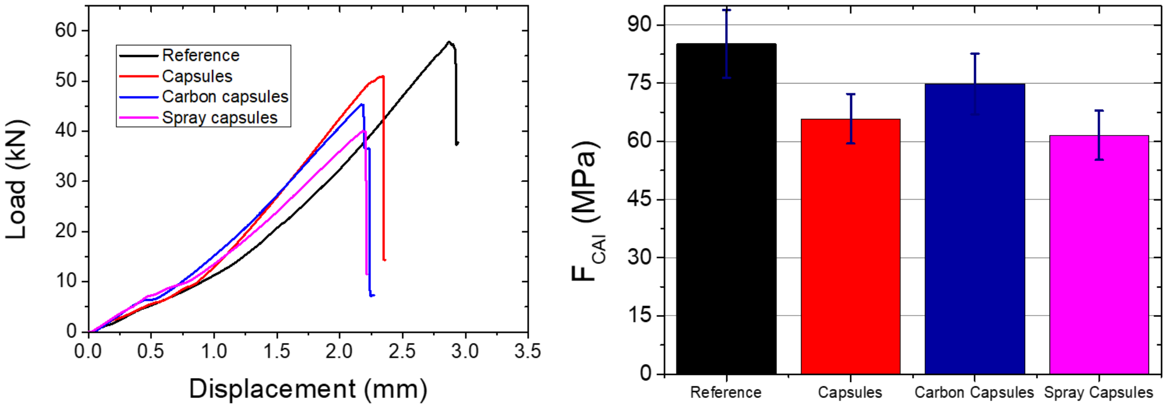

| System | Max Load (kN) | $F_{CAI}$ (MPa) | Change of properties ($F_{CAI}$, %) |
|---|---|---|---|
| Reference | 57.36 ± 5.00 | 85.15 ± 8.76 | |
| Capsules | 50.14 ± 5.04 | 65.82 ± 6.36 | -22.7 |
| Carbon Capsules | 50.03 ± 5.35 | 74.80 ± 7.86 | +13.6 |
| Spray Capsules | 42.27 ± 5.15 | 61.59 ± 6.35 | -6.4 |

**Figure 87.** Representative plots and change of initial mechanical properties of reference, capsules, carbon capsules, and spray capsules specimens of CAI tests.

### 6.5.8 Non-destructive evaluation of the damage after the CAI test

**Figure 88** depicts IR thermography images after CAI tests from reference, capsules, carbon capsules, and spray capsules specimens. Results in all cases revealed an appropriate CAI damage inside the material depicted as an almost straight line [157]. Therefore, the addition of the self-healing system did not affect the initial mechanical performance of the composites.

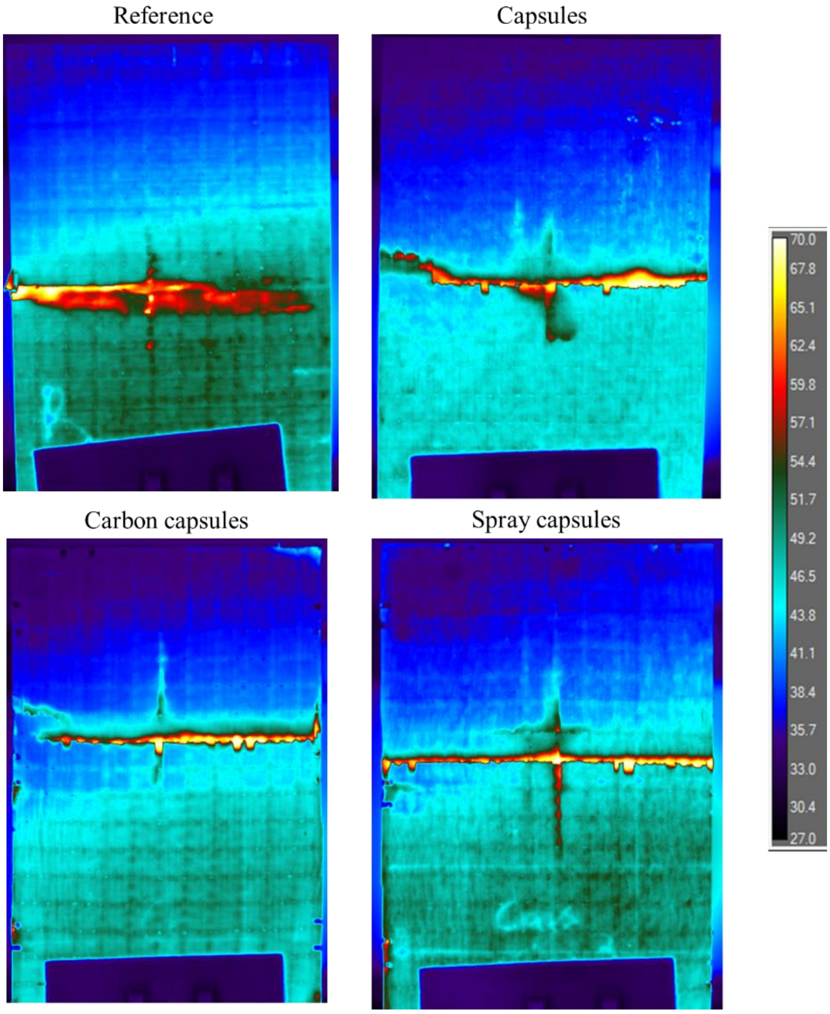

**Figure 88.** IR thermography images after CAI test from reference specimens, capsules, carbon capsules, and spray capsules specimens.

### 6.5.9 Recovery of Lap Strap strength

**Figure 89** depicts representative stress-strain curves from the reference, neat capsules system, and nanomodified capsule system of lap strap specimens. A sudden and brittle failure of the adhesive between the lap and the strap occurred in all cases, as was expected, that manifested with a small drop at the stress-strain curve. The same mechanical behaviour was also observed after the healing process (healed specimens), as shown in **Figure 90**. Incorporating the healing system in both systems (neat and nanomodified) within the adhesive polymer did not affect the initial properties of the coupons. A negligible reduction of the initial strength properties of -2% was observed in neat systems since, in nano-modified systems, the same values were exhibited with the maximum reference stress.

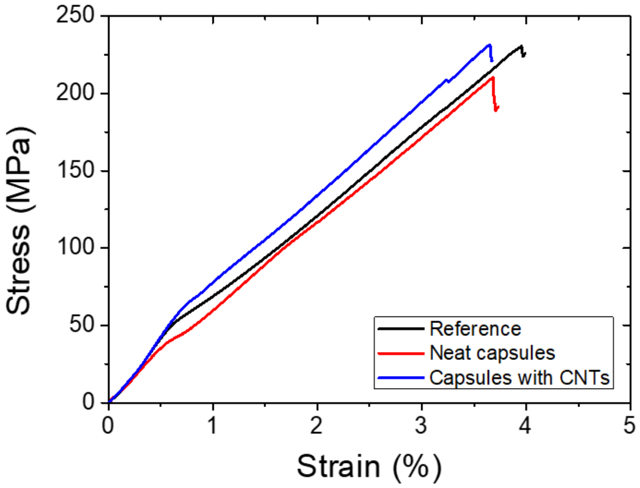

**Figure 89.** Representative plots of reference (black line), neat system (red line), and nanomodified system (blue line) of lap strap specimens.

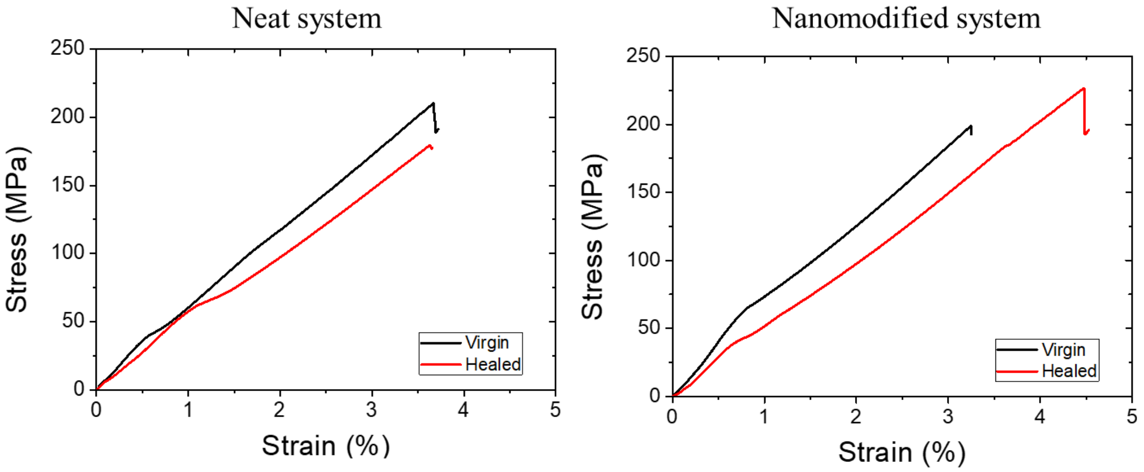

**Figure 90.** Representative plots of the virgin (black line) and healed (red line) lap strap specimens containing neat and nanomodified capsules.

Successful recovery of the stress at the delamination point of the strap was also estimated (**Figure 91**). In detail, neat systems restored their mechanical properties by 90.67% (from 228.08 ± 17.24 to 207.33 ± 39.53 MPa), while nanomodified systems increased their healed values from 233.68 ± 18.25 to 240.07 ± 32.21 resulting in a healing efficiency of 107.36%. As in the case of the previous studied geometries of this research (matrix level, mode-ii and impact), the addition of the MWCNTs into the healing agent sufficiently improved the healing efficiency by ca. 17% compared to the neat capsule system.

| System | Mean Diameter (μm) | Max stress Virgin (MPa) | Max stress Healed (MPa) | Healing Efficiency (%) | Change of initial properties (%) |
|---|---|---|---|---|---|
| Reference | | 232.91 ± 7.33 | | | |
| Neat capsules | 205.8 ± 26.3 | 228.08 ± 17.24 | 207.33 ± 39.53 | 90.67 | -2.07 |
| Capsules with CNTs | 167.2 ± 10.2 | 233.68 ± 18.25 | 240.07 ± 32.21 | 107.36 | +0.03 |

**Figure 91.** Healing efficiency and change of initial mechanical properties of lap strap specimens containing neat and nanomodified capsules.

## 6.5.10 Recovery of electrical properties at lap strap geometry

The electrical healing efficiency of the lap strap geometry was evaluated from the values before and after the healing process. At neat systems, the initial conductivity values were estimated at $2.17 \times 10^{-5}$ S/m, while at healed specimens, the conductivity reached $5.54 \times 10^{-5}$ S/m. An electrical recovery of 24.9% was estimated. However, in the case of the specimens containing capsules with a nanomodified healing agent, the healing efficiency in terms of electrical properties was significantly increased by 37.6%. As can be seen, the inclusion of CNTs into the healing agent had a very beneficial effect on the restoration of the conductive network.

| System | σ (S/m) | Recovery of electrical properties (%) |
|---|---|---|
| Lap Strap– Neat System- Virgin | 2.17E-05 | |
| Lap Strap– Neat System- Healed | 5.54E-06 | 24.9 ± 5.2 |
| Lap Strap– Nanomodified System- Virgin | 1.00E-04 | |
| Lap Strap– Nanomodified System- Healed | 4.19E-05 | 62.5 ± 1.6 |

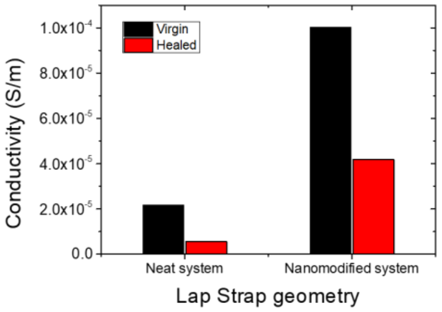

**Figure 92.** Healing efficiency of the lap strap specimens in terms of electrical properties.

## 6.6 Conclusions

This chapter reports the synthesis of self-sensing and self-healing capsule-based composites. Specifically, both capsules and catalysts were dispersed into composites with nano-modified epoxy matrix. The restoration of the electrical and mechanical properties was successfully evaluated at three geometries, mode-II fracture toughness ($G_{IIc}$), low-velocity impact, and lap strap geometry that can simulate the behaviour of a composite structure.

At Mode-II tests, 20 wt. % of neat and nanomodified capsules were incorporated with 2.5 wt. % of catalyst at the midplane of the specimens. The introduction of the self-healing system improved the initial mechanical properties in fracture toughness by +28% but decreased the maximum load by -7% in the case of neat capsules. The mechanical healing efficiency was calculated at 180% in $Gii_c$ and 109% for the max load. Electrical properties were recovered by 60%. However, in the nano-modified capsule system, the $Gii_c$ increased by +29%, and the maximum load was reduced by -3% after the incorporation of the healing system. Mode-II fracture toughness was regained by 191% and the maximum load by 117%. The electrical healing efficiency was recovered by 77%. It is evident that with the nanomodification of the healing agent, the healing efficiency was significantly improved by ca. 10%.

Two different cases were tested at low-velocity impact geometry to evaluate their mechanical and electrical healing efficiency. In the first case study, reference and self-healing systems were manufactured and compared. The maximum load was improved by +16%, although the specimens with self-healing properties absorbed less energy by -13%. A satisfying healing efficiency in both properties was revealed at ca. 101%. In the second case study, the introduction of the sensing technologies reduced the maximum load by -11 and -17% for the carbon specimens and spray coated specimens, respectively. However, the energy absorption was increased by +12% and 18%. When introducing the self-healing system to a sensing system, the carbon capsule systems increased their maximum load by +10% but reduced the absorption of the impacted energy by -7%. In the case of spray-coated specimens, the maximum load improved by 5%, as well as the energy absorption by 1%. The mechanical healing efficiency calculated at sensing systems was ranging at the same values from 99% to 102% for both measured properties.

CAI tests that were performed, revealed that incorporating a self-healing capsule-based system reduced the CAI strength by -23% when compared to reference composites. However, the introduction of the carbon tows into self-healing composites increased the strength by +14%, but the coating of the spray ink in lines decreased the properties by -6%. Considering that the residual CAI strength is one of the most important properties of composite material, the most promising technology for a self-sensing and self-healing composite concurrently was found to be the carbon tow system.

At the lap strap geometry or at the modeled structure level, the incorporation of both neat and nanomodified capsules at the adhesive area had a negligible effect on the strength by reducing the properties by -2% in the first case and remained stable in the second case, thus showing that the employment of capsule-based methodologies did not affect the initial properties. Mechanical healing efficiency calculations exhibited a recovery of 91% of the lap strap strength using neat capsules and a 107% recovery in the case of nanomodified capsules. The electrical recovery was estimated at 25% for the neat lap strap and 62% for the nanomodified systems. The calculated high mechanical and electrical healing efficiency values, along with the elimination of the knock-down effect, are promising factors for the scale-up of the employment of a nanomodified capsule-based self-healing method to model composite structures.

# CHAPTER 7

# Intrinsically self-healing composites

## 7.1 Introduction

The intrinsic approach does not have a segregated healing agent and can be triggered by an external stimulus such as heating. They are based on reversible reactions, molecular diffusion, chain mobility, ionic interactions, hydrogen bonding, or melting of thermoplastics [158]. Since these reactions are reversible, there can be multiple healing events.

The design cycle is different from the capsule-based systems since, in this case, the matrix is inherently self-healing, and no additional healing agent is needed (**Figure 93**). With the intrinsic approach, many problems with the compatibility and reactivity between the healing agent and matrix can be avoided. Firstly, the matrix material is synthesized, then the material is mechanically characterized, followed by the triggering process, and finally, the healing efficiency is evaluated.

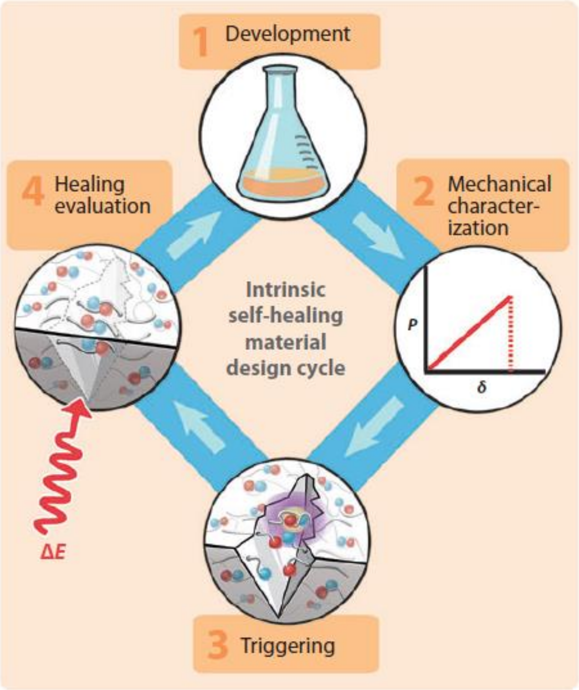

**Figure 93.** Design cycle of capsule-based self-healing materials. ("Used with permission of Annual Reviews, Inc., from Self-healing polymers and composites, B.J. Blaiszik, S.L.B. Kramer, S.C. Olugebefola, J.S. Moore, N.R. Sottos and S.R.White, 40:179-211, permission conveyed through Copyright Clearance Center, Inc.")

The self-healing can be achieved with the incorporation of meltable thermoplastic additives into the thermoset matrix. The self-healing process includes the melting and then the flowing of the material into the crack plane and fills the damage [159]. Hayes et al. [160] presented a self-healing matrix and composite system by incorporating different weight fractions of thermoplastic particles into the thermosetting matrix. After damage, the healing process took place at 100 °C to 130 °C. Results showed a recovery in load at failure from 40% to 66% when using 20 wt.% of particles. When the healing temperature was set at 130 °C for 1 hour and 20 wt. % of healing agents were dispersed, and a recovery of 75% was achieved. By introducing only 5 wt. % of particles in the composite, the values deceased at the half. Glass fiber composites were also manufactured with thermoplastic particles and tested under impact. The self-healing composites reduced the damaged area by ca. 30% after the healing.

Another category of intrinsically self-healing polymers is ionomeric materials. The healing chemistry, in this case, is based on the repeated ionic segments into their molecular chains [161]. They need an external stimulus such as ultraviolet (UV) irradiation or temperature for the triggering of the healing process. Sundaresan et al. [162] demonstrated a self-healing ionomeric polymer composite material tested under medium velocity impact. The composite material was prepared by embedding carbon fibers in Surlyn 8940. Surlyn was an ethylene/methacrylic acid (E/MAA) copolymer, and their MAA groups are partially counteracted with sodium ions. The healing process took place at 95 °C, which is the melting point of Surlyn. The heating for the healing process was performed by the incorporated carbon fibers with low electrical resistance and resistive heating connected with a power supply (**Figure 94**).

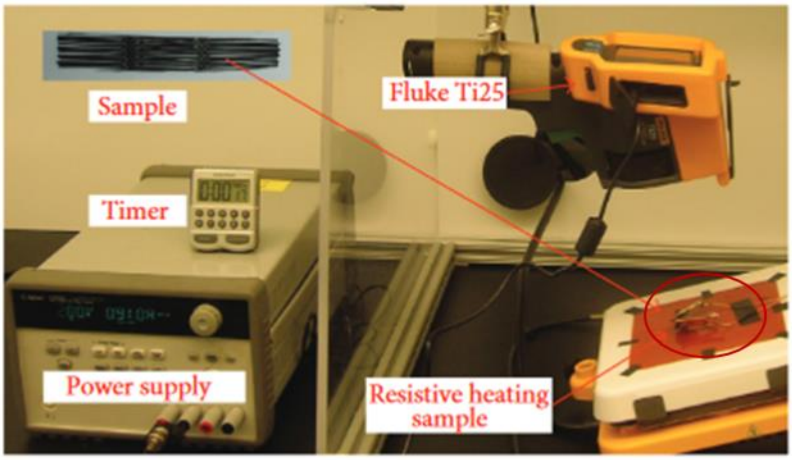

**Figure 94.** Experimental configuration for the healing process of the ionomeric composite.

Results indicated that the surface damage in the polymer was successfully healed completely in less than 30 seconds.

The supramolecular polymers are based on non-covalent interactions and usually are thermally triggered [163]. The non-covalent chemistry includes the electrostatic interactions, metal ion coordination, hydrogen bonding, pi-pi interactions, halogen bonding, hydrophobic interactions, or van der Walls forces [164]. Kostopoulos et al. [165] used a supramolecular polymeric interlayer for the toughening and healing of carbon fiber composites. Specimens tested under Mode-II interlaminar fracture toughness. The healing process was performed at 100 °C for 15 minutes under 1 kN of loading. A sufficient recovery of more than 85% in terms of maximum load and 100% in terms of fracture toughness. In a similar study, the same author investigated the Mode-I fracture toughness properties at the same composites [166]. The incorporation of the supramolecular film exhibited a significant increase of the peak load and the mode I interlaminar fracture energy (GIc) about 540% and 1550%, respectively, when compared with composites without film. The healing efficiency was estimated up to 64% and 59% for the peak load and $G_{Ic}$ properties, respectively. The recovery of the properties remained high after seven healing cycles.

One of the most important and studied reversible reactions that are based on dynamic bonds is the Diels-Alder (DS) reaction [167–169]. The Diels–Alder reaction is an organic [4+2] cycloaddition reaction between a conjugated diene and a dienophile [170]. This reaction results in the adduct in generally two exo and endo stereoisomers, and the product is usually a mixture of two products, i.e., a substituted cyclohexene system. The reverse reaction is known as the retro-Diels–Alder reaction (**Figure 95**). One major advantage is the theoretically infinite number of healing cycles [171–175].

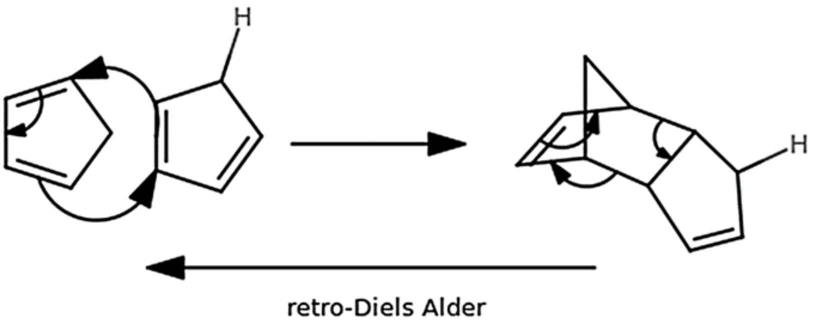

**Figure 95.** Diels-Alder and retroDiels-Alder reactions

The furan/maleimide is one of the most common pairs of diene/dienophile due to their electronic nature and high reactivity [176]. This reaction is a very effective method for the development of reversible polymer thermosets by three methods: i) polymerization of a monomer with furan or maleimide parts, ii) polymerization of a monomer bearing furan-maleimide cycloadduct, and iii) cross-linking of a thermoplastic with furans or maleimide pending groups in order to prepare reversible thermosets [177]. The DA mechanism can be incorporated into polymers using the conventional polymerization techniques in order to provide the self-healing functionality of a thermoset polymer [178,179]. Chen et al. [180] were the first that reported a DA self-healing material utilizing this strategy and indicated a recovery of 57% of the fracture load and 41% in terms of fracture toughness (**Figure 96**). The healing process was performed at 120 °C. Additionally, they observed a 20% reduction in the healing efficiency in failure load between the second and third healing cycles.

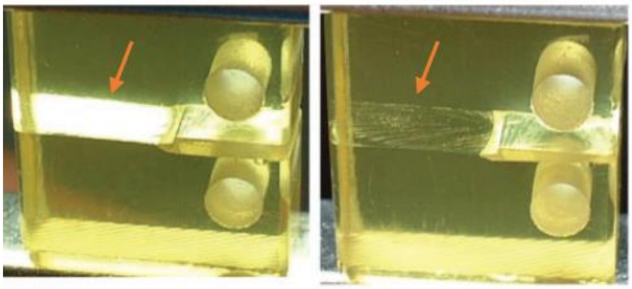

**Figure 96.** DA self-healing polymer before and after healing.

In a recent study, Orozco et al. presented an electroactive self-healing and shape memory polymer composite based on the DA reaction [181]. They prepared a furan-grafted polyketone polymer with dispersed MWCNTs cross-linked with bismaleimides. Results indicated that these polymers have efficient electroactive shape memory, self-healing, shape-reprogramming as well as excellent re-processability.

Kostopoulos et al. studied the use of self-healing DA epoxy films on a carbon fiber composite that was tested under low-velocity impact [182]. The DA material in unreacted form was dissolved into tetrahydrofuran (THF) solvent and then was electro-spuned into the desired areas of the composite between all carbon fiber prepreg layers. The introduction of the self-healing agents did not affect the impact and post-impact response, while the composites fully restored their properties.

Nevertheless, at the synthesis stage and/or the healing process of the polymers, several side reactions can occur and may weaken the healing ability of the system [171,183,184]. The side reactions are performed between the maleimide groups that react with the excess amine elements (Michael addition), and/or the exposed maleimides react together (homopolymerization) [185–187]. The most important parameter that encourages these side reactions is the processing time at high temperatures. If the polymer is exposed at an elevated temperature for a long time, the possibility of side reaction increases significantly. In order to avoid this phenomenon, Turkenburg, and Fischer [188] modified an epoxy system with DA thermo-reversible crosslinks by a two-step process. The first step consists of the polymerization reaction of the epoxy with the furfuryl amine, followed by the introduction and the network formation using 1,1-(methylene di-4,1-phenylene) bismaleimide (BMI). Rheological measurements indicated that cracking of crosslinking and then reforming the polymeric networks may be achieved repeatedly for at least five heating cycles

## 7.2 Scope

The work related to this chapter concerns the synthesis of intrinsically self-healing polymeric films capable of restoring the mechanical properties of a composite based on the Diels-Alder reaction. Specifically, the three cross-linkers, BMI-1500, BMI-1700, and BMI-3000, were incorporated into the DGEBA epoxy resin via a two-stage process. The self-healing polymer was then transformed into films for easy application into composite materials. The composites were tested into mode-ii fracture toughness tests, while the healing efficiency was estimated after three healing cycles. The identification of the changes in the molecular structure of the BMI polymers after the manufacturing and the three healing cycles was performed by Raman spectroscopy.

## 7.3 Experimental

### 7.3.1 Materials

The Diglycidyl ether of bisphenol A (DGEBA) epoxy resin was obtained from Hexion, Greece, and furfuryl amine (FA) was obtained from Sigma-Aldrich. The cross-linkers were the bismaleimide oligomers BMI-1500 (viscous liquid), BMI-1700 (viscous liquid), and

BMI-3000 (light yellow powder), kindly provided by Designer Molecules Inc. It should be pointed out that the number in the BMI name denotes the average Molecular Weight of the oligomer in daltons. According to the material datasheets, the average value of n lies between 1-10 for the BMI-1700 and BMI-3000, while for BMI-1500 was 1.3.

## 7.3.2 Synthesis of the intrinsic self-healing polymers

*7.3.2.1 Pre-polymerization of the DGEBA/FA* The pre-polymerization of the DGEBA with the furfuryl-amine is important since this step induces a significant degree of (irreversible) polymerization to the required material to ensure sufficient mechanical strength. DGEBA and FA were mixed in a beaker at a 5:1 ratio in order to ensure that each amine group would react twice (once as primary amine and once as secondary amine) with an epoxy group. Moreover, this process makes them inactive, ensuring the elimination of the unwanted side reactions to the maleimide [189]. The beaker was placed on a hot plate under continuous stirring. Gradual heating of 3 °C/min up to 125 °C was performed in order to avoid the evaporation of the FA in the early stages of polymerization. When the temperature reached 125 °C, the mixture was left for curing for 1.5 h, and the final prepolymer was left to cool down at room temperature. The final product was ground using a laboratory grinder mill at the end of the pre-polymerization process.

### *7.3.2.2 Synthesis of the reversible polymers*

According to previous research, the introduction of the reversible cross-linkers at the DGEBA resin occurred by adding a stoichiometric amount of BMI to the prepolymer with a 1:1 ratio. The reaction between the different BMI and the prepolymer was performed in a ceramic container under continuous stirring. In order to avoid unwanted side reactions that take place at high temperatures after a long period of exposure, the prepolymer/BMI mixture was rapidly heated up to 150 $^oC$ (time < 3 min). After this process, the final produced intrinsically self-healing polymer was left to cool down to room temperature and was ground using a laboratory grinder mill into powder (BMI powders).

*7.3.2.3 Manufacturing of the intrinsically self-healing BMI films*

The BMI films were produced at two different thicknesses, 0.1 and 0.4 mm. In order to achieve the desired thickness of the film, a spacer was added. The BMI powder that was produced was placed between two flat metallic plates covered with release film. The plates with BMI powder inside were placed in a hot press, and the temperature was set at 150 $^{o}$C. When the temperature reached, a pressure of 3 MPa was applied for 3 min, and then the temperature was rapidly decreased to room temperature.

### 7.3.3 Manufacturing of composite materials for Mode-II tests

Four composite laminates were manufactured for each film thickness (reference, BMI-1500, BMI-1700, and BMI-3000) using 16 plies of the UD glass fabric. The manufacturing process was the hand lay-up technique with an applied pressure of 3 MPa, and curing took place under ambient conditions for 24 hours. Spacers were used in order to ensure a uniform laminate thickness. The intrinsically self-healing BMI films were placed at the midplane of each laminate. Additionally reference, without BMI film, composites were manufactured for the evaluation of the knockdown effect. A thin high-temperature release film was also placed in the midplane to act as an initial pre-crack. After curing, specimens were cut at the desired dimensions according to AITM-1.0006 [141]. Hereafter, the produced specimens will be referred to as “reference” for unmodified specimens (no self-healing system), as “virgin system” for the initial specimens containing the BMI film, and “healed system” for the specimens after the healing process.

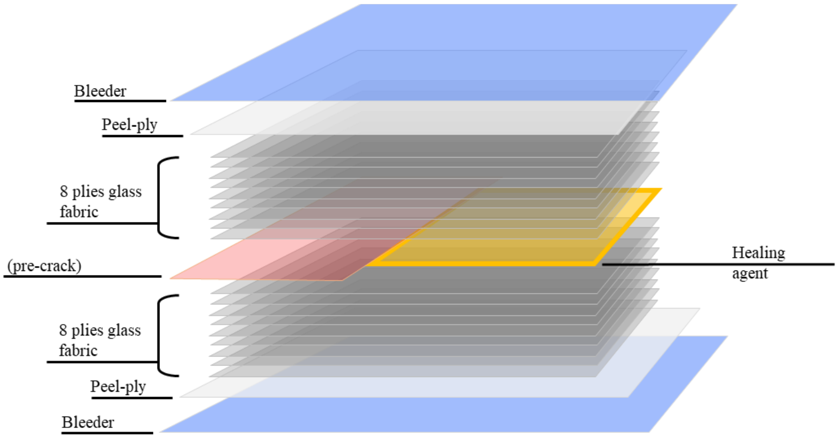

**Figure 97.** Schematic illustration of the lamination of the produced intrinsically self-healing composites.

## 7.4 Characterisation techniques and equipment

### 7.4.1 Raman spectroscopy

Raman spectroscopy was used in order to identify the changes in the molecular structure of the BMI polymers after manufacturing (powder), after the production of the film, and after the 1st, 2nd, and 3rd healing cycle. The 784 nm line NIR laser operating at 2mW at the focal plane was employed for the Raman measurements. An optical microscope served as the collector of the Raman scattering equipped with a 50x long working distance objective. Raman spectra were recorded in the range of 500–2000 $cm^{-1}$ using a Labram HR - Horiba scientific system. Spectral treatment included a quadratic baseline subtraction, and a subsequent normalization to the band with the highest intensity.

### 7.4.2 Mode II interlaminar fracture toughness

As previously, mode II tests were performed using a WDW-100 Jinan universal testing machine equipped with a 100 kN loadcell. The displacement rate was set at 1 mm/min. According to [143] the critical mode-II strain energy release rate, $G_{IIC}$, was calculated using the equation (4). The mechanical testing was stopped when the delamination at the mid-plane of the specimen occurred.

### 7.4.3 Healing process/ Healing efficiency of Mode II tests

Three healing cycles were performed for each BMI and film thickness. In the case of the Mode-II specimens, the healing process was achieved using a hot press at 150 °C for 3 minutes with applied pressure on the specimens. At the end of the healing process, the specimens were left to cool down at room temperature and retested under the same conditions (Figure 100). Healing efficiency was evaluated in terms of peak load ($P_c$) and mode-II interlaminar fracture toughness energy ($G_{IIc}$) recovery from equations (6) and (7), respectively:

$$\mathrm{n}_{p_x} = \frac{\mathrm{P_c^h}}{\mathrm{P_c^v}} \tag{6}$$

$$n_{G_x} = \frac{G_{IIc}^{h}}{G_{IIc}^{v}} \tag{7}$$

where $P_c^h$ and $P_c^v$ are the peak load of the healed and the virgin specimens and the $G_{IIc}^h$ and $G_{IIc}^v$ represent the mode-II interlaminar fracture toughness energies of the healed and the virgin specimens, respectively. The x was the healing cycle. The change of the initial properties after the self-healing system incorporation or the knockdown effect was evaluated using equation (1).

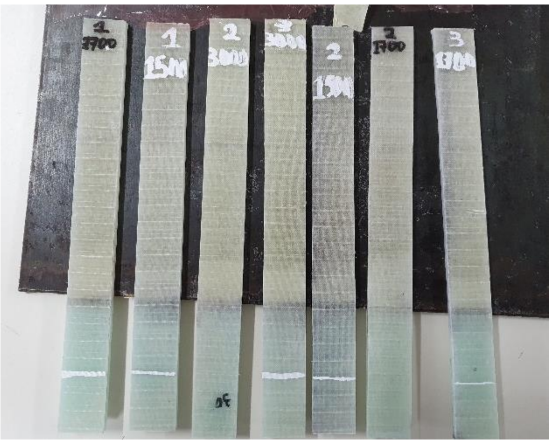

**Figure 98.** Mode-II specimens with BMI films after the healing process.

## 7.5 Results

### 7.5.1 Recovery of the Mode II fracture toughness using 0.1 mm films

**Figure 99** shows representative load versus displacement curves obtained from the mode II interlaminar fracture toughness tests of the reference, BMI-1500, BMI-1700, and BMI-3000 composites using films of 0.1 mm in thickness. As previously mentioned on capsule-based mode II geometry, the curves showed a linear increase of the load followed by a change in the slop. A small load drop was observed when the crack propagated inside the specimen.

The knockdown effect was eliminated in terms of the mode II fracture toughness energy $G_{IIc}$, since the modified composites with the BMI-1500 and BMI-1700 films exhibited an increase of their initial properties by +16.3% and +2.5%, respectively. This indicated that the BMI films positively influenced the mode-ii performance and increased toughening as other interleaves [190]. However, the BMI-3000 composites significantly decreased their initial properties by -77.9%, showing that incorporating such a high molecular weight BMI film is not suggestive. A similar trend was also observed at the maximum load values ($P_{max}$). BMI-1500 and BMI-1700 composites exhibited an increase of ca. +17%, while the BMI-3000 composites revealed a decrease of -39.6% of their maximum load.

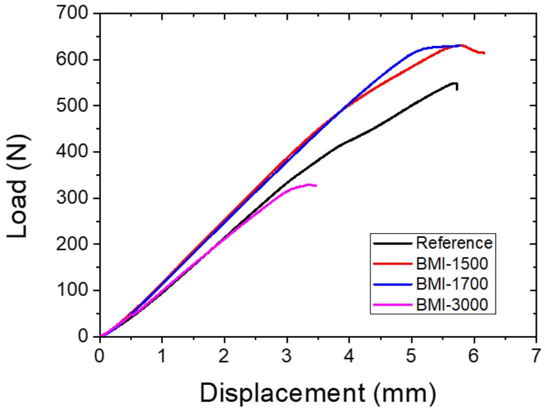

**Figure 99.** Representative plots of reference (black line), BMI-1500 (red line), BMI-1700 (blue line), and BMI-3000 (purple line) Mode-II specimens with 0.1 mm films.

The similar mechanical behaviour of a linear increase of the load followed by a change in the slop was also observed in all specimens after the three healing cycles (**Figure 100**). However, a smaller displacement can be observed in healed specimens after the second healing cycle due to the increase in the stiffness after the second exposure to high temperatures.

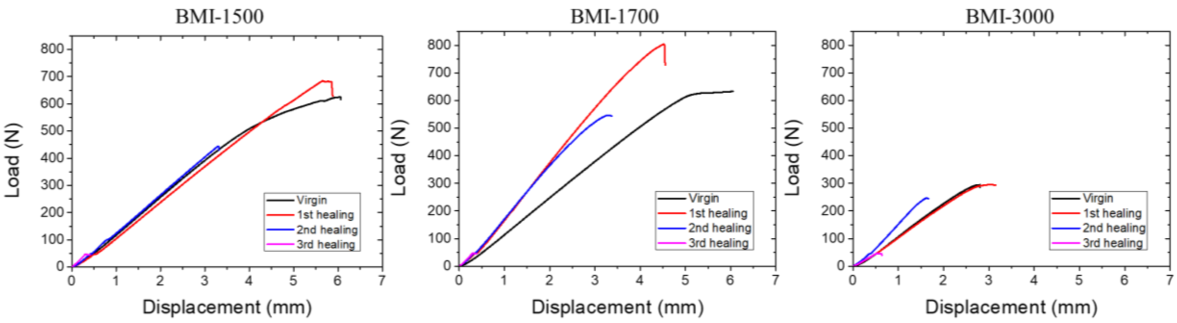

**Figure 100.** Representative plots of Mode-II specimens with BMI-1500 (left), BMI-1700 (middle), and BMI-3000 (right) using 0.1 mm films after 3 healing cycles.

**Figure 101** & **Figure 102** depict the calculated healing efficiencies of the mode-II specimens both in terms of mode II fracture toughness energy and maximum load. The BMI-1500 composites recovered their initial properties by 97.3% after the first healing cycle, 51.8% after the second healing cycle, and 4.3% after the third healing cycle in terms of $G_{IIc}$. The maximum load was regained by 111.6% after the first healing cycle, 61.3% after the second, and 15.1% after the third healing process. After the first two healing processes, a satisfying recovery in both values was calculated. After the first healing process, the significant-high values can be attributed to the better interlocking between the two midplanes. The film at the manufacturing stage was incorporated in a solid phase. During the healing process, the BMI film melted, and after its solidification, the consolidation at the midplane was improved.

Results also indicated that after the third healing cycle, the reversible polymer could not effectively regain its initial properties. This behavior can be attributed to the healing processes performed at high temperatures. At this temperature, the side reactions are enhanced; thus, the reversible properties of the BMI were decreased. Even though the intrinsic self-healing polymers are theoretically capable of recovering their initial properties for an infinite number of repetitions, in practice, there is a limit to this reversible character, and it is associated with the side reactions [191,192].

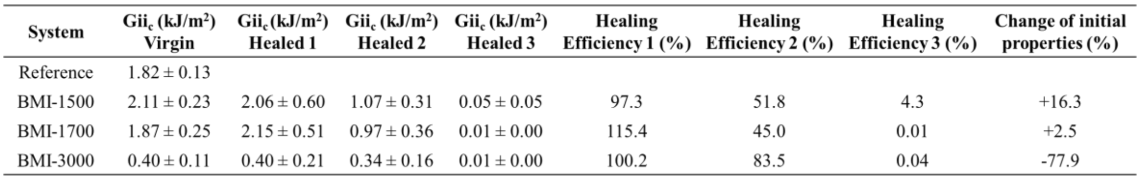

| System | $Gii_c$ (kJ/m$^2$) Virgin | $Gii_c$ (kJ/m$^2$) Healed 1 | $Gii_c$ (kJ/m$^2$) Healed 2 | $Gii_c$ (kJ/m$^2$) Healed 3 | Healing Efficiency 1 (%) | Healing Efficiency 2 (%) | Healing Efficiency 3 (%) | Change of initial properties (%) |
|---|---|---|---|---|---|---|---|---|
| Reference | 1.82 ± 0.13 | | | | | | | |
| BMI-1500 | 2.11 ± 0.23 | 2.06 ± 0.60 | 1.07 ± 0.31 | 0.05 ± 0.05 | 97.3 | 51.8 | 4.3 | +16.3 |
| BMI-1700 | 1.87 ± 0.25 | 2.15 ± 0.51 | 0.97 ± 0.36 | 0.01 ± 0.00 | 115.4 | 45.0 | 0.01 | +2.5 |
| BMI-3000 | 0.40 ± 0.11 | 0.40 ± 0.21 | 0.34 ± 0.16 | 0.01 ± 0.00 | 100.2 | 83.5 | 0.04 | -77.9 |

**Figure 101.** Healing efficiency & change of initial properties in terms of $G_{IIc}$ after 3 healing cycles using 0.1 mm films.

A similar self-healing behaviour was observed at BMI-1700 composites using 0.1 mm films with BMI-1500 composites with 0.1 mm films. Healing efficiencies of $G_{IIc}$ values were calculated at 115.4% after the first healing cycle, 45.0% after the second healing cycle, and 0.01% after the third healing cycle. In terms of maximum load, the first healing efficiency was 127.4% (due to the better interlocking), the second 62.4%, and 9.4% after the third cycle. As mentioned above, results exhibited that after the third healing cycle, the reversible polymers were not able to recover their mechanical properties.

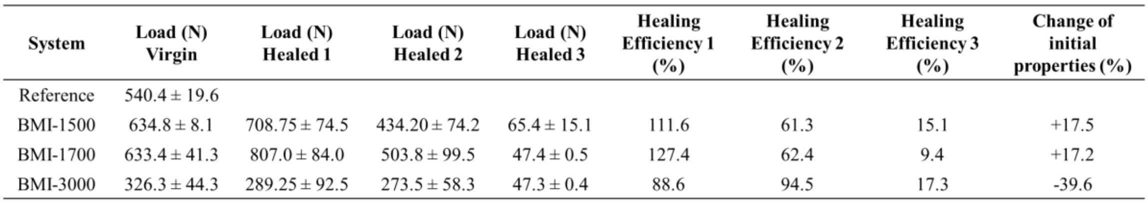

| System | Load (N) Virgin | Load (N) Healed 1 | Load (N) Healed 2 | Load (N) Healed 3 | Healing Efficiency 1 (%) | Healing Efficiency 2 (%) | Healing Efficiency 3 (%) | Change of initial properties (%) |
|---|---|---|---|---|---|---|---|---|
| Reference | 540.4 ± 19.6 | | | | | | | |
| BMI-1500 | 634.8 ± 8.1 | 708.75 ± 74.5 | 434.20 ± 74.2 | 65.4 ± 15.1 | 111.6 | 61.3 | 15.1 | +17.5 |
| BMI-1700 | 633.4 ± 41.3 | 807.0 ± 84.0 | 503.8 ± 99.5 | 47.4 ± 0.5 | 127.4 | 62.4 | 9.4 | +17.2 |
| BMI-3000 | 326.3 ± 44.3 | 289.25 ± 92.5 | 273.5 ± 58.3 | 47.3 ± 0.4 | 88.6 | 94.5 | 17.3 | -39.6 |

**Figure 102.** Healing efficiency & change of initial properties in terms of maximum load after 3 healing cycles using 0.1 mm films.

A similar performance was observed in the case of the incorporation of BMI-3000 films. The healing efficiency in terms of $G_{IIc}$ of the first healing process was calculated at 100.2%, 83.5% after the second healing cycle, and 0.04% after the final process. The max load was recovered by 88.6%, 94.5%, and 17.3% for the first, second, and third healing cycles, respectively. As with the rest of BMIs, the polymers did not recover their properties after the third healing process despite the high efficiencies obtained from the previous cycles. However, the high knockdown effect that presented the incorporation of the BMI-3000 film inside the composite indicates that this polymer is not identical to modifying a system toward the development of a reversible polymer.

### 7.5.2 Recovery of the Mode II fracture toughness using 0.4 mm films

A thicker BMI film of 0.4 mm in thickness was used in order to investigate the change in the initial mechanical properties and the healing efficiency. **Figure 103** depicts representative plots of the reference, BMI-1500, BMI-1700, and BMI-3000 composites with the relative films with 0.4 mm thickness. As observed in the previous cases, a typical mode-II mechanical performance was also revealed. Nevertheless, the thicker films exhibited a significant knockdown effect at both $G_{IIc}$ and max load values. The incorporation of BMI-1500 films reduced the mode-II fracture toughness by -41.3% and the max load values by -21.5%. Additionally, using BMI-1700 films, the $G_{IIc}$ decreased by -27.3% and the peak load by -15.7%. The introduction of BMI-3000 films revealed a reduction of $G_{IIc}$ by -49.0% and of max load by -27.3%. It is evident that using thicker BMI films in order to convert a conventional composite into a self-healing composite with intrinsic polymers had a significant effect on the initial fracture toughness properties.

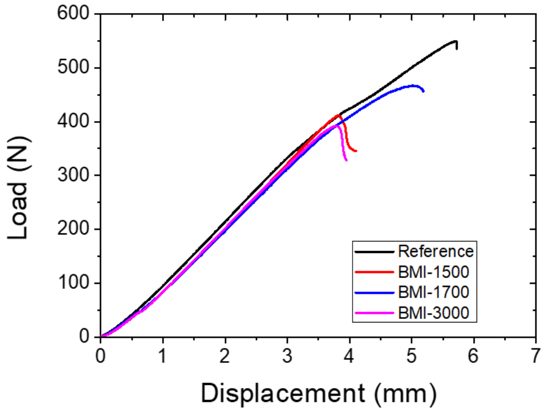

**Figure 103.** Representative plots of reference (black line), BMI-1500 (red line), BMI-1700 (blue line), and BMI-3000 (purple line) mode-II specimens with 0.4 mm films.

**Figure 104** depicts the representative plots of all composites with BMI films of 0.4 thickness after three healing cycles. Typical load-displacement curves were revealed at all BMI-modified composites, i.e., they did not affect in terms of their mechanical behaviour after three healing cycles.

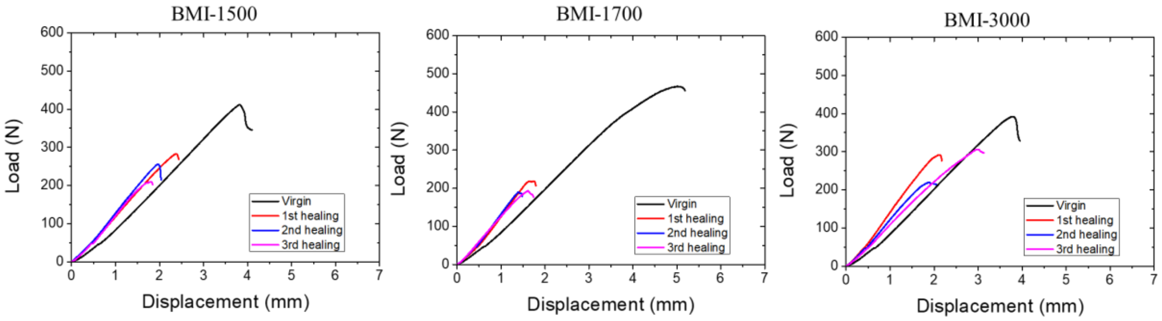

**Figure 104.** Representative plots of Mode-II specimens with BMI-1500 (left), BMI-1700 (middle), and BMI-3000 (right) using 0.4 mm films after 3 healing cycles.

As previously, healing efficiencies were also calculated in terms of GIIc (Figure 107) and max load (Figure 108). BMI-1500 composites regained their $G_{IIc}$ values by 49.2%, 98.9%, and 53.6% after one, two, and three healing processes, respectively. The maximum load was recovered by 64.8% after the first process, 89.1% after the second healing cycle, and 88.0% after the third healing process. The calculated percentages were higher after the second healing cycle, probably due to the greater amount of the reversible polymer that seems to remain unreacted. The same trend was observed in the case of BMI-1700 and BMI-3000 modified composites. $G_{IIc}$ regained by 16.7% after the first healing process, 85.2% after the second, and 112.9% after the final healing cycle of BMI-1700 composites. The maximum load was recovered by 46.7%, 89.7%, and 103.9% at the first, second, and third healing processes, respectively. BMI-3000 composites exhibited a recovery of 40.5%, 68.5%, and 168.9% of their fracture toughness values and 75.6%, 70.7%, and 143.2% of the peak load. As resulted of both knockdown effect and healing efficiency values, the 0.4 mm in thickness films are not appropriate for the intrinsically self-healing composites.

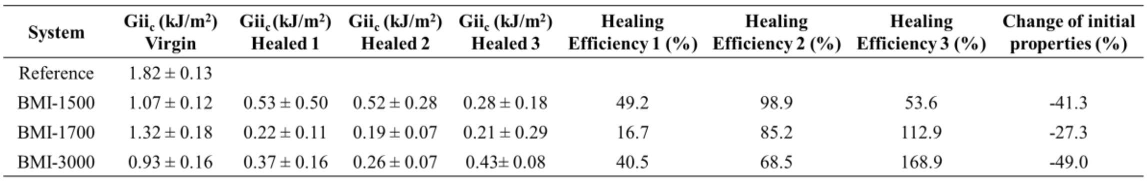

| System | $Gii_c$ (kJ/m$^2$) Virgin | $Gii_c$ (kJ/m$^2$) Healed 1 | $Gii_c$ (kJ/m$^2$) Healed 2 | $Gii_c$ (kJ/m$^2$) Healed 3 | Healing Efficiency 1 (%) | Healing Efficiency 2 (%) | Healing Efficiency 3 (%) | Change of initial properties (%) |
|---|---|---|---|---|---|---|---|---|
| Reference | 1.82 ± 0.13 | | | | | | | |
| BMI-1500 | 1.07 ± 0.12 | 0.53 ± 0.50 | 0.52 ± 0.28 | 0.28 ± 0.18 | 49.2 | 98.9 | 53.6 | -41.3 |
| BMI-1700 | 1.32 ± 0.18 | 0.22 ± 0.11 | 0.19 ± 0.07 | 0.21 ± 0.29 | 16.7 | 85.2 | 112.9 | -27.3 |
| BMI-3000 | 0.93 ± 0.16 | 0.37 ± 0.16 | 0.26 ± 0.07 | 0.43± 0.08 | 40.5 | 68.5 | 168.9 | -49.0 |

**Figure 105.** Healing efficiency & knockdown effect in terms of $G_{IIc}$ after 3 healing cycles using 0.4 mm films.

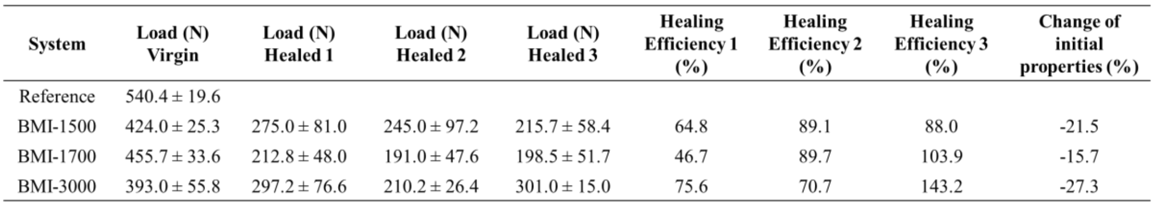

| System | Load (N) Virgin | Load (N) Healed 1 | Load (N) Healed 2 | Load (N) Healed 3 | Healing Efficiency 1 (%) | Healing Efficiency 2 (%) | Healing Efficiency 3 (%) | Change of initial properties (%) |
|---|---|---|---|---|---|---|---|---|
| Reference | 540.4 ± 19.6 | | | | | | | |
| BMI-1500 | 424.0 ± 25.3 | 275.0 ± 81.0 | 245.0 ± 97.2 | 215.7 ± 58.4 | 64.8 | 89.1 | 88.0 | -21.5 |
| BMI-1700 | 455.7 ± 33.6 | 212.8 ± 48.0 | 191.0 ± 47.6 | 198.5 ± 51.7 | 46.7 | 89.7 | 103.9 | -15.7 |
| BMI-3000 | 393.0 ± 55.8 | 297.2 ± 76.6 | 210.2 ± 26.4 | 301.0 ± 15.0 | 75.6 | 70.7 | 143.2 | -27.3 |

**Figure 106.** Healing efficiency & knockdown effect in terms of maximum load after 3 healing cycles using 0.4 mm films.

## 7.5.3 Molecular structure changes via Raman Spectroscopy

Raman spectroscopy was used in order to examine the changes in the molecular structure that occurred with the manufacturing of the BMI films and after each healing cycle. **Figure 107** depicts the obtained Raman spectra from all BMIs after their synthesis and grinding (BMI powders). All BMIs showed similar Raman spectra as well as peaks. Their differences were encountered in the peaks' intensity or/and shape or even at their position with small down or upshifts. The successful incorporation of the addition of maleimides into the polymer were confirmed via the presence of the following peaks: i) the furan ring vibration placed at 1500-

1505 cm$^{-1}$ for all BMIs [193] and ii) the maleimide out-of-plane C-H bending vibration found at 820 cm$^{-1}$, 831 cm$^{-1}$ and 827 cm$^{-1}$ for BMI-1500, BMI-1700 and BMI-3000, respectively [194]. A significant difference in the intensity of the maleimide out-of-plane C-H bending vibration peak in the case of the BMI-3000 (827 cm-1) can be observed compared to BMI-1500 and BMI-1700. This can be attributed to the decreased ability of BMI-3000 to be inserted into the prepolymer's polymeric chains due to its high molecular weight.

These two Raman peaks (820-830 cm$^{-1}$ and 1500 cm$^{-1}$) were examined at their intensity changes in order to identify the maleimide's ability for reversibility. The black arrows in **Figure 107** indicate the peaks of interest for the current analysis.

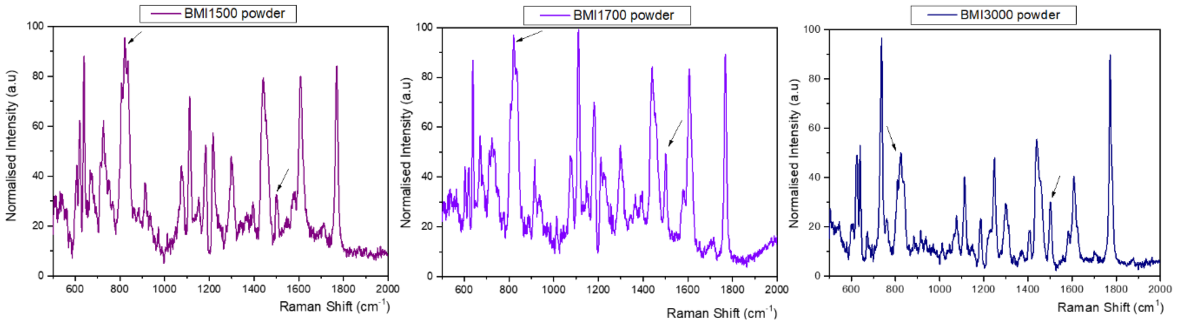

**Figure 107.** Raman spectra from the produced intrinsically self-healing polymeric powders of BMI-1500, BMI-1700 and BMI-3000.

**Figure 108** depicts the Raman spectra of the BMI-1500 powder in comparison to the BMI-1500 film. As can be observed, the transformation of BMI powder into a film did not significantly change Raman spectra since the intensity of the 820 cm$^{-1}$ band increased by +0.3% and the 1500 cm$^{-1}$ by 13.9%. This can be ascribed to the unreacted furan rings that remained after the production of the BMI and reacted after the film manufacturing. **Figure 109** illustrates the Raman spectra of the BMI-1500 film after the three healing processes. The healing cycles did not affect the quality of the BMI since the intensities of the above bands decreased from 2 to 8% after the three healing processes, even though the healing efficiencies decreased after each cycle (**Figure 110**). These results revealed that the decrease as well as the elimination of the healing efficiency after the three processes, probably attributed to the exposure of the composite to heating three times and not to the BMI's ability to regain its properties. In addition, with the external pressure used for the healing process, the film was squeezed out of the composite, thus affecting the healing efficiency (**Figure 111**).

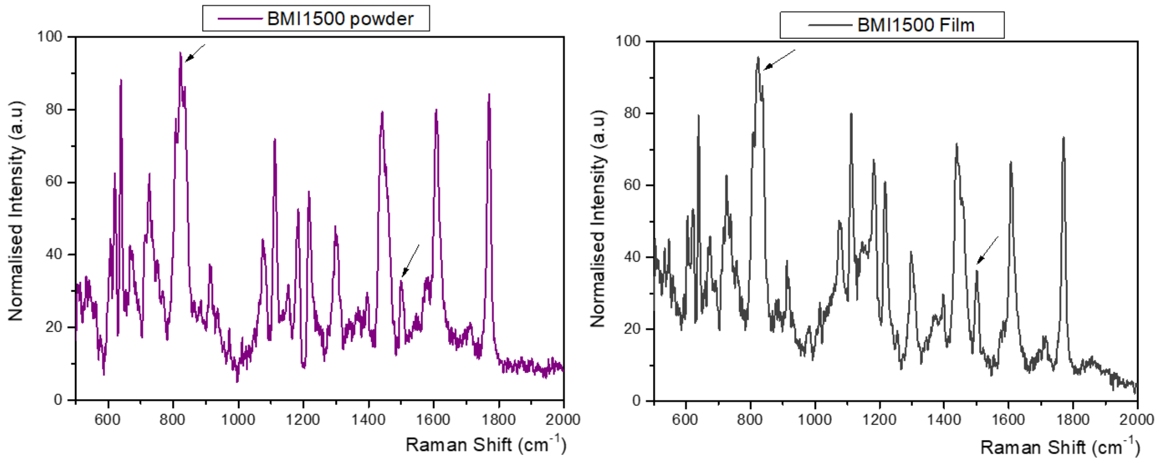

**Figure 108.** Raman spectra from BMI-1500 powder (left) and BMI-1500 film (right).

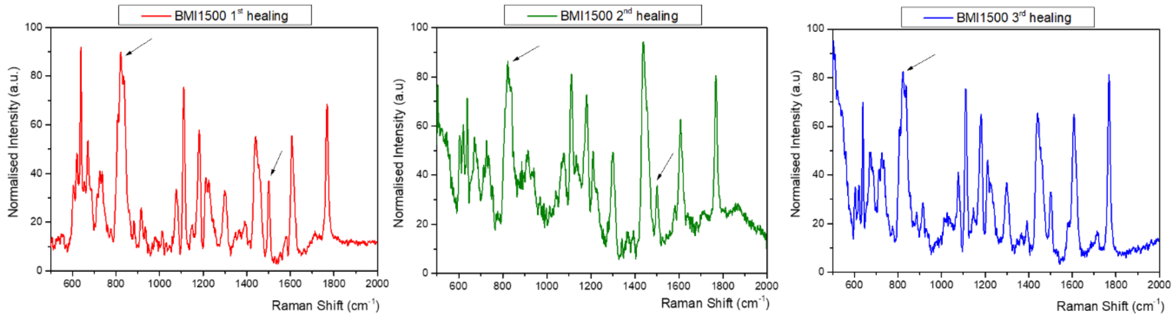

**Figure 109.** Raman spectra from BMI-1500 film after 1st, 2nd and 3rd healing cycle.

| BMI-1500 | System | Raman Intensity (a.u.) | Change (%) |
|---|---|---|---|
| 820 cm$^{-1}$ | powder | 95.26 | |
| | film | 95.63 | +0.30 |
| | 1st healing | 89.86 | -6.03 |
| | 2nd healing | 86.25 | -4.02 |
| | 3rd healing | 82.42 | -4.44 |

| BMI-1500 | System | Raman Intensity (a.u.) | Change (%) |
|---|---|---|---|
| 1500 cm$^{-1}$ | powder | 32.47 | |
| | film | 37.00 | +13.9 |
| | 1st healing | 36.32 | -1.84 |
| | 2nd healing | 35.75 | -1.57 |
| | 3rd healing | 32.95 | -7.83 |

**Figure 110.** Raman intensity changes of 820 cm$^{-1}$ and 1500 cm$^{-1}$ peaks of BMI-1500.

**Figure 111.** Composite specimen after the healing process with squeezed BMI film at its edges.

The Raman spectra from BMI-1700 powder did not significantly change with the production of the BMI-1700 film, as seen in **Figure 112**. However, after the second healing cycle, a major decrease in the intensity at both peaks was observed (**Figure 113**). This can be directly correlated with the low healing efficiency values obtained in the third cycle. After the third healing, the intensity of the peaks was lower, proving that the BMI-1700 film was destroyed and unable to recover the mechanical properties of the composite (**Figure 114**).

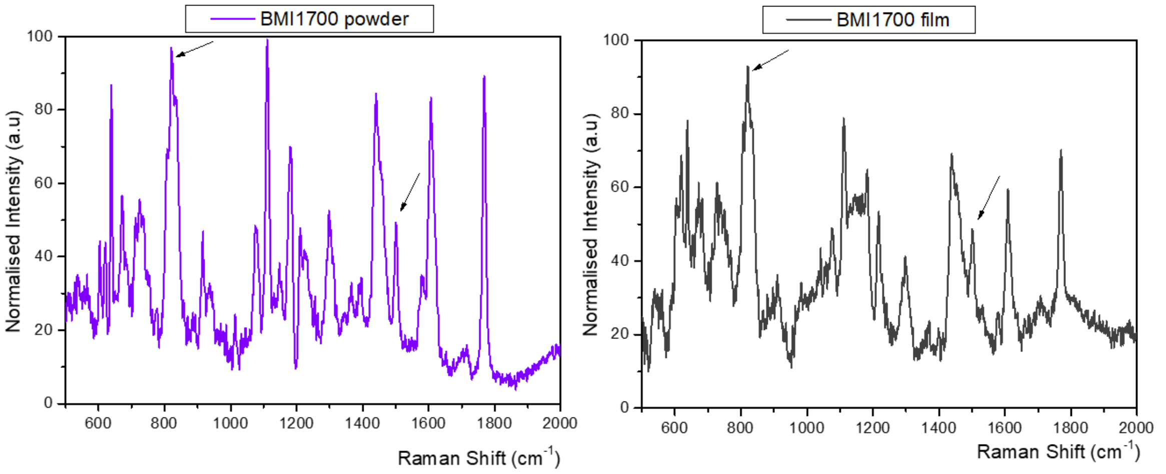

**Figure 112.** Raman spectra from BMI-1700 powder (left) and BMI-1700 film (right).

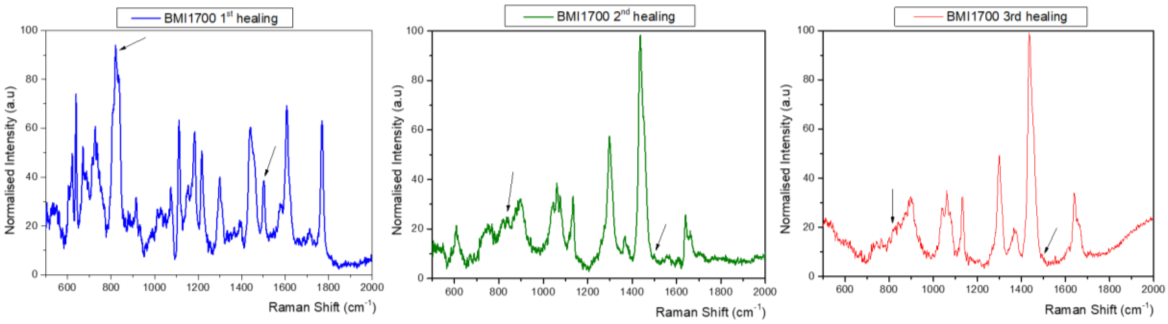

**Figure 113.** Raman spectra from BMI-1700 film after 1st, 2nd and 3rd healing cycle.

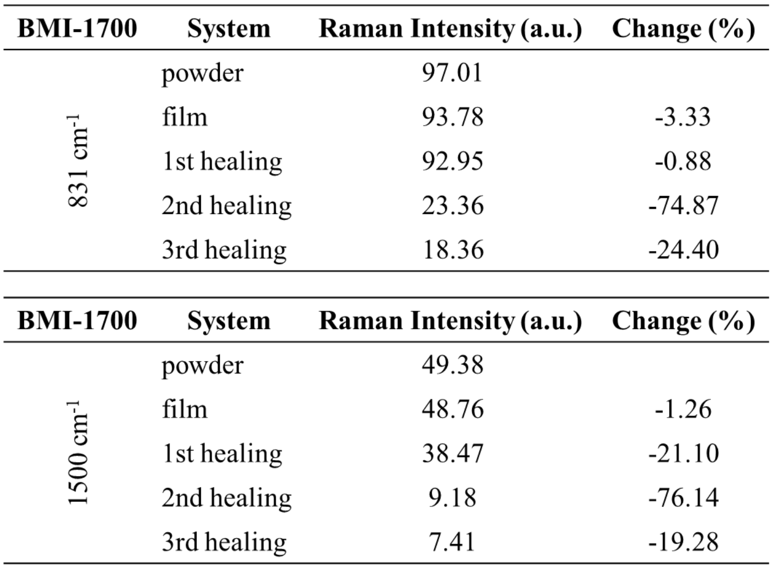

| BMI-1700 | System | Raman Intensity (a.u.) | Change (%) |
|---|---|---|---|
| 831 $cm^{-1}$ | powder | 97.01 | |
| | film | 93.78 | -3.33 |
| | 1st healing | 92.95 | -0.88 |
| | 2nd healing | 23.36 | -74.87 |
| | 3rd healing | 18.36 | -24.40 |

| BMI-1700 | System | Raman Intensity (a.u.) | Change (%) |
|---|---|---|---|
| 1500 $cm^{-1}$ | powder | 49.38 | |
| | film | 48.76 | -1.26 |
| | 1st healing | 38.47 | -21.10 |
| | 2nd healing | 9.18 | -76.14 |
| | 3rd healing | 7.41 | -19.28 |

**Figure 114.** Raman intensity changes of 831 $cm^{-1}$ and 1500 $cm^{-1}$ peaks of BMI-1700.

In the case of BMI-3000, the spectra of the film presented an increment of the related bands' intensity of 39% for the 827 $cm^{-1}$ and 25% for the 1500 $cm^{-1}$ (**Figure 115**). This can be related to the decreased ability of BMI to be inserted into the prepolymer’s polymeric chains due to its high molecular weight, as mentioned before. The unreacted furan and maleimide groups that existed after the manufacturing of the film react, resulting in an increase in the intensity of the peaks. As at BMI-1700, the intensity of the peaks decreased by a large amount, between 67 to 76% after the first healing process (**Figure 116**). The decreased ability to heal the BMI-3000 that resulted from the mechanical characterization results, compared to the BMI-1500 and BMI-1700, can be confirmed via the lower intensity values as illustrated in **Figure 117**.

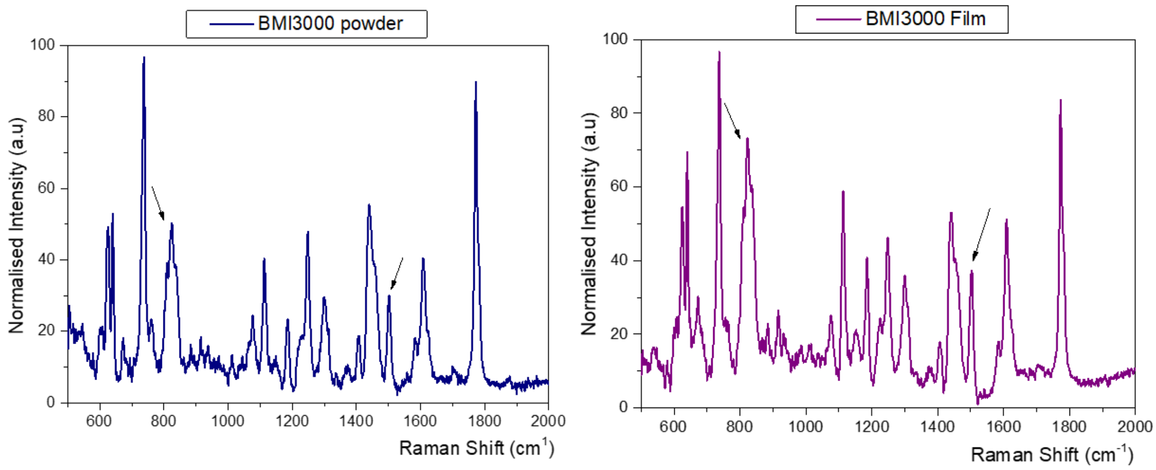

**Figure 115.** Raman spectra from BMI-3000 powder (left) and BMI-3000 film (right).

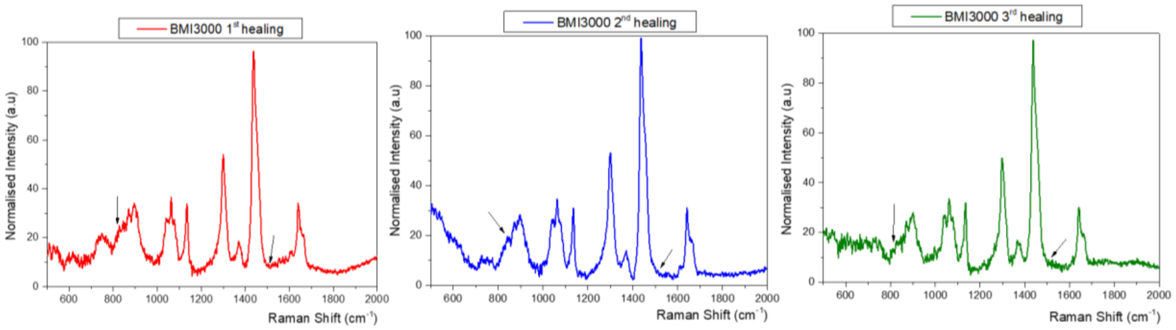

**Figure 116.** Raman spectra from BMI-3000 film after 1$^{st}$, 2$^{nd}$ and 3$^{rd}$ healing cycle.

| BMI-3000 | System | Raman Intensity (a.u.) | Change (%) |
|---|---|---|---|
| 827 cm$^{-1}$ | powder | 50.11 | |
| | film | 69.61 | +38.90 |
| | 1st healing | 22.96 | -67.02 |
| | 2nd healing | 14.98 | -34.76 |
| | 3rd healing | 11.42 | -23.77 |

| BMI-3000 | System | Raman Intensity (a.u.) | Change (%) |
|---|---|---|---|
| 1500 cm$^{-1}$ | powder | 29.95 | |
| | film | 37.33 | +24.65 |
| | 1st healing | 9.00 | -75.89 |
| | 2nd healing | 7.51 | -16.55 |
| | 3rd healing | 7.04 | -6.26 |

**Figure 117.** Raman intensity changes of 827 cm$^{-1}$ and 1500 cm$^{-1}$ peaks of BMI-3000.

## 7.6 Conclusions

This chapter successfully synthesized three reversible epoxy resin films via a three-step process. The BMI-1500, BMI-1700, and BMI-3000 oligomers were incorporated into the polymeric chains of the DGEBA epoxy resin (Epikote 828) via the Diels-Alder reaction. The produced reversible polymers were ground into powder and then shaped into film via a hot press process. Two different thicknesses were chosen for the films at 0.1 mm and 0.4 mm. The films were incorporated into the midplane of fiber-reinforced polymer composites and were mechanically tested under the mode-II fracture toughness test. The mechanical performance was evaluated after three healing cycles.

Mechanical characterization results indicated that the introduction of 0.1 mm in thickness films of BMI-1500 and BMI-1700 did not alter the fracture toughness properties of the system, and a sufficient healing performance was also revealed after three healing processes. However, in the case of BMI-3000, a significant knockdown effect was observed; thus, this reversible polymer is not indicative. In the case of the 0.4 mm in thickness films, all BMI systems exhibited significant values of knockdown effect in both terms of mode-II fracture toughness and maximum load. The healing efficiencies were increased after each healing cycle, showing that a lot of BMI material remained unreacted.

Raman spectroscopy was utilized in order to identify and correlate any molecular changes of the BMIs with their ability to regain their bonds, after the production of the films and after each healing cycle. For this investigation, two Raman bands that are directly correlated with the ability of the BMIs to reverse their bonds were selected: the furan ring vibration placed at 1500-1505 cm$^{-1}$ for all BMIs and ii) the maleimide out-of-plane C-H bending vibration found at 820 cm$^{-1}$, 831 cm$^{-1}$ and 827 cm$^{-1}$ for the BMI-1500, BMI-1700, and BMI-3000, respectively. The samples used were taken from the composites with 0.1 mm films in thickness that exhibited the most sufficient mechanical properties. Results proved that the BMI-1500 did not significantly affect the exposure to high temperature, conversely with BMI-1700 and BMI-3000, proving that the low healing efficiency values probably resulted from the squeezed BMI film. These two BMIs revealed a decrease in the intensity of the aforementioned bands after each process resulting in decreased healing efficiency values. In conclusion, BMI reversible polymers proved to be an excellent choice for manufacturing intrinsically self-healing composites.

# CHAPTER 8

# General conclusions, Publications and Suggestions for Future Work

## 8.1 General conclusions

The current thesis presents novel concepts for the optimization of self-healing composites and consists of two parts. The first part includes the manufacturing of multifunctional self-healing capsule-based composites capable of recovering both their mechanical and electrical properties. Healing efficiencies were investigated at the polymer level, and then in a try to scale up, capsule-based systems were incorporated at the composite and model structure level. The second part concerns the synthesis of intrinsically self-healing polymeric films capable of restoring the mechanical properties of a composite based on the Diels-Alder reaction.

Before the main experimental campaign, a preliminary study on the dispersion of different percentages of fillers (CNTs & CB) at different dispersion hours in the DGEBA epoxy resin was performed. This resin was used as a healing agent and matrix at polymer level experiments. The study included the investigation of electrical and mechanical properties. The modification of the epoxy resin generally increased its fracture toughness. In terms of electrical properties, conductivity measurements revealed that systems containing MWCNTs indicated the formation of a conductive network for concentrations over 0.3 wt. % MWCNTs. The optimal electrical properties were found at 0.5 wt% CNTs after three hours of dispersion. The conductivity and mechanical measurements showed a direct correlation between the electrical and mechanical properties of the nanomodified epoxy resin.

Subsequently, the evaluation of healing efficiency in terms of mechanical and electrical properties was performed at the polymer matrix level using capsules with a nano-modified healing agent. The most efficient protocols from the experimental campaign of this chapter performed in the context of case studies one and two were evaluated and transferred in chapter six to scale up this research to composite level. The selected capsule percentage for composites was higher than studied at 25 wt. % since in order to scale up the technologies at composite level, a sufficient quantity of healing agent will be necessary. Considering the cost of the catalyst, the percentage selected to be used at composite level was 2.5 wt. %. Regarding the different healing times studied, results indicated that the healing duration for the self-healing composites was 48 hours.

The incorporation of a low percentage of CNTs (0.1 wt.%) led to the successful recovery of both mechanical and electrical properties concurrently. Observing the above results, it was decided that the CNT’s percentage can remain stable at 0.5 wt.% and since the viscosity was too high and the results with 0.1 wt.% CNTs were sufficient.

Then, the encapsulation of the healing agent into a nanomodified UF polymeric shell wall was performed with different percentages of MWCNTs. The roughness of the exterior wall was substantially improved, resulting in a better interlocking between capsules and matrix. TDCB fracture toughness tests of nanomodified resin with capsules of increasing the percentage of CNTs also exhibited an improvement in the initial mechanical properties.

The healing efficiency was measured at ca. 47% and did not change with the introduction of 0.3 % and 0.5 % capsules. However, in the case of 1 % capsules, it decreased ca. 20%. In terms of electrical conductivity properties, the addition of modified capsules into a semi-conductive matrix resulted in an increase in the conductivity indicating that the percolation was achieved via the combined CNT and microcapsule loading.

After that, the effect of adding different types and sizes of capsules into nanomodified polymer matrices on the percolation threshold was evaluated. The selected systems were the 0.3 wt. % and 0.5 wt. % of MWCNTs. At the incorporation of capsules in 0.3 wt. % CNTs matrix results indicated that the conductive network was successfully formatted in case of introducing capsules smaller than 90μm with both nanomodified healing agent and shell-wall. The conductive network that was formatted after the dispersion of 0.5 wt. % CNTs into the matrix was not significantly affected after incorporating neat capsules and nano-core capsules at all sizes. Nevertheless, the nano-wall capsules integration into the matrix exhibited higher conductivity values as their mean diameter increased. Sufficiently improved electrical properties were achieved after the incorporation of nano-all capsules into the matrix, with the conductivity to be improved when reducing capsule size.

The final part of capsule-based self-healing materials reports the manufacturing and characterization of the multi-functional self-healing composites. The self-healing composites were tested at two different mechanical tests, mode-II fracture toughness and low-velocity impact. All tests included the evaluation of the concurrent restoration of both mechanical and electrical properties, too.

At Mode-II tests, 20 wt. % of neat and nanomodified capsules were incorporated with 2.5 wt. % of catalyst at the midplane of the specimens. In the nano-modified capsule system, the $G_{IIC}$ was regained by 191% and the maximum load by 117%. The electrical healing efficiency was recovered by 77%. At low velocity impact, the maximum load was improved by +16%, although the specimens with self-healing properties absorbed less energy by -13%. A satisfying healing efficiency in both properties was revealed at ca. 101%. The introduction of the sensing technologies reduced the maximum load by -11 and -17% for the carbon specimens and spray coated specimens, respectively. However, the energy absorption was increased by +12% and 18%. When introducing the self-healing system to a sensing system, the carbon capsule systems increased their maximum load by +10% but reduced the absorption of the impacted energy by -7%. In the case of spray-coated specimens, the maximum load improved by 5% and the energy absorption by 1%. The mechanical healing efficiency calculated at sensing systems ranged at the same values from 99% to 102% for both measured properties.

CAI tests were also performed, considering that the residual CAI strength is one of the most important properties of a composite material. The most promising technology for a self-sensing and self-healing composite concurrently was the carbon tow system.

At the lap strap geometry or the model structure level, the calculated high mechanical and electrical healing efficiency values and the elimination of the knock-down effect are promising factors for the scale-up of the employment of a nanomodified capsule-based self-healing method to model composite structures.

The work related to the second part of this thesis concerns the synthesis of intrinsically self-healing polymeric films based on the Diels-Alder reaction. Specifically, the three cross-linkers, BMI-1500, BMI-1700, and BMI-3000, were incorporated into the DGEBA epoxy resin via a two-stage process. The composites were tested into mode-ii fracture toughness tests, while the healing efficiency was estimated after three healing cycles.

Two different thicknesses were chosen for the films at 0.1 mm and 0.4 mm. Mechanical characterization results indicated that the introduction of 0.1 mm in thickness films of BMI-1500 and BMI-1700 did not alter the fracture toughness properties of the system, and a sufficient healing performance was also revealed after three healing processes. However, in the case of BMI-3000, a significant knockdown effect was observed; thus, this reversible polymer is not indicative. In the case of the 0.4 mm in thickness films, all BMI systems exhibited significant values of knockdown effect in both terms of mode-II fracture toughness and maximum load. The healing efficiencies were increased after each healing cycle, showing that a lot of BMI material remained unreacted.

Raman spectroscopy results proved that the BMI-1500 did not significantly affect the exposure to high temperature, conversely with BMI-1700 and BMI-3000, proving that the low healing efficiency values probably resulted from the squeezed BMI film. In conclusion, BMI reversible polymers proved to be an excellent choice for manufacturing intrinsically self-healing composites.

## 8.2 Future work

Within the scope of this study, self-healing capsule-based composites proved highly efficient and were capable for producing both self-healing and self-sensing structures. However, there are several issues that should be addressed before the multifunctional concept can be adopted as a reliable technology.

More improvement should be made towards the development of a fully autonomous self-healing system. For that purpose, some of the efforts should be focused on the autonomous heating or on other healing chemistries that the heating is not needed (e.g. magnetic or UV triggering).

In addition, the capsule- based systems can restore other functionalities such as magnetic properties, pH and corrosion resistance, etc. The healing agent can be modified with appropriate fillers that can regain their special functionalities.

Also, the use of the proposed nanomodified capsule-based self-healing system that can act also as a sensing system, can be used as coating at metallic structures at aerospace for the detection of any external damage and prevent any further internal or external damage.

Another important issue that should be countered is the easy incorporation of the capsule-based healing concepts on advanced composite structures without reducing their performance. Capsules can be incorporated into solvents that after heating, they evaporate, and the healing system remains in the targeted area.

At intrinsically self-healing polymers, the nanomodification of the BMI polymers in order to enable the restoration of the electrical properties as in capsule-based systems can be performed. The transformation of the nanomodified BMI to intrinsic films for an easy application can be also achieved. The healing process and the molecular structure changes can be assessed through advanced characterization techniques such as Raman and Impedance spectroscopies.

Also, a lot of effort should be given at the new and very promising vitrimer technology. The vitrimer-thermoset concept represents an excellent candidate for the improvement of the durability and recyclability of thermoset-based structures. An environmentally friendly modification (e.g. clays) of their matrix can also provide sensing capabilities through other techniques (non-electrical).

## 8.3 Publications

### 8.3.1 Published

1. **M. Kosarli,** D.G. Bekas, K. Tsirka, D. Baltzis, D.T. Vaimakis-Tsogkas, S. Orfanidis, G. Papavassiliou, A.S. Paipetis**,** *Microcapsule-based self-healing materials: Healing efficiency and toughness reduction vs. capsule size,* Composites Part B: Engineering, (DOI: 10.1016/j.compositesb.2019.04.030)
2. **M. Kosarli,** K. Tsirka, S. Chalari, A. Palantza, A.S. Paipetis, *Recovery of Fracture Toughness on Self-Healing Epoxies using Ternary Nanomodified Microcapsules: A Parametric Study,* Key Engineering Materials, (DOI: 10.4028/www.scientific.net/KEM.827.258)
3. R. Rodriguez, D.G. Bekas, S. Florez, **M. Kosarli,** A.S. Paipetis, *Development of self-contained microcapsules for optimised catalyst position in self-healing materials*, Polymer, (DOI: 10.1016/j.polymer.2019.122084)
4. X. Tsilimigkra, D.G. Bekas, **M. Kosarli**, S. Tsantzalis, A.S. Paipetis, V. Kostopoulos, *Mechanical Properties Assessment of Low-Content Capsule-Based Self-Healing Structural Composites,* Applied Sciences, (DOI: 10.3390/app10175739)
5. **M. Kosarli**, D.G. Bekas, K. Tsirka, A.S. Paipetis, *Capsule based self-healing polymers and composites,* Chapter on Book entitled: Self-healing polymer-based materials, *by Elsevier*, 2020
6. **M. Kosarli**, G. Foteinidis, K. Tsirka, D.G. Bekas, A.S. Paipetis, *Concurrent recovery of mechanical and electrical properties in nanomodified capsule-based self-healing epoxies*, Polymer, (DOI: 10.1016/j.polymer.2021.123843)
7. **M. Kosarli**, A. Polymerou, G. Foteinidis, C. Vazouras, A.S. Paipetis*, Healing Efficiency of CNTs-Modified-UF Microcapsules That Provide Higher Electrical Conductivity and EMI Shielding Properties,* Polymers, (DOI: 10.3390/polym13162753)

### 8.3.2 Under review

1. **M. Kosarli**, G. Foteinidis, K. Tsirka, N. Markaide, D. Calderon, S. Weidmann, A.S. Paipetis, *3R composites: Knockdown effect assessment & repair effi-ciency via mechanical and NDE testing,*
2. K. Dimitriadis, G. Foteinidis, **M. Kosarli**, D. Moschovas, A.S. Paipetis, S. Agathopoulos, *Selective Laser Melting: A reliable modern technique for constructing removable partial denture frameworks,* Journal of Materials Engineering and Performance

### 8.3.3 Under preparation

1. **M. Kosarli**, G. Foteinidis, A.S. Paipetis, *Capsule-based self-healing composites and structures recovering both mechanical and electrical properties*
2. **M. Kosarli,** D.G. Bekas, D. Moschovas, A. Avgeropoulos, A.S. Paipetis, *Intrinsically self-healing interleaves for composite materials*
3. G. Foteinidis, **M. Kosarli**, K. Anagnostou, A.S. Paipetis, *A multi-functional self-healing and self-sensing composite under low velocity impact test*
4. G. Foteinidis, **M. Kosarli**, K. Tsirka, A. Martinez, N. Markaide, A. Leroy, V. Gayraud, S. Weidmann, A.S. Paipetis, *Development of SHM technology on 3R-Repairable composites and 3R bonding techniques produced by different processes and their repair efficiency*
5. G. Foteinidis, **M. Kosarli**, A. Poulia, A.S. Paipetis, *The effect of capsule size and type on the percolation threshold of nanomodified epoxies*
6. K. Tsirka, A. Huegun, M. E. Kouli, A. Llorente, A. Ntaflos, A. Rekondo, G. Foteinidis, **M. Kosarli**, K. Anagnostou, A. S. Paipetis, *Repairability of carbon fiber reinforced 3R and modify 3R epoxy laminates*

# CHAPTER 9

# References

[1] Zweben C. Advanced composites for aerospace applications. Composites 1981;2:235–40. https://doi.org/10.1080/17458080701376348.

[2] Vassilopoulos AP. Fatigue life prediction of composites and composite structures. 2010. https://doi.org/10.1533/9781845699796.

[3] Swait TJ, Rauf A, Grainger R, Bailey PBS, Lafferty AD, Fleet EJ, et al. Smart composite materials for self-sensing and self-healing. Plastics, Rubber and Composites, vol. 41, 2012, p. 215–24. https://doi.org/10.1179/1743289811Y.0000000039.

[4] Rana S, Fangueiro R. Advanced composite materials for aerospace engineering: processing, properties and applications. n.d.

[5] Riccio A, Pietropaoli E, Raimondo A. Damage Growth in Aerospace Composites. 2015.

[6] Oterkus E, Diyaroglu C, De Meo D, Allegri G. Fracture modes, damage tolerance and failure mitigation in marine composites. Elsevier Ltd.; 2016. https://doi.org/10.1016/B978-1-78242-250-1.00004-1.

[7] Harizi W, Chaki S, Bourse G, Ourak M, Moustakidis S, Anagnostis A, et al. Non-destructive inspection of aircraft composite materials using triple IR imaging. Composites Part B: Engineering 2014;49:291–6. https://doi.org/10.1016/j.compositesb.2014.05.017.

[8] Maio L, Memmolo V, Boccardi S, Meola C, Ricci F, Boffa ND, et al. Ultrasonic and IR Thermographic Detection of a Defect in a Multilayered Composite Plate. Procedia Engineering 2016;167:71–9. https://doi.org/10.1016/j.proeng.2016.11.671.

[9] Kenari MA, Verma D. An introduction to self-healing of polymer composite materials and conventional repairing process. LTD; 2022. https://doi.org/10.1016/b978-0-12-822291-1.00003-8.

[10] Armstrong KB, Cole W, Bevan G. Care and Repair of Advanced Composites. 2005. https://doi.org/10.4271/r-336.

[11] Archer E, McIlhagger A. Repair of damaged aerospace composite structures. Elsevier Ltd; 2015. https://doi.org/10.1016/B978-0-85709-523-7.00014-1.

[12] Dry C. Matrix cracking repair and filling using active and passive modes for smart timed release of chemicals from fibers into cement matrices. Smart Materials and Structures 1994;3:118–23. https://doi.org/10.1088/0964-1726/3/2/006.

[13] Singh AP, Singh K, Pandey AJ| AK| AK| A. Self-Healing Capabilities in Polymeric Materials: An Introduction to Techniques. International Journal of Trend in Scientific Research and Development 2019; Volume-3:735–8. https://doi.org/10.31142/ijtsrd23886.

[14] Blaiszik B, Kramer SLB, Moore JS, Sottos NR, Blaiszik BJ, Kramer SLB, et al. Self-Healing Polymers and Composites. Annu Rev Mater Res 2010;40:179–211. https://doi.org/10.1146/annurev-matsci-070909-104532.

[15] Zhong N, Post W. Self-repair of structural and functional composites with intrinsically self-healing polymer matrices: A review. Composites Part A: Applied Science and Manufacturing 2015;69:226–39. https://doi.org/10.1016/j.compositesa.2014.11.028.

[16] Park JS, Darlington T, Starr AF, Takahashi K, Riendeau J, Thomas Hahn H. Multiple healing effect of thermally activated self-healing composites based on Diels-Alder reaction. Composites Science and Technology 2010;70:2154–9. https://doi.org/10.1016/j.compscitech.2010.08.017.

[17] Williams HR, Trask RS, Knights AC, Williams ER, Bond IP. Biomimetic reliability strategies for self-healing vascular networks in engineering materials. Journal of the Royal Society Interface 2008;5:735–47. https://doi.org/10.1098/rsif.2007.1251.

[18] Hamilton AR, Sottos NR, White SR. Self-healing of internal damage in synthetic vascular materials. Advanced Materials 2010;22:5159–63. https://doi.org/10.1002/adma.201002561.

[19] Hansen CJ. Microvascular-based self-healing materials. Elsevier Ltd.; 2015. https://doi.org/10.1016/B978-1-78242-280-8.00005-4.

[20] Zhu DY, Rong MZ, Zhang MQ. Self-healing polymeric materials based on microencapsulated healing agents: From design to preparation. Progress in Polymer Science 2015;49–50:175–220. https://doi.org/10.1016/j.progpolymsci.2015.07.002.

[21] Swait TJ, Rauf A, Grainger R, Bailey PBS, Lafferty AD, Fleet EJ, et al. Smart composite materials for self-sensing and self-healing. Plastics, Rubber and Composites 2012;41:215–24. https://doi.org/10.1179/1743289811Y.0000000039.

[22] Giurgiutiu V. Structural health monitoring (SHM) of aerospace composites. Elsevier Ltd; 2019. https://doi.org/10.1016/B978-0-08-102679-3.00017-4.

[23] Bekas DG, Sharif-Khodaei Z, Baltzis D, Aliabadi MHF, Paipetis AS. Quality assessment and damage detection in nanomodified adhesively-bonded composite joints using inkjet-printed interdigital sensors. Composite Structures 2019;211:557–63. https://doi.org/10.1016/j.compstruct.2019.01.008.

[24] Luan C, Movva S, Wang K, Yao X, Zhang C, Wang B. Towards next-generation fiber-reinforced polymer composites: A perspective on multifunctionality. Functional Composites and Structures 2019;1. https://doi.org/10.1088/2631-6331/ab47f9.

[25] Bekas DG, Paipetis AS. Study of the effect of damage on the electrical impedance of carbon nanotube reinforced epoxy nanocomposites. Journal of Sensors 2015;2015. https://doi.org/10.1155/2015/805303.

[26] Abry JC, Choi YK, Chateauminois A, Dalloz B, Giraud G, Salvia M. In-situ monitoring of damage in CFRP laminates by means of AC and DC measurements. n.d.

[27] Foteinidis G, Paipetis AS. A novel composite with structural health monitoring functionality via 2d and 3d impedance mapping topography. Applied Sciences (Switzerland) 2021;11:1–19. https://doi.org/10.3390/app11041647.

[28] Brøndsted P, Lilholt H, Lystrup A. Composite Materials for Wind Power Turbine Blades. Annual Review of Materials Research 2005;35:505–38. https://doi.org/10.1146/annurev.matsci.35.100303.110641.

[29] Gkikas G, Sioulas D, Lekatou A, Barkoula NM, Paipetis AS. Enhanced bonded aircraft repair using nano-modified adhesives. Materials and Design 2012;41:394–402. https://doi.org/10.1016/j.matdes.2012.04.052.

[30] Wernik JM, Meguid SA. On the mechanical characterization of carbon nanotube reinforced epoxy adhesives. Materials and Design 2014;59:19–32. https://doi.org/10.1016/j.matdes.2014.02.034.

[31] Garg AC, Mai YW. Failure mechanisms in toughened epoxy resins-A review. Composites Science and Technology 1988;31:179–223. https://doi.org/10.1016/0266-3538(88)90009-7.

[32] Chung SL, Lin JS. Thermal conductivity of epoxy resin composites filled with combustion synthesized h-BN particles. Molecules 2016;21:1–11. https://doi.org/10.3390/molecules21050670.

[33] Zdobyslaw Goraj. An overview of the Deicing and Antiicing Technologies With Prospects for the Future. 24Th International Congress of the Aeronautical Sciences 2004:1–11.

[34] Domun N, Hadavinia H, Zhang T, Sainsbury T, Liaghat GH, Vahid S. Improving the fracture toughness and the strength of epoxy using nanomaterials-a review of the current status. Nanoscale 2015;7:10294–329. https://doi.org/10.1039/c5nr01354b.

[35] Liu S, Chevali VS, Xu Z, Hui D, Wang H. A review of extending performance of epoxy resins using carbon nanomaterials. Composites Part B: Engineering 2018;136:197–214. https://doi.org/10.1016/j.compositesb.2017.08.020.

[36] Kenzhebayeva A, Bakbolat B, Sultanov F, Daulbayev C, Mansurov Z. A mini-review on recent developments in anti-icing methods. Polymers (Basel) 2021;13. https://doi.org/10.3390/polym13234149.

[37] Bekas DG, Paipetis AS. Damage monitoring in nanoenhanced composites using impedance spectroscopy. Composites Science and Technology 2016;134:96–105. https://doi.org/10.1016/j.compscitech.2016.08.013.

[38] Mittal G, Dhand V, Rhee KY, Park SJ, Lee WR. A review on carbon nanotubes and graphene as fillers in reinforced polymer nanocomposites. Journal of Industrial and Engineering Chemistry 2015;21:11–25. https://doi.org/10.1016/j.jiec.2014.03.022.

[39] Potts JR, Dreyer DR, Bielawski CW, Ruoff RS. Graphene-based polymer nanocomposites. Polymer (Guildf) 2011;52:5–25. https://doi.org/10.1016/j.polymer.2010.11.042.

[40] Fenner JS, Daniel IM. Hybrid nanoreinforced carbon/epoxy composites for enhanced damage tolerance and fatigue life. Composites Part A: Applied Science and Manufacturing 2014;65:47–56. https://doi.org/10.1016/j.compositesa.2014.05.023.

[41] Iijima S. Helical microtubules of graphitic carbon. Nature 1991;354:56–8.

[42] Yakobson BI, Avouris P. Mechanical Properties of Carbon Nanotubes. Carbon Nanotubes, Springer Berlin Heidelberg; 2007, p. 287–327. https://doi.org/10.1007/3-540-39947-x_12.

[43] Qian D, Wagner GJ, Liu WK, Yu MF, Ruoff RS. Mechanics of carbon nanotubes. Applied Mechanics Reviews 2002;55:495–532. https://doi.org/10.1115/1.1490129.

[44] Jamal-Omidi M, ShayanMehr M. Improving the dispersion of SWNT in epoxy resin through a simple Multi-Stage method. Journal of King Saud University - Science 2019;31:202–8. https://doi.org/10.1016/j.jksus.2018.01.007.

[45] Jakubinek MB, Ashrafi B, Zhang Y, Martinez-Rubi Y, Kingston CT, Johnston A, et al. Single-walled carbon nanotube-epoxy composites for structural and conductive aerospace adhesives. Composites Part B: Engineering 2015;69:87–93. https://doi.org/10.1016/j.compositesb.2014.09.022.

[46] Baltzis D, Bekas DG, Tzachristas G, Parlamas A, Karabela M, Zafeiropoulos NE, et al. Multi-scaled carbon reinforcements in ternary epoxy composite materials: Dispersion and electrical impedance study. Composites Science and Technology 2017;153:7–17. https://doi.org/10.1016/j.compscitech.2017.09.035.

[47] Gkikas G, Barkoula NM, Paipetis AS. Effect of dispersion conditions on the thermo-mechanical and toughness properties of multi walled carbon nanotubes-reinforced epoxy. Composites Part B: Engineering, vol. 43, 2012, p. 2697–705. https://doi.org/10.1016/j.compositesb.2012.01.070.

[48] Krause B, Villmow T, Boldt R, Mende M, Petzold G, Pötschke P. Influence of dry grinding in a ball mill on the length of multiwalled carbon nanotubes and their dispersion and percolation behaviour in melt mixed polycarbonate composites. Composites Science and Technology 2011;71:1145–53. https://doi.org/10.1016/j.compscitech.2011.04.004.

[49] Montazeri A, Chitsazzadeh M. Effect of sonication parameters on the mechanical properties of multi-walled carbon nanotube/epoxy composites. Materials and Design 2014;56:500–8. https://doi.org/10.1016/j.matdes.2013.11.013.

[50] Baltzis D, Bekas DG, Tzachristas G, Parlamas A, Karabela M, Zafeiropoulos NE, et al. Multi-scaled carbon reinforcements in ternary epoxy composite materials: Dispersion and electrical impedance study. Composites Science and Technology 2017;153:7–17. https://doi.org/10.1016/j.compscitech.2017.09.035.

[51] D5045-99(2007). Standard Test Methods for Plane-Strain Fracture Toughness and Strain Energy Release Rate of Plastic Materials. ASTM Book of Standards 2013;99:1–9. https://doi.org/10.1520/D5045-14.priate.

[52] Zhang MQ, Yu G, Zeng HM, Zhang HB, Hou YH. Two-Step Percolation in Polymer Blends Filled with Carbon Black. 1998.

[53] Chen A, Tong L, Wu L, Liu Y, Yang X, Liao Z, et al. Research progress of microcapsule self-healing anticorrosive coatings. Journal of Physics: Conference Series 2021;2076. https://doi.org/10.1088/1742-6596/2076/1/012083.

[54] Wen N, Song T, Ji Z, Jiang D, Wu Z, Wang Y, et al. Recent advancements in self-healing materials: Mechanicals, performances and features. Reactive and Functional Polymers 2021;168:105041. https://doi.org/10.1016/j.reactfunctpolym.2021.105041.

[55] Rodriguez R, Bekas DG, Flórez S, Kosarli M, Paipetis AS. Development of self-contained microcapsules for optimised catalyst position in self-healing materials. Polymer (Guildf) 2020;187. https://doi.org/10.1016/j.polymer.2019.122084.

[56] Li Q, Siddaramaiah, Kim NH, Hui D, Lee JH. Effects of dual component microcapsules of resin and curing agent on the self-healing efficiency of epoxy. Composites Part B: Engineering 2013;55:79–85. https://doi.org/10.1016/j.compositesb.2013.06.006.

[57] Tian R, Fu X, Zheng Y, Liang X, Wang Q, Ling Y, et al. The preparation and characterization of double-layer microcapsules used for the self-healing of resin matrix composites. Journal of Materials Chemistry 2012;22:25437–46. https://doi.org/10.1039/c2jm34195f.

[58] Da Costa SF, Zuber M, Zakharova M, Mikhaylov A, Baumbach T, Kunka D, et al. Self-healing triggering mechanism in epoxy-based material containing microencapsulated amino-polysiloxane. Nano Select 2022;3:577–93. https://doi.org/10.1002/nano.202100091.

[59] Mookhoek SD, Fischer HR, Zwaag S van der. A numerical study into the effects of elongated capsules on the healing efficiency of liquid-based systems. Computational Materials Science 2009;47:506–11. https://doi.org/10.1016/j.commatsci.2009.09.017.

[60] Lv Z, Li S, Chen H. Analytical model for effects of capsule shape on the healing efficiency in self-healing materials. PLoS ONE 2017;12:1–15. https://doi.org/10.1371/journal.pone.0187299.

[61] Brown EN, Kessler MR, Sottos NR, White SR. In situ poly(urea-formaldehyde) microencapsulation of dicyclopentadiene. Journal of Microencapsulation 2003;20:719–30. https://doi.org/10.1080/0265204031000154160.

[62] Tsilimigkra X, Bekas D, Kosarli M, Tsantzalis S, Paipetis A, Kostopoulos V. Mechanical properties assessment of low-content capsule-based self-healing structural composites. Applied Sciences (Switzerland) 2020;10. https://doi.org/10.3390/APP10175739.

[63] Mookhoek SD, Fischer HR, Sybrand van der Zwaag. A numerical study into the effects of elongated capsules on the healing efficiency of liquid-based systems. Computational Materials Science 2009;47:506–11. https://doi.org/10.1038/35057232.

[64] Coope TS, Mayer UFJ, Wass DF, Trask RS, Bond IP. Self-healing of an epoxy resin using scandium(III) triflate as a catalytic curing agent. Advanced Functional Materials 2011;21:4624–31. https://doi.org/10.1002/adfm.201101660.

[65] Ghazali H, Ye L, Amir AN. Microencapsulated healing agents for an elevated-temperature cured epoxy: Influence of viscosity on healing efficiency. Polymers and Polymer Composites 2021;29:S1317–27. https://doi.org/10.1177/09673911211045373.

[66] Jin H, Mangun CL, Stradley DS, Moore JS, Sottos NR, White SR. Self-healing thermoset using encapsulated epoxy-amine healing chemistry. Polymer (Guildf) 2012;53:581–7. https://doi.org/10.1016/j.polymer.2011.12.005.

[67] Brown EN, Sottos NR, White SR. Fracture testing of a self-healing polymer composite. Experimental Mechanics 2002;42:372–9. https://doi.org/10.1177/001448502321548193.

[68] Coope TS, Mayer UFJ, Wass DF, Trask RS, Bond IP. Self-healing of an epoxy resin using scandium(III) triflate as a catalytic curing agent. Advanced Functional Materials 2011;21:4624–31. https://doi.org/10.1002/adfm.201101660.

[69] Zhang H, Zhang X, Bao C, Li X, Duan F, Friedrich K, et al. Skin-Inspired, Fully Autonomous Self-Warning and Self-Repairing Polymeric Material under Damaging Events. Chemistry of Materials 2019;31:2611–8. https://doi.org/10.1021/acs.chemmater.9b00398.

[70] Caruso MM, Schelkopf SR, Jackson AC, Landry AM, Braun P V., Moore JS. Microcapsules containing suspensions of carbon nanotubes. Journal of Materials Chemistry 2009;19:6093–6. https://doi.org/10.1039/b910673a.

[71] Odom SA, Tyler TP, Caruso MM, Ritchey JA, Schulmerich M V., Robinson SJ, et al. Autonomic restoration of electrical conductivity using polymer-stabilized carbon nanotube and graphene microcapsules. Applied Physics Letters 2012;101. https://doi.org/10.1063/1.4737935.

[72] Zamal HH, Barba D, Aïssa B, Haddad E, Rosei F. Recovery of electro-mechanical properties inside self-healing composites through microencapsulation of carbon nanotubes. Scientific Reports 2020;10:1–13. https://doi.org/10.1038/s41598-020-59725-6.

[73] Bailey BM, Leterrier Y, Garcia SJ, Van Der Zwaag S, Michaud V. Electrically conductive self-healing polymer composite coatings. Progress in Organic Coatings 2015;85:189–98. https://doi.org/10.1016/j.porgcoat.2015.04.013.

[74] Foteinidis G, Tsirka K, Tzounis L, Baltzis D, Paipetis AS. The Role of Synergies of MWCNTs and Carbon Black in the Enhancement of the Electrical and Mechanical Response of Modified Epoxy Resins. Applied Siences 2019;9:3757.

[75] Blaiszik BJ, Caruso MM, McIlroy DA, Moore JS, White SR, Sottos NR. Microcapsules filled with reactive solutions for self-healing materials. Polymer (Guildf) 2009;50:990–7. https://doi.org/10.1016/j.polymer.2008.12.040.

[76] Kosarli M, Bekas DG, Tsirka K, Baltzis D, Vaimakis-Tsogkas D, Orfanidis S, et al. Microcapsule-based self-healing materials: Healing efficiency and toughness reduction vs. capsule size. Composites Part B: Engineering 2019;171:78–86. https://doi.org/10.1016/j.compositesb.2019.04.030.

[77] Hia IL, Pasbakhsh P, Chan ES, Chai SP. Electrosprayed Multi-Core Alginate Microcapsules as Novel Self-Healing Containers. Scientific Reports 2016;6:1–8. https://doi.org/10.1038/srep34674.

[78] Coope TS, Wass DF, Trask RS, Bond IP. Metal triflates as catalytic curing agents in self-healing fibre reinforced polymer composite materials. Macromolecular Materials and Engineering 2014;299:208–18. https://doi.org/10.1002/mame.201300026.

[79] Esser-Kahn AP, Odom SA, Sottos NR, White SR, Moore JS. Triggered release from polymer capsules. Macromolecules 2011;44:5539–53. https://doi.org/10.1021/ma201014n.

[80] Cosco S, Ambrogi V, Musto P, Carfagna C. Properties of poly(urea-formaldheyde) microcapsules containing an epoxy resin. Journal of Applied Polymer Science 2007;105:1400–11. https://doi.org/10.1002/app.26263.

[81] Naveen V, Raja S, Deshpande AP. A two-step approach for synthesis, characterization and analysis of dicyclopentadiene–urea formaldehyde–siloxane-based double-walled microcapsules used in self-healing composites. International Journal of Plastics Technology 2019. https://doi.org/10.1007/s12588-019-09247-2.

[82] Bolimowski PA, Bond IP, Wass DF. Robust synthesis of epoxy resin-filled microcapsules for application to self-healing materials. Philosophical Transactions of the Royal Society A: Mathematical, Physical and Engineering Sciences 2016;374. https://doi.org/10.1098/rsta.2015.0083.

[83] Dresselhaus MS, Dresselhaus G, Saito R, Jorio A. Raman spectroscopy of carbon nanotubes. Physics Reports 2005;409:47–99. https://doi.org/10.1016/j.physrep.2004.10.006.

[84] Bokobza L, Bruneel JL, Couzi M. Raman spectroscopy as a tool for the analysis of carbon-based materials (highly oriented pyrolitic graphite, multilayer graphene and multiwall carbon nanotubes) and of some of their elastomeric composites. Vib Spectrosc 2014;74:57–63. https://doi.org/10.1016/j.vibspec.2014.07.009.

[85] T. LY, L. KJ. DEVELOPMENTS IN REINFORCED PLASTICS-4 CONTENTS OF VOLUMES 1 TO 3 Volume 1. Elsevier Applied Science Publishers LTD; 1984. https://doi.org/10.1007/978-94-009-5620-9.

[86] Bokobza L, Zhang J. Raman spectroscopic characterization of multiwall carbon nanotubes and of composites. Express Polymer Letters 2012;6:601–8. https://doi.org/10.3144/expresspolymlett.2012.63.

[87] Min Li, Zhenzhen Wang, Qianli Liu, Shaokai Wang, Yizhuo Gu, Yanxia Li ZZ. Polyvinyl Alcohol-Modified Pithecellobium Clypearia Benth Herbal Residue FiberPolypropylene Composites. Polymer Composites 2016;37:915–24. https://doi.org/10.1002/pc.

[88] Levita G, De Petris S, Marchetti A, Lazzeri A. Crosslink density and fracture toughness of epoxy resins. Journal of Materials Science 1991;26:2348–52. https://doi.org/10.1007/BF01130180.

[89] Tzavidi S, Zotiadis C, Porfyris A, Korres DM, Vouyiouka S. Epoxy loaded poly(urea-formaldehyde) microcapsules via in situ polymerization designated for self-healing coatings. Journal of Applied Polymer Science 2020;137:1–11. https://doi.org/10.1002/app.49323.

[90] Zhang H, Zhang X, Bao C, Li X, Sun D, Duan F, et al. Direct microencapsulation of pure polyamine by integrating microfluidic emulsion and interfacial polymerization for practical self-healing materials. Journal of Materials Chemistry A 2018;6:24092–9. https://doi.org/10.1039/c8ta08324j.

[91] Zhang H, Zhang X, Bao C, Li X, Duan F, Friedrich K, et al. Skin-Inspired, Fully Autonomous Self-Warning and Self-Repairing Polymeric Material under Damaging Events. Chemistry of Materials 2019;31:2611–8. https://doi.org/10.1021/acs.chemmater.9b00398.

[92] Zhang H, Xiao K, Lin Z, Shi S. Epoxy microcapsules for high-performance self-healing materials using a novel method via integrating electrospraying and interfacial polymerization. Journal of Materials Science and Technology 2022;112:59–67. https://doi.org/10.1016/j.jmst.2021.09.045.

[93] Xu X, Zhou Z, Qin L, Yu C, Zhang F. Preparation of PVA/PU/PUA microcapsules and application in self-healing two-component waterborne polyurethane coatings. Journal of Coatings Technology and Research 2022. https://doi.org/10.1007/s11998-021-00577-8.

[94] Mookhoek SD, Blaiszik BJ, Fischer HR, Sottos NR, White SR, Van Der Zwaag S. Peripherally decorated binary microcapsules containing two liquids. Journal of Materials Chemistry 2008;18:5390–4. https://doi.org/10.1039/b810542a.

[95] Farzi G, Davoodi A, Ahmadi A, Neisiany RE, Anwer MK, Aboudzadeh MA. Encapsulation of Cerium Nitrate within Poly(urea-formaldehyde) Microcapsules for the Development of Self-Healing Epoxy-Based Coating. ACS Omega 2021;6:31147–53. https://doi.org/10.1021/acsomega.1c04597.

[96] White SR, Sottos NR, Geubelle PH, Moore JS, Kessler MR, Sriram SR, et al. Autonomic healing of polymer composites. Nature 2001;409:794–7. https://doi.org/10.1038/35057232.

[97] Liu X, Sheng X, Lee JK, Kessler MR. Synthesis and Characterization of Melamine-Urea-Formaldehyde Microcapsules Containing ENB-Based Self-Healing Agents. Macromolecular Journals 2009;294:289–395.

[98] Liu X, Zheng H, Li G, Li H, Zhang P, Tong W, et al. Fabrication of polyurethane microcapsules with different shapes and their influence on cellular internalization. Colloids and Surfaces B: Biointerfaces 2017;158:675–81. https://doi.org/10.1016/j.colsurfb.2017.06.036.

[99] Alizadegan F, Pazokifard S, Mirabedini SM, Danaei M, Farnood R. Polyurethane-based microcapsules containing reactive isocyanate compounds: Study on preparation procedure and solvent replacement. Colloids and Surfaces A: Physicochemical and Engineering Aspects 2017;529:750–9. https://doi.org/10.1016/j.colsurfa.2017.06.058.

[100] Ahangaran F, Navarchian AH, Picchioni F. Material encapsulation in poly(methyl methacrylate) shell: A review. Journal of Applied Polymer Science 2019;136:1–21. https://doi.org/10.1002/app.48039.

[101] Ma Y, Liu J, Zhang Y, Ge Y, Wu R, Song X, et al. Mechanical behavior and self-healing mechanism of polyurea-based double-walled microcapsule/epoxy composite films. Progress in Organic Coatings 2021;157:106283. https://doi.org/10.1016/j.porgcoat.2021.106283.

[102] Sun G, Zhang Z. Mechanical strength of microcapsules made of different wall materials. vol. 242. 2002.

[103] Yuan L, Gu A, Liang G. Preparation and properties of poly(urea–formaldehyde) microcapsules filled with epoxy resins. Materials Chemistry and Physics 2008;110:417–25. https://doi.org/10.1016/J.MATCHEMPHYS.2008.02.035.

[104] Fereidoon A, Ghorbanzadeh Ahangari M, Jahanshahi M. Effect of nanoparticles on the morphology and thermal properties of self-healing poly(urea-formaldehyde) microcapsules. Journal of Polymer Research 2013;20. https://doi.org/10.1007/s10965-013-0151-3.

[105] Ghorbanzadeh Ahangari M, Fereidoon A, Jahanshahi M, Sharifi N. Effect of nanoparticles on the micromechanical and surface properties of poly(urea-formaldehyde) composite microcapsules. Composites Part B: Engineering 2014;56:450–5. https://doi.org/10.1016/j.compositesb.2013.08.071.

[106] Jackson AC, Bartelt JA, Marczewski K, Sottos NR, Braun P V. Silica-protected micron and sub-micron capsules and particles for self-healing at the microscale. Macromolecular Rapid Communications 2011;32:82–7. https://doi.org/10.1002/marc.201000468.

[107] Roche S, Ibarz G, Crespo C, Chiminelli A, Araujo A, Santos R, et al. Self-sensing polymeric materials based on fluorescent microcapsules for the detection of microcracks. Journal of Materials Research and Technology 2022;16:505–15. https://doi.org/10.1016/j.jmrt.2021.11.014.

[108] Matsuda T, Jadhav N, Kashi KB, Jensen M, Gelling VJ. Release behavior of pH sensitive microcapsules containing corrosion inhibitor. Progress in Organic Coatings 2019;132:9–14. https://doi.org/10.1016/j.porgcoat.2019.03.032.

[109] Brown EN, Kessler MR, Sottos NR, White SR. In situ poly(urea-formaldehyde) microencapsulation of dicyclopentadiene. Journal of Microencapsulation 2003;20:719–30. https://doi.org/10.1080/0265204031000154160.

[110] Fereidoon A, Ghorbanzadeh Ahangari M, Jahanshahi M. Effect of nanoparticles on the morphology and thermal properties of self-healing poly(urea-formaldehyde) microcapsules. Journal of Polymer Research 2013;20. https://doi.org/10.1007/s10965-013-0151-3.

[111] Ghorbanzadeh Ahangari M, Fereidoon A, Jahanshahi M, Sharifi N. Effect of nanoparticles on the micromechanical and surface properties of poly(urea-formaldehyde) composite microcapsules. Composites Part B: Engineering 2014;56:450–5. https://doi.org/10.1016/j.compositesb.2013.08.071.

[112] Bekas D, Grammatikos SA, Kouimtzi C, Paipetis AS. Linear and non-linear electrical dependency of carbon nanotube reinforced composites to internal damage. IOP Conference Series: Materials Science and Engineering 2015;74. https://doi.org/10.1088/1757-899X/74/1/012002.

[113] Bekas DG, Baltzis D, Paipetis AS. Nano-reinforced polymeric healing agents for vascular self-repairing composites. Materials and Design 2017;116:538–44. https://doi.org/10.1016/j.matdes.2016.12.049.

[114] Vavouliotis A, Karapappas P, Loutas T, Voyatzi T, Paipetis A, Kostopoulos V. Multistage fatigue life monitoring on carbon fibre reinforced polymers enhanced with multiwall carbon nanotubes. Plastics, Rubber and Composites 2009;38:124–30. https://doi.org/10.1179/174328909X387928.

[115] Kosarli M, Tsirka K, Chalari S, Palantza A, Paipetis AS. Recovery of Fracture Toughness on Self-Healing Epoxies Using Ternary Nanomodified Microcapsules : A Parametric Study 2020;827:258–62.

[116] He Z, Jiang S, An N, Li X, Li Q, Wang J, et al. Self-healing isocyanate microcapsules for efficient restoration of fracture damage of polyurethane and epoxy resins. Journal of Materials Science 2019;54:8262–75. https://doi.org/10.1007/s10853-018-03236-3.

[117] Yuan L, Huang S, Hu Y, Zhang Y, Gu A, Liang G, et al. Poly(phenylene oxide) modified cyanate resin for self-healing. Polymers for Advanced Technologies 2014;25. https://doi.org/10.1002/pat.3290.

[118] Zhu DY, Rong MZ, Zhang MQ. Preparation and characterization of multilayered microcapsule-like microreactor for self-healing polymers. Polymer (Guildf) 2013;54:4227–36. https://doi.org/10.1016/j.polymer.2013.06.014.

[119] Ismail NA, Khan A, Fayyad E, Kahraman R, Abdullah AM, Shakoor RA. Self-healing performance of smart polymeric coatings modified with tung oil and linalyl acetate. Polymers (Basel) 2021;13. https://doi.org/10.3390/polym13101609.

[120] Yin T, Rong MZ, Zhang MQ, Yang GC. Self-healing epoxy composites - Preparation and effect of the healant consisting of microencapsulated epoxy and latent curing agent. Composites Science and Technology 2007;67:201–12. https://doi.org/10.1016/j.compscitech.2006.07.028.

[121] Wang Y, Li Y, Zhang Z, Zhang Y. Effect of doping microcapsules on typical electrical performances of self-healing polyethylene insulating composite. Applied Sciences (Switzerland) 2019;9. https://doi.org/10.3390/app9153039.

[122] Khan MZ, Farooq U, Imtiaz MA, Khan U, Khan A, Zaib A, et al. Effect of microcapsules doping on dielectric performance of self-healing epoxy resin composites. Bulletin of Materials Science 2021;44. https://doi.org/10.1007/s12034-021-02536-w.

[123] Icduygu MG, Asilturk M, Yalcinkaya MA, Hamidi YK, Altan MC. Three-Dimensional Nano-Morphology of Carbon Nanotube / Epoxy Filled Poly(methyl methacrylate) Microcapsules. Materials 2019;12:26. https://doi.org/doi:10.3390/ma12091387.

[124] Yashchenok AM, Bratashov DN, Gorin DA, Lomova M v., Pavlov AM, Sapelkin A v., et al. Carbon nanotubes on polymeric microcapsules: Freestanding structures and point-wise laser openings. Advanced Functional Materials 2010;20:3136–42. https://doi.org/10.1002/adfm.201000846.

[125] Lanzara G, Yoon Y, Liu H, Peng S, Lee WI. Carbon nanotube reservoirs for self-healing materials. Nanotechnology 2009;20. https://doi.org/10.1088/0957-4484/20/33/335704.

[126] Kosarli M, Bekas DG, Tsirka K, Baltzis D, Vaimakis-Tsogkas D, Orfanidis S, et al. Microcapsule-based self-healing materials: Healing efficiency and toughness reduction vs. capsule size. Composites Part B: Engineering 2019;171:78–86. https://doi.org/10.1016/j.compositesb.2019.04.030.

[127] Foteinidis G, Tsirka K, Tzounis L, Baltzis D, Paipetis AS. The role of synergies of MWCNTs and Carbon Black in the enhancement of the electrical and mechanical response of modified epoxy resins. Applied Sciences (Switzerland) 2019;9. https://doi.org/10.3390/app9183757.

[128] Blaiszik BJ, Sottos NR, White SR. Nanocapsules for self-healing materials. Composites Science and Technology 2008;68:978–86. https://doi.org/10.1016/j.compscitech.2007.07.021.

[129] Kessler MR, White SR. Self-activated healing of delamination damage in woven composites. Composites Part A: Applied Science and Manufacturing 2001;32:683–99. https://doi.org/10.1016/S1359-835X(00)00149-4.

[130] Kessler MR, Sottos NR, White SR. Self-healing structural composite materials. Composites Part A: Applied Science and Manufacturing 2003;34:743–53. https://doi.org/10.1016/S1359-835X(03)00138-6.

[131] Kontiza A, Semitekolos D, Milickovic TK, Pappas P, Koutroumanis N, Galiotis C, et al. Double cantilever beam test and micro-computed tomography as evaluation tools for self-healing of CFRPs loaded with DCPD microcapsules. Composite Structures 2022;279. https://doi.org/10.1016/j.compstruct.2021.114780.

[132] Tsilimigkra X, Bekas D, Kosarli M, Tsantzalis S, Paipetis A, Kostopoulos V. Mechanical properties assessment of low-content capsule-based self-healing structural composites. Applied Sciences (Switzerland) 2020;10. https://doi.org/10.3390/APP10175739.

[133] Razali N, Sultan MTH, Mustapha F, Yidris N, Ishak MR. Impact Damage on Composite Structures – A Review. The International Journal Of Engineering And Science 2014;3:8–20.

[134] Vintila IS, Draghici S, Petrescu HA, Paraschiv A, Condruz MR, Maier LR, et al. Evaluation of dispersion methods and mechanical behaviour of glass fibre composites with embedded self-healing systems. Polymers (Basel) 2021;13. https://doi.org/10.3390/polym13101642.

[135] Yuan YC, Ye Y, Rong MZ, Chen H, Wu J, Zhang MQ, et al. Self-healing of low-velocity impact damage in glass fabric/epoxy composites using an epoxy-mercaptan healing agent. Smart Materials and Structures 2011;20. https://doi.org/10.1088/0964-1726/20/1/015024.

[136] El Mahi A, Berthelot JM, Brillaud J. Stiffness reduction and energy release rate of cross-ply laminates during fatigue tests. Composite Structures 1995;30:123–30. https://doi.org/10.1016/0263-8223(94)00061-1.

[137] Kim SY, Sottos NR, White SR. Self-healing of fatigue damage in cross-ply glass/epoxy laminates. Composites Science and Technology 2019;175:122–7. https://doi.org/10.1016/j.compscitech.2019.03.016.

[138] Greenhalgh E, Huertas Garcia M. Fracture mechanisms and failure processes at stiffener run-outs in polymer matrix composite stiffened elements. Composites Part A: Applied Science and Manufacturing 2004;35:1447–58. https://doi.org/10.1016/j.compositesa.2004.05.006.

[139] Luterbacher R, Coope TS, Trask RS, Bond IP. Vascular self-healing within carbon fibre reinforced polymer stringer run-out configurations. Composites Science and Technology 2016;136:67–75. https://doi.org/10.1016/j.compscitech.2016.10.007.

[140] Foteinidis G, Paipetis AS. A novel composite with structural health monitoring functionality via 2d and 3d impedance mapping topography. Applied Sciences (Switzerland) 2021;11:1–19. https://doi.org/10.3390/app11041647.

[141] Directorate E. Airbus Industrie Test Method 2006:1–8.

[142] Standard D. Back to Composite Standards. ASTM International Designation: D 2011;i:4–6. https://doi.org/10.1520/D7136.

[143] Szekrényes a. Overview on the experimental investigations of the fracture toughness in composite materials. Hungarian Electronic Journal of Sciences, Http://Hej … 2002:1–19.

[144] Ebeling T, Hiltner A, Baer E, Fraser IM, Orton ML. Delamination failure of a woven glass fiber composite. Journal of Composite Materials 1997;31:1318–33. https://doi.org/10.1177/002199839703101304.

[145] Ghazali H, Ye L, Zhang MQ. Mode II interlaminar fracture toughness of CF/EP composite containing microencapsulated healing resins. Composites Science and Technology 2017;142:275–85. https://doi.org/10.1016/j.compscitech.2017.02.018.

[146] Bradley WL. Relationship of Matrix Toughness to Interlaminar Fracture Toughness. Composite Materials Series 1989;6:159–87. https://doi.org/10.1016/B978-0-444-87286-9.50009-7.

[147] Kessler MR, White SR. Self-activated healing of delamination damage in woven composites. Composites Part A: Applied Science and Manufacturing 2001;32:683–99. https://doi.org/10.1016/S1359-835X(00)00149-4.

[148] Hine PJ, Brew B, Duckett RA, Ward IM. Failure mechanisms in continuous carbon-fibre reinforced PEEK composites. Composites Science and Technology 1989;35:31–51. https://doi.org/10.1016/0266-3538(89)90069-9.

[149] Hine PJ, Brew B, Duckett RA, Ward IM. The fracture behaviour of carbon fibre reinforced poly(ether etherketone). Composites Science and Technology 1988;33:35–71. https://doi.org/10.1016/0266-3538(88)90054-1.

[150] Gergely RCR, Santa Cruz WA, Krull BP, Pruitt EL, Wang J, Sottos NR, et al. Restoration of Impact Damage in Polymers via a Hybrid Microcapsule–Microvascular Self-Healing System. Advanced Functional Materials 2018;28:35–9. https://doi.org/10.1002/adfm.201704197.

[151] Zhang H, Liu Y, Kuwata M, Bilotti E, Peijs T. Improved fracture toughness and integrated damage sensing capability by spray coated CNTs on carbon fibre prepreg. Composites Part A: Applied Science and Manufacturing 2015;70:102–10. https://doi.org/10.1016/j.compositesa.2014.11.029.

[152] Meola C, Carlomagno GM. Impact damage in GFRP: New insights with infrared thermography. Composites Part A: Applied Science and Manufacturing 2010;41:1839–47. https://doi.org/10.1016/j.compositesa.2010.09.002.

[153] Kostopoulos V, Kotrotsos A, Geitona A, Tsantzalis S. Low velocity impact response and post impact assessment of carbon fiber/epoxy composites modified with Diels-Alder based healing agent. A novel approach. Composites Part A: Applied Science and Manufacturing 2021;140:106151. https://doi.org/10.1016/j.compositesa.2020.106151.

[154] Williams GJ, Bond IP, Trask RS. Compression after impact assessment of self-healing CFRP. Composites Part A: Applied Science and Manufacturing 2009;40:1399–406. https://doi.org/10.1016/j.compositesa.2008.05.021.

[155] Wu W, Wang Q, Li W. Comparison of tensile and compressive properties of carbon/glass interlayer and intralayer hybrid composites. Materials 2018;11. https://doi.org/10.3390/ma11071105.

[156] Greenhalgh ES, Ankersen J, Asp LE, Bismarck A, Fontana Q, Houlle M, et al. Mechanical, electrical and microstructural characterisation of multifunctional structural power composites. Journal of Composite Materials 2015;49:1823–34. https://doi.org/10.1177/0021998314554125.

[157] D7137 Standard. Compressive Residual Strength Properties of Damaged Polymer Matrix Composite Plates. ASTM Standards 2012;i:1–17. https://doi.org/10.1520/D7137.

[158] Blaiszik BJ, Kramer SLB, Olugebefola SC, Moore JS, Sottos NR, White SR. Self-healing polymers and composites. Annual Review of Materials Research 2010;40:179–211. https://doi.org/10.1146/annurev-matsci-070909-104532.

[159] Hayes SA, Zhang W, Branthwaite M, Jones FR. Self-healing of damage in fibre-reinforced polymer-matrix composites. Journal of the Royal Society Interface 2007;4:381–7. https://doi.org/10.1098/rsif.2006.0209.

[160] Hayes SA, Jones FR, Marshiya K, Zhang W. A self-healing thermosetting composite material. Composites Part A: Applied Science and Manufacturing 2007;38:1116–20. https://doi.org/10.1016/J.COMPOSITESA.2006.06.008.

[161] Grande AM, Castelnovo L, Landro L di, Giacomuzzo C, Francesconi A, Rahman MA. Rate-dependent self-healing behavior of an ethylene-co-methacrylic acid ionomer under high-energy impact conditions. Journal of Applied Polymer Science 2013;130:1949–58. https://doi.org/10.1002/app.39384.

[162] Sundaresan VB, Morgan A, Castellucci M. Self-Healing of Ionomeric Polymers with Carbon Fibers from Medium-Velocity Impact and Resistive Heating. Smart Materials Research 2013;2013:1–12. https://doi.org/10.1155/2013/271546.

[163] Aida T, Meijer EW, Stupp SI. Functional Supramolecular Polymers. n.d.

[164] SELF-HEALING POLYMER-BASED SYSTEMS. 2020.

[165] Kostopoulos V, Kotrotsos A, Baltopoulos A, Tsantzalis S, Tsokanas P, Loutas T, et al. Mode II fracture toughening and healing of composites using supramolecular polymer interlayers. Express Polymer Letters 2016;10:914–26. https://doi.org/10.3144/expresspolymlett.2016.85.

[166] Kostopoulos V, Kotrotsos A, Tsantzalis S, Tsokanas P, Loutas T, Bosman AW. Toughening and healing of continuous fibre reinforced composites by supramolecular polymers. Composites Science and Technology 2016;128:84–93. https://doi.org/10.1016/j.compscitech.2016.03.021.

[167] Memon H, Wei Y, Zhu C. Recyclable and reformable epoxy resins based on dynamic covalent bonds – Present, past, and future. Polymer Testing 2022;105. https://doi.org/10.1016/j.polymertesting.2021.107420.

[168] Zhang Y, Ye J, Qu D, Wang H, Chai C, Feng L. Thermo-adjusted self-healing epoxy resins based on Diels–Alder dynamic chemical reaction. Polymer Engineering and Science 2021;61:2257–66. https://doi.org/10.1002/pen.25753.

[169] Puyadena M, Calafel I, González de San Román E, Martin L, González A, Irusta L. Recyclable Epoxy Resin via Simultaneous Dual Permanent/Reversible Crosslinking Based on Diels–Alder Chemistry. Macromolecular Chemistry and Physics 2021;222. https://doi.org/10.1002/macp.202100146.

[170] Houk KN, Montgomery LK, Schueller K, Bartlett PD. 1,2-Cyclosddition Reactions. vol. 2. George Thieme Verlag; 1963.

[171] Tian Q, Yuan YC, Rong MZ, Zhang MQ. A thermally remendable epoxy resin. Journal of Materials Chemistry 2009;19:1289–96. https://doi.org/10.1039/b811938d.

[172] Chen X, Wudl F, Mal AK, Shen H, Nutt SR. New thermally remendable highly cross-linked polymeric materials. Macromolecules 2003;36:1802–7. https://doi.org/10.1021/ma0210675.

[173] Zhang W, Duchet J, Gérard JF. Self-healable interfaces based on thermo-reversible Diels-Alder reactions in carbon fiber reinforced composites. Journal of Colloid and Interface Science 2014;430:61–8. https://doi.org/10.1016/j.jcis.2014.05.007.

[174] Park JS, Darlington T, Starr AF, Takahashi K, Riendeau J, Thomas Hahn H. Multiple healing effect of thermally activated self-healing composites based on Diels-Alder reaction. Composites Science and Technology 2010;70:2154–9. https://doi.org/10.1016/j.compscitech.2010.08.017.

[175] Kötteritzsch J, Stumpf S, Hoeppener S, Vitz J, Hager MD, Schubert US. One-component intrinsic self-healing coatings based on reversible crosslinking by diels-alder cycloadditions. Macromolecular Chemistry and Physics 2013;214:1636–49. https://doi.org/10.1002/macp.201200712.

[176] Roos K, Dolci E, Carlotti S, Caillol S. Activated anionic ring-opening polymerization for the synthesis of reversibly cross-linkable poly(propylene oxide) based on furan/maleimide chemistry. Polymer Chemistry 2016;7:1612–22. https://doi.org/10.1039/c5py01778e.

[177] Gaina V, Ursache O, Gaina C, Buruiana E. Novel Thermally-Reversible Epoxy-Urethane Networks Viorica Gaina, Oana Ursache, Constantin Gaina & Emil Buruiana Novel Thermally-Reversible Epoxy-Urethane Networks. Designed Monomers and Polymers 2012;15:63–73. https://doi.org/10.1163/156855511X606155.

[178] Bai N, Saito K, Simon GP. Synthesis of a diamine cross-linker containing Diels-Alder adducts to produce self-healing thermosetting epoxy polymer from a widely used epoxy monomer. Polymer Chemistry 2013;4:724–30. https://doi.org/10.1039/c2py20611k.

[179] Bai N, Simon GP, Saito K. Investigation of the thermal self-healing mechanism in a cross-linked epoxy system. RSC Advances 2013;3:20699–707. https://doi.org/10.1039/c3ra43746a.

[180] Chen X, Dam MA, Ono K, Mal A, Shen H, Nutt SR, et al. A thermally re-mendable cross-linked polymeric material. Science (1979) 2002;295:1698–702. https://doi.org/10.1126/science.1065879.

[181] Orozco F, Kaveh M, Santosa DS, Lima GMR, Gomes DR, Pei Y, et al. Electroactive Self-Healing Shape Memory Polymer Composites Based on Diels-Alder Chemistry. ACS Applied Polymer Materials 2021;3:6147–56. https://doi.org/10.1021/acsapm.1c00999.

[182] Kostopoulos V, Kotrotsos A, Geitona A, Tsantzalis S. Low velocity impact response and post impact assessment of carbon fiber/epoxy composites modified with Diels-Alder based healing agent. A novel approach. Composites Part A: Applied Science and Manufacturing 2021;140. https://doi.org/10.1016/j.compositesa.2020.106151.

[183] Aubert JH. Thermally removable epoxy adhesives incorporating thermally reversible Diels-Alder adducts. Journal of Adhesion 2003;79:609–16. https://doi.org/10.1080/00218460309540.

[184] Pratama PA, Peterson AM, Palmese GR. The role of maleimide structure in the healing of furan-functionalized epoxy-amine thermosets. Polymer Chemistry 2013;4:5000–6. https://doi.org/10.1039/c3py00084b.

[185] McElhanon JR, Wheeler DR. Thermally responsive dendrons and dendrimers based on reversible furan-maleimide diels-alder adducts. Organic Letters 2001;3:2681–3. https://doi.org/10.1021/ol0101281.

[186] Yasuda K, Takahashi Y, Sugane K, Shibata M. Self-healing high-performance thermosets utilizing furan/maleimide Diels–Alder, epoxy/amine nucleophilic ring-opening, and maleimide/amine Michael reactions. Polymer Bulletin 2021. https://doi.org/10.1007/s00289-021-03912-6.

[187] Chen S, Feng Y, Zhang ZY, Li XY, Zhang JY, Zhao JB. Catalyzed Michael addition, polycondensation, and the related performance of Diels–Alder self-healing crosslinked polyamides. Polymer Engineering and Science 2022;62:1269–80. https://doi.org/10.1002/pen.25924.

[188] Turkenburg DH, Fischer HR. Diels-Alder based, thermo-reversible cross-linked epoxies for use in self-healing composites. Polymer (United Kingdom) 2015;79:187–94. https://doi.org/10.1016/j.polymer.2015.10.031.

[189] Bai N, Saito K, Simon GP. Synthesis of a diamine cross-linker containing Diels-Alder adducts to produce self-healing thermosetting epoxy polymer from a widely used epoxy monomer. Polymer Chemistry 2013;4:724–30. https://doi.org/10.1039/c2py20611k.

[190] Kostopoulos V, Kotrotsos A, Baltopoulos A, Tsantzalis S, Tsokanas P, Loutas T, et al. Mode II fracture toughening and healing of composites using supramolecular polymer interlayers. Express Polymer Letters 2016;10:914–26. https://doi.org/10.3144/expresspolymlett.2016.85.

[191] Bai N, Simon GP, Saito K. Investigation of the thermal self-healing mechanism in a cross-linked epoxy system. RSC Advances 2013;3:20699–707. https://doi.org/10.1039/c3ra43746a.

[192] Aubert JH. Thermally removable epoxy adhesives incorporating thermally reversible Diels-Alder adducts. Journal of Adhesion 2003;79:609–16. https://doi.org/10.1080/00218460309540.

[193] Socrates G. Infrared and Raman characteristic group frequencies. 2004. https://doi.org/10.1002/jrs.1238.

[194] Parker SF, Mason SM, Williams KPJ. Fourier Transform Raman and infrared spectroscopy of N-phenylmaleimide and methylene dianiline bismaleimide. Spectrochimica Acta Part A: Molecular Spectroscopy 1990;46:315–21. https://doi.org/10.1016/0584-8539(90)80100-D.

## Appendix A

The sensing elements (sensors) were not attached to the external surface of specimens but formed inside the material. For the third category, three carbon tows with 2 cm space (not in contact) were placed between the top and the second ply, parallel to the second ply (at $90^o$ direction). Three more carbon tows were placed at zero degrees between plies 6 and 7, parallel with the glass fibers. Between plies 13 and 14, three more carbon tows were positioned at the $90^o$ direction, parallel with the 14th ply (at $90^o$). The final three-carbon tows were placed between the 17 and the 18th ply of the composite specimen at $0^0$, parallel with the last ply. The specific layout was the formation of sensing elements in the junction points between the carbon tows that form a 90 angle with the direction of each upper series of tows. At the edge of each carbon tow, a copper strip was attached with conductive silver tape replacing the cables attached at Mode-II and lap strap specimens (**Figure 119**).

For the fourth category, each carbon tow was replaced with the spray coating of SWCNTs ink at parallel lines according to the previous pattern using the HVLP G/F PAINT GUN with a nose diameter of 2.5 mm. The ink was manufactured with the sonication of 0.35 wt. % SWCNTs into water/surfactant (SDBS) solution at 1:1 ratio. The percentages were chosen after resistance measurements of inks with different content of SWCNTs and according to their viscosity. The glass fabrics were examined via SEM and resistance measurements after applying a variety of layers to the fabrics. The most sufficient results were exhibited after coating 12 layers of the conductive ink (0.35 wt. % SWCNTs) that revealed sufficient coating (**Figure 118**) and low resistance values of 34.8 Ohm. A copper strip was attached with conductive silver tape at the edge of each spray line.

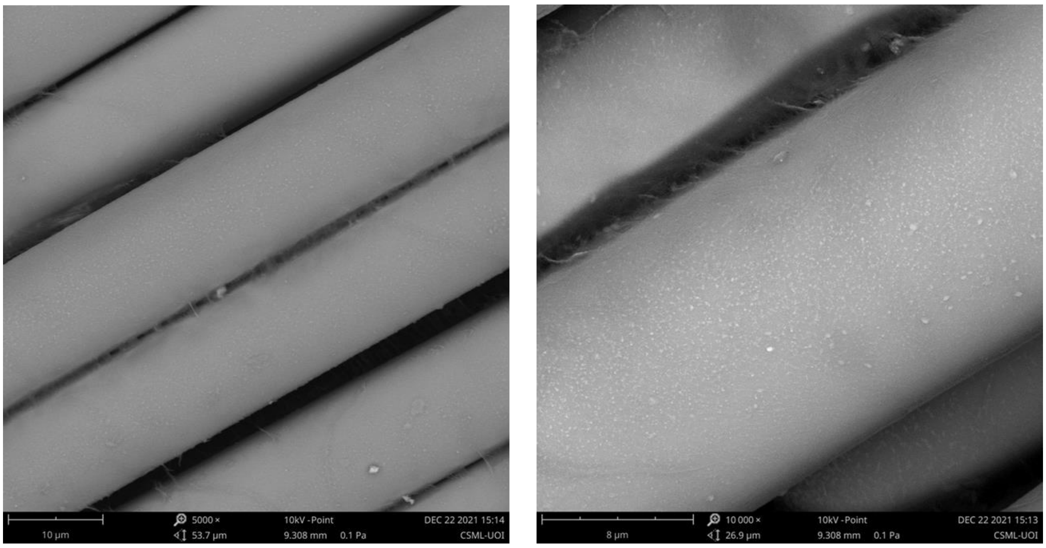

**Figure 118.** SEM images of spray-coated glass fabrics with 12 layers of ink at different magnifications.

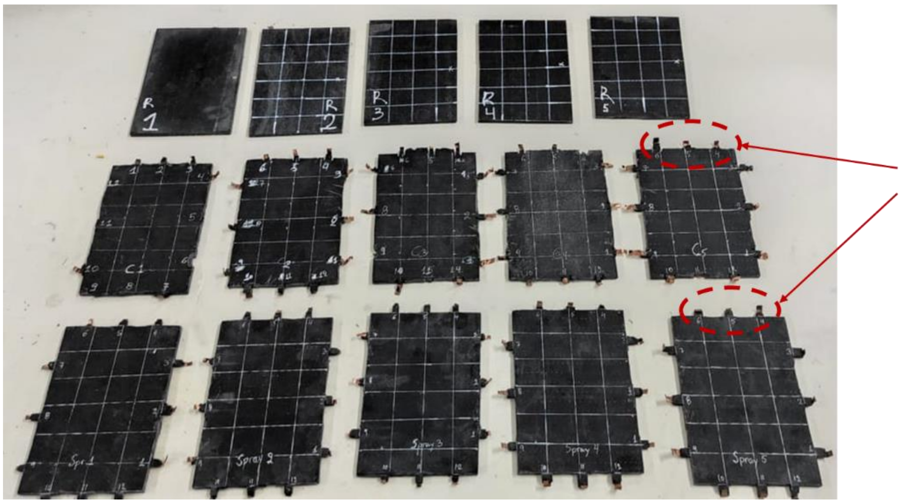

Copper strips for impedance measurements

**Figure 119.** Low-velocity impact specimens. The marked areas depict the copper strips incorporated for the electrical conductivity measurements.